



TECHNICAL UNIVERSITY OF LIBEREC  
Faculty of Mechatronics, Informatics  
and Interdisciplinary Studies ■

# Computational spectroscopy of optical materials

*Habilitation thesis*

Karel Žídek

Turnov 2021



## Abstract

This habilitation thesis summarizes a significant part of the work carried out between the years 2016-2021 by myself and my Group of Computational Spectroscopy and Imaging. The link connecting the presented work is the search for new efficient ways to characterize the properties of optical materials via optical spectroscopy. Optical spectroscopy, a set of non-contact and non-destructive methods, is a toolbox of choice to study absorption, photoluminescence, or refractive index changes in optical materials. Continuously increasing demand for higher robustness of optical coating, sensitive mapping of luminescing samples, or mapping quality of highly reflective layers – all these concerns stimulate the development of new methods to map various optical properties with improved sensitivity, acquisition time, or setup simplicity.

Firstly, the thesis covers the measurements where a weak response is to be mapped across the sample. A typical example is the measurement of photoluminescence spectra, where the weak signal needs to be integrated over a long period on a single spot. In such a case, mapping a sample by its gradual scanning is not realistic, and a different approach must be used. The possible solution is the concept of compressed sensing, which reduces the acquisition time to approx. 20% compared to the simple scanning. The single-pixel camera experiment makes it possible to retain a standard nonimaging experiment and to convert it into the imaging mode using structured illumination. We studied the implementation of compressive imaging in laser spectroscopy, where we used laser speckles as the structured light for the imaging of ultrafast processes, or hyperspectral photoluminescence imaging. We also demonstrated that the laser speckles could efficiently be applied in the time domain to extract photoluminescence dynamics.

Secondly, the thesis includes the methods to characterize the interfaces between thin films. Such methods are essential for tracking the quality of an optical coating, which is often the most fragile part of the optical element. One possible option to study the interfaces is the so-called femtosecond sonar, where the pump-probe experiment makes it possible to track acoustic wave propagation through a sample. The signal of the congested acoustic wave propagating across the interfaces makes it possible to access the interface quality. Another optical method uses the second harmonic generation as a process, which is highly sensitive to the interfaces and their quality. We have built both the experiments described above and carried out initial studies of single-layer samples. In both cases, we discuss the benefits of using structured femtosecond pulses in these experiments.

Nevertheless, to experiment with structured pulses, it is necessary to ensure their targeted generation and reliable characterization. Therefore, a significant part of the thesis is focused on the frequency-resolved optical gating (FROG) technique for pulse retrieval and spatial-light-modulator-base 4f pulse shaper for the targeted pulse shaping. We study the effect of real-life experimental conditions and imperfections on the generation and retrieval of highly complex pulses.

Finally, the thesis provides an overview of our efforts to characterize refractive index profiles in layers and optical coatings with a gradually varying refractive index. By creating a complex model combining transmission, reflection, and ellipsometric spectra under a set of angles, we studied the attainable precision of optical characterization of such layers.

In each chapter, the thesis also provides many directions, which were opened by the presented research and which will be pursued by the Group of Computational Spectroscopy and Imaging in the following years.

## Acknowledgment

Since the first one to thank in a thesis is the supervisor, I would like to express my greatest appreciation to my wife Jana. The true description of her endless energy, enthusiasm, and support would sound far too affected and gushing for her ears. Therefore, I will just use the simple – Thank you! Actually, many of the ideas in this thesis were triggered by her hints and insight.

Secondly, I would like to pay special thanks to all my past and current colleagues from the Group of Computational Spectroscopy and Imaging – Petra, Mariem, Martina, Ondřej, Jiří and Jiří, Nirmal, Vít, Lukáš, Jakub, Jan, Petr. Owing to them, the work has been a true pleasure and fun, rather than an everyday duty. In particular, I would like to use the chance to revert the usual order and thank all the students for their work during their these and internships.

Finally, there is a long list of people who highly influenced my life and my work. Starting from my childhood up to the years spent abroad. I have been fortunate to grow up in a very kind environment and work in places where the colleagues create a kind of family feeling. Since I do not want to miss a single person important to me, I shall not provide a specific list. The right people will "see" their name themselves just by reading the lines above.

Nevertheless, there was an important person whose contribution can be easily overlooked – my high-school teacher of physics Eva Jedličková. Her classes were the first moments when I appreciated the beauty of physics. Therefore, she is definitely the person who stayed at the very beginning of the work described in this thesis.



## Declaration

I hereby certify I, myself, have written my habilitation thesis as an original and primary work using the literature listed below.

I acknowledge that the Technical University of Liberec will make my habilitation thesis public in accordance with Section 47b of Act No. 111/1998 Coll., on Higher Education Institutions and Amendment to Other Acts (the Higher Education Act), as amended. I am aware of the consequences which may under the Higher Education Act result from a breach of this declaration.

25th August 2021

Karel Žídek





## List of abbreviations

<b>2DES</b>	2D coherent electronic spectroscopy
<b>BBO</b>	$\beta$ -barium borate
<b>CASSI</b>	Coded aperture snapshot spectral imaging
<b>CCD</b>	Charge-coupled device
<b>CS</b>	Compressed sensing
<b>CUP</b>	Compressed ultrafast photography
<b>D-FROG</b>	Dispersion scan frequency-resolved optical gating
<b>FFT</b>	Fast Fourier transform
<b>FLIM</b>	Fluorescence lifetime imaging
<b>FROG</b>	Frequency-resolved optical gating
<b>FWHM</b>	Full width half maximum
<b>GDD</b>	Group delay dispersion
<b>IR</b>	Infrared
<b>PL</b>	Photoluminescence
<b>RATS</b>	Random temporal speckles
<b>RUSH</b>	Random-phase ultrafast spectroscopy
<b>SF</b>	Sum-frequency
<b>SFG</b>	Sum-frequency generation
<b>SHG</b>	Second-harmonic generation
<b>SLM</b>	Spatial light modulator
<b>SNR</b>	Signal-to-noise ratio
<b>TA</b>	Transient absorption
<b>TOD</b>	Third-order dispersion
<b>UV</b>	Ultraviolet
<b>VR-SFG</b>	Vibrationally-resonant sum-frequency generation
<b>XFROG</b>	Cross-correlation frequency-resolved optical gating





# Contents

<b>1</b>	<b>Introduction</b>	<b>1</b>
1.1	Scope of the work . . . . .	2
1.2	Thesis structure . . . . .	3
<b>2</b>	<b>Compressive imaging in laser spectroscopy</b>	<b>5</b>
2.1	Introduction . . . . .	5
2.2	State of the art . . . . .	6
2.2.1	Laser spectroscopy . . . . .	6
2.2.2	Compressed sensing . . . . .	7
2.2.3	Compressed sensing in laser spectroscopy . . . . .	8
2.3	Results . . . . .	9
2.3.1	Laser speckles . . . . .	9
2.3.2	Speckle-based hyperspectral imaging . . . . .	10
2.3.3	Speckle-based ultrafast imaging . . . . .	11
2.3.4	PL decay measurements via random temporal speckles (RATS) . . . . .	13
2.4	Outlook . . . . .	14
2.5	Summary . . . . .	16
<b>3</b>	<b>Random phase ultrafast spectroscopy</b>	<b>17</b>
3.1	Introduction . . . . .	17
3.2	State of the art . . . . .	18
3.2.1	Pulse shaping . . . . .	18
3.2.2	Pulse characterization . . . . .	19
3.2.3	Frequency-resolved optical gating . . . . .	20
3.3	Results . . . . .	21
3.3.1	Frequency-resolved optical gating . . . . .	21
3.3.2	4f pulse shaper . . . . .	26
3.3.3	Dispersion scan frequency-resolved optical gating . . . . .	28
3.3.4	Pump-probe spectroscopy . . . . .	33
3.4	Outlook . . . . .	33
3.5	Summary . . . . .	35
<b>4</b>	<b>Optical characterization of thin films</b>	<b>37</b>
4.1	Introduction . . . . .	37
4.2	State of the art . . . . .	38
4.2.1	Optical characterization of thin films . . . . .	38
4.2.2	Second-order nonlinear interaction at interfaces . . . . .	39
4.3	Results . . . . .	40



4.3.1	Optical characterization of gradient thin films . . . . .	40
4.3.2	Second harmonic generation in thin films . . . . .	42
4.4	Outlook . . . . .	45
4.4.1	Second harmonic generation in thin films . . . . .	45
4.4.2	Optical characterization of gradient thin films . . . . .	45
4.5	Summary . . . . .	46
<b>5</b>	<b>Conclusions</b>	<b>47</b>
<b>6</b>	<b>Reprints</b>	<b>55</b>
	List and contribution statement . . . . .	55
	O. Denk et al., Opt. Expr. 2019; Ultrafast compressive imaging . . . . .	57
	J. Junek et al., Opt. Expr. 2020; Random temporal speckles . . . . .	70
	J. Junek et al., Opt. Expr. 2021; FLIM via RATS . . . . .	80
	K. Židek et al., Sci. Rep. 2017; Lensless PL imaging . . . . .	94
	P. Vesela et al., Opt. Expr. 2021; Delay line jitter in SHG FROG . . . . .	101
	M. Guesmi et al., arXiv 2020; D-FROG . . . . .	114
	V. Kanclir et al., arXiv 2020; Gradient SiON <sub>x</sub> layers . . . . .	127
	N. K. Das et al., J. Opt. 2021; SHG on Si <sub>3</sub> N <sub>4</sub> layers . . . . .	135



# Chapter 1

## Introduction

Visual perception of the world around us - its shapes and colors - is the dominating way how we learn about nature and its processes. For instance, we can easily distinguish a ripe blueberry from the unripe one or similar poisonous berries just by looking at the plant and the berry – without tasting it or doing the chemical analysis. Moreover, we can track the slow transition of the blueberry in time – from its first appearance to the ripe berry –, and we can make conclusions out of that.

Current scientific tasks are more advanced in the desired characteristics, yet the idea remains the same. For instance, in the field of optics fabrication, it would be of immense interest to “see” the spots where the interface between a lens and the coating layer suffers from imperfections. These imperfections need to be identified long before the layer will peel off in a harsh environment, or the interface will be damaged by intense laser light. At the same time, one needs to test the optical element without damaging the piece. The natural choice is to use the same concept, which worked for blueberries, i.e., spectroscopic imaging of a dynamic process.

The standard concept of image acquisition has remained the same since its first realization in 1822. An optical system creates an image in a plane, where we place a means to capture the light intensity. During the 200 years of development, the camera obscura was replaced by sophisticated lenses, photochemical processes were replaced by an electronic array detector. Nevertheless, the general idea remained the same.

Analogously, when we focus on the dynamic processes, the current scientific setups allow us to track phenomena down to the femtosecond timescale. Yet, if we examine the primary method used for these measurements, the pump-probe technique, we find out that this inconceivably fast measurement uses the principles of photographic flash. The concept established in the 19th century, combined with our ability to attain and control femtosecond pulses, allows us to carry out these cutting-edge experiments.

The effort to outperform this simple sampling of spatial, temporal, or spectral information has been present for many years. A successful example is the Fourier-transform infrared (FTIR) spectrometer, where the infrared spectral information is more effectively scanned in the Fourier domain. Nevertheless, an entirely new area to explore opened with the rapid increase in computer computational power and the development of signal processing algorithms, which enabled the rise of new concepts of signal acquisition. The new methods are often more simple or able to bypass the limitations of the current techniques [1, 2].

Such computational enhancement of image acquisition has been well known to occur for human perception. Our eyes, which consist of a single lens and a relatively inhomogeneous array of “pixels,” provide us with a superb image quality without chromatic and image aberrations and color dispersion. This image augmentation is enabled by the sophisticated signal processing in



the neural network of our brain. The effort for computational image acquisition, to some extent, copies the idea of using an incomplete or low-quality measurement to extract the complete information.

## 1.1 Scope of the work

This habilitation thesis summarizes a major part of the work carried out by myself and my group within the research center TOPTEC during the years 2016-2020. The central direction of the TOPTEC research center is the development and manufacturing of sophisticated, unconventional optical elements for space and high-power laser applications. The thesis addresses three central questions triggered by the work of the center and its collaborators.

Firstly, the thin film coating is one of the essential parts of the optical element and often the most fragile one. Since the element preparation often employs unconventional optical materials (special optical glasses, monocrystals, etc.), the adhesion between the thin films and the surface of an element can be corrupted by many factors, which all affect the quality of the element-coating interface. The important factors are the strain in the coating, which induces the delamination, or simply a certain extent of layer porosity, which allows ambient oxygen and water vapor to deteriorate the interface. These factors can be determined only after the coating is fully deposited and can often be visually identified during the coating tests only after a long period. The possibility to optically evaluate and map the quality of thin films and the interfaces between the layers and substrate would bring an immense advantage in this direction.

Secondly, the thin film coating is typically the limiting factor for the highest laser intensity, for which the element can be used. This intensity level is denoted as laser-induced damage threshold, and it is one of the critical parameters for the application in high-power and femtosecond lasers. Frequently, the “weakest link in the chain” is again the presence of interfaces in the optical coating, which consists of a stack of layers from distinct materials with different refractive indices. A possible way to bypass this problem is to avoid the interfaces between the layers and gradually change the refractive index. The possibility to use an arbitrary shape of the refractive index gradient provides us with extra parameters to attain the desired coating properties. On the other hand, it is clearly very problematic to control and monitor the coating properties.

Finally, our collaboration with Crytur company showed the continuous need for simple and effective characterization of light-emitting monocrystals. The information about the intensity, spectrum and dynamics of the emitted photoluminescence (PL) contains much information about the monocrystal composition. At the same time, taking a hyperspectral and hypertemporal image of a PL is a lengthy and demanding task, typically requiring a sophisticated set of instruments. Hence, an efficient way to carry out this acquisition of a highly multidimensional dataset is needed.

Many of the problems explained in the previous paragraphs can be efficiently solved by a clever implementation of computational data acquisition in laser spectroscopy, namely, the concept of compressed sensing (CS). The idea of CS was introduced by Candes et al. in 2004 [3]. A storm of various optical implementations of CS can be tracked between the years 2007-2012, leading to the demonstration of a single-pixel camera [4], which is a new concept of imaging; compressed ultrafast photography able to capture a traveling laser pulse with the picosecond temporal resolution [5]; or single-snapshot hyperspectral imaging [6]. The concept of CS and some of its implementations will be presented in this thesis in Chapter 2. Already here, we can stress that the vast majority of the published results have focused on the use of CS in imaging, and they have used standard means of light manipulation and modulation. The light modulation is an integral part of CS, as the methods rely on encoding the measured signal with a random

or a pseudo-random pattern.

Within the broad stream of work of many groups studying optical implementations of CS, the possibility to apply CS to track time-resolved signals was seldom addressed, and the use of CS for the retrieval of femtosecond ultrafast dynamics was not studied at all. At the same time, the use of laser light in some applications calls for the use of laser speckles - a random pattern, which can be used for information encoding. Yet - this direction stayed unexplored by CS until 2015, while it was broadly used by the so-called ghost imaging. All these missing parts in the CS research, together with the above-listed principal questions, directed my work and frame the scope of this thesis.

This thesis does not contain many important results of my group, where we applied the standard methods of CS, such as a differential single-pixel camera for IR imaging [7], single-pixel camera time-correlated single-photon counting microscope [8], or single-snapshot hyperspectral imaging [9]. We point the potential reader to the respective articles for closer details.

## 1.2 Thesis structure

The chapters of the thesis follow the development of the research interest chronologically, starting from the interest in the the-called compressive imaging, which can be easily implemented in the laser spectroscopy by using the laser light coherence (Chapter 2). This idea was further developed into the possibility to transpose the concept of random temporal signal sampling, namely in the opportunity to utilize random femtosecond pulses to track ultrafast processes (Chapter 3). Finally, the aim of this research was targeted at the thin-film study with the accent on the interfaces in thin films, which are often the problematic parts of the system (Chapter 4).

Each of the chapters is divided into three parts, where: (i) the research direction and central aims are presented, (ii) state-of-the-art and work of other groups are introduced, (iii) part describing the results attained within the work of my group and myself, completed with (iv) opened lines of future research.

Finally, the thesis includes reprints of the articles and manuscripts, which contain the discussed results. For each article, a description denoting my personal contribution to the research is provided.





## Chapter 2

# Compressive imaging in laser spectroscopy

### 2.1 Introduction

Laser spectroscopy is one of the key toolboxes for materials research - an indispensable field for developing new materials and understanding processes in nature. The term “laser spectroscopy” denotes a broad range of techniques studying the response of the material under laser illumination — for instance, photoluminescence (PL) emission or changes in absorption [10].

Laser spectroscopy has undergone tremendous progress in the last decades. Many new techniques have arisen, providing different dimensions of knowledge — information about the dynamics of processes in the material, material structure, or energy states. Some methods (for instance, a 2D coherent nanoscopy [11]) acquire as much as a 5-dimensional dataset carrying spatially resolved information about the correlation between energy states and their dynamics. We denote the image, where more than a single quantity is acquired, as hyperdimensional imaging. As an example – a subset of hyperdimensional images are hyperspectral datasets, where each pixel contains information about the light spectrum instead of a single intensity value. Hyperdimensional information is essential to understand the physics of complex materials. On the other hand, such techniques often suffer from their complexity and time-consuming data acquisition. In some cases (e.g., for photodegrading materials), the lengthy measurements can even disqualify the method from being used.

In this context, a significant turn was brought by the development of the so-called compressed sensing (CS) [12]. It enables the measurement of complete information about an object (e.g., an image) while using a highly reduced number of measurements compared to the standard scanning - for instance, less than 5000 datapoints suffice to reconstruct a 1 MPix image [13]. The concept is based on encoding the information (image, spectrum, or anything else) with a random pattern and consequent computational restoration of the information. CS enables breathtaking applications, such as 2D images recorded by a single-pixel camera [13] or a possibility to store a video in a single CCD exposition [5].

The potential of CS in laser spectroscopy is obvious, and the interest is steadily increasing over the last years. There has been reported a number of experiments, where CS imaging was turned into the laser spectroscopy imaging [5, 6, 14–16]. Impressive results can be achieved, such as creating a “photography” of the processes on the timescale of hundreds of ps (see Figure 1) [5]. On the other hand, laser spectroscopy has its specific features: the coherent nature of the exciting (or probing) laser light and the availability of a static scene for long measurements. For a long period, using these specific properties was an unexplored field, which promises a large room

for improvement in the practical realization of CS. The promise consists in using the coherence of the laser light to create a random pattern via random wavefront interference, the so-called laser speckles, and thus to provide a coding pattern for CS in a straightforward way.

## 2.2 State of the art

### 2.2.1 Laser spectroscopy

Laser spectroscopy is a toolbox of choice for studying any system, where an optical response matters – ranging from semiconductor nanostructures to macroscopic photosynthetic complexes [10]. In this section, we will restrict the scope to the two directions relevant for this chapter: absorption and photoluminescence (PL) spectroscopy. Both can be studied by using simple, incoherent light sources. However, the laser light adds a different quality to the measurements by concentrating energy into a collimated beam, narrow spectral range, or a pulse as short as a few femtoseconds.

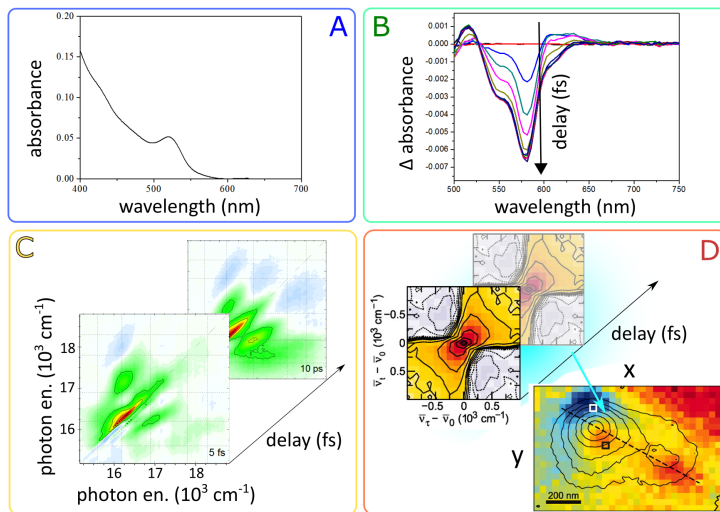


Figure 2.1: Increasing the complexity of spectroscopic data measured for CdSe quantum dots: absorption (A, 1-dimensional dataset) [17], transient absorption (B, 2D dataset), 2DES (C, 3D datasets) [17]. Spatially-resolved 2DES (D, 5D datasets) – measured for a rough metal surface, adopted from Ref. [11]. Reprinted with permission from AAAS.

pulses for transient absorption measurements adding information about dynamics in the material (Figure 2.1B) [18]. Consequently, a 2D electronic spectroscopy [19] introduced in 1998 added another dimension in the excitation energy dependence, thus enabling tracking correlation between energy states in a material – see Figure 2.1C. By including demand on imaging with new methods, some methods can acquire as many as 5-dimensional datasets – for instance, see the 2DES nanoscopy published in 2011 – Figure 2.1D [11].

This development is indispensable for studying complex structured materials, where a maximum amount of information is needed to identify the electronic states and governing processes. A typical example is the recent halide perovskite structures, where the large carrier mobility causes the charge carrier dynamics to be highly affected by the proximity of an interface or a defect.

Laser spectroscopy has been developed for many years to gain the widest possible spectral range with the highest spatial and temporal resolution. The development has reached natural limitations in all these directions – (i) diffraction-limited spatial resolution (or even super-resolution); (ii) temporal resolution on the scale of fs (limited by a laser pulse length); (iii) measurements extending far into UV and IR or even THz.

A general trend in the development is combining or extending techniques to obtain more profound information about the measured sample. To provide an example: simple light absorption measurements provide information about optically active transitions (Figure 2.1A). Those were extended by using short laser

At the same time, the data acquisition is becoming progressively longer, and it might disqualify some approaches to be used in praxis. To provide a very concrete case — a typical spectrally resolved pump-probe measurement on a system of CdSe quantum dots on ZnO nanowires [18] (studied for catalysis and photovoltaics) using a desirable excitation intensity demands approx. 1 hour of acquisition. In order to obtain an image with a moderate resolution of  $32 \times 32$  pixel images (spatially-resolved measurement), we can either use the original setup by scanning a sample for 1024 hours (43 days) or sacrifice some other information (e.g., fix pump-probe delay, or use single-color probe).

A completely different approach, offering a solution to the problem, consists in using the capabilities of compressed sensing.

### 2.2.2 Compressed sensing

From our everyday experience, we know that an extensive dataset of an image can be easily reduced many times without any apparent loss of image quality, as illustrated in Figure 2.2 A-C. This is caused by the fact that in a certain basis (FFT or wavelet basis in imaging) the information is sparse-like [4]. In other words, only several important components carry the primary information in the image, and the rest can be neglected without significant loss of information.

Compressive sampling (CS), introduced in 2004, is an alternative approach to data acquisition that exploits information sparsity [3, 12]. CS theory has proven that, if we do not know a-priori the important components, the most efficient way of extracting the information is to measure randomly – i.e., in the case of an image to measure a random combination of Fourier components. Nevertheless, practical experiments show that choosing a random Hadamard matrix (0 and 1 pixels randomly set) is almost as efficient as the ideal pseudo-random case [1].

Since CS is one of the cornerstones of the project, it is worth explaining the principles closely on an example of the so-called single-pixel camera [13, 20]. The experiment is able to acquire an image by encoding its information by a random mask and measuring the total intensity. In order to acquire image  $i$ , which will be used in the form of a vector (vectorized 2D image) with  $N$  pixels, we take  $M$  different random patterns, superimpose them on the image and measure the total intensity  $y_{1..M}$  (see Fig. 2 D). If we vectorize the random patterns and set them into the columns of a matrix, we obtain an  $M \times N$  matrix  $A$  – the so-called measurement matrix. This enables

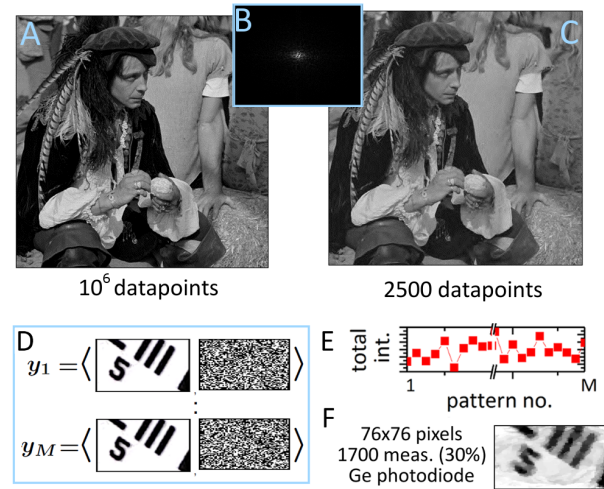


Figure 2.2: Natural scene (A), typically features a small number of significant Fourier transform components (B). A selection of the 2.5 % largest components is enough to reproduce the image (C). Projection via random masks (D) is a general approach enabling efficient extraction of the complete useful information from the total measured intensities (E). The CS functionality is illustrated by our SPC infrared microscope. An image of a USAF 1951 target can be compared to its reconstructed version (F)  $76 \times 76$  pixels from 1700 intensity measurements of random projections via a single-pixel detector (Ge photodiode).

us to express the measurement mathematically as:

$$y = Ai \quad (2.1)$$

For  $M \ll N$ , this is a heavily underdetermined system of equations, which it is impossible to solve. However, by including a term denoted as a regularization term  $\Phi(i)$ , we apply an additional criterion, which (under certain conditions) ensures that the correct image can be retrieved, for instance, via the following minimization:

$$\min\{\|y - Ai\|_2^2 + \mu\Phi(i)\}. \quad (2.2)$$

The regularization term is weighted with a factor  $\mu$  and, simply speaking, it can express our expectations about the measured information. For instance, in the case of an image, it can be the sum of the absolute values of all wavelet components (the so-called  $l_1$  norm). The minimization in Eq.(2.2) will therefore converge to an image, which corresponds to the measured values and can be described by the lowest number of components in the wavelet basis [1]. Interestingly, the primary information of the image can be restored by using  $M \simeq 0.2N$  — see Figure 2.2 E. The above described single-pixel camera counts, besides coded aperture snapshot spectral imaging (CASSI) [15], among the most used applications of CS.

In summary, CS enables us to reconstruct information under two main conditions: (i) the possibility to encode the information with uncorrelated random patterns, (ii) sparsity of the information expressed as a regularization term. To provide a deeper insight into CS, it is useful to compare standard and CS-based imaging. In standard imaging, we illuminate the studied object evenly with light, and we need to have a spatially resolved 2D sensor (or 2D scanning optics) to acquire an image. The concept of a single-pixel camera enables us to “trade” the spatial resolution of the sensor by using spatially resolved illumination (random pattern). This trade-off is beneficial, for instance, in THz imaging, where acquiring a 2D detector poses an issue while modulating the THz light with a random mask is straightforward [21]. For this reason, the concept also has excellent potential in ultrafast spectroscopy or PL imaging, as we will show in the following section.

### 2.2.3 Compressed sensing in laser spectroscopy

There are two main directions for exploiting CS. Firstly, a detector with a limited number of pixels is used to reconstruct a complex image. The ultimate version is represented by single-pixel cameras (simply a photodiode), which are able to reliably detect a 2D scene (see 2.2) [13]. Such an approach has a huge advantage in the regimes, where a multi-pixel detector poses a complicated problem – for instance, a THz imaging [21].

Another model uses conventional imaging detectors with many pixels; however – it tries to encode additional information into the image (single-shot hyperspectral or hypertemporal imaging). One of the prominent methods is CASSI [15], where an image is encoded by a random matrix, spectrally dispersed (by a prism or a grating), and finally projected on a CCD. This enables to derive a spectrum for each measured point in the image – of course, at the expense of losing some fine details of the scene. A similar approach is used in CUP [5], where a streak camera is used to encode data temporally. This enables capturing a single-shot image, from which one can reconstruct the changes in the scene on a timescale of few tens of ps.

Since 2008, many publications have been focused on a direct transposition of CS-based imaging to laser spectroscopy applications [5, 6, 14–16]. However, these published approaches did

not use the benefit of the unique properties of laser spectroscopy – usage of coherent laser light and a “static” scene available for a long time. We will show in the next section that using light coherence can significantly simplify the CS-based setups.

## 2.3 Results

We were able to implement the compressive imaging based on laser speckles in various spectroscopic methods, where such an approach is the enabling step to transfer the standard nonimaging experiments into the imaging ones just by using a simple modification of the setup. Our approach is suitable for any setup, where the acquisition time of a single measurement is relatively long. In many cases, it is simply possible to carry out imaging by continuously scanning the sample point-by-point, as it is, for instance, done in laser scanning microscopes. However, when we assume a long acquisition time, e.g., 1 s, we can easily calculate that even if we apply an extremely rapid sample positioning, the acquisition of  $100 \times 100$  pixels will take almost 3 hours. If we apply CS-based imaging, we can lower the number of measured datapoints down to 20 % or even less, which is about 35 minutes.

The need for a long acquisition time often arises due to the measurement of weak light intensity. This applies for the PL imaging presented in Section 2.3.2. Another typical example is the necessity to analyze small changes in the light intensity, which is the case for the pump-probe spectroscopy presented in Section 2.3.3. Finally, the use of a random speckle pattern also makes it possible to entirely revise the approach to the measurement itself, as it is presented in Section 2.3.4.

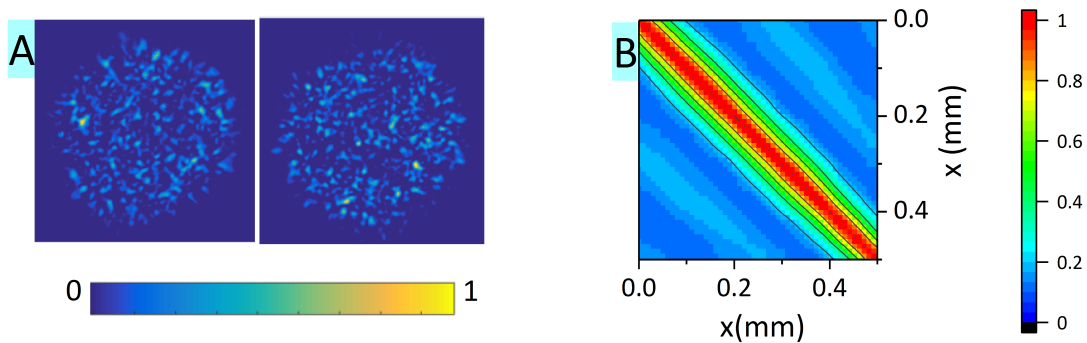


Figure 2.3: (A) Image of two speckle patterns attained for two different positions of a diffuser (ground float glass). (B) Correlation degree between speckle patterns for a varying diffuser position. The correlation degree was calculated according to Eq. 2.3. Studied with laser at 532 nm. Figure adopted from Ref. [22] following NPG author’s right policy.

### 2.3.1 Laser speckles

All of the experiments listed below depend on the use of laser speckles as a random pattern. Spatial speckle patterns arise when a coherent light source, such as a laser beam, is retarded with a randomly varying phase across the beam [23]. The interference of many wavefronts with a random phase leads to a pattern with specific statistics.

To be able to employ speckles in CS, we need to gain a set of uncorrelated patterns. Since we used a diffuser to generate the laser speckles, the common question of interest for all methods was to study the degree of correlation between two speckle patterns generated for two adjacent



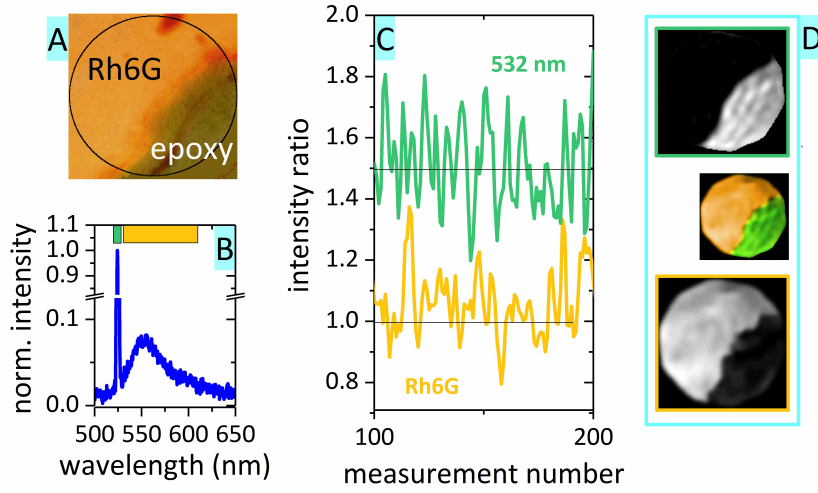


Figure 2.4: Compressive hyperspectral PL imaging. (A) Photo of a testing sample – dark circle denotes the measured area. (B) Example of a spectrum acquired for the sample, with the dominating laser scattering at 532 nm and PL emission. (C) The intensity of the scattered (green line) and emitted (orange line) light for a subset of speckle patterns. (D) Reconstructed images of the scattering area (upper panel), light-emitting area (lower panel), and their merged image (middle panel). Figure adopted from Ref. [22] following NPG author’s right policy.

positions of the diffuser. The correlation degree between patterns  $I$  and  $J$  was defined as follows:

$$C(I, J) = \sum_{k,l} \frac{I(k, l) - \langle I \rangle}{\sigma_I} \frac{J(k, l) - \langle J \rangle}{\sigma_J} \quad (2.3)$$

We observed that the so-called memory effect is a crucial process [24]. Simple speaking, the memory effect causes that a slight shift in the beam position on the diffuser causes the speckle pattern to be shifted in space. A pattern shift larger than the mean speckle size will cause the new pattern to be uncorrelated. For the tested diffusers, a shift on the scale of tens of micrometers was sufficient to attain two uncorrelated patterns – see Figure 2.3. The study of pattern correlation is described in detail in the reprint of Ref. [22].

### 2.3.2 Speckle-based hyperspectral imaging

We developed a new approach to spectrally-resolved PL imaging, or in other words, hyperspectral PL imaging. The experiment was carried out using a single-pixel camera technique, where a fiber spectrometer was the single-pixel detector, and a diffuser was used as a source of a random spatial pattern (speckle pattern). A diffuser placed on a motorized translation stage can provide us with an unlimited number of random patterns, as we described in the previous text. The total spectrum of light together with the knowledge of the speckle pattern, which was measured by a reference camera, contains enough information to reconstruct the image by using Eq. (2.2).

The principal testing sample was an interface between a scattering epoxy layer and a Rhodamine 6G solution – see Figure 2.4 (A) – where the epoxy layer scattered the excitation laser (532 nm), while the luminescing part with Rhodamine 6G covered the wavelengths up to 650 nm – see Figure 2.4 (B). Measured spectra for a set of random speckle patterns depicted in Figure 2.4 (C) allowed us to image the scattering part – see the upper panel in (D) – as well as the PL-emitting area – see the lower panel in (D). The result is in perfect agreement with the

sample image – see, for instance, the dark spot on the top of the PL-emitting area in both panels (A) and (D).

We also studied the effect of speckle pattern properties on the setup resolution, where we changed the mean size of the laser speckles by varying the diameter of the laser spot on the diffuser. The attainable image resolution followed the mean size of the speckles in the speckle patterns. Moreover, we also discussed the number of measurements required for accurate retrieval of the hyperspectral image. All the results are described in detail in the attached reprint of Ref. [22].

### 2.3.3 Speckle-based ultrafast imaging

The pump-probe technique is a standard method able to detect dynamics in a material with the highest contemporary resolution [25]. It is based on the excitation of a sample with a strong pump pulse. The second probe pulse typically features low intensity, and it is used to track absorption in the sample. The attainable temporal resolution of the standard pump-probe experiment depends on the duration of the pulses since the probe pulse senses the sample transmittance only during its propagation through the material.

The pump-probe signal, i.e. transient absorption (TA)  $\Delta T(t)$  is typically provided as a change in transmittance of the sample between the excited sample  $T_{exc}$  and the unexcited sample  $T_{unexc}$ , where the probe pulse is delayed by a time  $t$  compared to the pump pulse:

$$\frac{\Delta T}{T} = \frac{T_{exc} - T_{unexc}}{T} = \frac{I_{exc}^{probe} - I_{unexc}^{probe}}{I_{unexc}^{probe}}. \quad (2.4)$$

The TA signal can be determined by measuring the intensity of the probe pulse transmitted through an excited sample  $I_{exc}^{probe}$ , or an unexcited sample  $I_{unexc}^{probe}$ .

Since the pump-probe experiment typically needs to resolve changes in the probe intensity in the order of  $10^{-6}$  to  $10^{-3}$ , a sensitive method for the signal extraction needs to be applied. Therefore, the standard pump-probe setups work in a “single-pixel” mode, where a photodiode or a fast-scan single-line CCD measures the probe intensity, while the pump beam is modulated by an optical chopper on a selected frequency. By analyzing the oscillation of the probe intensity at this particular frequency via a lock-in amplifier, it is possible to extract the TA signal with a very low noise level [25]. The important information derived from the pump-probe experiments is the dynamics of charge carriers in the sample of interest, which is reflected in  $\Delta T$  dependence of  $t$ . To extract the temporal information, the pump-probe delay  $t$  is scanned.

While the nonimaging pump-probe measurement is relatively simple and well-established, the imaging counterpart is much less common. Due to the long acquisition time, scanning a sample is very time-consuming, as we discussed previously. Moreover, it is worth noting that the scanning would need to take place for each delay  $t$ . By sacrificing the information about the pump-probe spectra, it is possible to carry out pump-probe imaging by using low-noise 2D array detectors [26]. While such a TA signal mapping is rapid, it can be used only to measure the strong signal.

Therefore, we transposed the knowledge from the previous experiments to measure the spatially resolved ultrafast spectroscopy via probe beam coding. In other words, we used a standard pump-probe experiment, where we hit the sample not with a focused probe beam, as it is typically the case. Instead, we use the probe beam to generate the speckle pattern as it is indicated in Figure 2.5 (A). By scattering a fs laser beam through a thin diffuser (ground glass), we obtained again a set of random fs patterns, which can be used for single-pixel imaging. An example of such a speckle pattern is depicted in panel (B).

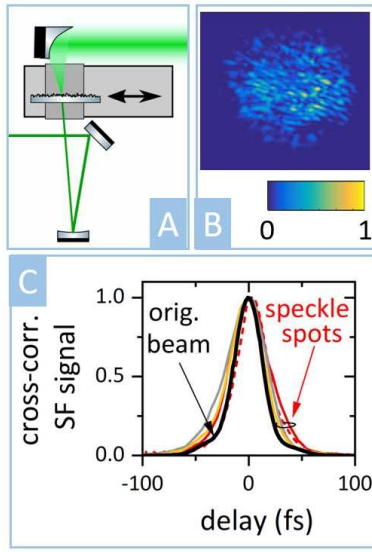


Figure 2.5: Generation of speckle patterns from the fs pulses. (A) Scheme of the used setup. (B) Example of a fs speckle pattern. (C) Cross-correlation of a compressed probe pulse with a beam without diffuser (black line) and various spots in the speckle pattern (color lines).  $\lambda_{probe} = 560$  nm, orig.  $t_{pulse} = 22$  fs.

tation of the sample, where the oval shape follows the excitation beam shape. By measuring the changing position of the TA signal onset with the delay, we could verify that the signal behavior corresponds to the set pump beam angle.

A detailed description of the results, together with the measurement of the second testing sample, can be found in the attached reprint of Ref. [27].

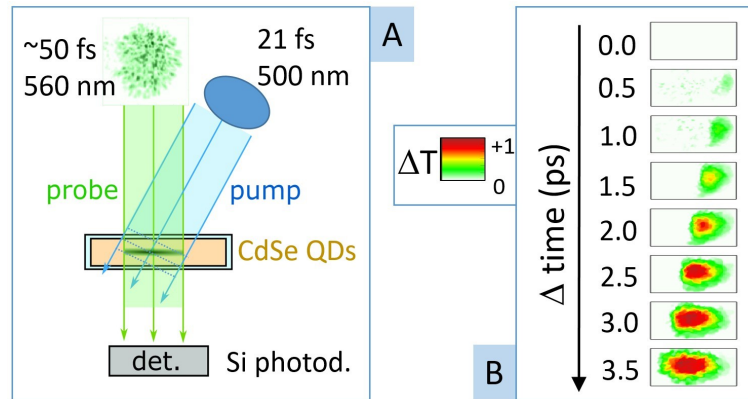


Figure 2.6: Pump-probe imaging by using a randomly modulated probe beam: (A) scheme of the setup with a tilted pump beam exciting a sample and a randomly-patterned probe beam detected by a single-pixel detector. (B). Computationally reconstructed snapshots of gradually appearing transient absorption signal in the sample (CdSe quantum dots) due to pump probe tilt causing the gradual sample excitation. Figure adopted from Ref. [27] following OSA author's right policy.

However, the pump-probe experiment temporal resolution is set by the length of the pump and probe pulses. The critical question was whether the use of a diffuser would stretch the pulses in time. By using a cross-correlation technique of the speckle patterns with a compressed pulse, we were able to track the pulse structure of different spots among the speckle pattern – see Figure 2.5 (C). Due to the varying diffuser thickness, the pulse is slightly stretched in time, nevertheless, in the temporal sense, it is relatively close to the compressed pulse, and the temporal resolution of the setup is below 50 fs.

As a proof-of-concept experiment, we measured the onset of a signal from a tilted pump pulse exciting a homogeneous sample (colloidal CdSe quantum dots) as it is schematically shown in Figure 2.6 (A). The large tilt, which was set between the pump beam and the sample, causes the sample to be firstly excited on the right-hand side, while on the opposite side of the beam, the excitation will be delayed by several picoseconds. We measured the TA signal for a large set of probe speckle patterns and 10 delays. The reconstructed images for each delay – see Figure 2.6 (B) – show very nicely the gradual excitation of the sample, where the oval shape follows the excitation beam shape. By measuring the changing position of the TA signal onset with the delay, we could verify that the signal behavior corresponds to the set pump beam angle.



### 2.3.4 PL decay measurements via random temporal speckles (RATS)

#### RATS method

In the two implementations described above, we focused on using speckle spatial patterns to carry out single-pixel imaging. Nevertheless, it is possible to utilize also random temporal speckles (RATS), where the light intensity randomly fluctuates in time due to interference of a coherent light source. There is an endless variety of approaches, how to generate random speckles both in time or space. We used a simple modification of the previous setups, where the speckles were generated by scattering on a diffuser. We placed a pinhole in the spatial speckle pattern, and by rotating the diffuser, we were able to gain a light intensity rapidly fluctuating in time. For the optimized conditions, namely, diffuser fineness, rotation speed, and beam diameter, we were able to attain fluctuations up to the scale of hundreds of nanoseconds.

We studied the possibility to use the RATS to measure PL dynamics. The randomly fluctuating light intensity has a lot in common with a short pulse, which is the most frequent means to excite and track PL decays. Both the random waveform and short pulse cover an extensive range of frequencies – see simulated curves in Figure 2.7 (A-B), blue lines. While the shortest pulse arises when all frequencies share the same constant phase, the random waveform results from a randomly varying phase. Nevertheless, both can reveal the same information.

For the samples, where we can assume that the observed PL emission is linear, i.e. the intensity of the emitted light scales linearly or nearly linearly with the excitation intensity, the PL intensity in time  $I_{PL}(t)$  is a convolution of excitation intensity in time  $I_{exc}(t)$  and the PL decay  $D(t)$ :

$$I_{PL}(t) = I_{exc}(t) \otimes D(t) \quad (2.5)$$

For an infinitely short excitation pulse, we can directly measure the PL dynamics, as the convolution with a Kronecker  $\delta$ -function is an identity. Nevertheless, the same expression is valid also for an arbitrary waveform, and we can use the convolution theorem for Fourier transform to extract the PL decay  $D(t)$  based on the Fourier representation of the measured PL and excitation traces – see 2.7 (A-B):

$$D(t) = \text{Re} \left\{ \mathcal{F}^{-1} \left[ \frac{\mathcal{F}(I_{PL})\mathcal{F}^*(I_{exc})}{\mathcal{F}^*(I_{PL})\mathcal{F}(I_{exc}) + \epsilon\mathcal{F}(I_{exc})\mathcal{F}^*(I_{exc})} \right] \right\} \quad (2.6)$$

In this expression, we used the so-called Tikhonov regularization weighted with the factor  $\epsilon$ . This is important because the straightforward deconvolution by a ratio of two Fourier spectra is typically an ill-posed problem. The extracted PL decay curve in 2.7 (C) demonstrates that the PL decay can be retrieved from the random waveform equally well compared to the short pulse excitation. In line with this case, the highest attainable frequency in RATS is the factor limiting the temporal resolution of the method.

We carried out an experimental demonstration of the RATS methods on the samples of a color glass filter (Schott OG 565) and a layer of nanoporous Si [29]. The attained results and their comparison to a standard method for the PL decay measurement can be found in the reprint of Ref. [28]. It is worth noting that compared to the standard methods, our setup is extremely simple and robust. It allows us to use any coherent light source for excitation - without the necessity to create a short pulse or control the light intensity. The measurement is very robust against the offset in the measured intensities or timing in the setup.

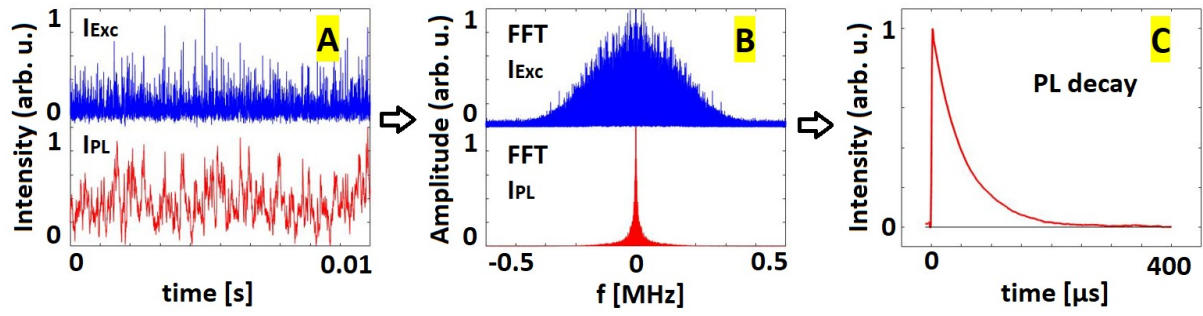


Figure 2.7: (A) Measured intensity of random temporal speckles used as the excitation (blue line) and a simulated PL intensity for a single-exponential decay (red line). (B) Fourier representation of the excitation and PL signal. (C) PL decay retrieved from the datasets by using Eq. (2.6). Figure adopted from Ref. [28] following OSA author's right policy.

## 2D RATS imaging

A natural step forward is to combine temporal speckles (RATS) and spatial speckles to track PL intensity both in time and space. In other words, we can combine the RATS experiment with the single-pixel camera experiment described in the previous sections. We denote this concept as a 2D-RATS technique. Such an approach allowed us to create the setup for fluorescence lifetime imaging (FLIM) [30]. Our approach provides FLIM on microsecond timescales with unmatched simplicity.

The demonstration setup was created by using a series of two diffusers. The first diffuser, which was rotating, created a randomly varying intensity waveform. The fluttering beam was refocused on the second diffuser, which gave rise to a spatial speckle pattern. Altogether, we attained a spatio-temporal speckle pattern, which was random both in time and space.

For a set spatial speckle pattern, we used the RATS extraction of PL decay described in Eq. (2.6). By changing the position of the second diffuser, which was placed on a motorized stage, we were able to attain a large number of reconstructed PL decays – see Figure 2.8 (A). Each curve  $I_{DA}$  is an average decay of the illuminated excitation pattern on the sample. The same dataset is displayed in Figure 2.8 (B), where we see PL decay intensities for each time  $t$  (different line colors) for the set of random speckle masks. By using the algorithm TVAL3 [31] applied on Eq. (2.2), we can reconstruct a PL intensity map of the sample for each time  $t$  – Figure 2.8 (C).

The reconstruction of the 3D dataset, where we gain PL dynamics for each pixel, is depicted in Figure 2.8 (C) - (D) for a sample of a color filter (lower part of the sample) and a layer of nanoporous Si decaying on the microsecond timescale (upper part of the sample). The two regions are delimited with non-emitting dark tape. In line with the control measurements, we observed that while the PL of the color filter is initially brighter, for longer times, PL from nanoporous Si becomes more prominent, as the PL decay features significantly longer lifetimes – see panel (D).

We tested the 2D RATS concept on two samples and evaluated the effect of various factors on the resulting image and lifetime reconstruction quality. Details of the setup and attained results are provided in the reprint [32].

## 2.4 Outlook

Currently, the 2D RATS method has proven to be a compelling approach to map the PL dynamics. However, the current implementation with diffusers is limited regarding the attainable

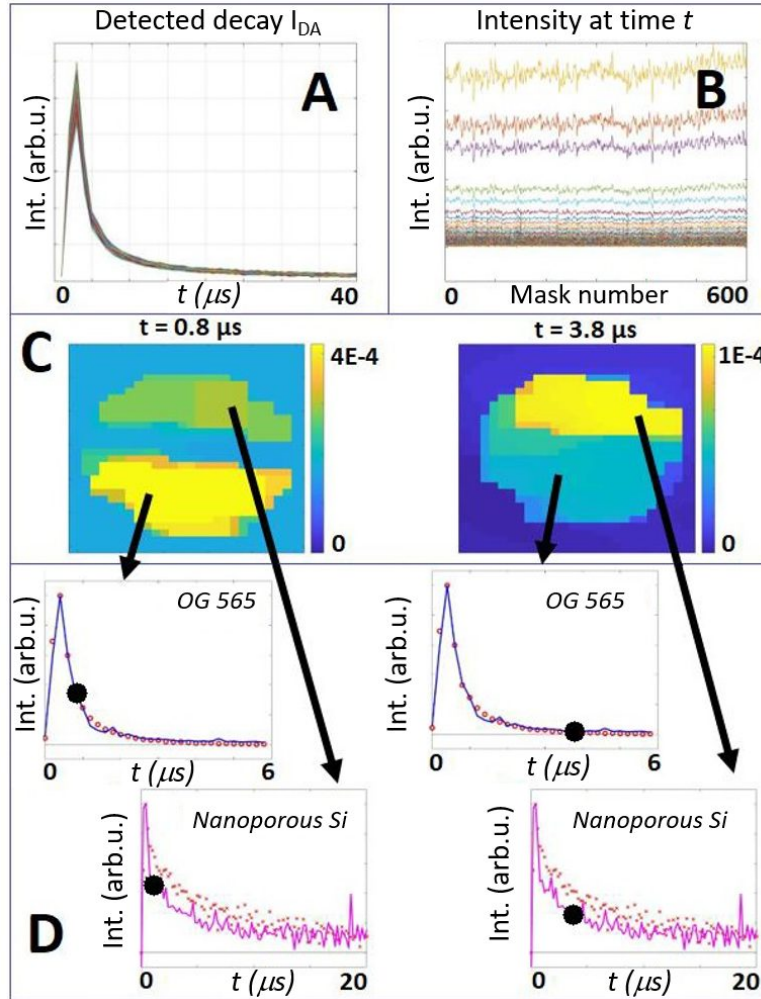


Figure 2.8: (A) Set of PL decays detected for various excitation spatial masks. (B) Intensity of PL for selected times  $t$  for each random mask - the same set of PL decays depicted as in panel A. (C) Images of PL retrieved for two different delays after excitation. (D) Reconstructed PL decays from two selected pixels emitted by the color filter (upper panels) and nanoporous Si (lower panels), where the 2D RATS curves (solid lines) and compared to a single-spot measurement by the non-imaging RATS experiment. Figure adopted from Ref. [28] following OSA author's right policy.

temporal resolution and the low efficiency of excitation light. Therefore, we will focus on creating an entirely new approach to generating spatio-temporal speckles based on the electronic modulation of the laser and digital micromirror device. By using the improved “speckle” generation, this approach can reach higher image quality and reach the temporal resolution on the scale of nanoseconds.

At the same time, a promising application of the RATS and 2D-RATS methods is the cavity-ringdown spectroscopy [33], where the light intensity decay is used to track subtle losses in mirrors or optical materials. Another open route to explore is to employ neural networks to process the RATS datasets and extract the information of interest.

## 2.5 Summary

Overall, we succeeded in the implementation of speckle-based compressive imaging in a range of spectroscopic techniques, opening an entirely new approach to imaging in laser spectroscopy, which we denote as “speckloscopy”. We demonstrated that speckloscopy can be implemented in various experiments, including PL hyperspectral mapping [22], ultrafast imaging [27], or FLIM [32].

The most prominent was our demonstration of compressive imaging of ultrafast processes with temporal resolution 50 fs, where we reported as the first group in the world on the possibility to modify a standard setup to the imaging mode [27]. This method can be applied in any single-pixel detected technique in ultrafast spectroscopy, such as 2D coherent spectroscopy or up-conversion PL decay measurement.

For the sake of future research, it is perhaps more important that we were able to transfer the idea of signal retrieval via random modulation into the measurement of rapid dynamics in spectroscopy. Namely, we built a unique simple setup, which can capture sub-microsecond photoluminescence (PL) dynamics with a randomly fluctuating excitation intensity [28]. While the demonstration setup suffers from certain drawbacks – for instance, very inefficient use of excitation light, which is two times scattered by a diffuser – I believe that the results will become a cornerstone for further use of random patterns or pulses in laser spectroscopy.

## Chapter 3

# Random phase ultrafast spectroscopy

### 3.1 Introduction

Ultrafast spectroscopy is the art of capturing rapid processes in materials on a timescale starting from several femtoseconds [25]. Current state-of-the-art experiments can optically track processes such as charge and energy relaxation in materials [34], or trace an acoustic shock wave propagation through a sample [35]. Studying such processes allows us to answer the basic questions concerning the studied system.

The principles of ultrafast spectroscopy follow the idea of using a flash in photography transposed into the femtosecond regime. This can be explained in the case of the pump-probe technique, which is one of the most used ultrafast experiments – see Figure 3.1. In panel (A), a bullet triggered a process (a splash of water), and a photographic flash captured one moment with a certain delay after the trigger. Analogously, in an ultrafast spectroscopic experiment, we use an extremely short fs pulse as a flash – see panel (B). First, we send a strong pulse (pump), which triggers photoinduced dynamics in a sample. The second pulse (probe) follows with a certain delay and captures the change in the studied system at a set moment. By changing the pump-probe delay, we can observe the entire dynamics of interest.

Clearly, in order to obtain a better temporal resolution, we need a shorter pulse. This implies, in the Fourier space, obtaining a spectrally broad laser pulse with a spectrally independent phase. Setting the constant spectral phase of a pulse is denoted as pulse compression, and for broadband pulses, it becomes a demanding and alignment-intensive task. To provide an idea of the scales, a 7 fs pulse at 600 nm requires, in the ideal case generating a spectrum with 115 nm FWHM and compressing the spectral range of 500–775 nm. The broadband pulse compression needs to be solved on a case-by-case basis for different spectral ranges and pulse sources. In some cases, the available spectral bandwidth even has to be truncated to maintain the pulse compression, and the full potential of the temporal resolution cannot be used [36]. The difficulty of broadband pulse manipulation confines ultrafast spectroscopy with femtosecond temporal resolution to laboratories featuring dedicated instrumentation for pulse compression and experienced personnel.

The random phase ultrafast spectroscopy, which we shortly denote as RUSH, aims at re-

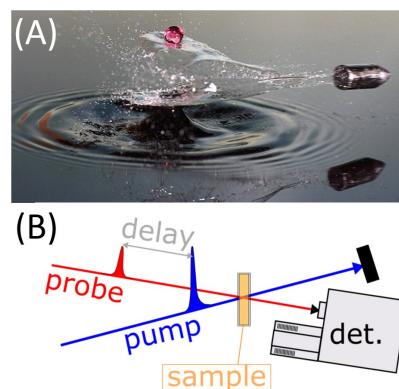


Figure 3.1: (A) High-speed photography of a bullet (pump) captured by using a short flash (probe); courtesy of L. Augusteijn. (B) Scheme of the standard pump-probe technique.

moving the barrier set by using an ultrashort pulse by reformulating the basic idea of ultrafast spectroscopy, i.e., the idea of a photography flash. This is possible by applying the so-called compressive sampling (CS), a new approach to data acquisition and signal reconstruction [12]. As it was explained in the previous chapter, CS enables us, under certain conditions, to leave the intuitive approach of the simple step-by-step data acquisition and use a random pattern to encode and later reconstruct a signal. Such signal retrieval can be an immense advantage in the field of ultrafast spectroscopy, where obtaining a random broadband pulse, i.e., setting random spectral phases, is incomparably more straightforward than pulse compression. Truncating the spectral bandwidth of a random pulse is no longer necessary, and the bandwidth can be fully used to gain the best attainable temporal resolution. Moreover, by using a random pulse, we can reform the standard pump-probe experiment into a method using the same random pulse as a pump and a probe at the same time – a random self-probe experiment. This method would provide simple access to measuring processes on the femtosecond timescale without any complex setup alignment.

In our research, we specifically aim to use ultrafast spectroscopy to study interfaces in thin-film layers within the optical coating. In this case, the use of randomized pulse waveforms can provide us with a significant advantage in the effort to characterize buried interfaces between layers or between a layer and a substrate. Overall, the RUSH concept can offer an alternative toolbox for measuring femtosecond dynamics in a very broad range of samples, outperforming the current methods owing to its simplicity and attainable temporal resolution.

## 3.2 State of the art

### 3.2.1 Pulse shaping

The natural choice for nonlinear spectroscopy is to use very short femtosecond pulses, which feature a very high peak power even for low-energy pulses. As a beneficial side effect, short pulses allow us to track very fast processes in a material. Obtaining a short femtosecond pulse with the desired spectrum consists of two steps: (i) generating a coherent spectrally-broad light and (ii) compressing the pulse by setting a constant spectral phase. In general, pulse compression compensates for the positive dispersion of optical elements and, in the case of ultrashort pulses, even of air [25]. The most sophisticated approach to pulse compression is the pulse shaper. Two technologies are commonly used [37]: amplitude/phase modulators in zero-dispersion/4-f line, and acousto-optic dispersive filters, often denoted as Dazzlers. Both require a trade-off between parameters and suffer from certain side effects, such as pixelation and pixel gaps, when using spatial light modulators (SLMs).

In general, the problem of pulse compression consists in the need for attaining a constant phase, which needs to be adjusted for each case. Moreover, in certain cases – for instance, by its transmission through a highly scattering medium – the pulse compression is highly deteriorated. Under such circumstances, the pulse must be restored by reconstructing the phase shift across the beam. In practical cases, this means that the scattering medium disables the measurement by using a standard setup.

The opposite case are the pulses with a random phase, leading to random temporal intensity fluctuations on the fs timescale. Such pulses arise due to multiple scattering or can be attained by a pulse shaper [38, 39]. The random pulses are robust against changes in the setup, scattering, and other factors. The overall length of the random pulse is given by “phase coherence”, i.e., the spectral width between the random phase changes in the spectrum. Unless the pulse becomes excessively stretched due to dispersion, the random pulse length is dominated by the phase coherence, and the pulse is resistant to propagation in the material.



### 3.2.2 Pulse characterization

Pulse compression or a targeted manipulation can be carried out only with a sufficient pulse characterization. This field was revolutionized by the invention of frequency-resolved optical gating (FROG) devised by R. Trebino and D. J. Kane [40]. It uses a spectrogram of two replicas of the same pulse interacting in a nonlinear medium for pulse characterization. Any fast nonlinear interaction (e.g., non-resonant optical interaction, second harmonic generation) can be used to carry out the measurement, and a mathematical algorithm is subsequently used to retrieve the spectral dependence of the phase. Since FROG is extensively used, artifacts connected to the method are well studied and described in the literature [41, 42]. We will describe the FROG method in detail in the following subsection.

An important modification of the FROG experiment is the XFROG setup [43], which determines a pulse waveform based on nonlinear interaction of the pulse with another pre-characterized pulse. The use of the second pulse brings several advantages: the possibility to measure relatively weak pulses, reduced detection bandwidth compared to SH generation, and variability in the measurable temporal range.

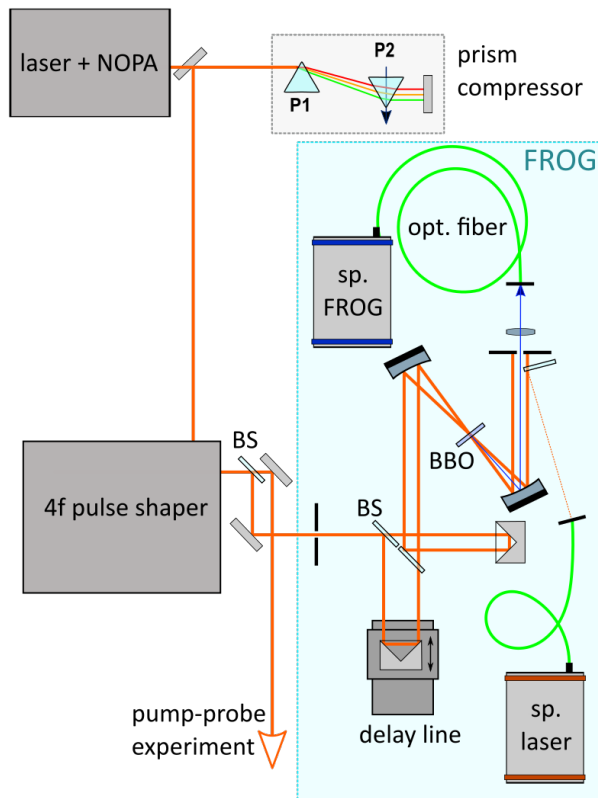


Figure 3.2: Scheme of the used setup to carry out pulse characterization via FROG method. BS - beam splitter; P1, P2 - prisms, sp. - spectrometers.

A competing method based on spectral-phase interferometry for direct electric-field reconstruction (SPIDER) uses sum frequency generation from three pulse replicas, one of which is highly stretched in a dispersive medium [44]. Each technique has its advantages: rapid pulse information retrieval and more simple spectrometer calibration for SPIDER; more simple measurement of long pulses and consistency check for FROG. Both methods also provide shot-to-shot laser pulse measurements [45, 46].

Additionally, new approaches to pulse retrieval have recently become of interest. Prominent advantages provide ptychographic reconstruction [47] and COPRA algorithm [48] which outperform the commonly used generalized projection algorithms in noise robustness, which is essential for measuring weak broadband pulses. The new methods also make it possible to reliably reconstruct a pulse from under-sampled or truncated datasets.

Pulse characterization has reached a sufficient maturity level to reliably characterize even a complex broadband random pulse and to provide information that can be used for data analysis. On the other hand, I see an opportunity for further enhancement in the missing implementation of the side information about the pulse into its reconstruction.

### 3.2.3 Frequency-resolved optical gating

The pulse characterization used in our laboratory was built on the combination of FROG and XFROG methods. Here we focus on the FROG setup itself depicted in Figure 3.2. The measured pulse was split into two replicas, where a high-precision delay line can adjust the delay between the replicas. The two focused pulses generate a signal in a nonlinear medium, which was, in our case, a thin BBO (50  $\mu\text{m}$ ) crystal for second-harmonic generation (SHG).

The FROG spectrum  $I_{FROG}$  measured for each delay can be calculated from the electric field  $E(t)$  of the measured pulse by using Fourier transform of the generated SHG field as:

$$I_{FROG}(\omega, \tau) = \left| \int E(t)E(t - \tau) \exp(-i\omega t) dt \right|^2 \quad (3.1)$$

The FROG trace with  $N \times N$  datapoints is an overdetermined system. Namely,  $N^2$  FROG datapoints, which are unique for each pulse, are determined by  $2N$  datapoints of the pulse waveform. Therefore, the ideal FROG trace corresponds to a single pulse shape, and the correct pulse shape can be retrieved even for a trace corrupted by noise. The real trace can be reproduced by a pulse, where the discrepancies between the measured and reconstructed FROG traces can serve to pinpoint experimental imperfections of the system and provide a consistency check of the experimental data.

The consistency check is enhanced by the possibility to separately measure the original pulse spectrum (“sp. laser” in Figure 3.2) and to use the spectrum in the FROG reconstruction.

The discrepancies between the experimental and theoretical traces can originate from a variety of effects. The most common cases for the SHG FROG experiment are:

- error in the delay line position
- random noise present in the spectral measurements
- pulse replicas not being identical
- violated phase-matching conditions in BBO
- imprecise calibration of spectrometers
- astigmatism in the beam focusing
- interaction of tilted beams within the crystal
- pulse being unstable in time and space

The degree of experiment – theory agreement is typically expressed by the so-called  $G$ -error introduced by the group of R. Trebino:

$$G = \sqrt{1/N^2 \sum_{ij} (I_{ij}^{exp} - \mu I_{ij}^{rec})^2}, \quad (3.2)$$

where the experimental FROG trace  $I^{exp}$  normalized to its peak value is compared to the recovered trace  $I^{rec}$ . The scaling factor  $\mu$  is optimized to gain the lowest the  $G$ -error. A lower  $G$  error value means a better quality of the experimental data. Nevertheless, since the  $G$  error depends



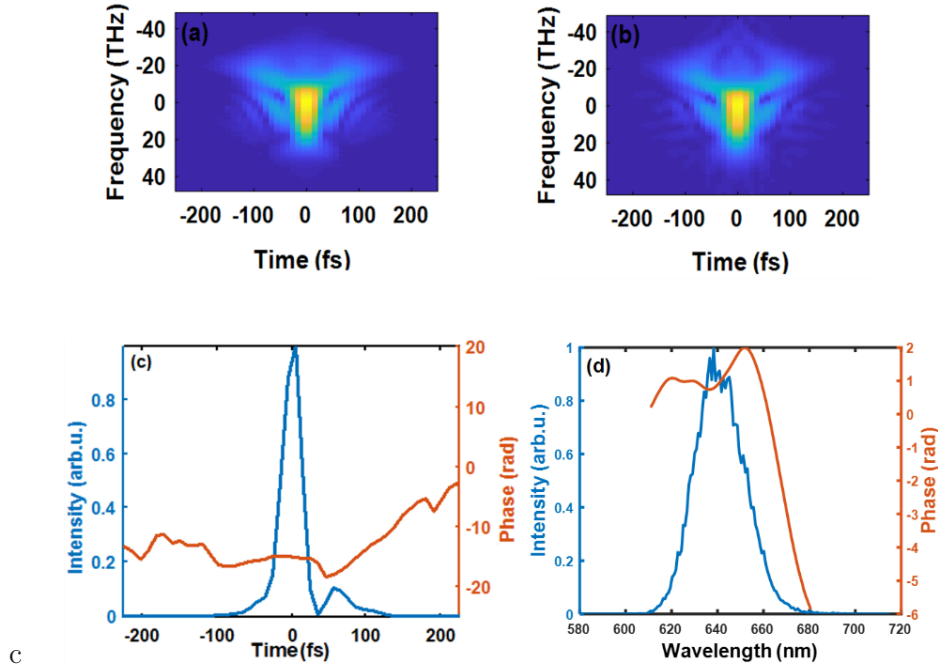


Figure 3.3: Measured (a) and Retrieved (b) FROG traces from a compressed NOPA pulse. (c) Retrieved temporal intensity profiles and phases. (d) Retrieved spectral intensity profiles and phases.  $N=156$ ,  $T=800$  fs,  $\Delta t = 10.32$  fs.

on the number of pixels  $N$ , we propose a different measure of the experimental data error, which we denote as normalized FROG error:

$$\epsilon_{FROG} = \frac{\sqrt{1/N^2 \sum_{ij} (I_{ij}^{exp} - I_{ij}^{rec})^2}}{\sqrt{1/N^2 \sum_{ij} I_{ij}^{exp}}} \quad (3.3)$$

It is worth noting that the FROG error or the  $G$ -error contains information about the FROG trace discrepancy. However, this does not imply that also pulse reconstruction has low quality. Therefore, we introduced the intensity error, reflecting the similarity between the actual and reconstructed pulse intensity temporal profiles. Such information is not available in an experiment and can be attained only by simulations. Therefore, one of the essential goals of our work was to determine whether the experimentally available FROG error can provide us with information about the quality of pulse retrieval.

### 3.3 Results

The overall effort to gain random-pulse ultrafast spectroscopy requires mastering pulse shaping and characterization. Therefore, the thesis will focus on using the FROG method to reliably characterize the complex random pulses and applying liquid-crystal-modulated 4f pulse shapers for targeted pulse shaping.

#### 3.3.1 Frequency-resolved optical gating

We will first focus on the reconstruction of pulses with various complexity of their waveform. Figure 3.3 provides an example of a measured FROG trace from NOPA (left upper panel) and a

reconstructed FROG trace (upper right panel), which corresponds to the pulse shapes depicted in the lower panels both in the spectral and temporal representation. In all our calculations, we employed a ptychographic algorithm of P. Sidorenko for the FROG reconstruction [47], which provided us with an excellent ability to reproduce even the complex pulses. Nevertheless, we also tested the use of COPRA algorithm [48], or SVD-based algorithm [40].

Despite the simplicity of the FROG setup, there is a number of factors, which can effectively distort the measured trace. In the following parts, I will address the main shortcomings commonly experienced in the SHG-FROG experiment, which were listed in the theoretical introduction to FROG.

## Delay line jitter

Eq. (3.1) assumes that we can determine the delay between the two pulse replicas  $\tau$  with absolute precision. However, this is impossible to attain with a real setup and, instead, we observe the real  $\tau$  value vary around the expected value. We will refer to this error as a delay line jitter. The jitter can originate from a mechanical instability of the FROG experiment or from an error in the determination of delay line position.

The understanding of the effect of the delay line jitter is important for two reasons. Firstly, lower demands on the delay line precision can significantly reduce the costs of such a delay line. Secondly, we can decrease the FROG acquisition time by using a shorter settling time of a delay line, i.e., a worse delay line precision. In the extreme case, it is possible to measure in the sweep mode, where the delay line is constantly moving.

We carried out an extensive set of simulations, where we used two different modes of delay line jitter. A random jitter can arise due to mechanical instability, and it causes the delay line error to fluctuate around the ideal value randomly. In other words, random jitter is a random number from a normal distribution with the standard deviation of  $\sigma_{jitter}$ . A random-walk jitter, on the contrary, is calculated by shifting the delay line from the previous position by a distance fluctuating as a normal distribution with the standard deviation of  $\sigma_{jitter}$ . In such a mode, delay line displacement shows a long-term drift around the ideal value. To simulate the real behavior, we also restricted the maximum delay line displacement below a certain threshold ( $4\sigma_{jitter}$ ).

The calculations were done for jitter values ranging from high-precision delay lines (100 nm, 0.67 fs delay) up to extremely unstable measurements ( $> 1000$  nm,  $> 6.7$  fs). In line with our expectations, we observe that

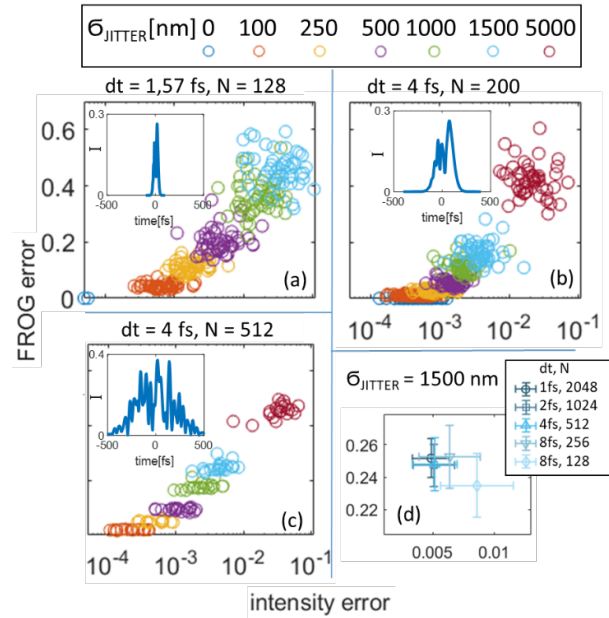


Figure 3.4: The effect of random jitter on relation between intensity and normalized FROG error for three sets of pulses – see text and reprint of Ref. [49] for details. Only the best solutions from 30 reconstructions are shown for every pulse. Colors depict different  $\sigma_{jitter}$ . a) Set 1, b) Set 2, c) Set 3; insets show an example of a pulse. The time interval and the size of the grid are written above the graphs. d) shows an enlargement of this relation for different (coarser and finer) FROG trace divisions for the pulses from Set 3 with  $\sigma_{jitter} = 1500$  nm. Figure adopted from Ref. [49] following OSA author's right policy.

the effect of delay line jitter scales with the pulse bandwidth, i.e., bandwidth-limited pulse length. The simulations were done for three sets of pulses featuring different bandwidths and pulse complexity. We observed that FROG error was correlated with the pulse reconstruction quality for the low delay line jitter. However, this correlation is absent for the large jitter values.

The two studied modes of jitter – random and random-walk jitter – significantly differed in their effect on the pulse reconstruction. The randomly displaced delay (random jitter) provided reliable pulse retrieval even in cases where the jitter value was comparable to the bandwidth-limited pulse length. Nevertheless, the random-walk jitter had a significantly more pronounced effect, and the reliable pulse retrieval required  $\sigma_{jitter}$  more than  $2 \times$  lower. Since each experiment can differ in the behavior of the delay line and apparatus in general, we aimed to identify a general criterion, which would be available from experimental data and serve as a benchmark to assure high-fidelity pulse retrieval.

We consistently observed that in the simulations, where the normalized FROG error was below 0.2, the vast majority of pulses featured intensity error below 0.02, see Figure 3.4, which in turn implies that the FROG reconstruction well reproduces all significant features of the pulse. Nevertheless, the normalized FROG error being well above the 0.2 threshold does not imply that the reconstructed pulse shape will be deteriorated – see Figure 3.5 – as we will discuss in the following paragraph.

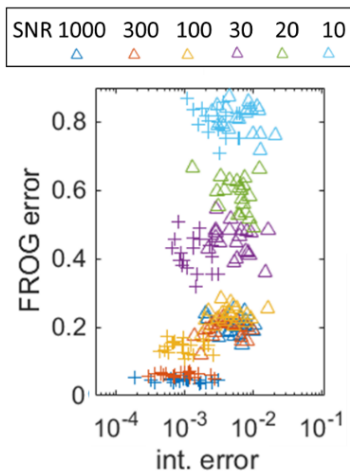


Figure 3.5: Random-walk jitter with  $\sigma_{jitter} = 100$  nm (crosses) and 500 nm (triangles) applied together with noise to a set of random pulses. Colors depict different signal-to-noise ratio (SNR). Figure adopted from Ref. [49] following OSA author's right policy.

A detailed description of the results is presented in the attached reprint of Ref. [49].

### Random noise

Random noise in the measured spectra is inevitably present in the data due to the shot noise, readout noise, and noise of the dark counts on the spectrometer. However, numerous reports show that the FROG reconstruction is very robust to random spectral noise up to extreme signal-to-noise ratios [50]. We tested the relation between the effect of spectral noise and the effect of delay line jitter. In line with these studies, we observed that the random noise has a pronounced effect on the FROG error, while the pulse retrieval is not deteriorated. Significant differences can be spotted only for SNR 10-30.

It is possible to retrieve high-quality pulse reconstruction even from a badly deteriorated FROG trace, where the normalized FROG error is well above 0.2. Therefore, this metric cannot evaluate the quality of the FROG trace and its reconstruction for the low SNR.

Details are presented in the attached reprint of Ref. [49].

### Difference in pulse replicas

Such a situation can occur when the two replicas used for sum-frequency generation in the FROG experiment are passing through a different thickness of glass in the beam splitters (BS in Figure 3.2). While the SHG FROG traces have to be symmetrical across the zero delay, the difference in pulse replicas will cause the SHG FROG trace to be asymmetric.

For spectrally broad laser pulses, it is therefore essential to use the symmetric generation of two replicas with two beam splitters, where each replica is once transmitted through a beam splitter and once reflected from a beam splitter (see Figure 3.2).

### Violated phase-matching conditions in BBO

The efficiency of SHG in a BBO crystal for a set wavelength depends both on the crystal thickness and its rotation. The rotation changes the phase matching between the fundamental photons and sum-frequency photons. A thinner crystal provides worse conversion efficiency, allowing efficient conversion of a broader range of wavelengths. Therefore, a shorter broadband pulse requires a thinner crystal. For this reason, the use of a thin BBO crystal ( $50\mu\text{m}$  in our case) is essential for the FROG experiment.

For our  $50\mu\text{m}$  thin BBO crystal, the phase-matching condition leads to a conversion efficiency with a Gaussian shape, which features the FWHM of 55 nm at the wavelength of 640 nm. This value was derived based on the simulation of the sum-frequency generation on the BBO crystal, which was, for the sake of simplicity, considered as a uniaxial birefringent material with the refractive index adopted from Tamošauskas et al. [51]. The attained bandwidth was in perfect agreement with the actual measurements. Surprisingly, the simulated bandwidth did not strongly depend on the angle between the two replicas, which we studied for angles below 3 degrees.

When the phase-matching bandwidth is comparable to the pulse bandwidth, it is needed to correct the FROG data for the spectral intensity. Here, it is possible to use the fact that in the frequency domain, the total FROG sum along the delay axis (spectral marginal) has to match the autoconvolution of the laser spectrum [50]. Since the laser spectrum is measured without restriction, the FROG shape can be corrected to match this condition. This procedure is called a spectral marginal correction.

At the same time, this correction can be applied only for a limited range of wavelengths. For the laser spectrum exceeding this range, it is required to truncate the spectrum (can be done within the 4f pulse shaper) or to measure with multiple crystal angles [52].

### Calibration of spectrometers

The most common problem encountered is a mismatch in the spectral calibration, namely, a shift of the wavelength calibration of a spectrometer. Such a shift leads to a discrepancy between the position of the measured FROG and laser spectra. This problem can be easily identified and corrected by using a wavelength calibration lamp (AvaLight-CAL-MINI in our case), making it possible to correct the wavelength calibration down to the precision of 0.1 nm. We have not encountered FROG reconstruction, where a better spectral calibration would be required.

The spectral sensitivity of the spectrometer, on the other hand, is typically not affecting the FROG traces even for the relatively broadband pulses reaching 20 fs pulse length. The sensitivity can be, to some extent, compensated by the spectral marginal correction (see the previous subsection).

### Astigmatism in beam focusing

The characterization of short femtosecond pulses typically requires the pulse to be transmitted through the thinnest possible mass of the glass, as each mm of the glass leads to significant pulse stretching and has to be compensated in the experiment. Therefore, the beams (replicas) are commonly focused by a spherical mirror, which is tilted to reflect the focused beam away from the original direction.

By simulating the tilted spherical mirror and calculating the corresponding difference in delay between two pulse replicas, we found that for the beam reflected 20 degrees away from the original direction, the delay between replicas will differ by 10 fs for two spots in the beam separated by 1 mm. In other words, by using a 1 mm wide beam in such a configuration, we will encounter the FROG trace to be significantly smeared along the delay axis.

From our simulations, we also found that the focused beams must be reflected by less than 5 degrees away from their input direction to attain the FROG smearing to be  $< 2$  fs per 1 mm of the beam, which is sufficient for our measurements. Therefore, we built our setup to comply with this rule, and the reflected focused beams were only tilted by 3 degrees in the vertical direction.

### interaction of tilted beams within the crystal

The non-collinear arrangement of the FROG experiment provided us with the advantage that the sum-frequency signal of interest was spatially separated from the other unwanted components. Using the iris diaphragm, we could greatly reduce the strong intensity of the pulses transmitted through the crystal and the background signal originating from the SHG of the incident beams themselves.

The non-collinearity of the signal has implications for mutual delay of the beams within the crystal. Since the two wavefronts of the two beams are tilted to each other, their respective delay will change across the spot where the two beams overlap. In our case, the angle between the laser beams was 2 degrees. For such a small angle, we can neglect the effect of light refraction on the BBO crystal.

The width of the laser beam can be estimated based on the value expected for the ideal Gaussian beam, which reached approx.  $80 \mu\text{m}$  for the  $1/e^2$  width. The effective beam width will be further reduced by the fact that we use the second-order nonlinear process, which will reduce the effective beam width by the factor of  $\sqrt{2}$ . Using simple trigonometry, we can derive that the difference between the delay on the two opposite edges of the beam will reach 9 fs (corresponds to  $2.7 \mu\text{m}$  optical path difference). This value is seemingly very high, but we should keep in mind that this corresponds to the  $1/e^2$  width of the beam. By recalculating the value of FWHM of the beam, we can derive that the delay between the replica differs by 5 fs.

In other words, the angle of 3 degrees between the two beam replicas on the BBO crystal causes the FROG signal to be convoluted with a Gaussian function with 5 fs FWHM. For the pulses studied in our work, where the bandwidth-limited length is between 15-20 fs, this fact does not pose any limit in the measurement. However, in the case of few-cycle pulses, such a phenomenon has to be considered.

### Spatial and temporal pulse variation

The FROG pulse retrieval assumes that the pulse shape is constant throughout the acquisition time and across the measured laser beam. This assumption might be corrupted by the pulse instability in time. The instability arises, for instance, due to thermal fluctuations in the modulating element in the pulse shaper (see the next section) [53]. The spatial pulse variation across the laser beam also commonly occurs, e.g., due to the misalignment of the prism compressor or space-time coupling in the 4f pulse shaper (see the next section) [54]. In all the listed cases, the laser spectrum stays constant, but the chirp of the pulse varies.

In our setup, we observed an apparent effect of chirp variation for the laser pulses processed by a 4f pulse shaper (described in the following subsection). One of the symptoms was the variation in the attained pulse length, which depended on the laser beam cropping by entering the iris diaphragm in the FROG setup.



To evaluate and control the chirp variation, which is essential for the reliable simulation of the pulse shape, we developed a new method “dispersion scan frequency-resolved optical gating” (D-FROG), which is introduced in part 3.3.3.

### 3.3.2 4f pulse shaper

Pulse shaping is commonly attained by using the so-called 4f pulse shaper [37]. A scheme of such a shaper, which was used in our experiments, is depicted in Figure 3.6. A grating (600 gr/mm in our experiments) was used to disperse the pulse spectrum in the horizontal direction. The primary reflection mode set by the grating blazing was reflected by a spherical mirror  $f = 500$  mm. The mirror collimated the spectrally dispersed horizontal direction and focused the beam in the vertical direction. Hence, in the distance of  $f = 500$  mm from the spherical mirror, in the so-called Fourier plane, we obtain each wavelength of the laser-focused in a single spot. In this plane, we can modify the phase of each wavelength individually and thus set, in principle, any spectral phase. Using an inverse beam path after the Fourier plane, the pulse wavelengths are recombined into a single beam with the pulse shape given by the Fourier transform of the set spectral complex amplitude.

In our case, we aimed to modify only the phase of the laser spectrum. This was done dominantly by the spatial light modulator (SLM), where an array of pixels with liquid crystals can adjust the phase. The other option consisted in using a plate with a profile on the micrometer scale, which changed the phase depending on the particular thickness at each spot.

In principle, the 4f pulse shaper is a straightforward and elementary apparatus to get an arbitrary pulse shape. This is, however, true only for the idealized case. The actual performance is affected by several factors, from which the most important are (i) the finite size of the focused spot in the Fourier plane, (ii) limitations in the phase modulation. Hereafter we will address these points.

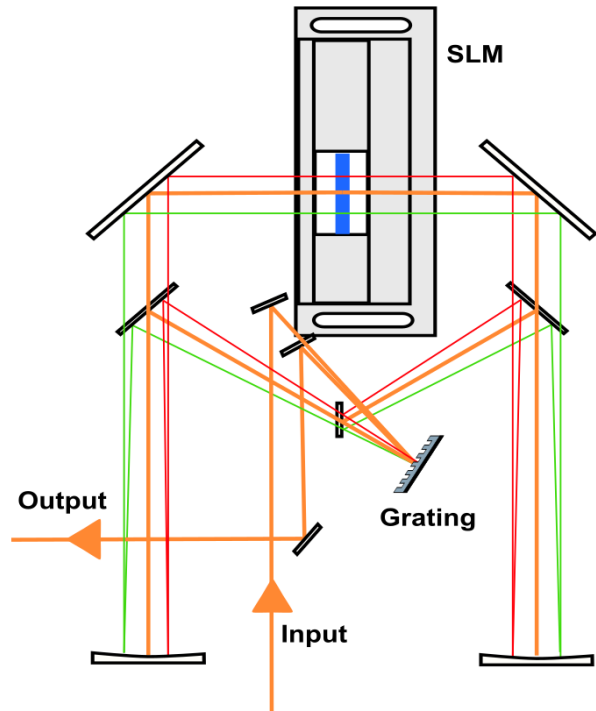


Figure 3.6: Scheme of the 4f pulse shaper.

### Limitations of the liquid-crystal-based SLM

SLM is a convenient way to adjust the laser phase. A voltage (0 – 4.5 V in the used Jenoptik SLM) applied across the thin layer of liquid crystals can vary the phase at 600 nm by more than  $3\pi$ . At the same time, SLM pixels feature certain width ( $100\mu\text{m}$  in our case), which causes the modulation of a phase to be step-like. Secondly, the phase set at one pixel can affect the orientation of the neighboring ones, which is denoted as pixel crosstalk. The crosstalk can originate from the so-called field fringing [55], where driving fields of pixels are affecting each other since pixels need to be separated only by a very thin stripe without an electrode ( $3\mu\text{m}$  in our case). An analogous effect has the elastic interaction between the long liquid crystal molecules

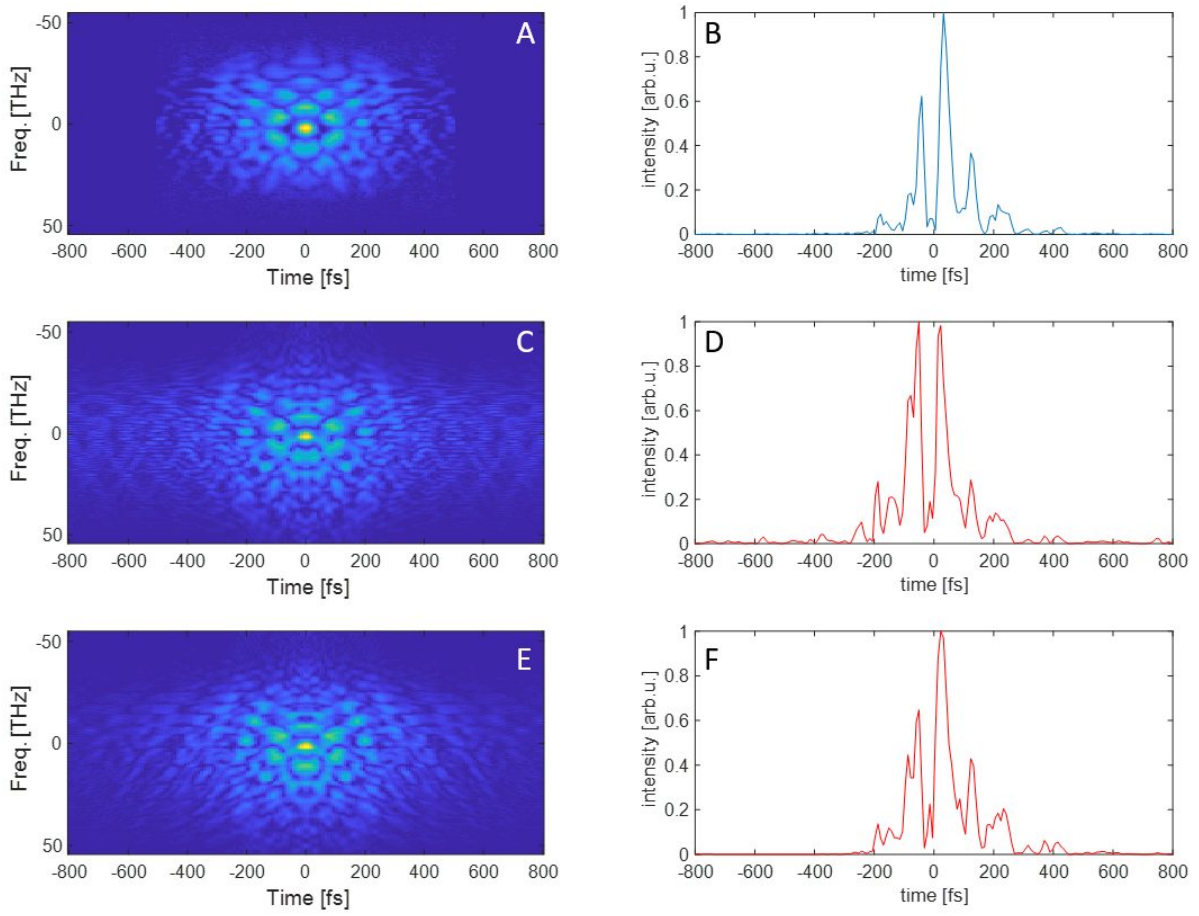


Figure 3.7: Illustration of the cross-talk effect in SLM applying several  $\pi$  jumps in the spectral phase. A) Measured FROG trace. B) Retrieved temporal shape of the pulse. C-D) Expected FROG trace and pulse shape in time without the cross-talk effect. E-F) Expected FROG trace and pulse shape in time with the cross-talk effect.

[56]. The interaction does not allow the orientation of the molecules to abruptly change across a small distance between the pixels.

The SLM pixel cross talk is commonly described as a convolution of the set SLM phase modulation with a Gaussian function. The width of the Gaussian function (standard deviation)  $\sigma_X$  is then the cross-talk parameter, which needs to be determined to ensure agreement between the expected phase modulation  $\phi_{set}$  and actual phase  $\phi_{SLM}$ :

$$\phi_{SLM}(\lambda) = \phi_{set}(p(\lambda)) \otimes \frac{1}{\sigma_X \sqrt{2\pi}} \exp\left(\frac{-p^2}{2\sigma_X^2}\right). \quad (3.4)$$

For the calculation, we also need to utilize the calibrated pixel position  $p$  depending on the laser wavelength  $p(\lambda)$ . For the known input complex spectrum  $E_{in}(\lambda)$ , we can include the SLM modulation as:

$$E_{SLM}(\lambda) = E_{in}(\lambda) \cdot \exp[i\phi_{SLM}(\lambda)]. \quad (3.5)$$

The effect of the pixel crosstalk is illustrated in Figure 3.7, where we set a pattern of several  $\pi$  jumps to modulate the spectral phase. The measured FROG trace and the actual pulse shape are shown in panels A-B. We can calculate the expected FROG trace and pulse shape based on the set SLM pattern and the known initial spectral phase of the pulse – see panel C-D. It is worth noting that while the measured pulse consists of three dominating peaks, the expected one without crosstalk has two prominent peaks. When we take into account the crosstalk effect, namely with the value of  $\sigma_{PCT}=0.85$  pixel, we gain a significantly better agreement between the measured and expected pulse shape – see panel D-E. At the same time, the FROG trace itself is visually very similar for the cases with and without the crosstalk.

### Finite size of the focused spot

Due to the finite width of the input laser beam, the laser beam dispersed by the grating is not focused by the spherical mirror into an infinitely thin stripe. Instead, by taking into account the beam width (3 mm) and the mirror focal length (500 mm), we can calculate that the expected width (FWHM) of the focal spot is approx. 80  $\mu\text{m}$ . This width can also be determined experimentally by capturing the width of the focused stripe with an array detector. In our case, the actual focal spot size was 110  $\mu\text{m}$ , which we ascribe to a reduced beam quality factor.

In both cases, the size of the focused laser beam in the SLM Fourier plane is comparable to the size of one pixel (100  $\mu\text{m}$ ) and cannot be simply neglected. To attain the actual pulse shape and laser spectrum, we need to use the information about the focal spot width  $\sigma_f$  and calculate the output beam of the pulse shaper as a convolution of the electric field modulated by the SLM  $E_{SLM}(\lambda)$  with a Gaussian point spread function:

$$E_{PS}(\lambda) = E_{SLM}(\lambda) \otimes \frac{1}{\sigma_f \sqrt{2\pi}} \exp\left(\frac{-\lambda^2}{2\sigma_f^2}\right). \quad (3.6)$$

By combining the effect of crosstalk and finite spot size in Eq. (3.5) and (3.6), we can reliably predict the pulse shapes induced by the pulse shaper.

### 3.3.3 Dispersion scan frequency-resolved optical gating

As stated in Section 3.2.3, the comparison of a FROG experimental dataset with the retrieved one can be used to identify potential issues in the experimental procedure. This is caused by the fact that FROG reconstruction is a highly overdetermined problem. On the other hand, there is a long list of possible causes of the experiment–theory discrepancies, which were listed above, and it is not always possible to discern their contribution from a single FROG trace. Moreover, even if we can identify the issue, it is hard to quantify this effect.

To provide a particular example, we observed the signatures of chirp variation in the FROG traces of fs pulses processed by an SLM-based 4f pulse shaper (see Figure 3.6). The presence of a chirp variation is expected here due to the inevitable space-time coupling in the SLM and due to the temporal instability of the SLM modulation [53, 54]. At the same time, we also observed a significant chirp variation across the beam, i.e., spatial chirp variation, when the pulse shaper was not well aligned. To use the random pulses in our future experiments, we need to quantify the chirp variation. This quantification makes it possible to judge the pulse shaper alignment quality, as well as the consistency of the pulse waveform across the beam.

Since a single FROG trace is not sufficient to reliably evaluate the chirp variation, we developed an additional consistency check by combining the FROG experiment with the dispersion scan (d-scan) characterization of the pulse [57]. The term “dispersion scan” denotes the fact that



we controllably varied the pulse shape by gradually changing its phase. We call the new method as dispersion scan FROG or short D-FROG. This method is based on the same setup as it is sketched in Figure 3.2, where we measure the FROG trace for a range of positions of the prism P2 placed in the prism compressor.

Since the prism insertion  $\Delta p$  in a prism compressor controllably changes the group delay dispersion (GDD,  $g$ ) and the third-order dispersion (TOD), we can calculate for each prism position the pulse electric field  $E(t)$  by using Fourier transform from the known laser spectrum  $S(\omega)$  and spectral phase  $\phi_c$  as:

$$E(t) = \mathcal{F}^{-1} \left\{ \sqrt{S(\omega)} \exp \left[ \phi_c + \frac{1}{2} g (\omega - \omega_0)^2 + \frac{1}{6} TOD(\Delta p) (\omega - \omega_0)^3 \right] \right\}. \quad (3.7)$$

The central frequency  $\omega_0$  is used to keep the phase change low and does not affect the pulse shape itself. The phase change alters the SHG spectrum and intensity, which is used in the d-scan technique. D-scan allows one to reconstruct the pulse shape based on SHG spectra measured for a range of prism insertions.

### Chirp variation

In the case of the chirp variation, the GDD is not a single value but rather a distribution of the values. Depending on the origin of the chirp variation, the GDD distribution shape can vary. Nevertheless, to make a simple representation, we describe the GDD variation as a normal distribution around the mean value  $GDD(\Delta p)$  with the width  $\sigma_{GDD}$ :

$$D(g) = \frac{1}{\sqrt{2\pi\sigma_{GDD}^2}} \exp \left[ -\frac{(g - GDD(\Delta p))^2}{2\sigma_{GDD}^2} \right] \quad (3.8)$$

### D-FROG results

We studied the quantification of chirp variation using three experimental methods: FROG, d-scan, and D-FROG. The comparison is presented in Figures 3.8 and 3.9. We denote the pulse with a sharp GDD value, i.e., no chirp variation, as an ideal pulse. On the contrary, the pulse with a chirp variation is denoted as a distorted pulse. Both illustrating figures (Figure 3.8 and Figure 3.9) present the D-FROG traces (panel a), d-scan traces (panel b), and single-FROG comparison (panel c). Moreover, for each technique, we present the measured trace, retrieved traces, and their differences.

The D-FROG dataset (panel a) is the most comprehensive one, and it is worth noting that the entire retrieved D-FROG trace for the ideal pulse arises from a single complex spectrum  $\sqrt{S(\omega)} \exp(-\phi_c(\omega))$  and two factors governing the linear dependence of GDD and TOD on the prism insertion. Despite this simplicity, we got an excellent agreement between the measured and calculated traces. This is a signature of a well-reconstructed pulse shape. However, even in the FROG traces, we can spot several discrepancies – see, for instance, the panel corresponding to the prism insertion -0.3 mm, where we expect to get features in the negative frequencies. These are, however, not present in the measured data.

When we turn to the other methods, the D-scan measurement (panel b) shows a slight discrepancy for the negative prism insertions. However, a single FROG trace at the zero prism shift (panel c) can be very well reproduced with the ideal pulse.

We implemented the GDD variation and fit  $\sigma_{GDD}$  in Eq. (3.8) to improve the agreement between the measured and calculated datasets. The agreement was evaluated based on the G-error defined in Eq. (3.2) and analogous quantities for the D-FROG and d-scan datasets. In Figure 3.9, we present results acquired for the best agreement, when the  $\sigma_{GDD}$  reached  $120 \text{ fs}^2$  based on the D-FROG fit. We observe an ideal agreement for all D-FROG, d-scan, and FROG traces. When we do an analogous fit for the FROG and d-scan data only, we obtained the values of  $80 \text{ fs}^2$  and  $120 \text{ fs}^2$ , respectively.

The question of interest was which method is the most reliable for chirp variation quantification. Therefore, we carried out the same  $\sigma_{GDD}$  fit for several different reconstructed pulses, which slightly differed from each other. We also reconstructed the pulse based on the d-scan dataset. For a set of ten different phases, we estimated that the D-FROG method could reliably determine the value with  $10 \text{ fs}^2$  precision. The extraction of  $\sigma_{GDD}$  from a single FROG trace lead to underestimated values, which were caused by the fact that the FROG trace was used for the pulse reconstruction and the reconstruction algorithm likely tended to compensate for the chirp variation by adjusting the pulse complex waveform.

Finally, we focused on the origin of the observed chirp variation. As stated previously, this can affect the pulse being unstable in time or the pulse shape variation across the beam. By carrying out a set of rapid-scan FROG measurements, where a single acquisition took 60 ms, we were able to show that on this time scale, the pulses are stable and do not vary between the scans. Therefore, we could conclude that the observed effect arises due to space-time coupling present in the 4f pulse shaper and due to its slight misalignment.

Details of the presented results are provided in the attached reprint of a manuscript under consideration [58].

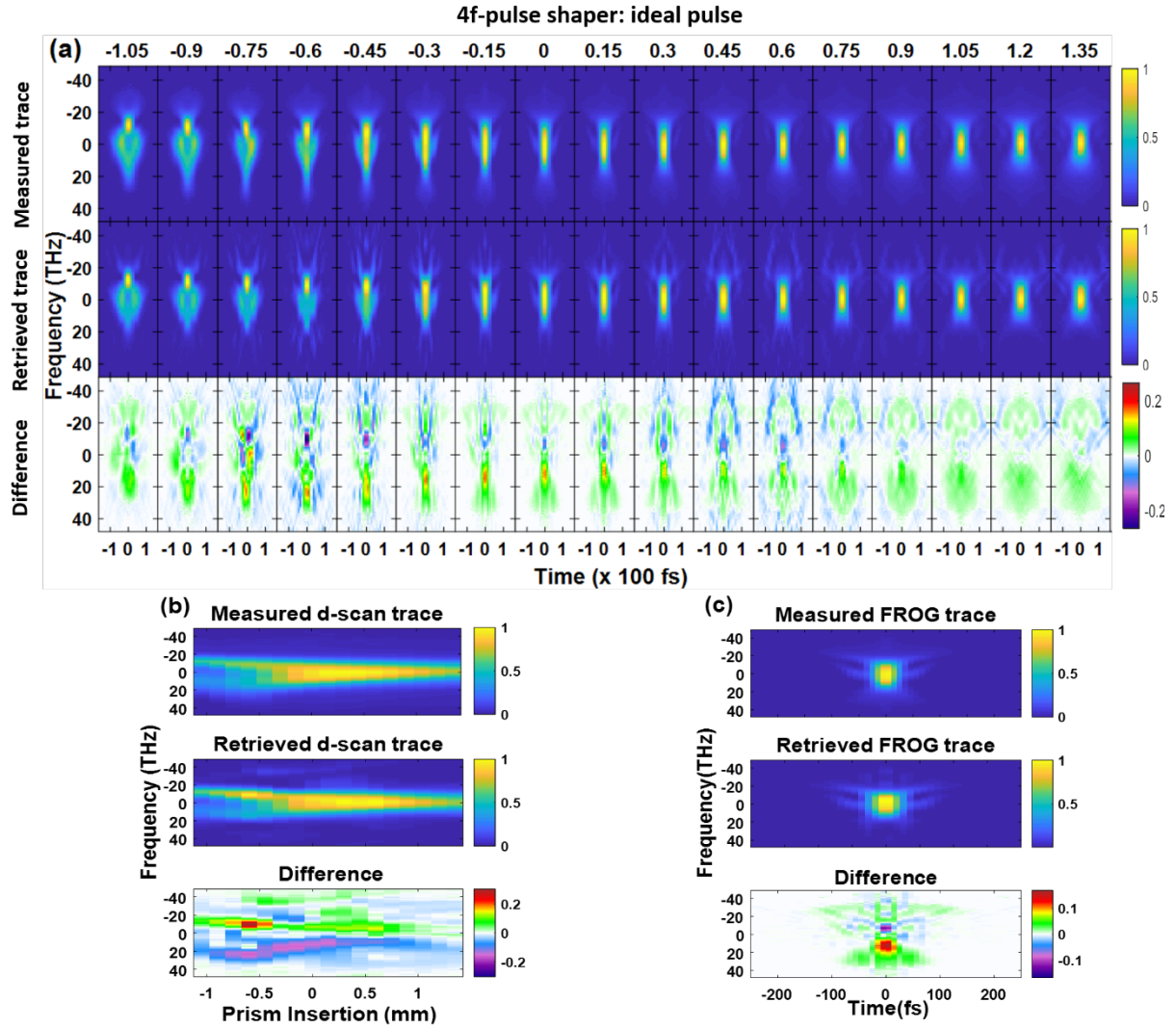


Figure 3.8: Measured D-FROG, d-scan and FROG traces of pulse generated from NOPA and processed by a 4f-pulse shaper; retrieved traces assuming an ideal pulse with no chirp variation; differences between the measured and retrieved traces. (a) D-FROG traces (the traces are acquired for different prism insertion positions from -1.05 to 1.35 mm, as mentioned above the panels) (b) d-scan trace (c) FROG trace of a compressed pulse.  $N=156$ ,  $T=800$  fs,  $\Delta t=10.32$  fs.

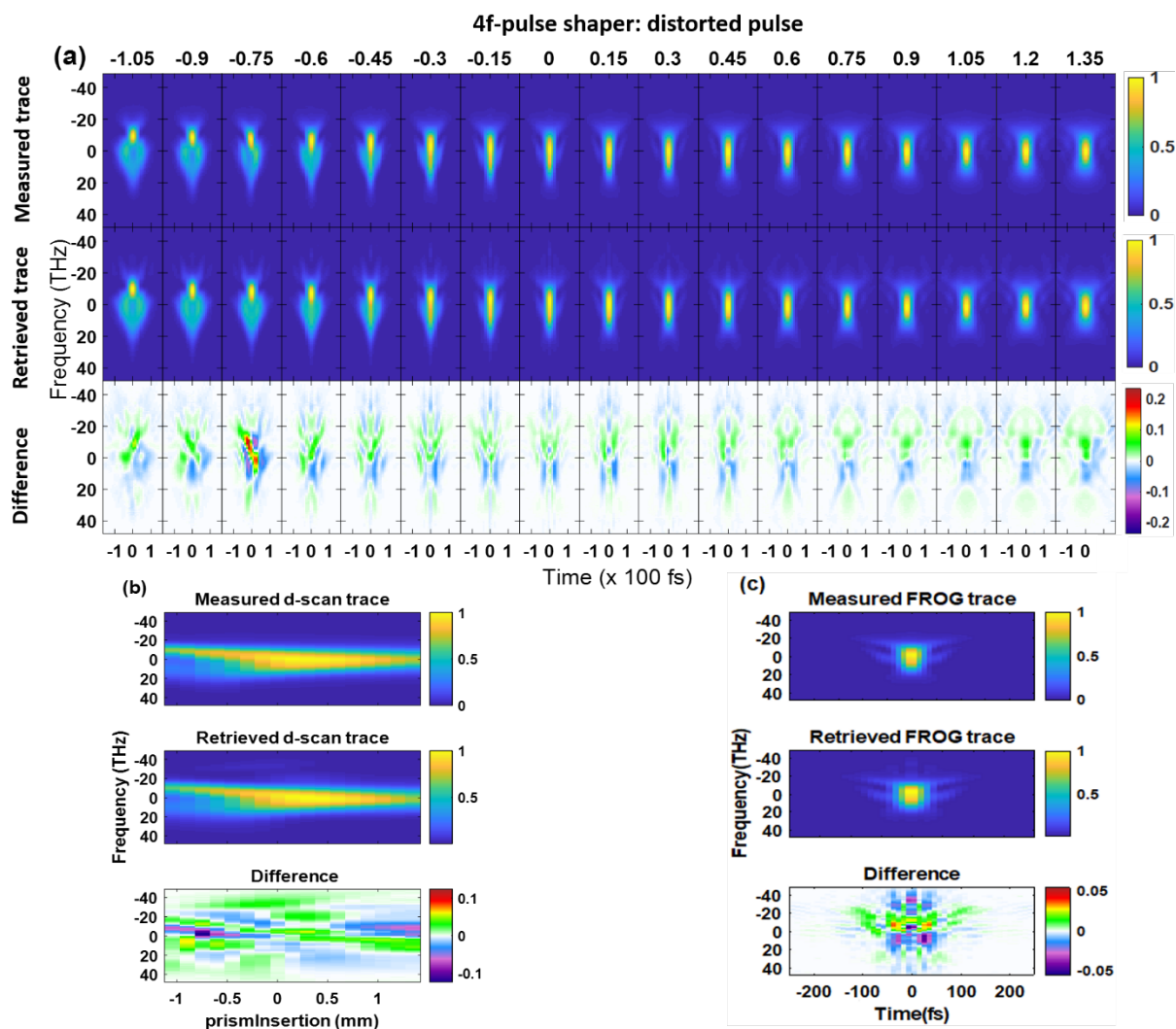


Figure 3.9: Measured D-FROG, d-scan and FROG traces of pulse generated from NOPA and processed by a 4f-pulse shaper; retrieved traces assuming a varying chirp across the beam; differences between the measured and retrieved traces. (a) D-FROG traces (the traces are acquired for different prism insertion positions from -1.05 to 1.35 mm, as stated above the panels) (b) d-scan trace (c) FROG trace of a compressed pulse.  $N=156$ ,  $T=800$ ,  $\Delta t = 10.32$  fs.

### 3.3.4 Pump-probe spectroscopy

In parallel to the effort towards high-fidelity targeted pulse shaping and characterization, we created a pump-probe experiment in the transmission and reflective mode. By using a digital lock-in amplifier and detection via a balanced pair of photodiodes, we were able to reach the precision of  $10^{-5}$  even for the probe pulses processed by the pulse shaper.

To provide an example of the measured data, we present in Figure 3.10 the measurement of transient reflection, where a two-layer sample (10 nm Ti/ 300 nm SiO<sub>2</sub>) on a Si substrate is excited by a short IR pulse (1028 nm, 240 fs pulse length). The excitation light was rapidly absorbed within the thin Ti layer, where it created a strong response (see black line in panel A) due to free carrier excitation and change in the effective temperature of the lattice. These are responsible for the initial oscillations and long-lived two-exponential decay of the signal (green line) tracked by a probe pulse at the wavelength of 610 nm. In addition to the two-exponential signal, we can observe oscillations, which arise due to interference of a traveling acoustic wave with the reflection on the sample surface (red line in panel B) [35, 59]. These so-called Brillouin oscillations feature a period set by the speed of light and sound in the material. Therefore, when the acoustic wave reaches the SiO<sub>2</sub>-Si interface (light blue and gray background interface), the oscillation period is rapidly changing. The attained oscillation periods were in perfect agreement with the results of E. Pontecorvo et al. [59] on the same system.

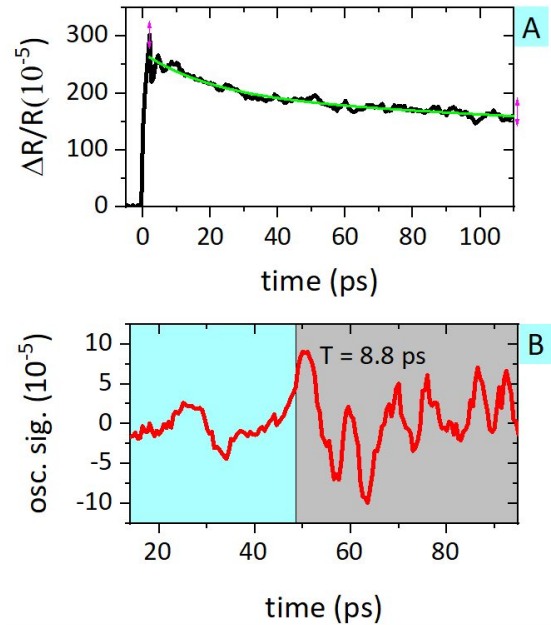


Figure 3.10: (A) Transient reflection signal (black line) of a Ti-SiO<sub>2</sub>-Si system – see text for details – fitted with a two-exponential decay (green line).  $\lambda_{exc}=1028 \text{ nm}$ ,  $\lambda_{probe} = 610 \text{ nm}$ . (B) Residual signal after fitting (red line) corresponds to the so-called Brillouin oscillations in the sample and reveals the acoustic wave traveling through the SiO<sub>2</sub> (light blue background) and Si (gray background)

## 3.4 Outlook

The ability to reliably shape and characterize random pulses makes it possible to carry out the random-phase ultrafast spectroscopy. The ongoing experimental work, which has not yet been published and included in thesis, provides all the required means.

Here, I will present the outlook for the so-called semi-random pump-probe experiment. In this case, a broadband white-light supercontinuum, which cannot be easily compressed into a single pulse, is intended to form a random probe pulse, while the sample will be excited with a standard compressed pump pulse. This experiment is needed to confirm the feasibility of the RUSH concept with the available pulse shaping and characterization.

This will enable the tracking of ultrafast dynamics even with an uncompressible broadband pulsed source. A simple scheme of the method is presented in Figure 3.11. We can use the known

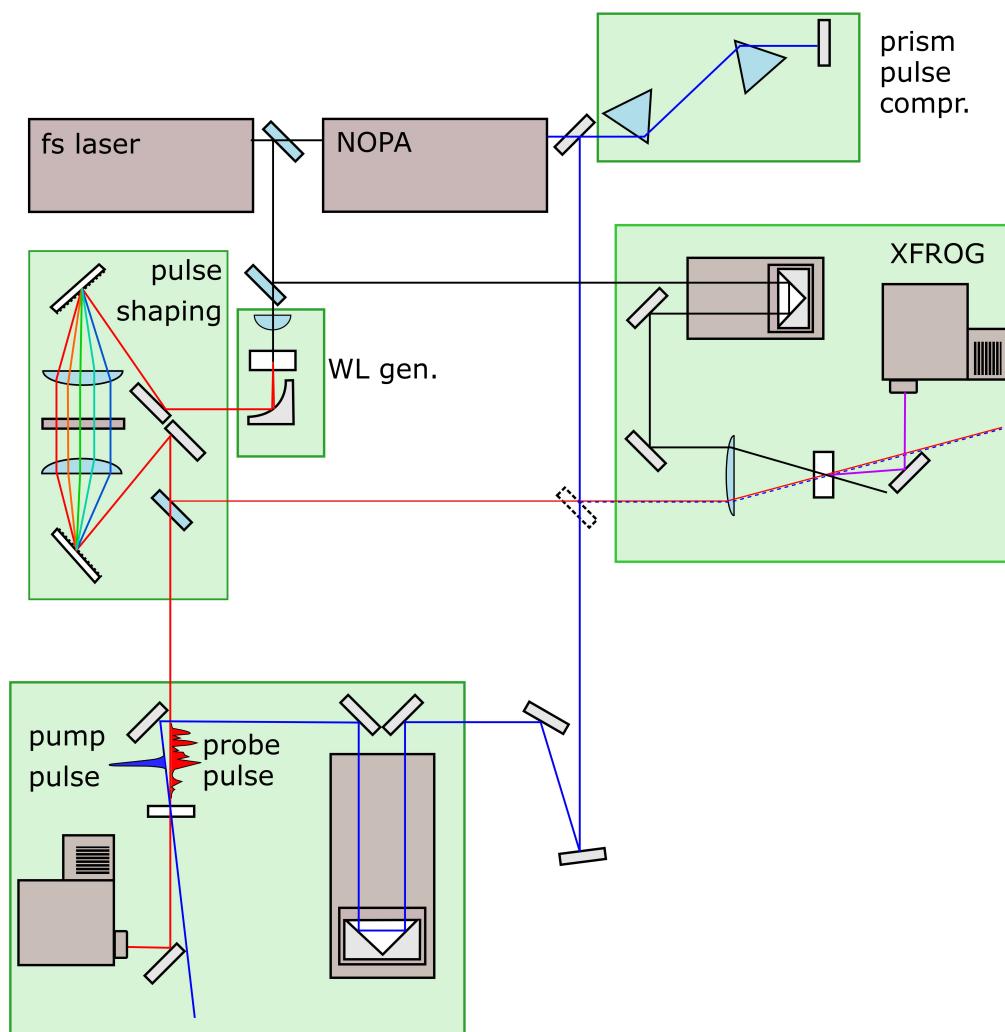


Figure 3.11: Scheme of the semirandom pump-probe experiment.



waveform of random pulses to extract the time-dependent transient absorption signal by using the time-domain analogy of the single-pixel camera technique – see Section 2.2.2.

The measurements will be initially carried out in the spectrally-unresolved mode by using amplified photodiode detection. This brings several advantages: (i) simplicity of the experiment alignment, (ii) faster mathematical reconstruction, (iii) ability to use a balanced pair of detectors. In general, pump-probe measurement requires a detector with a high dynamic range due to the need to measure subtle variations of the probe intensity. Due to the random scanning over the system dynamics, the random probe method decreases the variation even further (see the preliminary data). For this reason, a pair of balanced photodiodes can improve the measurement quality considerably. The spectrally-resolved measurements will employ a cooled CCD coupled to a spectrograph. An emphasis will be put on the dynamic range of the CCD, which can exceed  $10^5$ .

In Figure 3.12, we provide a simulation of the semi-random PP experiment. The simulated decay (two-exponential transient absorption decay, amplitude  $10^{-2}$ , excited by a 10 fs pulse) was measured via 1000 datapoints using random waveforms. The total random pulse intensity was calculated to simulate the pump-probe data acquisition. The detection featured noise root-mean-square (RMS)  $10^{-5}$  and a detector dynamic range of  $10^5$  to simulate realistic error levels. The relative change in the detected pulse intensity varied with RMS  $10^{-4}$ . We can see that the reconstructed signal agrees very well with the actual, and the dynamics are well resolved over two orders of magnitude.

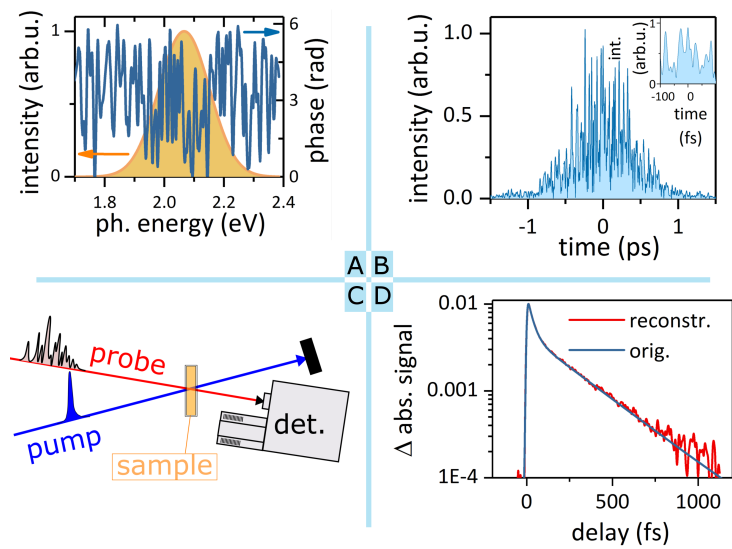


Figure 3.12: Simulation of a semi-random pump-probe experiment. A broadband pulse with a randomly set phase (A) leads to a randomly fluctuating waveform (B). A series of 1000 pulses was used to simulate semi-random experiments (C) and was proven to reliably reconstruct (TwIST algorithm) [60] a two-exponential decay of transient absorption.

### 3.5 Summary

We presented the concept of random-phase ultrafast spectroscopy RUSH, which can offer an entirely different approach to measuring ultrafast dynamics. Such measurements so far depended on the use of very short compressed laser pulses. With the decreasing pulse length and increasing bandwidth of the pulses, the task becomes more and more demanding or even impossible. We propose that using randomly modulated random pulses is equally well suited for extracting ultrafast dynamics, while the random pulses are much more robust to their propagation through dispersive and scattering materials.

In this chapter, we present a detailed description of the random pulse shaping, characterization, and evaluation of the main obstacles in the way towards targeted random pulses. Namely,

we focus on our results concerning the effect of noise and delay-line jitter in the FROG experiment [49], pixel crosstalk in the spatial light modulator [58], and the quantification of chirp variation present in the measured pulse [58]. We demonstrate our results on the pump-probe technique, which will demonstrate the use of a randomly-shaped probe pulse for the data acquisition. Finally, we provide an insight into the future use of the random pulses in the random-pulse pump-probe experiment.





## Chapter 4

# Optical characterization of thin films

### 4.1 Introduction

The deposition of thin films is an inherent part of optics fabrication. The elements designed for specific applications are typically coated with an appropriate coating – an anti-reflective stack of layers for lenses, reflective coatings for mirrors, or by an interference filter for a spectrally-selective response. On the one hand, the thin film coating commonly protects against surface corrosion or radiation damage induced in delicate optical materials. On the other hand, the properties of the thin films and their interfaces might become the limiting factor for mechanical or laser-induced damage [61, 62]. This applies, in particular, to the interfaces between layers in the coating and between the coating and substrate. This brings the necessity to characterize very well the layers and their interfaces.

An interface embedded between two materials is a specific species with its distinct morphology and optical properties. Laser spectroscopy is a natural choice for studying deeply buried interfaces in transparent materials. However, the problem is to viably track the properties of a few nanometers thin interface layer embedded in a mass of matter with its own optical response. The solution is provided by the process of sum-frequency generation (SFG), where two photons merge into one possessing the sum energy; a particular case is the more noted second-harmonic generation (SHG). Due to symmetry reasons, SFG inside material with inversion symmetry is very inefficient. On the contrary, the interface always lacks inversion symmetry and features a relatively strong SFG [63].

Unfortunately, the sum-frequency (SF) signal from bulk and interfaces can vary from one experiment to the next, and no general approach can secure distinction between the two [63]. Their contribution can only be deduced by using a complex set of measurements and a set of testing samples with varied parameters or by using a tunable generating laser addressing a particular resonance connected to the interface. This highly limits the use of SF spectroscopy despite a vast range of samples where the possibility to track properties and dynamics at the interface would be an immense advantage.

Therefore, in this chapter, we present our measurements of SHG on a single thin film, where we aim at discerning a signal originating from the buried interface from the bulk signal. By using two models and samples with varying layer thickness, we were able to disentangle the signal from an  $\text{Si}_3\text{N}_4$  layer and the  $\text{Si}_3\text{N}_4$ -Si interface. However, our results suggest that using the same approach for more complex systems will not be possible due to many parameters entering the calculation.

Another option to avoid the effect of interfaces is to deposit a coating, where the step-like abrupt changes in the material are replaced by a gradual variation in their composition and the



corresponding refractive index [64]. We denote such layers as gradient layers, which is a shorter name for a more rigorous name “graded refractive index layers”. As a trade-off for the possibility to avoid interfaces, the gradient layers are relatively hard to optically control, as the refractive index does not follow a simple step-like behavior. Instead, the gradient can have whatever shape.

To form gradient layers with targeted gradient shapes for specific applications, we need to characterize the gradient with the highest possible accuracy. Therefore, the optical characterization of such layers is a topic of immense interest, and it will also be addressed in this chapter.

## 4.2 State of the art

### 4.2.1 Optical characterization of thin films

Spectroscopy is the natural choice of means to characterize optical thin films [64]. The coatings are designed to feature a specific optical response – a low or high reflectivity or transmittance – which can be calculated for any polarization state or incident angle, even for a stack consisting of a high number of layers. The calculation requires the knowledge of the layer thicknesses and their refractive index. Vice versa, we can use the experimentally measured optical response, such as ellipsometric spectra, to fit the layer thickness or its refractive index.

To get the optical response, the so-called matrix method is commonly used. A layer is represented as a matrix that takes into account phase delay and Fresnel coefficients. The contribution of each layer is calculated in terms of admittance  $Y$ , defined as the ratio between the magnetic and electric field for the particular polarization of interest. The total admittance can be calculated by multiplying the matrices of each layer. From admittance, it is then possible to directly calculate with the system reflectivity and transmission. The complete derivation of the matrix theory can be found in the book of H. A. Macleod [64].

The commonly used experimental techniques are transmission and reflection spectroscopy combined with ellipsometry. All methods can be used ex-situ for the complete deposited sample, as well as in-situ during the deposition, where they can complement other means of layer thickness measurement, such as a quartz crystal monitor. Combining a quartz crystal monitor and broadband transmittance measurement is a golden standard in optical coating deposition.

Due to the limitations posed by the transmittance of the most common optical materials (BK7) and the detectivity range of the commonly used spectrometers, optical monitoring is typically limited to the visible and near-infrared spectral range (400-950 nm). This causes the optical monitor to suffer a low precision for layers with a low optical thickness (physical thickness multiplied by refractive index) below 30-40 nm. At the same time, the optical monitor requires a high contrast between the refractive index of two consequent layers to reach a good precision.

The major engineering concerns in this field are the selection of particular spectral ranges to track the optical response and the synergy between optical and crystal layer monitoring. The precision of each method depends on the deposition system, layer thickness, layer refractive index, or contrast to the monitoring sample. It is, therefore, very complex to create a general set of rules applicable for any case.

The gradient thin films pose a severe issue to optical monitoring. They can be perceived as a stack of very thin films with very low contrast between the refractive indices of the neighboring layers. In other words, gradient thin films combine two critical negative factors for optical monitoring. Therefore, it is of high interest to develop the most reliable means of their optical characterization.

### 4.2.2 Second-order nonlinear interaction at interfaces

Electromagnetic field propagating through a material induces in the material polarization  $P$  which can be expressed as a Taylor-series expansion of electric field  $E$  – the most significant source of polarization [63]. For the lowest two terms in the dipole approximation represented by  $\chi$  electric susceptibility matrix and  $\chi^{(2)}$  second-order susceptibility tensor, we obtain:

$$P_i(\omega) = \sum_j \chi_{ij} E_j(\omega) + \sum_{j,k} \chi_{ijk}^{(2)}(\omega = \omega_j + \omega_k) E_j(\omega_j) E_k(\omega_k), \quad (4.1)$$

where  $\omega$  denotes the polarization frequency and  $i, j, k \in [x, y, z]$  can be one of the Cartesian components of the field or polarization.

The second term – the so-called second-order nonlinearity – can be interpreted as an interaction of two photons. A well-known example is the process of second harmonic generation (SHG), where two identical photons merge into one with double energy or, more generally, sum-frequency generation (SFG) from two photons.

Intuitively, second-order nonlinearities are expected to be the most prominent ones. However, due to symmetry reasons in the dipole approximation, SFG is forbidden in any centrosymmetric material. On the contrary, the boundary between two bulk phases can be perceived as a polarization sheet with no inversion symmetry [65]. This opens a way to observe a strong response from any optical interface. Therefore, SFG is an excellent means of studying the optical response of an interface – in particular for deeply buried interfaces in transparent materials.

The ideal situation is complicated by the fact that second-order nonlinear interactions occur even in centrosymmetric materials due to quadrupole electronic or dipole magnetic interactions. Although the quadrupole contribution can be, in many cases, described by a small number of independent parameters, it is still demanding to eliminate the bulk signal [63, 65]. Its contribution depends highly on the sample properties and experimental conditions – for instance, the contribution induced by the electric field gradient appears only for samples with multiple reflections or two-beam experiments, and it depends on the beam focusing [66].

There is no general approach to disclosing signals from a particular interface or bulk phase. Interface selectivity is often obtained by tuning one of the driving beams in SFG to a distinct vibrational resonance of the interface – the so-called vibrationally-resonant SFG (VR-SFG) [67]. In more general cases, the contributions of the bulk and the interfaces have to be deduced from a complex set of experiments, where the key tool is the interference caused by reflection on the interfaces [68, 69].

The interference causes the light field to be modulated in amplitude and phase for different parts of the sample, depending on Fresnel reflection from the interfaces and the optical path [70]. This means that the modulation at each interface depends on the wavelength, incident angles, and polarization state of both the incident and the sum-frequency light. As a consequence, the resulting SFG efficiency also varies from one interface to another. However, the incident angle and wavelength dependencies are typically smooth and featureless curves unless the layer thickness highly exceeds the wavelength of light. As a result, it is very demanding to reliably disclose the contribution of a buried interface from a single experiment. Such a study needs to combine knowledge from measurements of samples featuring varying layer thickness and simultaneous measurement in reflection and transmission geometry.

Disentangling a contribution of a specific interface for multiple buried interfaces is an incomparably more complex task. This task has been addressed frequently in articles in the past few years, documenting the importance of the topic. For instance, Wilson et al. used VR-SFG on specifically designed layer thicknesses to attain selective constructive or destructive interference

on a specific interface [67]. Azam et al. used measurements of SFG of two distinct wavelengths (IR and VIS) for a broad range of incident angles to disclose the contribution from two interfaces [71]. Moon et al. applied phase-sensitive heterodyne SF detection from electronic SFG on two interfaces to constrain viable models of the system [72]. Finally, the work of Kearns et al. used SF spectroscopy to precisely model the vibrational spectroscopic features to resolve signals from two interfaces of a polymer film [73]. Overall, even the most advanced methods report on the ability to experimentally resolve signals from no more than two interfaces. Moreover, the measurements are limited to a single method (VR-SFG), requiring knowledge about the usable vibrational resonances together with a tunable or a broadband IR source.

The SHG contributions from an interface and bulk volume of a layer follow a different interference pattern due to a varying local field intensity for different incident angles and light polarization. Therefore, by applying a model suited for the bulk response by M. Koskinen [74] and the model for the interface SHG contribution presented by A. Gielis [65], it is possible to calculate the contribution of these SHG sources for the set condition. It is natural to use the measurements of SHG with varying incident angles and polarization to discern the two contributions.

## 4.3 Results

### 4.3.1 Optical characterization of gradient thin films

The optical characterization of the bulk properties of a homogeneous thin film is a standard task in the field of optical coating. The precise knowledge of the complex refractive index of a layer, as well as the thickness of the layer, is essential for the targeted deposition of the coating. The complex refractive index is extracted by fitting the experimental data to a certain model of the material. An example of such a fit can be seen in Figure 4.1, where the optical response (reflectivity, transmittance, and ellipsometric curves) were fitted by a refractive index model (two-resonance Tauc-Lorentz [75], see Figure 4.1 lower panel). We attained a very good agreement between the theoretical and experimental curves.

For the gradient layers, where the refractive index is continuously changing, such characterization is much more demanding. Firstly, the gradient refractive index needs to be described with a sufficiently small number of parameters. Secondly, many of the parameters can compensate for each other and a smooth optical response, which is typical for the gradient layers, offers very limited precision of the fit.

We focused on the study of  $\text{SiO}_x\text{N}_y$  layer deposited via dual ion beam deposition described in detail in the reprint of Ref. [76]. The ratio between the oxygen and nitrogen gas flow into the assistant ion beam source was able to vary the layer stoichiometry, thus adjusting the refractive index at each moment of the deposition. From numerous publications devoted to this type of gradient material, it can be derived that the refractive index can vary between 1.5 and 2.05.

In order to capture the maximum available information about the deposited layer, we characterized the sample transmittance, reflectance, and ellipsometric response. The transmittance and reflectance curves were acquired for both S and P polarizations across a broad range of incident angles: 4-70 deg for transmittance, 8-70 deg for reflectance. The question of interest was the possibility of acquiring a precise gradient shape based on such a dataset. A prerequisite for this effort is to create a merit function  $M$ , which would quantify the experiment-theory agreement. This was done by using various spectra  $S_m(\lambda, \Theta)$  for methods  $m$  (reflectance  $R$ , transmittance  $T$ , and ellipsometric spectra  $\Delta$  and  $\Psi$ ) measured for a set of incident angles  $\Theta$  – see Figure 4.1

upper panels for example:

$$M = \sum_m \eta_m \sqrt{\sum_{\Theta} \sum_{\lambda} |S_m^{exp}(\lambda, \Theta) - S_m^{th}(\lambda, \Theta)|^2}. \quad (4.2)$$

Superscripts “exp” and “th” denote the experimental and theoretical curves, respectively. The weight of each method  $\eta_m$  to the overall merit function  $M$  is set so that each of the methods contributes equally to the merit function value.

### Homogeneous thin films of $\text{SiO}_x\text{N}_y$

To set the expected refractive index dependence and parametrize the gradient, we deposited two sets of seven homogeneous single-layer samples, for which the layer was deposited under constant oxygen flow ranging from 0 to 3 sccm. Each sample was characterized by the complete set of methods, and its refractive index, represented by the double-oscillator Tauc-Lorentz model, was fitted to the data. An example of such a fit for selected curves is presented in Figure 4.1. The excellent quality of the fit allowed us to set the initial estimate of the gradient refractive index shape.

### Gradient thin films $\text{SiO}_x\text{N}_y$

By depositing a layer where the oxygen flow linearly changed with time, we were able to gain a gradient refractive index layer. It is reasonable to expect that the refractive index of the thin layer deposited for a given oxygen flow will follow the refractive index of the homogeneous layer deposited under the same oxygen flow. Therefore, in principle, we can predict very well the expected refractive index gradient.

However, the deposition with varying oxygen flow is affected by several factors. Firstly, the oxygen pressure in the chamber reacts to the oxygen flow changes with an inevitable delay due to the limited speed of the vacuum system. Secondly, the bombardment of the ions from the assistant ion source could alter the oxygen stoichiometry of the deposited layers and change the layer, which had already been deposited. Finally, the deposition process is not stable, and the actual deposited profile of the refractive index can vary from case to case. Therefore, we needed to address the possibility of the actual shape of the refractive index profile.

Many potential fitting parameters combined with computationally costly calculations do not allow us to optimize the overall shape of the refractive index profile. Therefore, we needed to

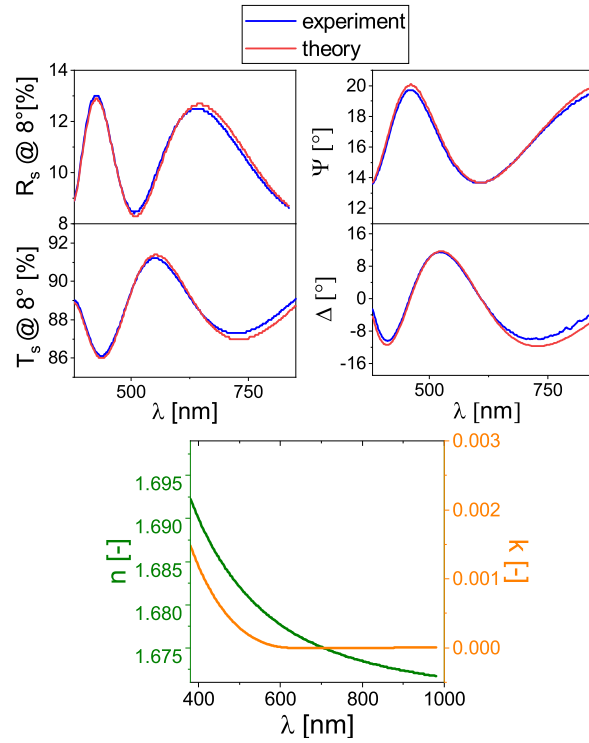


Figure 4.1: Upper panels: selected curves from the characterization of a homogeneous  $\text{Si}_3\text{N}_4$  layer, showing the calculated (red curves) and measured (blue curves) response of the layer on a BK7 substrate.  $R$  and  $T$ : s-polarization at 8 deg. incident angle; ellipsometry  $\Psi$  and  $\Delta$ : 70 deg. incident angle. Lower panel: real (green line) and imaginary (orange line) part of the extracted refractive index.

select a simple approach to parametrize the profile shape. As the most straightforward solution, we decided to set the expected profile shape as the initial point and studied the merit function  $M$  change by adding an offset and quadratic function to the profile. Here we provide a summary, while the details are provided in the reprint of Ref. [76].

We observed that the merit function was very sensitive to the offset change or an additional quadratic term. The change in the refractive index by a mere 0.005 led to a significant increase in the merit function value, and thus, this parameter can be optimized very precisely. Such a result would suggest that the gradient shape can be attained with very high precision.

To test the actual precision, we carried out fitting, where we randomly altered the refractive index profile by a smooth spline curve interpolated through a set of nine random points spread in the interval from -0.06 to 0.06. Therefore, for each simulation, we attained a slightly different profile shape, for which the merit function was optimized with respect to the layer thickness. The search for the optimum profile was done by 5000 simulations.

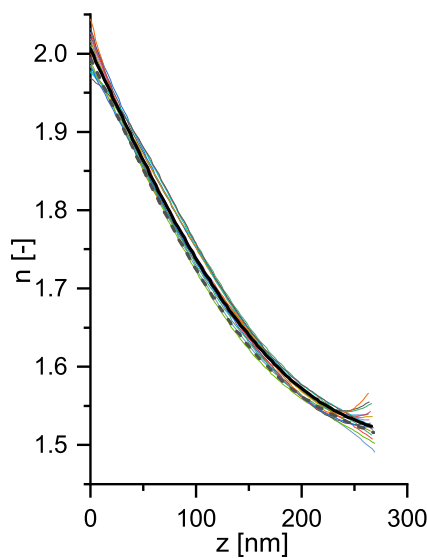


Figure 4.2: Gradient spatial profiles of refractive index describing the measured experimental data derived by a random optimization (color lines) and simple polynomial optimization (black lines). See the reprint of Ref. [76] for more details.

The curves with the lowest merit function value are shown in Figure 4.2 (colored lines) together with two curves optimized to their offset and quadratic shape from the expected profile (black lines). The spline interpolation of the random curves caused the curves to highly differ close to the layer edges, which is an artifact of the used approach. Nevertheless, the curves significantly differ even in their central part. We can observe that refractive index profiles varying by as much as 0.03 can describe the measured optical response very well.

### Optical monitoring of gradient thin films

Our results reveal a wide variety of profiles, which can reproduce even the extensive experimental set of data. For this reason, the identification of potential instabilities in the deposition or changes in the profile would be challenging. A natural step forward is to gain better precision by depositing multiple gradients or by depositing a different targeted gradient profile. This line of research is currently being studied, and we expect it to provide a deeper insight into the properties of the gradient layers.

### 4.3.2 Second harmonic generation in thin films

One of the possible ways to enhance the durability of the optical coating is to improve the quality of interfaces in the coating. This, in turn, brings the need for a reliable nondestructive characterization of interfaces in the coating, which is possible for single-layer systems by using SHG. Therefore, we built an experimental setup, which allowed us to track SHG from fs laser pulses (1028 nm, Yb:YAG) in a thin layer. The setup allowed us to measure both in the transmission and reflection mode with a varying incident angle in the range of 0–70 degrees in the transmission mode and 20–70 degrees in the reflection mode. It was possible to set the linear polarization of the incident fundamental beam and select S or P polarization of the SHG.



## SHG in the Si<sub>3</sub>N<sub>4</sub> layers

As the testing sample, we studied the Si<sub>3</sub>N<sub>4</sub> layers deposited by dual ion beam sputtering on the Si substrate. The SHG studies of Si<sub>3</sub>N<sub>4</sub> are frequently published, and this material is known to generate SHG [69, 74]. However, the conclusions of these studies are often controversial. Studies of the thin layers often report on the bulk dipole contribution from the layer itself [74], while other reports ascribe the SHG to the Si<sub>3</sub>N<sub>4</sub> – Si interface [77, 78]. Unlike in the previous measurements, our ability to trace angle-dependent SHG generation in the reflective mode made it possible to create a link between these two cases and to study Si<sub>3</sub>N<sub>4</sub> layers on a Si substrate.

We deposited three samples of Si<sub>3</sub>N<sub>4</sub> layer on the Si substrate, where the layer thickness was 600 nm, 1510 nm, and 3890 nm. The linear optical response of the samples was characterized based on the global fitting described in the previous section, Section 4.3.1. For all three samples, we used the same optical model to evaluate the local electric field in the layers and the corresponding SHG. SHG is calculated based on Green's function approach, where we first calculate the SHG response of a single infinitely thin polarization sheet. Subsequently, we can derive the interface SHG as a response from two polarization sheets on the layer surface and layer–substrate interface, and we adopted the calculation by Gielis et al. [65]. The bulk SHG is derived by integrating the polarization sheet response along with the layer thickness, and we used the model derived by Koskinen et al. [74].

The SHG signal for s and p polarization  $E_{SHG}^{s/p}$  can be expressed in general as:

$$\begin{aligned} E_{SHG}^p &= f(e^p)^2 + g(e^s)^2 \\ E_{SHG}^s &= h e^p e^s \end{aligned} \quad (4.3)$$

Where the factors  $f$ ,  $g$ , and  $h$  can be calculated based on the matrix  $\Omega$  set by interference of multiple reflections in the coating. Therefore, the relation to the respective non-linear  $\chi^{(2)}$  components is determined based on incident angle  $\Theta$ , layer thickness  $D$ , fundamental wavelength  $\lambda_F$ , and refractive index for the fundamental and SHG wavelength ( $n_F$ ,  $n_S$ ):

$$\begin{bmatrix} f \\ g \\ h \end{bmatrix} = \Omega(\Theta, D, n_F, n_S, \lambda_F) \begin{bmatrix} \chi_{zzz}^{(2)} \\ \chi_{zxx}^{(2)} \\ \chi_{zxz}^{(2)} \end{bmatrix} \quad (4.4)$$

From Equations (4.3) and (4.4) it is possible to recalculate the measured SHG intensity into the relative  $\chi^{(2)}$  values. The absolute values can only be attained by measuring a sample with a known  $\chi^{(2)}$  values and by comparing the attained SHG value with the measured one. A sample commonly used for this purpose, including our measurements, is the Y-cut silica crystal plate.

We carried out SHG measurement on the samples of Si<sub>3</sub>N<sub>4</sub> layers with three different thicknesses (600 nm, 1510 nm, and 3890 nm). Owing to different interference patterns in the samples, we attained three different angle dependencies of the interface and bulk SHG signal. Therefore, we can disentangle the contribution from the two – see Figure 4.3. The fit, where we include only the contribution from the bulk dipole SHG, is depicted as a dashed red line. Especially for the thin layer of 600 nm, the bulk model predicts significantly different angle dependence. For this reason, we also included the SHG from the layer surface and the layer – substrate interface. The resulting fit (black lines) significantly improves the agreement between the measured and calculate angle dependence. The fit leads to the conclusion that the interface SHG occurred dominantly on the Si<sub>3</sub>N<sub>4</sub> – Si interface, while the Si<sub>3</sub>N<sub>4</sub> – air interface contribution was negligible.



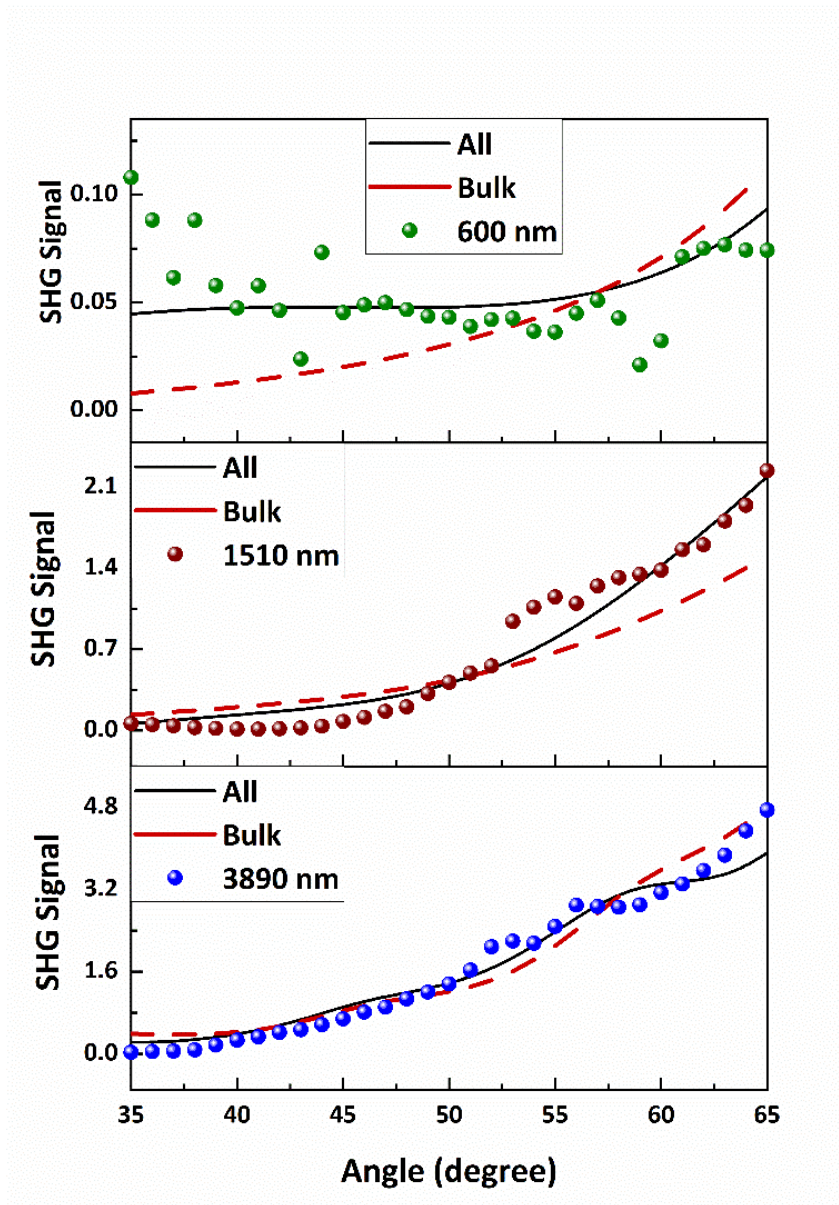


Figure 4.3: Angle dependent SHG responses from  $\text{Si}_3\text{N}_4$  thin films on Si substrate. Film thickness was: upper panel – 600 nm, middle panel – 1510 nm, and lower panel – 3890 nm, respectively. The solid black lines correspond to the fitted data by taking accounts of all contributions, whereas the dashed red lines represents corresponding fitting with bulk contribution only. Figure was adopted from Ref. [79] following the author rights policy of IOP Publishing Ltd.

At the same time, an efficient bulk dipole SHG from a “homogeneous”  $\text{Si}_3\text{N}_4$  layer is unexpected since the inverse symmetry should now allow such a process to occur. We can speculate that a local variation in stoichiometry and crystallinity can induce such an effect. Otherwise, we should observe the main contribution to originate from the electric quadrupoles and magnetic dipoles. It is worth noting that the quadrupole contribution can be separated into three independent terms. One cannot occur in our sample, one is indistinguishable from the interface contribution, and it is included in our model. The third term was not taken into account, but it was shown to provide a minor correction of the measured angle dependence.

Our results provide a link between the previously published measurements on the  $\text{Si}_3\text{N}_4$  layers deposited on quartz substrates and  $\text{Si}_3\text{N}_4$  – Si nanostructures [74, 77]. In the systems without any  $\text{Si}_3\text{N}_4$  – Si interface, the bulk dipole contribution from the layer is dominant. However, in the microstructures, on the contrary, thin  $\text{Si}_3\text{N}_4$  structure generates only small bulk contribution, and the SHG on the  $\text{Si}_3\text{N}_4$  – Si interface is dominating.

A detailed description of these results can be found in the reprint of Ref. [79].

## 4.4 Outlook

### 4.4.1 Second harmonic generation in thin films

The presented measurements of SHG in the thin film represent an initial stage of the development. Compared to the present results, we can currently attain approximately 10-times higher signal-to-noise ratio, and the experimental setup still offers room for optimization. Therefore, we can also attain a signal in the thinner layers on the fused silica substrate, where the signal level is lower than for the layers on the Si substrate. Nevertheless, even for superb data quality, we cannot realistically retrieve distinct SHG contributions in a complex system, where the model would introduce many unknown fitted parameters of the quadrupole response.

In general accordance, the wise use of the interference caused by buried interfaces is the key to disentangling various sources of SFG. In our particular case, we used three different layer thicknesses leading to three different interference patterns to extract the information of interest. Attention so far has been directed towards scanning the measured “system” in terms of wavelength (frequencies), layer thicknesses (i.e., optical paths), incident angles, or the necessity to create a precise model of the spectral features. However, an approach that has stayed out of the spotlight and has the potential to resolve the SFG source even in complex systems is the use of the temporal profile of the driving pulses.

Unlike a short compressed pulse, the random pulse carries a unique code formed by a randomly varying phase for each spectral component. SFG combines this code with an interference-induced footprint, which is unique for each interface and bulk. Uniqueness is caused by the fact that a random pulse features a different intensity temporal pattern at each spot of the sample and, therefore, the origin of the SFG can be computationally reconstructed by probing the system with many different pulses (codes).

### 4.4.2 Optical characterization of gradient thin films

We currently study the possible ways to improve the sensitivity of the refractive index model to the experimental data. This would, in turn, provide us with improved precision in the gradient profile extraction. Many different routes, including tuning the gradient layer profile, thickness, or periodicity, are available, and we systematically explore these options.

## 4.5 Summary

This chapter outlines some of the activities bounded by the effort towards improved robustness of optical coating. Since the most fragile part of the coating are the interfaces between the layers, we focused on two complementary approaches to avoid the issues.

Firstly, we studied the deposition of the layers, where the interfaces are replaced by a gradual change in the refractive index, i.e., gradient layers. We focused on one of the most used materials  $\text{SiO}_x\text{N}_y$ , which can be easily deposited with our deposition chambers. However, the deposition of the material for optical coating requires deep knowledge about the material's optical properties and the stability of the deposition process. We were, therefore, interested in the possibility of creating a thorough optical characterization in a similar way, as it is done for the standard layer.

We demonstrate that even by using an extensive dataset, combining several characterization methods, we cannot determine the correct refractive index profile with a precision better than 0.03. At the same time, our results show that some approaches to profile optimization, such as profile offset fit, can suggest that the precision is seemingly an order of magnitude better. This is because the complex multidimensional optimization landscape (9 parameters in our case) has many local minima that are locally sharp, yet all of them describe equally well the measured optical response [76].

In the next step, we will propose a more complex periodic shape of the refractive index profile. By optimizing this profile, we will be able to reach better precision and gain insight into the parameters and stability of the deposition process.

The second approach to improve the durability of optical coating is to develop a method to study the interface properties. For this reason, we built a setup for SHG in the thin films. This method is selectively sensitive to interfaces between homogeneous materials. However, the total signal consists of contribution from both the bulk and interface, as we demonstrated in our measurements of three  $\text{Si}_3\text{N}_4$  layers deposited on Si substrate. Currently, the contribution can be discerned with limited precision by using a set of measurements on a batch of single-layer samples with several layer thicknesses [79].

These results allowed us to draw conclusions about specific interfaces with stable, reproducible properties. However, this is not sufficient for the desired sample characterization. In such an application, a measurement of a single sample would need to provide information about the interface quality.

To make this real, we propose a new approach to SF spectroscopy, where we will use randomly modulated femtosecond pulses. The use of random pulses alters the contribution of each SHG origin depending on the actual pulse shape. Therefore, by using a set of many different random pulses, we can retrieve the interface and bulk contribution even for a single sample and, potentially, even for complex thin layer structures.

## Chapter 5

# Conclusions

This thesis summarized a major part of the work carried out between the years 2016–2021 within my Group of Computational Spectroscopy and Imaging at research center TOPTEC, Institute of Plasma Physics of the Czech Academy of Sciences. The original motivation to introduce a new way of compressive imaging in laser spectroscopy described in Chapter 2 triggered the idea of using a similar concept for the time-resolved measurement, which was presented in Section 2.3.4 for the PL decay on the microsecond timescale denoted as RATS method, and in Chapter 3 for the ultrafast processes on the femtosecond timescale.

The natural direction to apply the new methods has been the study of thin-film coating, which was an important part of my interest at TOPTEC. Therefore, the ultrafast spectroscopy methods are targeted to the femtosecond sonar experiment described in Section 3.3.4 and the femtosecond pulses can be utilized to carry out second-harmonic generation spectroscopy of interfaces in the thin films presented in Chapter 4. Nevertheless, the efficient application of random femtosecond pulses, which are needed for the planned experiments, requires deep knowledge of pulse shaping and characterization. Therefore, these topics cover a major part of my recent research, and they are described in Chapter 3.

To shortly summarize the main achievements described in this thesis, we were able to demonstrate compressive imaging of ultrafast processes with temporal resolution below 50 fs by using a simple modification of standard pump-probe setup. We also created an entirely new approach to photoluminescence decay measurement and fluorescence lifetime imaging (FLIM), which works with an unmatched simplicity compared to the standard setups.

By a detailed analysis of the factors governing the characterization and shaping of femtosecond pulses, we were able to attain a high-fidelity generation of complex pulses, which can be used to track ultrafast transient changes of transmittance or reflectance on the femtosecond timescale, even for relative changes on the scale  $10^{-5}$ .

We built a setup able to track second harmonic generation in the thin films and thus to characterize the second-order nonlinear response from interfaces and the bulk of single-layer samples. Finally, we developed an approach to simultaneous retrieval of the gradient refractive index profile from a broad set of experimental techniques.

As it is well known, each answer always brings forth several new questions. Also, here, the presented research cannot be taken as an attempt to provide a definite solution to the studied issues. Instead, each of the major results stands at the beginning of a research direction.

Namely, both the second-harmonic generation experiment and femtosecond sonar open the pathway towards efficient characterization of buried interfaces in thin films. The use of random pulses will enable us to extract much more detailed information about the interface and its morphology. For the gradient thin films, their deposition and reliable characterization are the

enabling steps to optical coating, where the gradient shape will be tuned to increase the coating durability. For instance, we can tune the gradient profile to attain a low electric field intensity on the critical spots and, thus, deposit layers with a high laser-induced damage threshold. Finally, the RATS method can be optimized to reach a spatial and temporal resolution, while its sensitivity will be much higher compared to the contemporary methods. Moreover, the use of complex excitation temporal patterns opens the possibility to use alternative ways to derive photoluminescence lifetimes from the measurements.

Each of the listed topics will be addressed by the Group of Computational Spectroscopy and Imaging in the upcoming years.



# Bibliography

- [1] A. Stern, *Optical Compressive Imaging*. Boca Ranton: CRC Press, 2017.
- [2] D. J. Brady, *Optical Imaging and Spectroscopy*. John Wiley and Sons, Inc., 2009.
- [3] E. Candes and M. Wakin, “An Introduction To Compressive Sampling,” *IEEE Signal Processing Magazine*, vol. 25, no. 2, pp. 21–30, 2008.
- [4] D. Thapa, K. Raahemifar, and V. Lakshminarayanan, “Less is more: compressive sensing in optics and image science,” *Journal of Modern Optics*, vol. 62, pp. 415–429, mar 2015.
- [5] L. Gao, J. Liang, C. Li, and L. V. Wang, “Single-shot compressed ultrafast photography at one hundred billion frames per second,” *Nature*, vol. 516, pp. 74–77, dec 2014.
- [6] A. Wagadarikar, R. John, R. Willett, and D. Brady, “Single disperser design for coded aperture snapshot spectral imaging,” *Applied Optics*, vol. 47, pp. B44–B51, apr 2008.
- [7] O. Denk, A. Musiienko, and K. Židek, “Differential single-pixel camera enabling low-cost microscopy in near-infrared spectral region,” *Optics Express*, vol. 27, p. 4562, feb 2019.
- [8] L. Klein and K. Židek, “Collection of micromirror-modulated light in the single-pixel broadband hyperspectral microscope,” *Review of Scientific Instruments*, vol. 91, no. 6, p. 63701, 2020.
- [9] J. Hlubuček, J. Lukeš, J. Václavík, and K. Židek, “Enhancement of CASSI by a zero-order image employing a single detector,” *Applied Optics*, vol. 60, no. 5, pp. 1463–1469, 2021.
- [10] W. Demtröder, *Laser Spectroscopy: Basic Concepts and Instrumentation*, vol. 1. Springer-Verlag Berlin Heidelberg, 2003.
- [11] M. Aeschlimann, T. Brixner, A. Fischer, C. Kramer, P. Melchior, W. Pfeiffer, C. Schneider, C. Strüber, P. Tuchscherer, and D. V. Voronine, “Coherent Two-Dimensional Nanoscopy,” *Science (New York, N.Y.)*, vol. 1723, pp. 1723–1726, aug 2011.
- [12] D. L. Donoho, “Compressed sensing,” *IEEE Transactions on Information Theory*, vol. 52, pp. 1289–1306, apr 2006.
- [13] M. F. Duarte, M. A. Davenport, D. Takbar, J. N. Laska, T. Sun, K. F. Kelly, and R. G. Baraniuk, “Single-pixel imaging via compressive sampling: Building simpler, smaller, and less-expensive digital cameras,” *IEEE Signal Processing Magazine*, vol. 25, no. 2, pp. 83–91, 2008.
- [14] X. An, M. S. Brittelle, P. T. Lauzier, J. R. Gord, S. Roy, G.-H. Chen, and S. T. Sanders, “Demonstration of temperature imaging by H<sub>2</sub>O absorption spectroscopy using compressed sensing tomography,” *Applied Optics*, vol. 54, p. 9190, nov 2015.





- [15] G. R. Arce, D. J. Brady, L. Carin, H. Arguello, and D. S. Kittle, “Compressive coded aperture spectral imaging: An introduction,” *IEEE Signal Processing Magazine*, vol. 31, pp. 105–115, jan 2014.
- [16] P. Llull, X. Liao, X. Yuan, J. Yang, D. Kittle, L. Carin, G. Sapiro, and D. J. Brady, “Coded aperture compressive temporal imaging,” *Optics Express*, vol. 21, p. 10526, may 2013.
- [17] K. Židek, M. Abdellah, K. Zheng, and T. Pullerits, “Electron relaxation in the CdSe quantum dot-ZnO composite: Prospects for photovoltaic applications,” *Scientific Reports*, vol. 4, no. 1, pp. 1–8, 2014.
- [18] K. Židek, K. Zheng, C. S. Ponseca, M. E. Messing, L. R. Wallenberg, P. Chábera, M. Abdellah, V. Sundström, and T. T. Pullerits, “Electron Transfer in Quantum-Dot-Sensitized ZnO Nanowires: Ultrafast Time-Resolved Absorption and Terahertz Study,” *Journal of the American Chemical Society*, vol. 134, pp. 12110–7, jul 2012.
- [19] D. M. Jonas, “Two-Dimensional Femtosecond Spectroscopy,” *Annual Review of Physical Chemistry*, vol. 54, pp. 425–463, jan 2003.
- [20] D. J. Starling, I. Storer, and G. A. Howland, “Compressive sensing spectroscopy with a single pixel camera,” *Applied Optics*, vol. 55, no. 19, p. 5198, 2016.
- [21] W. L. Chan, K. Charan, D. Takhar, K. F. Kelly, R. G. Baraniuk, and D. M. Mittleman, “A single-pixel terahertz imaging system based on compressed sensing,” *Applied Physics Letters*, vol. 93, no. 12, p. 121105, 2008.
- [22] K. Židek, O. Denk, and J. Hlubuček, “Lensless Photoluminescence Hyperspectral Camera Employing Random Speckle Patterns,” *Scientific Reports*, vol. 7, no. 1, pp. 1–7, 2017.
- [23] B. Frieden, *Laser speckle and related phenomena*, vol. 20 of *Topics in Applied Physics*. Berlin, Heidelberg: Springer Berlin Heidelberg, dec 1984.
- [24] J. W. Goodman, “Statistical properties of laser speckle patterns,” *Laser Speckle and Related Phenomena*, vol. 6, pp. 9–75, 1975.
- [25] C. Rullière, *Femtosecond Laser Pulses: Principles and Experiments*. Springer New York, 2003.
- [26] M. C. Fischer, J. W. Wilson, F. E. Robles, and W. S. Warren, “Invited Review Article: Pump-probe microscopy,” *Review of Scientific Instruments*, vol. 87, p. 031101, mar 2016.
- [27] O. Denk, K. Zheng, D. Zigmantas, and K. Židek, “Compressive imaging of transient absorption dynamics on the femtosecond timescale,” *Optics Express*, vol. 27, p. 10234, apr 2019.
- [28] J. Juneek, L. Ondič, and K. Židek, “Random temporal laser speckles for the robust measurement of sub-microsecond photoluminescence decay,” *Optics Express*, vol. 28, no. 8, p. 12363, 2020.
- [29] F. Trojánek, K. Neudert, K. Židek, K. Dohnalová, I. Pelant, and P. Malý, “Femtosecond photoluminescence spectroscopy of silicon nanocrystals,” *Physica Status Solidi (C) Current Topics in Solid State Physics*, vol. 3, pp. 3873–3876, dec 2006.
- [30] J. R. Lakowicz, *Principles of fluorescence spectroscopy*. Springer, 2006.



- [31] C. Li, W. Yin, and Y. Zhang, “User’s guide for TVAL3: TV minimization by augmented lagrangian and alternating direction algorithms,” *CAAM report*, vol. 20, pp. 46–47, 2009.
- [32] J. Junek and K. Židek, “Fluorescence lifetime imaging via spatio-temporal speckle patterns in a single-pixel camera configuration,” *Optics Express*, vol. 29, no. 4, pp. 5538–5551, 2021.
- [33] G. Berden and R. Engeln, *Cavity Ring-Down Spectroscopy: Techniques and Applications*. John Wiley and Sons, 2010.
- [34] N. Lenngren, M. A. Abdellah, K. Zheng, M. J. Al-Marri, D. Zigmantas, K. Židek, and T. Pulherits, “Hot electron and hole dynamics in thiol-capped CdSe quantum dots revealed by 2D electronic spectroscopy,” *Physical Chemistry Chemical Physics*, vol. 18, no. 37, pp. 26199–26204, 2016.
- [35] A. Devos and R. Côte, “Strong oscillations detected by picosecond ultrasonics in silicon: Evidence for an electronic-structure effect,” *Physical Review B - Condensed Matter and Materials Physics*, vol. 70, no. 12, pp. 1–6, 2004.
- [36] X. Ma, J. Dostál, T. Brixner, and A. Hubland, “Electronic Spectroscopy Using Hollow-Core Fiber Compression,” *Optics Express*, vol. 24, pp. 20781–20791, sep 2016.
- [37] A. M. Weiner, “Ultrafast optical pulse shaping: A tutorial review,” *Optics Communications*, vol. 284, pp. 3669–3692, jul 2011.
- [38] A. Tajalli, D. J. McCabe, D. R. Austin, I. A. Walmsley, and B. Chatel, “Characterization of the femtosecond speckle field of a multiply scattering medium via spatio-spectral interferometry,” *Journal of the Optical Society of America B*, vol. 29, p. 1146, jun 2012.
- [39] J. Aulbach, *Spatiotemporal control of light in turbid media*. 2013.
- [40] R. Trebino, K. W. DeLong, D. N. Fittinghoff, J. N. Sweetser, M. A. Krumbügel, B. A. Richman, and D. J. Kane, “Measuring ultrashort laser pulses in the time-frequency domain using frequency-resolved optical gating,” *Review of Scientific Instruments*, vol. 68, pp. 3277–3295, jun 1997.
- [41] J. Ratner, G. Steinmeyer, R. Bartels, T. C. Wong, M. Alderman, and R. Trebino, “The coherent artifact in modern pulse measurements,” in *Frontiers in Optics, FIO 2012*, vol. 37, p. 2874, Optical Society of America, jul 2012.
- [42] M. Rhodes, G. Steinmeyer, J. Ratner, and R. Trebino, “Pulse-shape instabilities and their measurement,” *Laser & Photonics Reviews*, vol. 7, pp. 557–565, jul 2013.
- [43] S. Linden, H. Giessen, and J. Kuhl, “XFROG - A new method for amplitude and phase characterization of weak ultrashort pulses,” *Physica Status Solidi (B) Basic Research*, vol. 206, pp. 119–124, mar 1998.
- [44] C. Iaconis and I. A. Walmsley, “Spectral phase interferometry for direct electric-field reconstruction of ultrashort optical pulses,” *Optics Letters*, vol. 23, p. 792, may 1998.
- [45] X. Gu, L. Xu, M. Kimmel, E. Zeek, P. O’Shea, A. P. Shreenath, R. Trebino, and R. S. Windeler, “Frequency-resolved optical gating and single-shot spectral measurements reveal fine structure in microstructure-fiber continuum,” *Optics Letters*, vol. 27, no. 13, p. 1174, 2002.



- [46] T. C. Wong, M. Rhodes, and R. Trebino, “Single-shot measurement of the complete temporal intensity and phase of supercontinuum,” *Optica*, vol. 1, pp. 119–124, Aug 2014.
- [47] P. Sidorenko, O. Lahav, Z. Avnat, and O. Cohen, “Ptychographic reconstruction algorithm for frequency-resolved optical gating: super-resolution and supreme robustness,” *Optica*, vol. 3, p. 1320, dec 2016.
- [48] N. C. Geib, M. Zilk, T. Pertsch, and F. Eilenberger, “Common pulse retrieval algorithm: a fast and universal method to retrieve ultrashort pulses,” *Optica*, vol. 6, p. 495, apr 2019.
- [49] P. Veselá and K. Žídek, “Influence of the delay line jitter on the SHG FROG reconstruction,” *Optics Express*, vol. 29, no. 3, pp. 4392–4404, 2021.
- [50] R. Trebino, *Frequency-Resolved Optical Gating: The Measurement of Ultrashort Laser Pulses*. Springer US, 2000.
- [51] G. Tamošauskas, G. Beresnevičius, D. Gadonas, and A. Dubietis, “Transmittance and phase matching of BBO crystal in the 3–5  $\mu\text{m}$  range and its application for the characterization of mid-infrared laser pulses,” *Optical Materials Express*, vol. 8, p. 1410, jun 2018.
- [52] P. O’Shea, M. Kimmel, X. Gu, and R. Trebino, “Increased-bandwidth in ultrashort-pulse measurement using an angle-dithered nonlinear-optical crystal,” *Optics Express*, vol. 7, p. 342, nov 2000.
- [53] E. Brühl, M. Motzkus, and T. Buckup, “Minimization of 1/f phase noise in liquid crystal masks for reliable femtosecond pulse shaping,” *Optics Express*, Vol. 25, Issue 19, pp. 23376–23386, vol. 25, pp. 23376–23386, sep 2017.
- [54] F. Frei, A. Galler, and T. Feurer, “Space-time coupling in femtosecond pulse shaping and its effects on coherent control,” *Journal of Chemical Physics*, vol. 130, no. 3, 2009.
- [55] J. Vaughan, T. Feurer, K. Stone, and K. Nelson, “Analysis of replica pulses in femtosecond pulse shaping with pixelated devices,” *Optics Express*, vol. 14, p. 1314, feb 2006.
- [56] S. Moser, M. Ritsch-Marte, and G. Thalhammer, “Model-based compensation of pixel crosstalk in liquid crystal spatial light modulators,” *Optics Express*, vol. 27, no. 18, p. 25046, 2019.
- [57] M. Miranda, C. L. Arnold, T. Fordell, F. Silva, B. Alonso, R. Weigand, A. L’Huillier, and H. Crespo, “Characterization of broadband few-cycle laser pulses with the d-scan technique,” *Optics Express*, vol. 20, p. 18732, aug 2012.
- [58] M. Guesmi, P. Veselá, and K. Žídek, “Dispersion scan frequency resolved optical gating for evaluation of pulse chirp variation,” *arXiv preprint arXiv:2102.09307*, 2021.
- [59] E. Pontecorvo, M. Ortolani, D. Polli, M. Ferretti, G. Ruocco, G. Cerullo, and T. Scopigno, “Visualizing coherent phonon propagation in the 100 GHz range: A broadband picosecond acoustics approach,” *Applied Physics Letters*, vol. 98, no. 1, pp. 98–100, 2011.
- [60] J. M. Bioucas-Dias and M. A. Figueiredo, “A new TwIST: Two-step iterative shrinkage/thresholding algorithms for image restoration,” *IEEE Transactions on Image Processing*, vol. 16, pp. 2992–3004, dec 2007.



- [61] Z. Yu, H. He, W. Sun, H. Qi, M. Yang, Q. Xiao, and M. Zhu, “Damage threshold influenced by the high absorption defect at the film–substrate interface under ultraviolet laser irradiation,” *Optics Letters*, vol. 38, p. 4308, nov 2013.
- [62] R. P. Netterfield, M. Gross, F. N. Baynes, K. L. Green, G. M. Harry, H. Armandula, S. Rowan, J. Hough, D. R. M. Crooks, M. M. Fejer, R. Route, and S. D. Penn, “Low mechanical loss coatings for LIGO optics: progress report,” in *Advances in Thin-Film Coatings for Optical Applications II* (M. L. Fulton and J. D. T. Kruschwitz, eds.), vol. 5870, p. 58700H, aug 2005.
- [63] Y. R. Shen, *Fundamentals of Sum-Frequency Spectroscopy*. Cambridge University Press, 2016.
- [64] H. Macleod, *Thin-film optical filters: 3rd edition*. Taylor and Francis Group, 2002.
- [65] J. J. H. Gielis, P. M. Gevers, I. M. P. Aarts, M. C. M. van de Sanden, and W. M. M. Kessels, “Optical second-harmonic generation in thin film systems,” *Journal of Vacuum Science & Technology A: Vacuum, Surfaces, and Films*, vol. 26, pp. 1519–1537, nov 2008.
- [66] H. Held, A. I. Lvovsky, X. Wei, and Y. R. Shen, “Bulk contribution from isotropic media in surface sum-frequency generation,” *Physical Review B*, vol. 66, no. 20, p. 205110, 2002.
- [67] P. T. Wilson, K. A. Briggman, W. E. Wallace, J. C. Stephenson, and L. J. Richter, “Selective study of polymer/dielectric interfaces with vibrationally resonant sum frequency generation via thin-film interference,” *Applied Physics Letters*, vol. 80, no. 17, pp. 3084–3086, 2002.
- [68] S. Lettieri, F. Merola, P. Maddalena, C. Ricciardi, and F. Giorgis, “Second harmonic generation analysis in hydrogenated amorphous silicon nitride thin films,” *Applied Physics Letters*, vol. 90, no. 2, p. 021919, 2007.
- [69] T. Ning, H. Pietarinen, O. Hyvärinen, J. Simonen, G. Genty, and M. Kauranen, “Strong second-harmonic generation in silicon nitride films,” *Applied Physics Letters*, vol. 100, p. 161902, apr 2012.
- [70] D. B. O’Brien and A. M. Massari, “Modeling multilayer thin film interference effects in interface-specific coherent nonlinear optical spectroscopies,” *Journal of the Optical Society of America B*, vol. 30, no. 6, p. 1503, 2013.
- [71] M. S. Azam, C. Cai, and D. K. Hore, “Selective Probing of Thin-Film Interfaces Using Internal Reflection Sum-Frequency Spectroscopy,” *Journal of Physical Chemistry C*, vol. 123, p. 23535–23544, 2019.
- [72] A. P. Moon, R. Pandey, J. A. Bender, D. E. Cotton, B. A. Renard, and S. T. Roberts, “Using Heterodyne-Detected Electronic Sum Frequency Generation to Probe the Electronic Structure of Buried Interfaces,” *Journal of Physical Chemistry C*, vol. 121, no. 34, pp. 18653–18664, 2017.
- [73] P. M. Kearns, D. B. Óbrien, and A. M. Massari, “Optical Interference Enhances Nonlinear Spectroscopic Sensitivity: When Light Gives You Lemons, Model Lemonade,” *Journal of Physical Chemistry Letters*, vol. 7, no. 1, pp. 62–68, 2016.
- [74] K. Koskinen, R. Czaplicki, A. Slablab, T. Ning, A. Hermans, B. Kuyken, V. Mittal, G. S. Murugan, T. Niemi, R. Baets, and M. Kauranen, “Enhancement of bulk second-harmonic

- generation from silicon nitride films by material composition,” *Optics Letters*, vol. 42, p. 5030, aug 2017.
- [75] B. Blanckenhagen, D. Tonova, and J. Ullmann, “Application of the Tauc-Lorentz formulation to the interband absorption of optical coating materials,” *Applied Optics*, vol. 41, no. 16, p. 3137, 2002.
  - [76] V. Kanclíř, J. Václavík, and K. Žídek, “Precision of silicon oxynitride refractive-index profile retrieval using optical characterization,” *arXiv preprint arXiv:2012.04260*, 2020.
  - [77] M. Cazzanelli, F. Bianco, E. Borga, G. Pucker, M. Ghulinyan, E. Degoli, E. Luppi, V. Véniard, S. Ossicini, D. Modotto, S. Wabnitz, R. Pierobon, and L. Pavesi, “Second-harmonic generation in silicon waveguides strained by silicon nitride,” *Nature Materials*, vol. 11, no. 2, pp. 148–154, 2012.
  - [78] J. S. Levy, M. A. Foster, A. L. Gaeta, and M. Lipson, “Harmonic generation in silicon nitride ring resonators,” *Optics Express*, vol. 19, p. 11415, jun 2011.
  - [79] N. K. Das, V. Kanclíř, P. Mokry, and K. Zidek, “Bulk and interface second harmonic generation in the Si<sub>3</sub>N<sub>4</sub> thin films deposited via ion beam sputtering,” *Journal of Optics*, vol. 23, p. 024003, 2021.



## Chapter 6

# Reprints

In this chapter, I provide reprints of my work summarized within the thesis. Namely, the reprints include in the respective order:

- O. Denk, K. Zheng, D. Zigmantas, and K. Žídek, “Compressive imaging of transient absorption dynamics on the femtosecond timescale,” *Optics Express*, vol. 27, p. 10234, apr 2019

**My contribution:** I proposed and designed the experiment, took part in the experimental work and data processing, and supervised the article preparation.

- J. Junek, L. Ondič, and K. Žídek, “Random temporal laser speckles for the robust measurement of sub-microsecond photoluminescence decay,” *Optics Express*, vol. 28, no. 8, p. 12363, 2020

**My contribution:** I proposed the experiment and carried out initial simulations; contributed to the experimental work and setup optimization; supervised data processing and the article preparation.

- J. Junek and K. Žídek, “Fluorescence lifetime imaging via spatio-temporal speckle patterns in a single-pixel camera configuration,” *Optics Express*, vol. 29, no. 4, pp. 5538–5551, 2021

**My contribution:** I proposed the experiment and assisted the experimental work, took part in the data processing and image retrieval, and supervised the article preparation.

- K. Žídek, O. Denk, and J. Hlubuček, “Lensless Photoluminescence Hyperspectral Camera Employing Random Speckle Patterns,” *Scientific Reports*, vol. 7, no. 1, pp. 1–7, 2017

**My contribution:** I proposed and designed the experiment, I carried vast majority of the experimental work and data processing, and wrote the article.

- P. Veselá and K. Žídek, “Influence of the delay line jitter on the SHG FROG reconstruction,” *Optics Express*, vol. 29, no. 3, pp. 4392–4404, 2021

**My contribution:** I proposed the simulation, partly evaluated the data, and co-authored the article.

- M. Guesmi, P. Veselá, and K. Žídek, “Dispersion scan frequency resolved optical gating for evaluation of pulse chirp variation,” *arXiv preprint arXiv:2102.09307*, 2021

**My contribution:** I proposed and designed the experiment, constructed a major part of the experimental setup, developed a model for chirp variation, took part in the experimental work and data processing, and supervised the article preparation.



- V. Kanclíř, J. Václavík, and K. Žídek, “Precision of silicon oxynitride refractive-index profile retrieval using optical characterization,” *arXiv preprint arXiv:2012.04260*, 2020

**My contribution:** I proposed and designed the experiment and simultaneous data fit, took part in the experimental work, data processing and fitting; supervised the article preparation.

- N. K. Das, V. Kanclíř, P. Mokry, and K. Zidek, “Bulk and interface second harmonic generation in the Si<sub>3</sub>N<sub>4</sub> thin films deposited via ion beam sputtering,” *Journal of Optics*, vol. 23, p. 024003, 2021

**My contribution:** I proposed and designed the experiment, constructed the experimental setup, created numerical models for the signal evaluation, took part in the experimental work and data processing, and supervised the article preparation





# Compressive imaging of transient absorption dynamics on the femtosecond timescale

ONDŘEJ DENK,<sup>1</sup> KAIBO ZHENG,<sup>2,3</sup> DONATAS ZIGMANTAS,<sup>2</sup> AND KAREL ŽÍDEK<sup>1,\*</sup>

<sup>1</sup>Regional Centre for Special Optics and Optoelectronic Systems (TOPTEC), Institute of Plasma Physics, Academy of Sciences of the Czech Republic, Za Slovankou 1782/3, 182 00 Prague 8, Czech Republic

<sup>2</sup>Chemical Physics, Lund University, PO Box, Lund SE-22100, Sweden

<sup>3</sup>Department of Chemistry, Technical University of Denmark, DK-2800 Kongens Lyngby, Denmark

\*zidek@ipp.cas.cz

**Abstract:** Femtosecond spectroscopy is an important tool used for tracking rapid photoinduced processes in a variety of materials. To spatially map the processes in a sample would substantially expand the method's capabilities. This is, however, difficult to achieve, due to the necessity of using low-noise detection and maintaining feasible data acquisition time. Here, we demonstrate realization of an imaging pump-probe setup, featuring sub-100 fs temporal resolution, by using a straightforward modification of a standard pump-probe technique, which uses a randomly structured probe beam. The structured beam, made by a diffuser, enabled us to computationally reconstruct the maps of transient absorption dynamics based on the concept of compressed sensing. We demonstrate the setup's functionality in two proof-of-principle experiments, where we achieve spatial resolution of 20  $\mu\text{m}$ . The presented concept provides a feasible route to imaging, by using the pump-probe technique and ultrafast spectroscopy in general.

© 2019 Optical Society of America under the terms of the [OSA Open Access Publishing Agreement](#)

## 1. Introduction

Ultrafast spectroscopy provides us with essential information about processes in many systems of interest, including semiconductor nanostructures, conjugated polymers, or light-harvesting biological complexes [1–5]. By using femtosecond (fs) pulses we can extract dynamics on the corresponding timescale and identify important parameters – for instance, to explore various factors limiting the lifetime of charge carriers in a solar cell [5]. Ultrafast spectroscopy has, therefore, established itself an indispensable tool in material and biological research.

The ability to carry out imaging of measured dynamics elevates the potential of the technique even higher [6]. By employing it one can, for instance, map and identify the “leaking” points of a solar cell, where the carriers rapidly recombine. However, implementation of imaging in ultrafast spectroscopy is a complex issue. We will illustrate this on the pump-probe (P-P) technique – an archetypal technique of ultrafast spectroscopy used to measure the kinetics of transient absorption (TA) or reflectance on the fs timescale [7]. In the P-P experiment, a strong pump pulse is used to excite photodynamics in a measured sample and the probe pulse, arriving with a certain delay, probes the photoinduced changes in the sample triggered by the pump pulse. The TA signal is measured as a difference in the probe beam intensity for the excited and unexcited sample. Since the measured relative probe change is often very weak, typically in the order of  $10^{-3}$  to  $10^{-6}$ , it is necessary to detect the probe intensity by using a low-noise detector with a high dynamic range, often in combination with a lock-in amplifier, or an equivalent approach. Usually, detection in a P-P setup is carried out by a photodiode array, a cooled line CCD coupled to a spectrograph, or simply a photodiode measuring the total probe intensity.

#357606

<https://doi.org/10.1364/OE.27.010234>

Journal © 2019

Received 15 Jan 2019; revised 2 Mar 2019; accepted 2 Mar 2019; published 28 Mar 2019





As far as imaging is concerned, all the commonly used detectors in P-P experiments are single-pixel detectors, which recover information from a single spot in the sample. A straightforward option to carry out imaging is to scan the position of the probe spot in the sample point-by-point [6,8,9]. However, by assuming that the acquisition time of a single datapoint takes mere 3 s (including data acquisition time, sample shift, and the data readout), we reach, for a  $100 \times 100$  pixel image, the total acquisition time of more than 8 hours. Clearly, measuring several TA maps can last well beyond the feasible time for the experimental setup or the stability of the measured sample. Another option which has been reported in literature consists in rebuilding the measurement apparatus to detect an image of the probe beam by using an array detector [10–14]. In this case, we gain an image of the sample in a single measurement. However, several drawbacks arise: (i) a suitable detector is an expensive piece of equipment; (ii) spectral information has to be sacrificed; (iii) only sufficiently high TA signal level can be measured.

A solution to the problem, which bypasses both the issues of array sensor and lengthy sample scanning, lies in the theory of compressed sensing (CS) and, more specifically, in compressive imaging [15,16]. We can utilize the fact that information contained in a common image is sparse. This means that in a certain basis, such as Fourier basis, the image can be expressed by using a data set where the vast majority of components are equal to zero or negligible. In other words, the actual information is contained in a small fraction of the components, which is a fact extensively used in digital image compression (JPEG compression). The CS theory makes it possible to exploit the image sparsity as early as during the image acquisition to minimize the acquisition time and, moreover, to revisit the entire approach to imaging.

One of the most used techniques of CS is denoted as single-pixel camera (SPC) [17]. Here, an image of interest is acquired by measuring the total intensity from a random combination of  $N$  image pixels. The total intensities measured for a sequence of  $M$  different random combinations provide us with enough information to computationally reconstruct the image – even for the cases, where  $M \ll N$ . We can, therefore, substantially reduce the number of measurements compared to the number of image pixels, yet we can capture the image by using a single-pixel detector. This advantage has been previously employed in various imaging setups ranging from microscopy, sum-frequency generation microscopy, to time-of-flight imaging [18–22].

In this article, we demonstrate the construction of an imaging P-P setup based on the concept of SPC. We exploited laser light coherence to generate random patterns (laser speckles), which are used to encode the P-P image [20]. Owing to that, the entire conversion of a standard P-P setup into the imaging one essentially consists in adding a diffuser on a motorized stage into the probe beam, along with a simple reference camera recording the speckle patterns. The use of the patterned probe beam together with a standard P-P detection provide us with the ability to computationally reconstruct an image of a TA signal with unmatched simplicity, while the required acquisition time is several times shorter compared to sample scanning. The functionality of our P-P imaging setup was verified on several proof-of-principle measurements. In this article we present imaging of a tilted pump beam gradually exciting a homogeneous sample of CdSe quantum dots and imaging of transient dynamics on a structured flat sample.

The presented experiment provides a simple tool for femtosecond ultrafast imaging, which can be used in a number of spectroscopic laboratories. As we will discuss in detail, compared to a sample scanning used on the same setup, the use of CS shortens the data acquisition time, resolves the sample microstructure at a long working distance of tens of centimeters, and makes it possible to drop an arbitrary subset of measurements from the data set. Moreover, under certain conditions the setup can be used for imaging of probe wavelengths in the infrared or THz spectral regions, where 2D array sensors are not commonly available.

## 2. Experimental setup

We built the P-P imaging setup, which is depicted in Fig. 1, by a minor modification of a classic low-noise P-P experimental setup, which we will hereafter call a ‘standard’ P-P setup. The standard setup has been used extensively to characterize a variety of samples on the fs and ps timescales [23,24]. We will first briefly describe the standard pump-probe setup and then the changes required to modify the setup into the imaging modality.

### 2.1. Standard low-noise pump-probe setup

We used two non-collinear optical parametric amplifiers (NOPAs) to convert seeding laser pulses (Light Conversion, Pharos 1030 nm) to ultrashort visible fs pulses. Two generated beams featuring the central wavelengths of 495 nm and 560 nm (see Fig. 2(A), solid lines) were used as a pump and a probe beam, respectively. The probe beam was directed through a time delay line to adjust the P-P delay. The laser repetition rate was set to 20 kHz in order to ensure that the testing samples return to their ground state before the arrival of the following pulse. The pump beam was modulated using an optical chopper.

The probe beam intensity at a sample was set for both the imaging and the standard setups to 1 nJ/pulse. The attained pump pulse energy of 40 nJ/pulse at a sample was fully used in the imaging experiment, because the beam covered a relatively large area of the sample (0.5-2 mm<sup>2</sup>, exc. energy density of 2-8 μJ/cm<sup>2</sup>). In the standard P-P setup the pump beam was attenuated to generate a TA signal level equal to the imaging setup.

The pump and probe pulses were compressed using a combination of chirp mirrors and prism compressors into ultrashort pulses with the FWHM of 21 fs and 22 fs, respectively. The pulse length was determined based on the second harmonic autocorrelation of the pulses – see Fig. 2(B). Analogously, the response function of the standard setup was acquired using a sum-frequency generation of the pump and probe pulses (FWHM 33 fs).

The pump and the probe pulses were focused onto a sample using spherical mirrors and the transmitted pump beam intensity was recorded by using a Si amplified photodiode (New Focus). The signal from the photodiode was digitized by using a data acquisition card and processed by the means of in-house lock-in detection analysis algorithm.

### 2.2. Conversion to the imaging setup

In the imaging setup in Fig. 1, the pump beam followed the standard P-P scheme. However, the sample was placed behind the focal plane of the focusing mirror to gain an excitation spot large enough to cover the area of interest for imaging. The used pump spot was elliptically shaped with approximately 1 × 0.5 mm dimensions.

The probe beam was focused by a spherical mirror onto a standard diffuser, giving rise to many laser wavefronts with random phases. The wavefronts form by their mutual interference a random speckle pattern which can be in the far-field regime considered as a spherical wave with a modulated intensity in various directions. Therefore, it was possible to collimate the speckle pattern into a beam by using an off-axis parabolic mirror. The mean size of the speckles in the collimated beam, i.e., the pattern fineness, is an important factor for the setup spatial resolution, as we showed in our previous work [20]. The fineness was determined by the size of the probe spot on the diffuser. The generating diffuser was placed on a motorized stage to attain a set of different speckle patterns by shifting the diffuser to different positions. An iris diaphragm was used to cut out the central part of the collimated speckle beam, which was reflected via a spherical mirror onto the sample. The sample was placed well before the focal plane of the focusing spherical mirror. Close to the sample, the patterned probe beam was partly reflected by a thin beam splitter (BK7 slide with an anti-reflective coating on one side) and a reference probe image was acquired by a reference camera. The camera was placed to match the sample – beam-splitter distance. However, since the sample was not in the beam waist proximity (Rayleigh range), the reference camera position could be set

roughly without losing a correlation between the sample and the reference speckle pattern [25]. The reference image was attained by a CMOS chip (IDS uEye) with a neutral density filter reducing the beam intensity.

To summarize, all that is required for the transformation of the standard P-P setup into the imaging one is the generation of a patterned probe beam using a diffuser on a motorized stage, and the use of a reference camera recording a reflected probe beam reference.

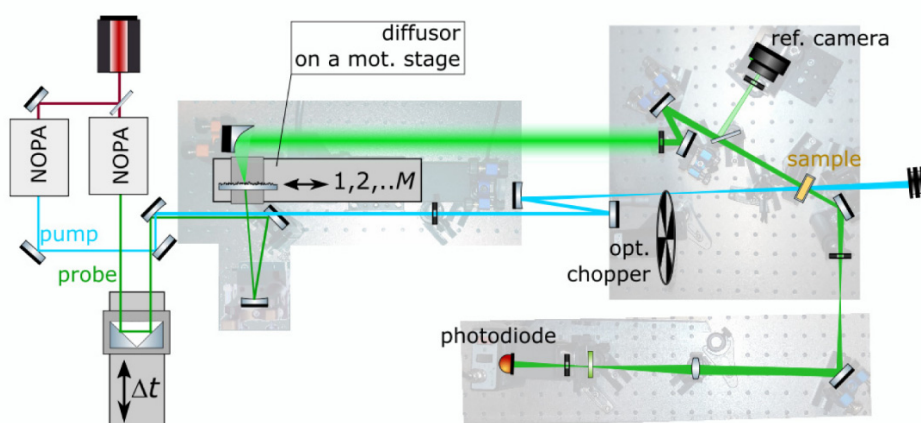


Fig. 1. Setup scheme used to carry out pump-probe imaging with a tilted pump beam – see text for details.

### 2.3. Testing samples

The experimental setup was tested by using a sample of colloidal CdSe quantum dots (QDs) with the lowest excitonic absorption maximum located at 560 nm (see Fig. 2(A)) [26]. This corresponds to the mean size of the QDs of about 3.4 nm. A solution of the QDs was placed in a 0.5 mm thick cuvette, featuring the optical density of 0.3-0.4 in the studied spectral range. The QDs had been previously extensively studied with respect to their optical and structural properties [27–29].

The second testing sample was a structured sample created by drop-casting a solution of QDs and Rhodamine 6G on a microscopic slide. After drying, the solutions created islands of agglomerated QDs and Rhodamine 6G molecules. In the case of the QDs, the spectral features do not change with the drop casting, whereas the Rhodamine 6G molecules encounter a shift in their resonances.

## 3. Results and discussion

### 3.1. Standard pump-probe setup

By using a standard pump-probe setup we were able to track TA kinetics in the solution of QDs and at several spots of the structured sample – see Fig. 2(C). The probe spectrum was chosen to match the region of the lowest excitonic state of the used QDs. Since the exact origin of the dynamics is not important for this work, we discuss it only briefly.

In the case of the colloidal sample (red line), the TA signal is dominated by a strong bleach of the lowest absorption band of the QDs. The kinetic follows an expected behavior, where we can observe a very rapid relaxation of carriers into the lowest excited state (TA signal onset) followed by a long-lived TA signal in the single-excited QDs decaying due to the electron-hole recombination. The excitation fluence is very low and thus we can neglect any effects arising from the multiply-excited QDs [29]. In the structured sample (black lines), in addition to the previous effects, we observe a rapid onset and decay in the TA signal due to

surface traps induced on the surface of the QDs and a range of lifetimes in a variety of Rhodamine 6G agglomerates [30,31].

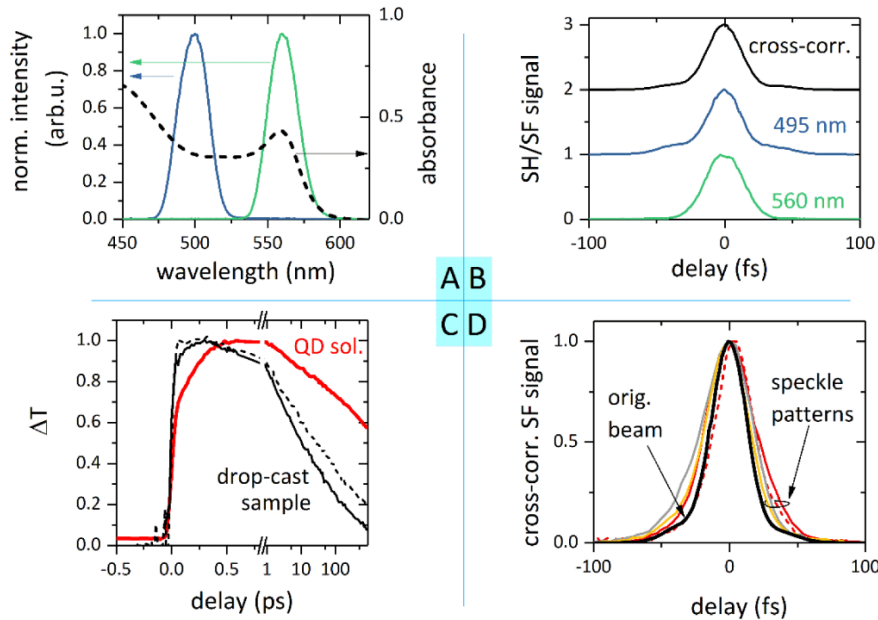


Fig. 2. (A) Spectra of the pump (blue) and probe (green) pulses. Absorbance of the measured quantum dots (dotted line). (B) Autocorrelation of the pump and probe beams together with the cross-correlation signal. (C) TA kinetics recorded by a standard PP setup for a colloidal sample (red line) and structured sample (black lines). (D) Cross-correlation between the pump beam and speckle patterned probe beam for various diffuser positions (colors) and selected regions (red lines) compared to the original cross-correlation (black line).

### 3.2. Pump-probe imaging setup utilizing single-pixel camera

The imaging is based on the method denoted as single-pixel camera (SPC) [17]. We point the reader to introductory articles on this topic, which elucidate this method and CS in general [15,32]. In the following, we provide a brief overview.

Using the SPC concept we need to illuminate the measured sample by a series of known uncorrelated random patterns. In our case, we used random speckle patterns which are created when coherent laser light is transmitted through a diffuser. This is due to interference of many wavefronts with random phases. By shifting the diffuser by sufficiently long steps, we attain a series of uncorrelated speckle patterns, as we showed in our previous work [20]. The random modification of a phase on the diffuser, however, also implies that the transmitted pulse is randomly delayed within the speckle pattern. Due to this effect, we observe that the patterned probe pulses are stretched in time. This was determined by measuring the cross-correlation between the pump and the patterned probe beam via sum-frequency generation. The cross-correlation, as a result of variable delay within the patterned probe pulse, varies with changing diffuser position (different colors in Fig. 2(D)) as well as between various spots in one pattern (red solid and dashed lines in Fig. 2(D)). The variation between pulses limits the temporal resolution of the imaging setup. Yet, the setup response function does not exceed the FWHM of 50 fs, which is sufficient for many processes of interest studied with ultrafast spectroscopy.

We will now explain the basic idea behind the P-P imaging using a patterned probe. When a patterned probe beam with the energy density of  $I(x, y)$  is transmitted through a sample, the recorded value is different in the case where the sample is in its ground state ( $I^{\text{gs}}$ ) and

where the sample is excited ( $I^{\text{exc}}$ ). The value is affected by a photoinduced change in transmittance  $\Delta T(x, y)$ , i.e., the TA signal. The corresponding measured lock-in signal  $s(x, y)$  is:

$$s(x, y) = I^{\text{exc}}(x, y) - I^{\text{gs}}(x, y) \approx \Delta T(x, y) I_{\text{pr}}(x, y). \quad (1)$$

We employed here the fact that  $\Delta T \ll 1$  since a small fraction of a sample is typically excited. By detecting the total probe intensity (i.e., by integrating over the whole probe spot) we get:

$$s_{\text{tot}} = \iint s(x, y) dx dy = \iint \Delta T(x, y) I_{\text{pr}}(x, y) dx dy = \sum_{i,j} \Delta T_{i,j} \mathcal{T}_{i,j}. \quad (2)$$

In the last term, we discretized the TA signal and the probe intensity into the form of matrices  $\Delta \mathcal{T}$  and  $\mathcal{T}$ . The physical meaning of the TA signal remains unchanged; the discretized probe intensity  $\mathcal{T}$  now denotes the probe energy in one pixel of the image. For the sake of simplicity, we can convert, i.e. vectorize, 2D matrices  $\Delta \mathcal{T}$  and  $\mathcal{T}$  into two vectors  $\Delta \vec{\mathcal{T}}$  and  $\vec{\mathcal{T}}$  sized  $N \times 1$  and  $1 \times N$ , respectively, where  $N$  denotes the number of data set elements (i.e., number of image pixels). Equation (2) can be then rewritten by using a scalar product between the vectors as

$$s_{\text{tot}} = \vec{\mathcal{T}} \cdot \Delta \vec{\mathcal{T}}. \quad (3)$$

When measuring the lock-in signal for  $M$  different probe patterns, we can create a matrix  $\mathcal{A}$  where each line of the matrix will be formed by a single probe pattern  $\vec{\mathcal{T}}$ . The lock-in signal values  $s_{\text{TOT}}$  can be placed in a  $1 \times M$  vector  $\vec{S}$  and the vector is related to the TA signal via matrix multiplication as:

$$\vec{S} = \mathcal{A} \Delta \vec{\mathcal{T}}. \quad (4)$$

Our goal is to extract the TA signal image  $\Delta \vec{\mathcal{T}}$  while both vector  $\vec{S}$  and matrix  $\mathcal{A}$  are known, since we acquire the speckle pattern reference and the lock-in signal for each speckle pattern. Yet, it is possible to obtain  $\Delta \vec{\mathcal{T}}$  directly only if  $\mathcal{A}$  is an invertible matrix. This cannot be satisfied for  $M < N$ .

Nevertheless, CS makes it possible to exactly recover the  $\Delta \vec{\mathcal{T}}$  even for a highly underdetermined system ( $M \ll N$ ). This is conditioned by three prerequisites: firstly, the  $\Delta \vec{\mathcal{T}}$  vector has to be sparse or sparse-like in certain basis – as stated before. This condition is satisfied for a vast majority of images. Secondly, the measured data needs to be encoded by random uncorrelated patterns. Finally, it is required to mathematically quantify an expected characteristics of the reconstructed image with a so-called regularizing term. Here, the CS theory benefits from extensive research in the field of image processing. One of the most commonly used properties is the total variation  $D$  of an image, which is an  $l_2$ -norm of the difference between the neighboring pixels in an image:

$$D(\Delta \mathcal{T}) = \sqrt{\sum_{i,j} (\Delta \mathcal{T}_{i,j} - \Delta \mathcal{T}_{i-1,j})^2 + \sum_{i,j} (\Delta \mathcal{T}_{i,j} - \Delta \mathcal{T}_{i,j-1})^2}. \quad (5)$$

The total variation of an image is low for the cases where the image contains a small number of transitions between the dark and bright pixels, which is the case for the vast majority of images. On the contrary, noisy random images feature a high value of total variation. We can combine our knowledge of the relation between the measured data and the TA map in Eq. (4)



and, consequently, we can apply the condition that the resulting TA map is expected to feature a low value of its total variation, Eq. (5). The image reconstruction can, therefore, be carried out by minimizing both the factors:

$$\Delta \vec{T}_{rec} = \arg \min_{\Delta \vec{T} \in \mathbb{R}^N} \left\{ D(\Delta T) + \frac{\mu}{2} \left\| \vec{S} - \mathcal{A} \Delta \vec{T} \right\|_2^2 \right\}. \quad (6)$$

The weight factor  $\mu$  is added either to promote the importance of the measured data set for a high  $\mu$  value, or to promote the minimization of the total variation when the  $\mu$  value is low. We will closely discuss the factor value and its effect in the text below. Nevertheless, Eq. (6) represents a standard problem in CS-based imaging, which can be solved by using the TVAL3 algorithm [33].

### 3.3. Proof-of-principle measurements

As a proof-of-principle experiment, we carried out imaging of a fully homogeneous sample (solution of CdSe QDs) excited by a tilted pump beam – see Fig. 3(A). The angle between the pump and the probe beam was intentionally set to the high value of 35 deg, which was determined by the relative position of the measurement spot on the sample and the pump and probe beam spots on the preceding mirrors. The sample was placed perpendicularly to the probe beam. Due to the tilt, the sample became gradually excited from the right-hand side as the P-P delay increased. Since the observed bleach in the excited QDs is long-lived and does not significantly decay during the measurement window, we observe, in fact, a gradual onset of the TA signal through the sample. We extracted TA maps which are in a perfect agreement with the expected behavior – see Fig. 3(B).

In this experiment, the size of the probe beam on the sample was set large (2.5 mm in diameter), exceeding the pump beam spot size. This means that the outer parts of image remain unexcited without any TA signal, and the central excited part follows the shape of the pump beam. Indeed, the TA map for the completely excited sample in Fig. 3(B), bottom image, matches the pump spot on the sample in Fig. 3(C). Note, that the pump spot is more elongated in panel C along the x-axis due to the tilt between the pump beam and the sample.

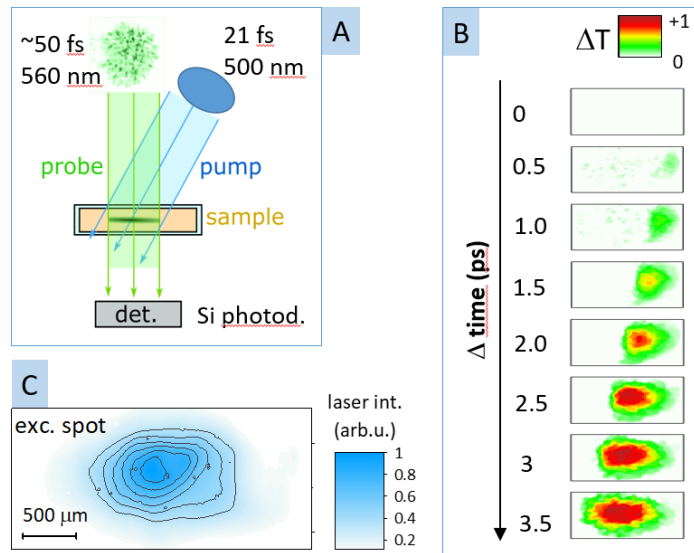


Fig. 3. Pump-probe imaging of a tilted pump beam ( $N = 128 \times 128 = 16384$  pixels,  $M = 1600$ ,  $M/N_{ph} = 0.27$ ). (A) Scheme of the measurement. (B) TA signal maps for pump-probe delay 0–3.5 ps. (C) Map of the excitation spot intensity.

The attained data set of 1600 speckle patterns and the corresponding total TA signal for a set of P-P delays make it possible to reconstruct the kinetics of the TA signal at each spot. We can, therefore, extract dynamics for different spots along the x-axis in the center of the image – see Fig. 4(A), solid lines. The curves show, as expected, a gradual excitation of the sample, often referred to as a “travelling wave” excitation. We have globally fitted the data using a step-function convoluted with a Gaussian response function (dotted lines), where the response function width was fitted as a common value for all curves. This enables us to extract the zero P-P delays for each curve, see Fig. 4(B), which lie, within the fit precision, on a line corresponding to the change of 36.9 fs/pixel – dotted line in Fig. 4(B). The only exception is the last point, where the onset was not fully captured in the measured time range. Therefore, the zero delay is likely to be underestimated. Since the dimensions of an image pixel in Fig. 3(B) can be calculated from the reference camera snapshots and corresponded to the size of 19  $\mu\text{m}$ , we can derive that the onset of the TA signal was travelling the distance of 1  $\mu\text{m}$  along the x axis in 1.9 fs. From this value and the speed of light we can derive the tilt of the pump beam as  $\sin \theta = (1.9 \frac{\text{fs}}{\mu\text{m}}) / (0.3 \frac{\mu\text{m}}{\text{fs}})$ , which implies that the angle between the P-P beams in air was 35 deg. This is in a perfect agreement with the set angle. Note that the pump beam is refracted in a cuvette and QD solution. However, since it propagates there at a lower speed due to a higher refractive index, the effects cancel out and the TA onset travelling speed remains the same.

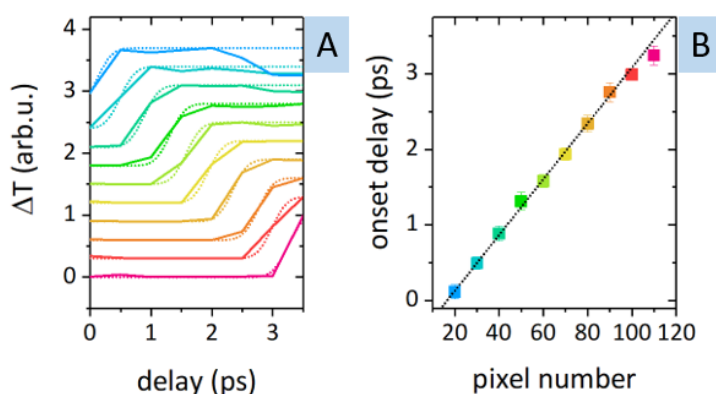


Fig. 4. Gradual sample excitation kinetics. (A) Normalized TA kinetics extracted for a single line (64) with varying pixel x coordinates (blue-red: 20, 30, 40, 50, 60, 70, 80, 90, 100, 110) – solid lines, global fit of the kinetics with a step function convoluted with a Gaussian function ( $\sigma = 140$  fs) – dotted lines. (B) Fitted onset delay for each of the TA kinetics (squares) fitted with a linear function (dotted line, 36.9 fs/pixel image).

### 3.4. Structured drop-cast sample measurements

In the experiment presented above we were able to verify the setup functionality and capture TA images which are in full agreement with the expected physical behavior. Thus, we turned to the measurement of the structured drop-cast sample on a microscopic slide described above. Here, the probe spot size was decreased to be fully covered by the pump spot, i.e., the retrieved image was not distorted by the pump beam shape. At the same time, the tilt between the pump and the probe beams was set to approximately 10 degrees to avoid the effect of the gradual sample excitation. Due to a lower sample optical density the TA signal was ~6 times lower as compared to the previous measurement.

The structured sample consists of overlapping islands of aggregated QDs and Rhodamine 6G molecules, which, despite not being pronounced under ambient illumination in Fig. 5(A),



can be clearly distinguished by their photoluminescence, as seen in Fig. 5(B) (excited by 488 nm cw laser,  $1 \text{ W/cm}^2$ ). The white circle in Fig. 5(B) denotes the probe spot coverage. From 800 measurements we were able to retrieve TA maps for a series of pump-probe delays – see Fig. 5(C). Due to the lower signal level and a relatively low number of the measured data points, the reconstructed maps were considerably noisier compared to the previous experiment. In the case of the drop-cast sample, the signal to noise ratio reached the value of around 1.5. Yet, in spite of a relatively low signal level and a 7 times reduced number of measurements as compared to the sample scan (discussed later in the text), we were able to retrieve the TA maps in Fig. 5(C), featuring patterns which match the structure observed via photoluminescence.

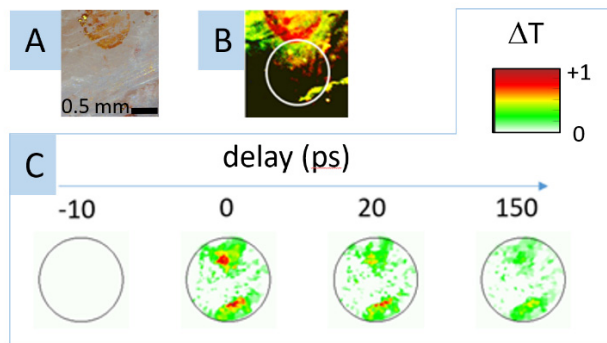


Fig. 5. Imaging of a structured sample – drop-cast Rhodamine 6G and CdSe QDs ( $N = 128 \times 128 = 16384$  pixels,  $M = 800$ ,  $M/N_{ph} = 0.14$ ). (A) Sample under microscope under an ambient light. (B) Photoluminescence of the sample under 488 nm cw laser excitation. (C) TA maps obtained by reconstruction using a complete data set ( $M = 800$ ) at given delays.

Unlike in standard imaging, the noise level in the resulting image can be reduced by decreasing the  $\mu$  factor in Eq. (5) and other parameters of the TVAL3 algorithm. In order to illustrate this fact, we have reconstructed the measured data on the structured sample for several sets of parameters – see Fig. 6(B) i-v. The upper line depicts the peak TA signal, whereas the lower line is a ratio of TA signals  $\Delta T(20 \text{ ps})/\Delta T(0 \text{ ps})$  reconstructed for the same parameters.

First, from the standard P-P measurement we know that the TA signal in the studied samples was only positive. We can, therefore, choose either to restrict the reconstruction to the positive values of  $\Delta T$  (Fig. 6(B) i-iii) or to solve the general case (Fig. 6(B) iv-v). For both options we can vary the parameter  $\mu$  in Eq. (6). For a lower  $\mu$  value (Fig. 6(B) i-iv), we enhance the importance of the total variation over the agreement with the measured TA data. On the contrary, for a high  $\mu$  value (Fig. 6(B) iii, v) we promote reconstruction which agrees with the measured TA data. This, of course, causes the image to be significantly noisier. In the panel Fig. 6(B) ii, the  $\mu$  value is set in between the extreme cases. We observe that the different reconstruction parameters provide us, in general, with the same picture of the sample, i.e., two prominent parts divided by an area with a lower TA signal. The image of the TA signal is in good agreement with the measured photoluminescence image showing a pronounced region of QDs, especially for the high  $\mu$  values. In all cases of Fig. 6(B), we also observe that the sample in the upper part decays more rapidly compared to the lower part. However, the exact shape and size of the reconstructed islands clearly depend on the value of  $\mu$ .

This raises the essential question regarding the correct selection of the  $\mu$  value. For instance, when the question of interest concerns the mean dimensions of the islands, the reconstruction parameters will have a huge effect on the result. In general, it is beneficial to use a high  $\mu$  value promoting the weight of the measured data in the TA map reconstruction.

This, on the other hand, gives rise to a number of small features in the image, and it is unclear whether they carry additional information about the sample or are consequence of the noise. To distinguish between the two cases, we can utilize one of the important properties of SPC, namely that each of the measurements provides information about the entire image. We can, therefore, reconstruct a TA map from an arbitrarily selected subset of measurements. In our case, we split the 800 measurement data sets into two parts and reconstructed TA maps for the two partial data sets – see Fig. 6(A). We observe analogous features in both cases, which were taken for entirely different speckle patterns and probe intensities. The resulting images are noisier because the lower number of patterns reduces the reconstruction precision for the noisy data sets. Nevertheless, it is possible to compare the two maps and identify regions common in both reconstructions, and thus identify sample features as opposed to the ones appearing from noise.

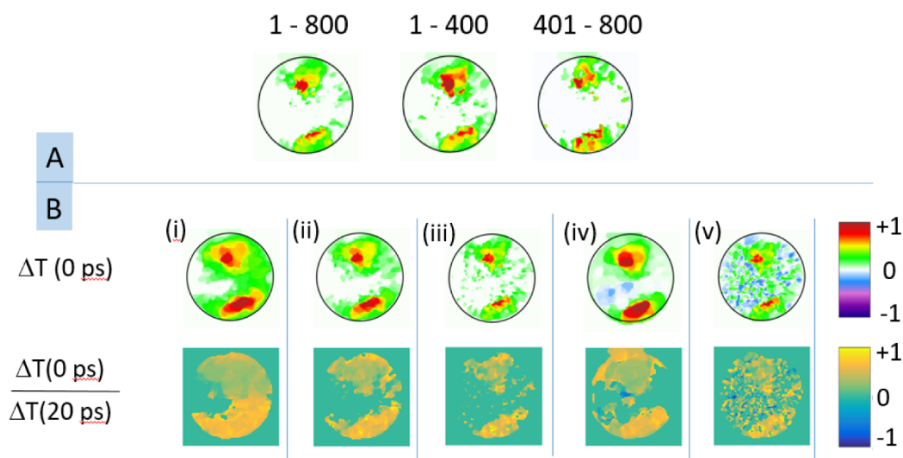


Fig. 6. (A) Comparison of TA maps  $\Delta T(0 \text{ ps})$  for a complete data set ( $i:1-800$ ;  $M = 800$ ) and two independent subsets ( $i:1-400$ ;  $i:401-800$ ;  $M = 400$ ). (B) Imaging of the structured sample – the effect of the reconstruction parameter  $\mu$ . Upper line: TA maps for a zero delay. Lower line: maps of  $\Delta T(20 \text{ ps}) / \Delta T(0 \text{ ps})$ . i)  $\mu = 90$ ,  $\Delta T \geq 0$ ; ii)  $\mu = 180$ ,  $\Delta T \geq 0$ ; iii)  $\mu = 510$ ,  $\Delta T \geq 0$ ; iv)  $\mu = 90$ ,  $\Delta T \in \mathbb{R}$ ; v)  $\mu = 510$ ,  $\Delta T \in \mathbb{R}$ .

### 3.5. Advantages and limitations of the method

In comparison to pixel-by-pixel scanning, the SPC-based approach has several advantages: (i) decreased number of measurements; (ii) attainable image resolution at a long working distance; (iii) possibility to discard arbitrary data points. We will address each of the advantages in turn.

The number of measurements  $M$  needed to reasonably reconstruct an image encoded by laser speckles is given both by the measurement noise level and the physical resolution of the image. The physical resolution can be different from the number of pixels of the reconstructed image. The number of pixels is only limited by the resolution of the reference camera capturing the reference speckle images. In our measurements, the speckle patterns covered approx.  $450 \times 450$  pixels and, in principle, we could solve Eq. (6) by using the speckle patterns in their full resolution and reach the number of pixels of  $450 \times 450 = 202500$  pixels. However, as we showed in our previous work, the actual physical resolution of the speckle-based imaging is limited to one half of the mean size of the speckles in the used speckle patterns [20]. The mean size can be determined based on the autocorrelation of the speckle patterns. For the  $450 \times 450$  speckle images, the mean speckle size was 9.7 pixels and 11.5 pixels in the horizontal and vertical sense, respectively. This value stayed constant for all measurements. Hence, the physical resolution of our images reached  $82 \times 72$  pixels ( $N =$

5900). Note that, for practical reasons, we performed all data processing by rescaling the raw speckle patterns to  $128 \times 128$  pixels prior to the TVAL3 reconstruction. The images were reconstructed using 800-1600 measurement data points, which correspond to 14-28% of the number of pixels for the physical resolution. In other words, the use of CS helps to reduce the number of measurements, compared to sample scanning, by the factor of 5-7. For a single measurement requiring about 5 s/data point (4 s signal averaging, 1 s for stage and delay adjustments), we achieve the measurement time of a single image of 1-2 hours for the CS as opposed to 8 hours for the pixel scan. Such difference is very important from the point of view of laser system stability, sample photostability, etc.

Since we attained the resolution of  $82 \times 72$  on a probe spot of  $1340 \mu\text{m}$  in diameter, we can resolve details down to approx.  $20 \mu\text{m}$ . For the pixel scan, the same resolution can be accomplished by focusing the probe beam onto a comparable spot. Practically, reaching such resolution would be conditioned by using microscopy optics implying a short working distance. In our case, we used standard spherical mirrors with a focal length of 10-25 cm. The experiment can be, therefore, easily used in combination with a cryostat, a magnet or similar devices, unlike a microscopy apparatus.

As stated above, we can reconstruct the image from an arbitrary subset of the measured data. We used this in our measurements to discard the speckle patterns, where the reference camera was saturated and could not provide full information about the pattern. Another possible application consists, for instance, in dealing with measurements where a random source of noise disturbs some data points. In the pixel scanning method the noise would corrupt certain areas of the image. In our method, such data points can be simply omitted.

A principal limitation of the presented imaging method is the fact that we have to have a basic preliminary knowledge of the measured sample to apply the method correctly. Generally, the used image reconstruction is based on the assumption that the desired image features a low value of total variation. Although this is true for the majority of cases, samples with a pronounced structure on a scale comparable to the imaging resolution will pose a problem. This fact can be, on the other hand, verified by comparing reconstruction from multiple independent subsets of the measured data. The method also features limited precision for the exact lifetime evaluation. Even though the reconstruction provides us with a good comparison of the signal strength for a given delay, decay curves might be distorted due to minimization of total variation. An example can be the decay curves in Fig. 4(A), where the initial signal on the right hand side (blue-green curves) is promoted. For this reason, the TA decay seems to vary from the blue to the yellow curves. In a homogenous solution of single-excited QDs, this is very likely to be an artefact of the mathematical reconstruction.

Finally, we would like to point out one very useful feature of the presented P-P imaging. In the cases where the TA signal strength linearly scales with the excitation intensity – and this applies in many cases where a low excitation level is used — we can derive Eq. (4) in an analogous way, where we use a homogeneous probe beam and a patterned pump beam. This means that the TA imaging can be, in such case, carried out by using a patterned pump beam, instead of the probe beam. Such approach is very appealing in the cases where the pump beam is in the visible/near-IR range whereas the probe beam can be in any spectral range (IR, THz, ...). The pump beam patterned can be easily captured by a reference camera and we still retain the advantage of measuring the probe beam with a single-pixel detector. Such experiment can, for instance, open the path for ultrafast THz imaging.

#### 4. Conclusions

We presented a concept which offers a straightforward access to imaging in the field of ultrafast spectroscopy. The presented pump-probe setup is able to map transient absorption signal with a sub-100-fs resolution by using a fraction of measurements compared to a point-by-point sample scanning. This is achieved by employing a patterned probe beam, generated by a diffuser, to randomly encode the transient absorption signal. We have demonstrated the

functionality of the setup on two proof-of-principle measurements. The experiment was able to reproduce a gradual excitation of a sample from a tilted pump beam and an inhomogeneous TA signal from a structured sample.

Owing to its simplicity, the presented approach can become simple means of imaging in ultrafast spectroscopy for a broad range of laboratories. The conversion from a standard time-resolved spectroscopy setup is straightforward and although the presented article focuses solely on the pump-probe setup, an analogous experiment can be carried out for any technique where the resulting signal is proportional to the probe beam or a local oscillator in heterodyne detection, e.g., the transient grating technique or certain types of two-dimensional spectroscopy.

Moreover, for the pump-probe signal, which is proportional to the pump intensity, it is possible to create an analogous experiment, where a patterned pump beam is used to encode the image. In this case, the imaging can be carried out for a broad spectral range of probe beams, including THz.

## Funding

Laserlab-Europe EU-H2020 (654148); Grant Agency of the Czech Republic (Project 17-26284Y); Independent Research Fund Denmark-Sapere Aude starting grant (7026-00037A).

## Acknowledgments

We thank Lukas Wittenbecher (Lund University) for his help during the experimental work and Ramūnas Augulis for the lock-in signal analysis software.

## References

1. V. M. Axt and T. Kuhn, "Femtosecond spectroscopy in semiconductors: a key to coherences, correlations and quantum kinetics," *Rep. Prog. Phys.* **67**(4), 433–512 (2004).
2. J.-Y. Bigot, V. Halté, J.-C. Merle, and A. Daunois, "Electron dynamics in metallic nanoparticles," *Chem. Phys.* **251**(1-3), 181–203 (2000).
3. I. G. Scheblykin, A. Yartsev, T. Pullerits, V. Gulbinas, and V. Sundström, "Excited state and charge photogeneration dynamics in conjugated polymers," *J. Phys. Chem. B* **111**(23), 6303–6321 (2007).
4. E. Thyrgaard, R. Tempelaar, M. J. P. Alcocer, K. Židek, D. Bina, J. Knoester, T. L. C. Jansen, and D. Zigmantas, "Identification and characterization of diverse coherences in the Fenna-Matthews-Olson complex," *Nat. Chem.* **10**(7), 780–786 (2018).
5. K. Zheng, K. Karki, K. Židek, and T. Pullerits, "Ultrafast photoinduced dynamics in quantum dot-based systems for light harvesting," *Nano Res.* **8**(7), 2125–2142 (2015).
6. M. C. Fischer, J. W. Wilson, F. E. Robles, and W. S. Warren, "Invited review article: pump-probe microscopy," *Rev. Sci. Instrum.* **87**(3), 031101 (2016).
7. J. Shah, *Ultrafast Spectroscopy of Semiconductors and Semiconductor Nanostructures* (Springer, 1999).
8. M. M. Gabriel, J. R. Kirschbrown, J. D. Christesen, C. W. Pinion, D. F. Zigler, E. M. Grumstrup, B. P. Mehl, E. E. M. Cating, J. F. Cahoon, and J. M. Papanikolas, "Direct imaging of free carrier and trap carrier motion in silicon nanowires by spatially-separated femtosecond pump-probe microscopy," *Nano Lett.* **13**(3), 1336–1340 (2013).
9. M. J. Simpson, B. Doughty, B. Yang, K. Xiao, and Y.-Z. Ma, "Spatial Localization of Excitons and Charge Carriers in Hybrid Perovskite Thin Films," *J. Phys. Chem. Lett.* **6**(15), 3041–3047 (2015).
10. S. Bourquin, R. P. Prasankumar, F. X. Kärtner, J. G. Fujimoto, T. Lasser, and R. P. Salathé, "High-speed femtosecond pump-probe spectroscopy with a smart pixel detector array," *Opt. Lett.* **28**(17), 1588–1590 (2003).
11. Y.-H. Kim and P. T. C. So, "Three-dimensional wide-field pump-probe structured illumination microscopy," *Opt. Express* **25**(7), 7369–7391 (2017).
12. T. Pezeril, C. Klieber, V. Shalagatskyi, G. Vaudel, V. Temnov, O. G. Schmidt, and D. Makarov, "Femtosecond imaging of nonlinear acoustics in gold," *Opt. Express* **22**(4), 4590–4598 (2014).
13. C. Schnedermann, J. M. Lim, T. Wende, A. S. Duarte, L. Ni, Q. Gu, A. Sadhanala, A. Rao, and P. Kukura, "Sub-10 fs Time-Resolved Vibronic Optical Microscopy," *J. Phys. Chem. Lett.* **7**(23), 4854–4859 (2016).
14. M. Seo, S. Boubanga-Tombet, J. Yoo, Z. Ku, A. V. Gin, S. T. Picraux, S. R. J. Brueck, A. J. Taylor, and R. P. Prasankumar, "Ultrafast optical wide field microscopy," *Opt. Express* **21**(7), 8763–8772 (2013).
15. E. J. Candes and M. B. Wakin, "An introduction to compressive sampling," *IEEE Signal Process. Mag.* **25**(2), 21–30 (2008).
16. A. Stern, *Optical Compressive Imaging* (CRC, 2017).
17. M. F. Duarte, M. A. Davenport, D. Takhar, J. N. Laska, T. Sun, K. F. Kelly, and R. G. Baraniuk, "Single-Pixel Imaging via Compressive Sampling," *IEEE Signal Process. Mag.* **25**(2), 83–91 (2008).



18. A. Bhandari, C. Barsi, and R. Raskar, "Blind and reference-free fluorescence lifetime estimation via consumer time-of-flight sensors," *Optica* **2**(11), 965 (2015).
19. W. L. Chan, K. Charan, D. Takhar, K. F. Kelly, R. G. Baraniuk, and D. M. Mittleman, "A single-pixel terahertz imaging system based on compressed sensing," *Appl. Phys. Lett.* **93**(12), 121105 (2008).
20. K. Židek, O. Denk, and J. Hlubuček, "Lensless photoluminescence hyperspectral camera employing random speckle patterns," *Sci. Rep.* **7**(1), 15309 (2017).
21. X. Cai, B. Hu, T. Sun, K. F. Kelly, and S. Baldelli, "Sum frequency generation-compressive sensing microscope," *J. Chem. Phys.* **135**(19), 194202 (2011).
22. O. Denk, A. Musiienko, and K. Židek, "Differential single-pixel camera enabling low-cost microscopy in near-infrared spectral region," *Opt. Express* **27**(4), 4562–4571 (2019).
23. N. Christensson, K. Židek, N. C. M. Magdaong, A. M. LaFountain, H. A. Frank, and D. Zigmantas, "Origin of the bathochromic shift of astaxanthin in lobster protein: 2D electronic spectroscopy investigation of  $\beta$ -crustacyanin," *J. Phys. Chem. B* **117**(38), 11209–11219 (2013).
24. L. Dall'Osto, S. Cazzaniga, M. Bressan, D. Paleček, K. Židek, K. K. Niyogi, G. R. Fleming, D. Zigmantas, and R. Bassi, "Two mechanisms for dissipation of excess light in monomeric and trimeric light-harvesting complexes," *Nat. Plants* **3**(5), 17033 (2017).
25. K. Židek, "Focal Plane Speckle Patterns for Compressive Microscopic Imaging in Laser Spectroscopy," in *Proceedings CoSeRa 2018 (EURASIP)*, <https://www.eurasip.org/Proceedings/Ext/CoSeRa2018/papers/p-zidek.pdf>.
26. K. Zheng, K. Židek, M. Abdellah, N. Zhu, P. Chábera, N. Lenngren, Q. Chi, and T. Pullerits, "Directed energy transfer in films of CdSe quantum dots: beyond the point dipole approximation," *J. Am. Chem. Soc.* **136**(17), 6259–6268 (2014).
27. N. Lenngren, M. A. Abdellah, K. Zheng, M. J. Al-Marri, D. Zigmantas, K. Židek, and T. Pullerits, "Hot electron and hole dynamics in thiol-capped CdSe quantum dots revealed by 2D electronic spectroscopy," *Phys. Chem. Chem. Phys.* **18**(37), 26199–26204 (2016).
28. K. Židek, K. Zheng, C. S. Ponseca, Jr., M. E. Messing, L. R. Wallenberg, P. Chábera, M. Abdellah, V. Sundström, and T. Pullerits, "Electron transfer in quantum-dot-sensitized ZnO nanowires: ultrafast time-resolved absorption and terahertz study," *J. Am. Chem. Soc.* **134**(29), 12110–12117 (2012).
29. K. Židek, K. Zheng, M. Abdellah, N. Lenngren, P. Chábera, and T. Pullerits, "Ultrafast dynamics of multiple exciton harvesting in the CdSe-ZnO system: electron injection versus auger recombination," *Nano Lett.* **12**(12), 6393–6399 (2012).
30. M. Chapman, M. Mullen, E. Novoa-Ortega, M. Alhasani, J. F. Elman, and W. B. Euler, "Structural evolution of ultrathin films of Rhodamine 6G on glass," *J. Phys. Chem. C* **120**(15), 8289–8297 (2016).
31. A. Kazakevičius, D. Peckus, O. Boiko, L. Valkunas, E. Leonenko, G. Telbiz, and V. Gulbinas, "Insights into the mechanism of enhanced Rhodamine 6G dimer fluorescence in mesoscopic pluronic-silica matrixes," *J. Phys. Chem. C* **119**(33), 19126–19133 (2015).
32. M. A. Davenport, M. F. M. Duarte, Y. C. Y. Eldar, and G. Kutyniok, "Introduction to compressed sensing," Preprint **93**, 1–68 (2011).
33. C. Li, W. Yin, and Y. Zhang, "User's guide for TVAL3: TV minimization by augmented lagrangian and alternating direction algorithms," *CAAM Rep.* **20**, 46–47 (2009).





# Random temporal laser speckles for the robust measurement of sub-microsecond photoluminescence decay

J. JUNEK,<sup>1,2</sup> L. ONDIČ,<sup>3</sup> AND K. ŽÍDEK<sup>1,\*</sup> 

<sup>1</sup>Regional Center for Special Optics and Optoelectronic Systems (TOPTEC), Institute of Plasma Physics, Czech Academy of Science v.v.i., Za Slovankou 1782/3, 182 00 Prague 8, Czech Republic

<sup>2</sup>Technical University in Liberec, Faculty of Mechatronics, Informatics and Interdisciplinary Studies, Studentská 1402/2, 461 17 Liberec, Czech Republic

<sup>3</sup>Institute of Physics, Czech Academy of Sciences v.v.i., Cukrovarnická 10, 162 53, Prague 6, Czech Republic

\*zidek@ipp.cas.cz

**Abstract:** Time-resolved photoluminescence (PL) is commonly used to track dynamics in a broad range of materials. Thus, the search for simplification of the acquisition of PL kinetics attracts continuous attention. This paper presents a new robust and straightforward approach to the measurement of PL decay, which is based on randomly fluctuating excitation intensity. The random excitation waveform is attained by using laser speckles generated on a rotating diffuser. Owing to this, the presented technique is able to utilize any coherent excitation source without the necessity to generate short pulses or to controllably modulate the light. PL decay can be computationally reconstructed from the Fourier image of the PL trace. The paper demonstrates the performance of the method, which is able to acquire sub-microsecond dynamics as the impulse response function reaches 300 ns. The reconstructed PL decays were compared to streak camera measurements to verify the method. Finally, potential limitations and applications of the technique are discussed.

© 2020 Optical Society of America under the terms of the [OSA Open Access Publishing Agreement](#)

## 1. Introduction

Photoluminescence (PL) spectra and dynamics provide a vast amount of information about the emitting material – revealing energy levels of charge carriers [1,2], resolving processes governing the excited energy routes [3,4], even resolving lifetimes of the processes [5]. All the information can be extracted in a non-contact experiment, even in opaque samples. Therefore, PL time-resolved spectroscopy counts among the most used characterization methods in the fields of chemical physics [6,7], biochemistry [8], and material sciences in general.

All reported methods for time-resolved PL measurements require an excitation source able to provide us with a short pulse or to be controllably modulated [9–11]. In general, all the methods can be divided into two groups, which measure PL kinetics in the time and the frequency domains. Methods working in the time domain need a source producing correspondingly short pulses. The pulses excite PL, which is either detected by a speedy detection system, is spatially swept (streak camera), or the PL signal is gated (by up-conversion technique, ICCD). Measurements of PL decay in the frequency domain demand using a controllably modulated light intensity, for instance, an acousto-optic modulator or a modulated laser. In order to capture PL decay stretched over different timescales, the intensity modulation has to be facilitated over a broad range of frequencies.

In this article, we present a method that, in contrast, can use any source of coherent light to measure PL dynamics on the microsecond and sub-microsecond timescales. The core of this method lies in the excitation of the measured sample with a randomly fluctuating intensity of light. This can be achieved by transmitting a coherent light source through a rapidly varying scattering





element creating fluctuating speckle patterns, which we denote as temporal speckles. The field of temporal speckles is cropped with an aperture, providing us with a random signal for sample excitation. Such a random excitation signal features a broad range of frequencies, which can be used to reconstruct back the PL decay from the measured fluctuations of the PL intensity. We demonstrate that this technique can be used to attain PL decay with sub-microsecond temporal resolution without the need for a pulsed excitation. We also prove that the attained decay is in agreement with conventional approaches to PL decay measurement.

Moreover, as we show later, this method is remarkably robust against various experimental conditions such as signal delay or offset. Owing to its simplicity, no elaborate setup alignment or calibration is needed.

## 2. Methodology and experimental setup

### 2.1. Principles of the method

For the sake of brevity, we will hereafter denote the method as RATS (RANdom Temporal Speckles). The goal of the RATS method is to excite the tested sample with temporal speckles, i.e., randomly fluctuating intensity of light. To reconstruct the PL decay  $I_{decay}$  we need to acquire the excitation signal  $I_{Exc}$  and the PL signal  $I_{PL}$ . We can illustrate the RATS concept on simulated data depicted in Figs. 1(A)–1(B). The excitation signal was attained by simulating the generation of laser speckles from a rotating diffuser via Fraunhofer diffraction (far-field speckle pattern) [12]. Following the real experimental setup, which is described later, the resulting random pattern was cropped with an aperture and the total intensity of light within the aperture is plotted in Fig. 1(A) as a random signal for the excitation  $I_{Exc}$ . The photoluminescence signal  $I_{PL}$  plotted in Fig. 1(B) was calculated via the convolution of  $I_{Exc}$  and  $I_{decay}$ :

$$I_{PL} = I_{Exc} * I_{decay} \quad (1)$$

It is worth noting that Eq. (1) holds only for PL intensity which is linearly proportional to the excitation intensity, as we discuss later.

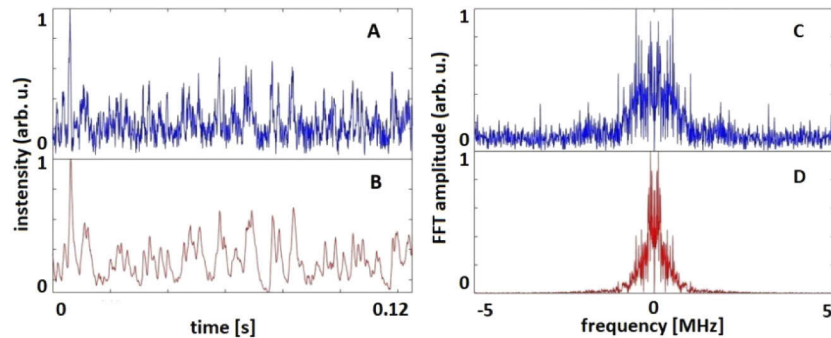


**Fig. 1.** Simulated intensity of the fluctuating temporal speckles (panel A) which are used to calculate a PL waveform (panel B). We assume a single-exponential PL decay with  $\tau = 1$  ms. Fourier transform of intensity of fluctuating temporal speckles (panel C) and Fourier transform of PL waveform (panel D).

For the sake of clarity, the PL decay lifetime in Fig. 1 was chosen to be mono-exponential with the lifetime in the millisecond range ( $\tau = 1$  ms), so that the difference between the excitation and the PL waveform is apparent both in the time domain and in the Fourier space. The Fourier transformations of  $I_{Exc}$  and  $I_{decay}$  are depicted in Figs. 1(C) and 1(D), respectively.

By using a fluctuating random signal for excitation, we get a wide range of frequencies in the Fourier space. This is important because the  $I_{decay}$  can be determined on the timescale

corresponding to the highest available frequency. The  $I_{decay}$  can be simply calculated via the convolution theorem. Equation (2) shows the used deconvolution applying the so-called Tikhonov regularization [13]. The regularization prevents cases from being ill-conditioned, which can happen when the denominator approaches zero due to data corrupted by noise.

$$I_{decay} = Re \left\{ F^{-1} \left[ \frac{F(I_{PL}) F^*(I_{Exc})}{F(I_{Exc}) F^*(I_{PL}) + \varepsilon F(I_{Exc}) F^*(I_{Exc})} \right] \right\} \quad (2)$$

We, therefore, attain the full PL decay dynamics  $I_{decay}$ , analogously to the other methods. The decay can be subsequently fitted with a set of exponential functions to determine the characteristic PL lifetimes.

Naturally, since the temporal speckle pattern is formed by a rotating diffuser, excitation and PL waveforms repeat with every period of rotation. Nevertheless, for the purpose of the PL decay retrieval, we do not need to determine the frequency of the diffuser and its timing, i.e., phase. This is owing to the fact that the shift in the “zero time” between the PL and the excitation data will cause the PL decay to be multiplied with a constant complex number  $e^{(-i\varphi)}$ , where the phase  $\varphi$  will scale with the timing difference. Such a problem can be easily eliminated.

## 2.2. Optical setup

A scheme of the optical setup used is presented in Fig. 2. In the setup, we used a cw laser (Sapphire, Coherent) at the wavelength of 488 nm, intensity 6 mW. But it should be stressed that one can use any coherent light source which is suitable for excitation of a sample. A diffuser (ground glass, diameter 10 cm, average grain size 1.52  $\mu\text{m}$ ) was mounted on a Mitsumi DC motor, which rotated up to the frequency of 65 Hz.

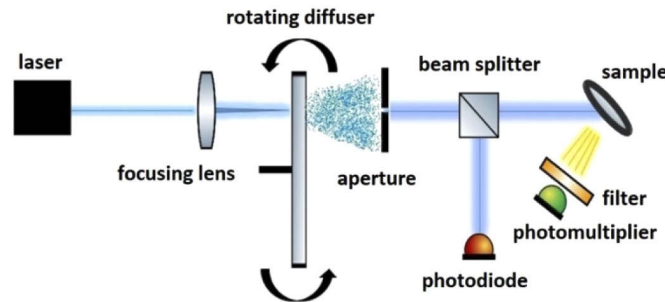


Fig. 2. Scheme of the experimental setup used.

The laser beam was focused onto the diffuser with a lens with a focal length of 30 mm. The laser beam hit the spinning diffuser 4.8 cm from the center and the beam spot size on the diffuser was approximately 50  $\mu\text{m}$ . Under those conditions, we generated speckle patterns in the so-called far-field regime, which means that the generated intensity pattern does not change with distance.

The field of speckles was cropped with an iris aperture at the distance of 110 mm from the diffuser. As a result, we attained a randomly fluctuating intensity of light behind the aperture, which was used to excite the sample of interest. The best results were achieved when the aperture diameter was set to the same size as the mean size of speckles. A larger size of the aperture decreases the contrast of the temporal speckles; a smaller size reduces the excitation light intensity.

A small fraction of the excitation intensity was divided by a thin BK7 window and directed onto a biased Si photodiode (Thorlabs, 35 ns rise time) to acquire the excitation signal. The remaining part was used to excite a sample. Samples were excited by a fluctuating excitation intensity

with the typical mean value of 5  $\mu\text{W}$ , hence the efficiency of the excitation light extraction is approximately 0.1%. The PL signal was detected with a Hamamatsu photomultiplier (PMT) module type H10721-20 (rise time 0.6 ns). The module was placed close to the sample so that no collecting lens needed to be used. A cut-off color filter (OG 515) was placed in front of the PMT to shield out the excitation wavelength. Both the excitation and the PL signals were amplified by an SRS amplifier model SR445A and read out by a TiePie Handyscope HS3 USB oscilloscope.

In order to compare the results of the RATS method with a commonly used technique, we measured the same test samples on the RATS setup and on a Hamamatsu StreakScope C10627-11 streak camera coupled with a spectrograph. In the streak-camera measurements, we excited the sample with 515 nm pulses featuring a low excitation energy of 15 nJ/pulse and 190 fs pulse length. The spectrally resolved PL dynamics were attained with the central detection wavelength of 650 nm.

The modulation frequency of a generated random excitation signal is proportional to the peripheral speed of the diffuser and increases when the mean grain size on the diffuser is reduced. The mean size of speckles is given by the size of the focused laser spot on the diffuser and we set accordingly the diameter of the iris aperture in order to crop the speckle pattern (see Fig. 2). It is possible to improve the modulation frequency of the random excitation signal by reducing both the speckle size and the iris aperture diameter. However, a significant improvement in the modulation frequency also leads to a vast reduction of the excitation intensity and this effect was not used in our experiments.

### 3. Results and discussion

#### 3.1. Instrument response function

A crucial parameter of time-resolved spectroscopy is the attainable temporal resolution of a method. This is characterized by the impulse response function (IRF) of the method. The IRF can be determined as a reconstruction of scattered excitation light, or by measuring a sample, where PL decays very rapidly compared to the expected IRF width. We measured IRF by using PL from Rhodamine 6G solution, which has got PL lifetime in units of nanoseconds [14], and evaluated its full width half maximum (FWHM) for each experimental parameter. The IRF width is affected by several factors, which we discuss in the following paragraphs.

Analogously to standard methods, the presented method can be limited by the available bandwidth of the used photodetectors and amplifier. Since we used detection systems and electronics with a bandwidth exceeding 300 MHz, this fact did not limit the performance of the RATS setup.

As the method is based on the use of Fourier transform, it holds that the detection acquisition rate is the principal limitation of the shortest attainable lifetime and the total acquisition time is the principal limitation of the longest measurable lifetime. Nevertheless, the detected signal in the RATS experiment has to be sampled on a level where no aliasing occurs. Aliasing can cause severe distortion of the reconstructed PL decay. Therefore, it is essential to adjust the sampling rate according to the highest available frequency in the temporal speckle fluctuation or to use a low-pass frequency filter before the signal sampling.

Finally, it transpired that the main limiting factor in the RATS method case is the rate of temporal speckle fluctuation. The width of the IRF is inversely proportional to the maximum frequency present in the temporal speckle waveform. The frequency of speckles is directly proportional to the peripheral speed of the diffuser  $v$ . The frequency of speckles increases when the mean grain size is reduced and also when the beam spot size is reduced. This fact can be represented by function  $h(g, d)$ . Dependence of  $h(g, d)$  will be described in our future work. For clarity, Eq. (3) can be written:

$$FWHM_{(IRF)} \propto \frac{h(g, d)}{v} \quad (3)$$

To test this fact, we evaluated the IRF for an increasing frequency of the rotating diffuser. The beam spot size was approximately 50  $\mu\text{m}$ . The diffuser was 100 mm in diameter, featuring the mean grain size  $g$  of 1.52  $\mu\text{m}$ . Since the frequency of the temporal speckles is proportional to the peripheral speed of the diffuser, the IRF becomes inversely proportional to the diffuser rotational frequency, as one can also observe in Fig. 3. For a diffuser frequency reaching 65 Hz, the FWHM of the IRF decreased to 870 ns. Hence, the presented setup allowed us to measure PL dynamics with the microsecond and sub-microsecond resolution. On the other hand, the longest measurable PL lifetime is only limited by the acquisition time.

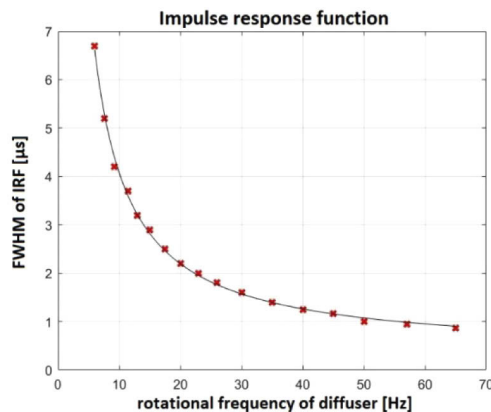


**Fig. 3.** Experimentally measured impulse response function width (FWHM) for different rotation frequencies of diffuser (red crosses) fitted with a reciprocal function (black line). Laser wavelength 488 nm, diffuser diameter 100 mm, grain size 1.52  $\mu\text{m}$ .

### 3.2. Test measurements

To test the presented method, we used an orange color filter (SCHOTT, OG 565, glass matrix containing  $\text{CdS}_x\text{Se}_{1-x}$  nanoparticles), which absorbs all wavelengths below 550 nm and can be therefore excited with the used laser (488 nm). Another test sample was a layer of nanoporous silicon, which was prepared by electrochemical etching of Si wafer in hydrofluoric acid and ethanol solution. Details of the porous silicon preparation process and its optical properties can be found in previous publications, see [2,15].

Figure 4 summarizes the detected random signals (top panels), their Fourier representation (middle panels), and the determined PL decay for both samples (black crosses in bottom panels). The PL decay of the OG 565 filter was fitted with a sum of two exponentials convolved with a Gaussian IRF (FWHM 1.2  $\mu\text{s}$ ), which shows good agreement between measured IRF for corresponding rotation frequency (55 Hz) and fitted IRF when the PL decay was evaluated (see Fig. 4(A), left panel). The PL fitted decay of the OG 565 filter (red line) was  $Ae^{t/\tau_1} + Be^{t/\tau_2}$ , where  $A = 0.14$ ,  $B = 0.006$ ,  $\tau_1 = 0.6 \mu\text{s}$  (sub-IRF),  $\tau_2 = 4.8 \mu\text{s}$ .

Nanoporous silicon PL features a broad range of lifetimes, as it decays via the so-called stretched exponential function  $A \cdot \exp[-(t/\tau)^\beta]$  [16]. The measurement of this sample was done for the frequency of the diffuser of 23 Hz (IRF FWHM of 1.9  $\mu\text{s}$ ). The determined PL decay [see Fig. 4(B), right panel] was fitted with the stretched exponential function convolved with the Gaussian IRF (red line). The attained fitted parameters of the PL decay were  $\tau = 0.7 \mu\text{s}$ ,  $\beta = 0.35$ .

The performance of the RATS method was verified by measuring the PL decay of the two test samples using a streak camera [17]. We picked the streak camera, as it is a commonly used device with a PL resolution very well below the RATS setup. The streak camera spectrograms were acquired on several timescales for each test sample. Figure 5(A) shows a selected spectrogram of

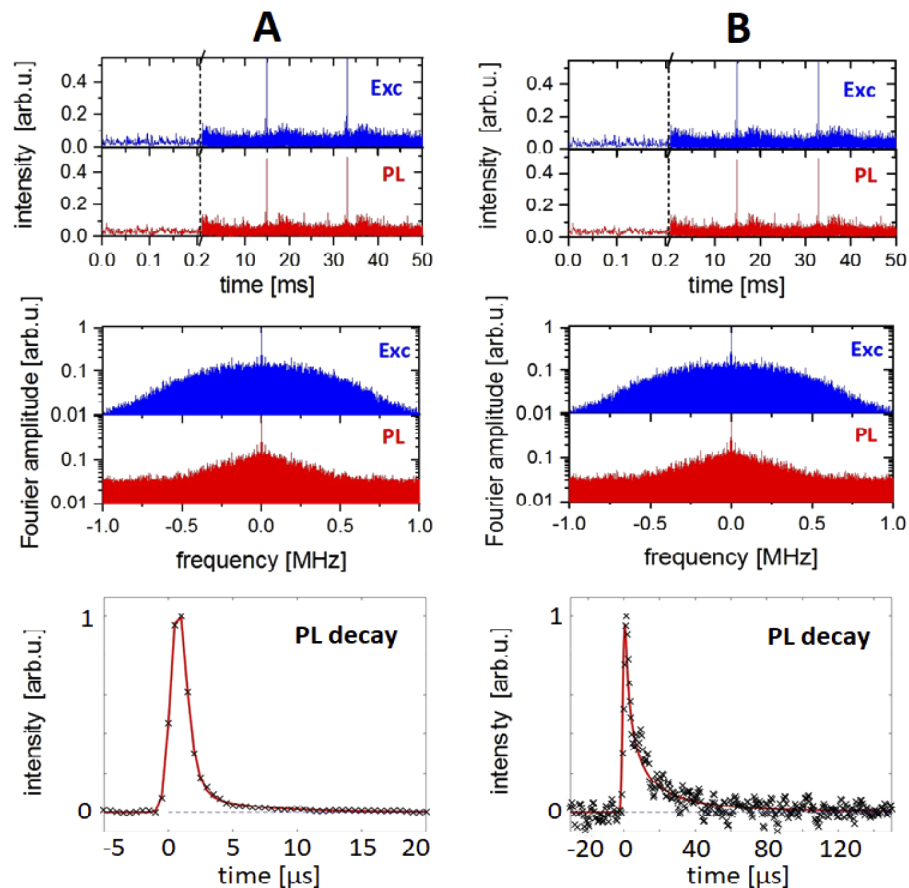


**Fig. 4.** Results of the RATS method for the orange filter OG565 (A) and nanoporous Si (B). Top panels: measured excitation and PL waveforms – note that the first 0.2 ms is zoomed in; middle panels: Fourier amplitudes of the signals – note the logarithmic y-axis; bottom panels: reconstructed PL kinetics (black crosses) fitted with PL decay convolved with Gaussian IRF (red lines).  $\lambda_{\text{exc}} = 488 \text{ nm}$ . IRF width: OG565:  $1.2 \mu\text{s}$ ; nanoporous Si:  $1.9 \mu\text{s}$ . Note that the sharp peaks in the temporal signals originate from a highly scattering spot on a diffuser.

the orange filter, in which the vertical axis represents the time axis, whereas the horizontal axis represents various wavelengths.

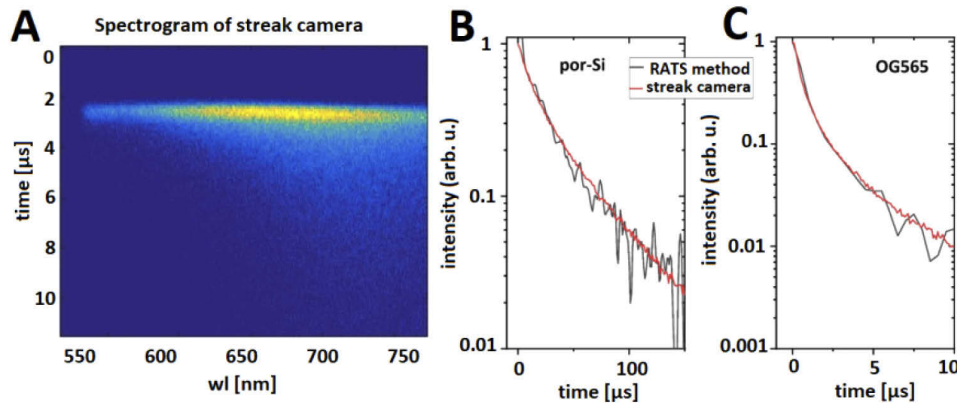


**Fig. 5.** Streak camera spectrogram of the orange filter sample (A). Excitation wavelength: 515 nm; energy 15 nJ/pulse; 190 fs pulse length. Comparison of PL decays of nanoporous silicon (B) and OG 565 filter (C) acquired by the RATS method (black curves) and integration of the streak camera data (red lines). For the sake of comparison, the data were normalized.

The attained PL decay curves are plotted in Figs. 5(B) and 5(C), where the red lines correspond to the streak camera curves, and the black lines were measured with the RATS method. The PL decays are in perfect agreement. The negligible difference could arise due to the fact that the PMT used in the RATS setup and the streak camera feature different spectral sensitivities. Since PL decay depends on PL wavelength (as can be clearly seen in Fig. 5), the total decay can vary for distinct sensitivities.

#### 4. Method potential and limitations

The presented method has several advantages compared to its standard counterparts. Firstly, as we stressed previously, the excitation source can be any coherent light source without the necessity to be modulated controllably. Instability of the source is not an issue since it will only positively contribute to the random fluctuations.

Moreover, the method is very robust against signal offsets both in the temporal and detector background sense. A temporal offset between the PL and the excitation intensity will lead to a constant offset in the complex phase in the reconstructed decay, i.e., the resulting curve will be the actual decay curve multiplied by  $e^{-i\varphi}$ . This can be corrected easily. At the same time, the background offset of the signals will manifest only on the zero-frequency edge of the Fourier transform and can again be avoided by removing the low frequencies from the decay reconstruction. It is worth noting that all presented results were acquired without any timing or background correction.

In order to demonstrate the robustness of the method, we provide in Fig. 6 a reconstruction of the simulated data from Fig. 1, where we applied the mutual delay between the PL and the excitation signal (see panel A) and the offset of excitation and the PL signal (see panel B). Signals were delayed up to 7.2% compared to the total acquisition time without any observable significant effect on the reconstructed decay curve. Analogously, the signal offset reaching 400% of the original signal amplitude did not affect the reconstructed PL decay curve. For the sake of better comparison, the PL decay curves are presented vertically stacked in a semi-logarithmic scaling.

The method has specific advantages compared to both the time-domain and the frequency-domain methods. Although the phase-based measurement in the frequency domain is well



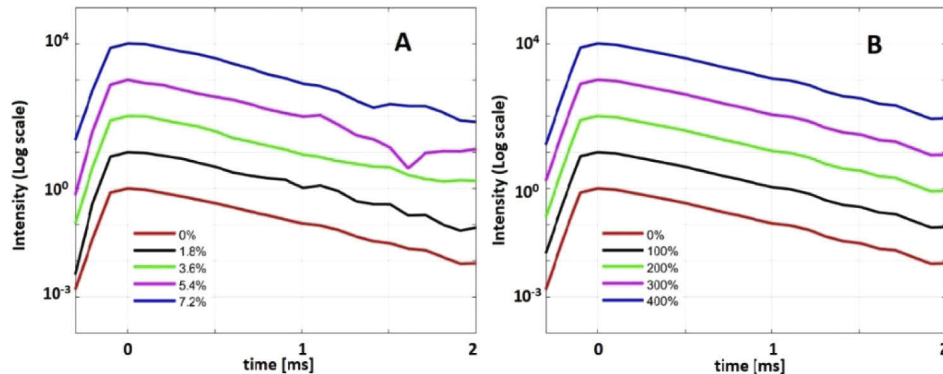


**Fig. 6.** Effect of temporal and background detection signal offset on the PL decay reconstruction. The simulated data from Fig. 1 were reconstructed for various delays between PL and excitation signal (panel A). The relative delay (0-7.2%) is given with respect to the total acquisition time. The same data were reconstructed for several offsets in the PL intensity signals (panel B). The relative offset (0-400%) is given with respect to the PL signal amplitude. Note that all curves are vertically stacked in a semilogarithmic scale in order to allow a better comparison.

developed on the sub-microsecond timescales, PL decay with a broad range of lifetimes – for instance, nanoporous silicon – requires scanning of the modulation frequencies. On the contrary, the RATS method, owing to the random sample excitation, extracts the PL decay from a single dataset. This is caused by the fact that the randomness of the signal covers a wide set of frequencies which is needed for proper reconstruction of PL decay.

The PL decay measurements in the time domain can be carried out efficiently at a low cost by using LED pulsed excitation sources [18]. However, the proposed method raises the term “low-cost” to a different level, as the excitation source can essentially be any laser module combined with a rotating diffuser (or any different means of random modulation).

The RATS method provides a very simple means of signal averaging. Experiments with pulsed excitation sources often rely on the measurements of many sequential excitations, where the detection has to be triggered with a corresponding precision. This part is entirely skipped in our setup, as the PL signal can be acquired for any period sufficient for the desired signal-to-noise ratio and the detection timing has no impact on the signal reconstruction.

At first sight, the proposed method uses inefficiently the excitation light, which is scattered by a diffuser. The ratio between the laser power and the mean excitation power in our experiments was 0.1%. Nevertheless, the sample is continuously excited by the source, whereas pulsed excitation uses a short flash of light from an LED. As a result, the LED provides a significantly lower number of excitation photons.

The presented method shares with the other methods for the measurement of PL decay in the temporal domain the need for a fast detection system and electronics. Nevertheless, such devices are widely available on the market, providing bandwidth of several hundreds of MHz. Therefore, the real limiting factor in our case lies in the properties of the diffuser, i.e., its peripheral speed and its grain size. The principal limitation of the method lies in the fact that the intensity of the PL emission must be linearly proportional to the excitation intensity. Under this condition, the measured PL waveform follows Eq. (1) and the convolution theorem can be used. Nevertheless, since the method relies on using a weak excitation intensity, this condition is satisfied for the majority of materials. Moreover, the method can be extended to be used for more general PL properties, namely, by changing the approach to PL decay reconstruction, where PL properties and lifetimes would be fitted to agree with the measured data.

The presented method can be simplified even more by pre-calibrating the  $I_{Exc}$  waveform. For a fixed position of the diffused beam and the diffuser center of rotation, the waveform will remain the same and does not need to be measured for each sample. Therefore, the entire optical setup can become even simpler by avoiding using a beam splitter and a reference photodiode.

## 5. Conclusions

We present a new approach to measuring PL decay, which can be used as a simple means of material characterization. The RATS (RANdom Temporal Speckles) method generates sample excitation by using a rotating diffuser without any need for a dedicated light source. With that approach, the method overcomes the need for advanced optical equipment and becomes a low-cost option for PL decay measurement.

By using this entirely different approach to the excitation signal, we can benefit from several advantages. Namely, no special requirements are put on the excitation source and its stability, and the method uses a low-cost setup enabling rapid data acquisition. Moreover, the random character of the excitation signal allows us to bring in advanced methods for computational reconstruction of PL decay, which will be addressed in our future work.

It should be mentioned that we optimized the diffuser and its peripheral speed so that the IRF width of 300 ns was achieved. Further reduction of the IRF width can be attained with a finer diffuser, a better-focused beam, or higher peripheral speed. However, the optimized diffuser was produced by using one of the finest abrasives (SiC 1000) and further increase in the peripheral speed is demanding with respect to the balancing of the diffuser disc. But e.g. using a proper microscope objective, it is still possible to reduce the size of the focused spot on the diffuser and thus reduce the width of IRF.

Nevertheless, the power of the idea of using a random signal for excitation of the measured sample can be, in principle, implemented by using any means of random modulation.

## Funding

Akademie Věd České Republiky (ERC-CZ/AV-B, project RUSH); Grantová Agentura České Republiky (Project 17-26284Y); Ministerstvo Školství, Mládeže a Tělovýchovy (Reg. No. CZ.02.1.01/0.0/0.0/16\_026/0008390); Grantová Agentura České Republiky (Project 19-14523S).

## Acknowledgments

We gratefully acknowledge Jakub Junek and Jakub Nečásek for their help with improving the diffuser rotation speed.

## Disclosures

The authors declare no conflicts of interest.

## References

1. L. Foglia, S. Vempati, B. Tanda Bonkano, L. Gierster, M. Wolf, S. Sadofev, and J. Stähler, "Revealing the competing contributions of charge carriers, excitons, and defects to the non-equilibrium optical properties of ZnO," *Struct. Dyn.* **6**(3), 034501 (2019).
2. K. Žídek, F. Trojánek, P. Malý, L. Ondič, I. Pelant, K. Dohnalová, L. Šiller, R. Little, and B. R. Horrocks, "Femtosecond luminescence spectroscopy of core states in silicon nanocrystals," *Opt. Express* **18**(24), 25241–25249 (2010).
3. A. Lavie-Cambot, C. Lincheneau, M. Cantuel, Y. Leydet, and N. D. McClenaghan, "Reversible electronic energy transfer: a means to govern excited-state properties of supramolecular systems," *Chem. Soc. Rev.* **39**(2), 506–515 (2010).
4. K. Kůsová, O. Cibulka, K. Dohnalová, I. Pelant, J. Valenta, A. Fučíková, K. Žídek, J. Lang, J. Englich, P. Matějka, P. Štěpánek, and S. Bakardjieva, "Brightly Luminescent Organically Capped Silicon Nanocrystals Fabricated at Room Temperature and Atmospheric Pressure," *ACS Nano* **4**(8), 4495–4504 (2010).



5. R. M. Clegg and P. C. Schneider, "Fluorescence Lifetime-Resolved Imaging Microscopy: A General Description of Lifetime-Resolved Imaging Measurements," in *Fluorescence Microscopy and Fluorescent Probes*, J. Slavík, ed. (Springer, US, 1996), pp. 15–33.
6. A. Fojtik and A. Henglein, "Surface Chemistry of Luminescent Colloidal Silicon Nanoparticles," *J. Phys. Chem. B* **110**(5), 1994–1998 (2006).
7. K. Zheng, K. Židek, M. Abdellah, M. E. Messing, M. J. Al-Marri, and T. Pullerits, "Trap States and Their Dynamics in Organometal Halide Perovskite Nanoparticles and Bulk Crystals," *J. Phys. Chem. C* **120**(5), 3077–3084 (2016).
8. P. I. H. Bastiaens and A. Squire, "Fluorescence lifetime imaging microscopy: spatial resolution of biochemical processes in the cell," *Trends Cell Biol.* **9**(2), 48–52 (1999).
9. M. J. Booth and T. Wilson, "Low-cost, frequency-domain, fluorescence lifetime confocal microscopy," *J. Microsc.* **214**(1), 36–42 (2004).
10. H. Szmajnski and J. R. Lakowicz, "Fluorescence lifetime-based sensing and imaging," *Sens. Actuators, B* **29**(1-3), 16–24 (1995).
11. H. Wang, Y. Qi, T. J. Mountziaris, and C. D. Salthouse, "A portable time-domain LED fluorimeter for nanosecond fluorescence lifetime measurements," *Rev. Sci. Instrum.* **85**(5), 055003 (2014).
12. F. Gascón and F. Salazar, "A simple method to simulate diffraction and speckle patterns with a PC," *Optik* **117**(2), 49–57 (2006).
13. A. N. Tikhonov and V. Y. Arsenin, "Solutions of ill-posed problems," (1977).
14. K. A. Selanger, J. Falnes, and T. Sikkeland, "Fluorescence lifetime studies of Rhodamine 6G in methanol," *J. Phys. Chem.* **81**(20), 1960–1963 (1977).
15. K. Dohnalová, L. Ondič, K. Kůsová, I. Pelant, J. L. Rehspringer, and R.-R. Mafouana, "White-emitting oxidized silicon nanocrystals: Discontinuity in spectral development with reducing size," *J. Appl. Phys.* **107**(5), 053102 (2010).
16. J. Linnros, N. Lalic, A. Gelackas, and V. Grivickas, "Analysis of the stretched exponential photoluminescence decay from nanometer-sized silicon crystals in SiO<sub>2</sub>," *J. Appl. Phys.* **86**(11), 6128–6134 (1999).
17. I. Pelant and J. Valenta, *Luminescence Spectroscopy of Semiconductors* (Oxford University, 2012).
18. M. Sulkes and Z. Sulkes, "Measurement of luminescence decays: High performance at low cost," *Am. J. Phys.* **79**(11), 1104–1111 (2011).



# Fluorescence lifetime imaging via spatio-temporal speckle patterns in a single-pixel camera configuration

J. JUNEK<sup>1,2,\*</sup> AND K. ŽÍDEK<sup>1</sup> 

<sup>1</sup>Regional Center for Special Optics and Optoelectronic Systems (TOPTEC), Institute of Plasma Physics, Czech Academy of Science v.v.i., Za Slovankou 1782/3, 182 00 Prague 8, Czech Republic

<sup>2</sup>Technical University in Liberec, Faculty of Mechatronics, Informatics and Interdisciplinary Studies, Studentská 1402/2, 461 17 Liberec, Czech Republic

\*[junekj@ipp.cas.cz](mailto:junekj@ipp.cas.cz)

**Abstract:** Photoluminescence (PL) spectroscopy offers excellent methods for mapping the PL decay on the nanosecond time scale. However, capturing maps of emission dynamics on the microsecond timescale can be highly time-consuming. We present a new approach to fluorescence lifetime imaging (FLIM), which combines the concept of random temporal speckles excitation (RATS) with the concept of a single-pixel camera based on spatial speckles. The spatio-temporal speckle pattern makes it possible to map PL dynamics with unmatched simplicity. Moreover, the method can acquire all the data necessary to map PL decay on the microsecond timescale within minutes. We present proof-of-principle measurements for two samples and compare the reconstructed decays to the non-imaging measurements. Finally, we discuss the effect of the preprocessing routine and other factors on the reconstruction noise level. The presented method is suitable for lifetime imaging processes in several samples, including monitoring charge carrier dynamics in perovskites or monitoring solid-state luminophores with a long lifetime of PL.

© 2021 Optical Society of America under the terms of the [OSA Open Access Publishing Agreement](#)

## 1. Introduction

Fluorescence lifetime imaging (FLIM) is an essential spectroscopic method in various fields, including medicine, biology, and material science. Interest in FLIM and its broad applicability stimulate its development. Therefore, FLIM has many different implementations based on a variety of fundamental methods for measuring photoluminescence (PL) decay, which include gated photoluminescence counting [1], streak camera [2], time-domain analog recording technique [3], or frequency-domain analog recording technique [4]. However, the most commonly used method is time-correlated single-photon counting (TCSPC) [5,6].

TCSPC is a powerful method to trace PL decay with a lifetime in the order of nanoseconds. However, due to the principle of TCSPC operation, data acquisition can take several hours for samples with a PL lifetime on the microsecond timescale. Therefore, the reduction of the acquisition time in FLIM has become a topic discussed in the literature in its own right [7]. A possible way to reduce the acquisition time is to apply so-called compressed sensing, where the image can be reconstructed from a highly reduced dataset [8,9]. However, these works rely on TCSPC and, despite reducing the acquisition times, FLIM of the samples with a long-lived PL decay still represents an issue. It is also worth noting that standard FLIM methods usually require costly setups.

In this paper, we present an entirely new concept of FLIM. The concept is based on the use of speckle patterns, both in the spatial and temporal sense, to map the PL decay of a sample. We combine compressive imaging, namely the concept of a speckle-based single-pixel camera [10], with our recent work [11], where random temporal speckles (abbr. RATS) make it possible to trace PL dynamics. In the presented concept, we employ spatio-temporal speckles, which are



generated by using two diffusers. The speckles can be generated with any coherent excitation source, i.e., without the need for a pulsed laser. At the same time, the detector is a standard single-pixel detector, e.g., a photomultiplier. The setup is, therefore, very simple, robust, and low-cost. Owing to the novel approach to PL decay acquisition, the method is highly suitable for mapping PL dynamics on the microsecond timescale, where the FLIM dataset can be acquired within minutes. We demonstrate this on proof-of-principle measurements by imaging PL decay of selected scenes (colour filters and Si nanocrystal layers) and we also discuss the effect of speckle properties on the resulting noise level.

The presented method can serve as a simple approach to characterizing the morphology of samples with prominent PL decay in the order of microseconds, which include halide perovskite samples, solid-state luminophores, or Si nanocrystals [12–14].

## 2. Principle of the method

### 2.1. Concept of RATS method

The cornerstone of the presented FLIM concept is the RATS method, which is described in detail in our previous work [11]. This novel method for the measurement of PL decay uses randomly fluctuating intensity  $I_{EXC}$  to excite a sample. The PL signal  $I_{PL}$  is then given as a convolution of  $I_{EXC}$  and PL decay  $I_D$ :

$$I_{PL} = I_{EXC} * I_D. \quad (1)$$

Therefore,  $I_D$  can be extracted via the convolution theorem using the Fourier transform, where we apply the so-called Tikhonov regularization weighted with the factor  $\varepsilon$  [15]:

$$I_{decay} = Re \left\{ \mathbb{F}^{-1} \left[ \frac{\mathbb{F}(I_{PL}) \mathbb{F}^*(I_{EXC})}{\mathbb{F}(I_{EXC}) \mathbb{F}^*(I_{PL}) + \varepsilon \mathbb{F}(I_{EXC}) \mathbb{F}^*(I_{EXC})} \right] \right\}. \quad (2)$$

The random character of  $I_{EXC}$  allows us to measure a broad range of frequencies. Thus, a single measurement of  $I_{EXC}$  and  $I_{PL}$  provides information sufficient for the complete  $I_D$  reconstruction. Since the original method acquires PL decay for a single spot only, we will hereafter denote the method as 0D-RATS. The principle of the method is described in Fig. 1, based on simulated data. In order to get a randomly-fluctuating excitation signal, the demonstrated 0D-RATS method uses temporal speckles generated via a rotating diffuser. However, the presented approach can use any principle of random temporal signal generation, which means the RATS method can be understood in more general terms as the Random Temporal Signals method.

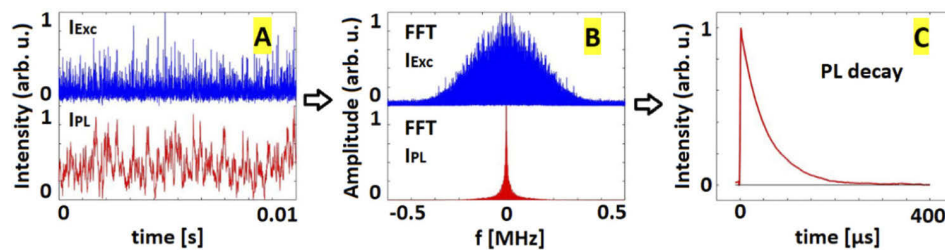


**Fig. 1.** Sequence showing the principle of  $I_D$  evaluation using the 0D-RATS method. A) Simulated temporally fluctuating intensity  $I_{EXC}$  (blue) and detected photoluminescence signal  $I_{PL}$  (red) arising due to a monoexponential decay (lifetime  $\tau = 50 \mu s$ ). For clarity, a shorter time section is shown, than was used for reconstruction (0.1 s). B) Amplitudes of Fourier transform of  $I_{EXC}$  (blue) and  $I_{PL}$  (red). C) Reconstructed  $I_D$  via convolution theorem, Eq. (2).

New approaches to generating a temporally random light signal are likely to be found. This could mean an improvement both in terms of excitation intensity and higher frequency of the excitation signal.

## 2.2. Concept of proposed 2D-RATS method

An efficient approach to converting the 0D-RATS method to the imaging mode is to use the single-pixel camera. The principle of a single-pixel camera can be seen in many review articles [16]. In a single-pixel camera experiment, the measured sample is illuminated by a set of masks (see Fig. 2), which, in our experiment, were speckle patterns. Each illuminating random mask excites PL in different parts of the sample. After illuminating the sample with a sufficient number of masks, it is possible to retrieve the spatial information by detecting the overall level of the emitted PL and by using dedicated algorithms, as we will describe below. However, the condition that must always be met is the linear dependence between the measured and the reconstructed data.

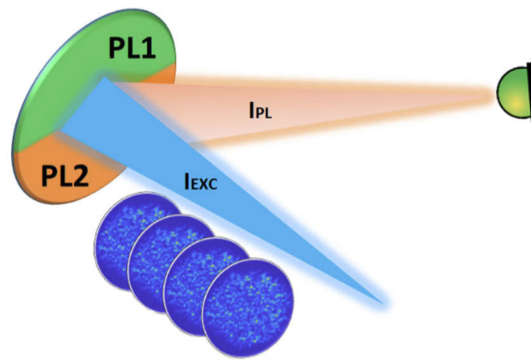


**Fig. 2.** Scheme of single-pixel camera image acquisition by using speckle patterns – see text for details.

In our FLIM approach, the illuminating masks are generated with a movable diffuser, which is placed behind the source of light with randomly fluctuating intensity in time, i.e., temporal speckles. Thus, we attain spatio-temporal speckles, which retain the same spatial pattern  $S(x,y)$ , while the overall intensity is blinking rapidly as  $I_{EXC}(t)$ . In other words, the measured sample is illuminated with a blinking pattern  $P(x,y,t) = S(x,y)I_{EXC}(t)$ . To map the PL decay  $I_D$ , i.e., to retrieve  $I_D(x,y,t)$ , it is necessary to detect  $I_{EXC}(t)$  with a diode,  $I_{PL}(t)$  with a photomultiplier, and the speckle pattern  $S(x,y)$  with an array 2D detector (e.g., CMOS camera).

Equation (1) can be rewritten for a 2D sample into a more general case, where  $n$  areas with different  $I_D$  are measured. The total emitted  $I_{PL}$  is the sum of the contributions from all sample spots:

$$\sum_{i=1}^n I_{PL(i)} = I_{EXC} * \sum_{i=1}^n I_{D(i)}. \quad (3)$$

For a given mask, we can evaluate from the measured data an average PL decay of the entire illuminated area  $I_{DA}$ :

$$I_{DA} = Re \left\{ \mathbb{F}^{-1} \left[ \frac{\mathbb{F} \left( \sum_{i=1}^n I_{PL(i)} \right) \mathbb{F}^*(I_{EXC})}{\mathbb{F}(I_{EXC}) \mathbb{F}^* \left( \sum_{i=1}^n I_{PL(i)} \right) + \epsilon \mathbb{F}(I_{EXC}) \mathbb{F}^*(I_{EXC})} \right] \right\}. \quad (4)$$



A different  $I_{DA}$  will be detected for each mask, as illustrated in Fig. 3(A). The variation of the  $I_{DA}$  value, i.e., PL decay, for a selected time and different masks will be denoted as  $d$ . See Fig. 3(B) for an example of a short subset of seven masks and four different times. We can vectorize each illumination mask into a single row of the so-called observing matrix  $A$  and we can also vectorize the map of the PL intensity into a vector  $m$ . In this case, we can express their relation as a simple matrix multiplication:

$$d = Am. \quad (5)$$

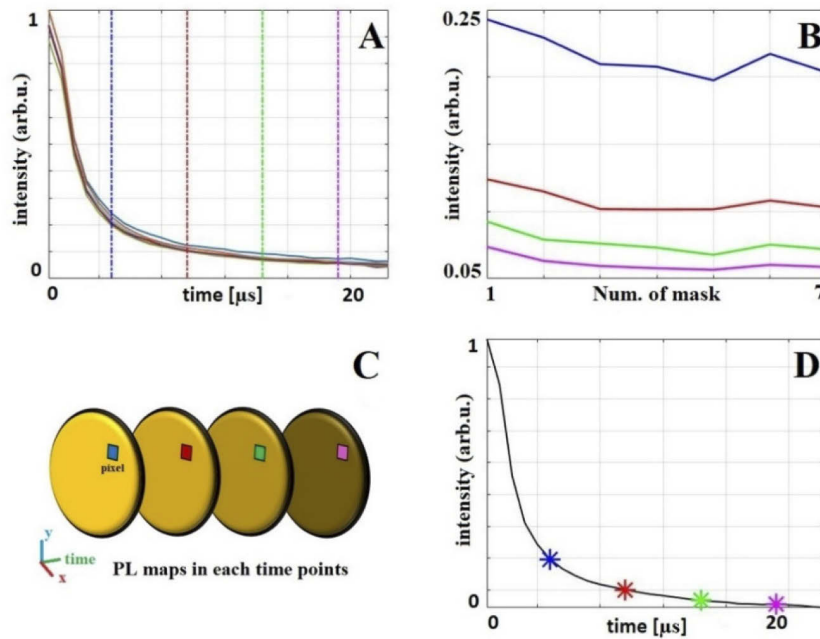


**Fig. 3.** (A) Examples of simulated  $I_D$  curves, which differ due to the change of the illuminating mask. (B) Varying intensity for the seven different masks in selected time-points of simulated  $I_D$  curves – see dashed lines in panel A. (C) Example of reconstructed PL maps. Selected pixels are marked with a colour corresponding to the time point. (D) A simulated example of reconstructed  $I_D$  in four time points. Reconstruction at multiple points would copy the entire  $I_D$  (solid black line).

Matrix  $A$  has a number of columns corresponding to the number of map pixels  $N$ , while the number of rows follows the number of used masks  $M$ , i.e., the number of measurements. The ratio between  $M$  and  $N$  determines the compression ratio  $k = M/N$ .

We aim at solving an underdetermined system, which can be accomplished by means of a compressed sensing algorithm where we employ a regularization. In this work, we used the algorithm TVAL3 [17,18], which is based on the minimization of total variation  $TV$  of reconstructed images and follows Eq. (6) [19].

$$\min\{\|d - Am\|_2^2 + TV(m)\}. \quad (6)$$

Using Eq. (6), it is possible to reconstruct the PL map  $m(x,y)$  for each time point  $t$  [see Fig. 3(C)]. Knowing that we are reconstructing a PL image, we can constrain the solution to  $m \in R$  and  $m \geq 0$ . If we stack the individual  $m(x,y)$  behind each other, we create a 3D matrix  $m(x,y,t)$

that corresponds to the appropriate PL intensity  $I_D(x, y, t)$  of the sample. Therefore, we can also extract PL decay for any selected spot of the sample [see Fig. 3(D)] and we can fit the obtained PL dynamics  $I_D$  with a single- or multi-exponential decay to get the lifetime map.

### 3. Optical setup

The used optical setup is depicted in Fig. 4. We used a CW laser at wavelength 405 nm (IO matchbox laser diode, free-space) as a light source. The combination of a focusing lens A ( $f = 25.4$  mm), a rotating diffuser (average grain size  $3.87 \mu\text{m}$ ) with a collimating lens B ( $f = 75$  mm), and an aperture (diameter 1.5 mm) generated intensity randomly fluctuating in time  $I_{EXC}(t)$ .

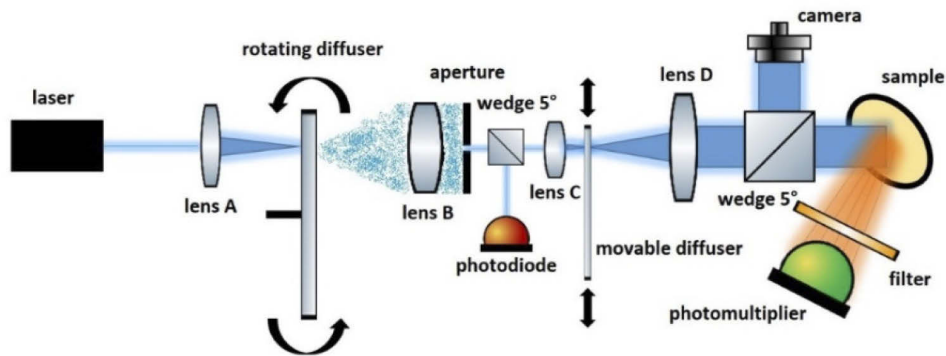


Fig. 4. Scheme of the used optical setup – see text for details.

The generation of a random mask (spatial speckles) is achieved with another focusing lens C ( $f = 25.4$  mm). The beam is focused on a movable diffuser (average grain size  $8.06 \mu\text{m}$ ) and the diffused light is again collimated with lens D ( $f = 50$  mm). The resulting mask pattern was blinking, according to  $I_{EXC}(t)$ .

The patterned beam is split twice with two N-BK7 glass wedges ( $5^\circ$ ), which reflect about 6% of the incident intensity. The first reflection is used to detect  $I_{EXC}(t)$  with a Si amplified photodetector (Thorlabs PDA8A2, rise time 7 ns). The second reflected beam is used to acquire the mask pattern with a camera (CMOS, IDS UI-3240ML-M-GL). The transmitted pattern is used to illuminate the measured sample. The PL emitted from the excited sample, i.e., the  $I_{PL}(t)$  signal, was detected with a type H10721-20 Hamamatsu photomultiplier (PMT) module (rise time 0.6 ns). The scattered excitation light was blocked by a cut-off filter at 500 nm (Thorlabs, FEL0500). The detected PL signal was amplified by a model SR445A SRS amplifier and read out by a TiePie Handyscope HS5-110XM USB oscilloscope.

The laser beam intensity entering the setup is 138.5 mW, while the full average intensity that illuminates the measured sample oscillates around  $5.5 \mu\text{W}$ . The overall efficiency of the system is about 0.003%, which can be, however, improved approximately 10 times by optimizing the parameters of the optical elements. The size of the measured area was about  $18 \text{ mm}^2$  and is given by the size of the generated speckle masks. It is possible to scale the field of view by adjusting the collimating lens D.

The TCSPC setup which was employed for the reference measurements used a picosecond laser at 405 nm, 100 kHz repetition rate, and 0.2 nJ/pulse. The laser pulses excited a PL signal detected by a PMT. The decay data were acquired by a PicoHarp 300 module. The impulse response function (IRF) of the TCSPC setup was negligible ( $< 1$  ns) in comparison with the lifetimes of the measured samples, and, therefore, it has not been taken into account.

#### 4. Results and discussion

As a proof-of-principle experiment, we carried out imaging of a combination of an OG565 orange absorbing cut off filter and a Si wafer with a nanoporous surface prepared by electrochemical etching of the Si wafer in hydrofluoric acid and ethanol solution [14,20]. Both samples had been measured previously by the 0D-RATS method and the resulting PL decay shapes had been verified with a standard method, namely the streak camera, and can be found in a previously published article [11].

In order to compare the data with methods commonly used for FLIM, we verified the 0D-RATS method with a reference TCSPC method. The comparison depicted in Fig. 5 confirms the correctness of the RATS approach. The 0D-RATS data (symbols) were measured in the same configuration and with the excitation light parameters described in Section 3. For the sake of this comparison, the detected spectral region in both setups (RATS and TCSPC) was restricted by colour filters to 500–800 nm. To compare the decays from the zero time, the TCSPC data were convoluted with the IRF of the 0D-RATS method, i.e., Gauss function with a full width half maximum (FWHM) equal to 0.59  $\mu\text{s}$ . This convolution caused the depicted TCSPC curves (blue curves in Fig. 5) to be very smooth, in spite of the significant noise level in the raw data.

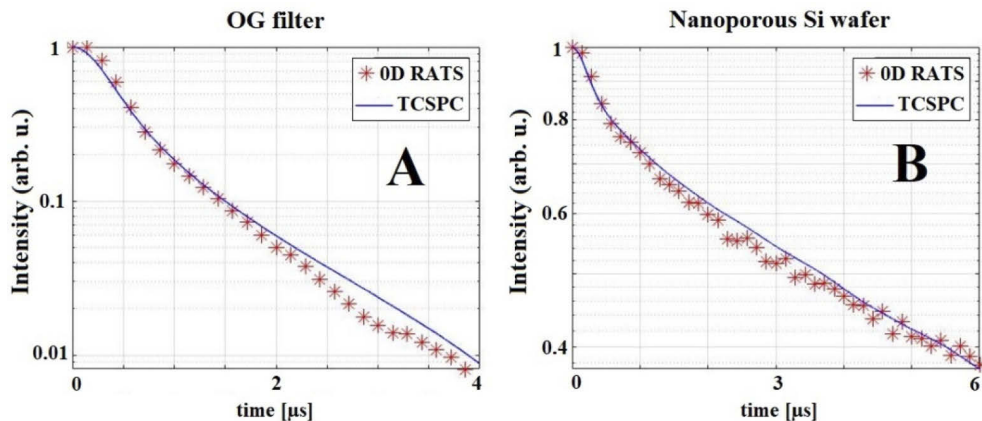


**Fig. 5.** 0D-RATS method verification with TCSPC method. Excitation wavelength: 405 nm; energy 19  $\mu\text{W}$ /pulse, 100 kHz repetition rate. Comparison of PL decays of OG 565 filter (A) and nanoporous Si wafer (B) acquired by 0D-RATS method (blue lines) and TCSPC data convoluted with impulse response function of RATS measurement (red marks). See text for details. For the sake of comparison, the data have been normalized.

For the benefit of the comparison of the two methods, it is worth noting that, due to the long PL lifetimes, it was necessary to use a low excitation repetition rate (100 kHz) in the TCSPC setup. This led to the TCSPC acquisition time of 20 minutes (used for data in Fig. 5). In contrast, the 0D-RATS method acquired the PL decay data within 2 seconds. This value is proportionate to the acquisition time of the methods commonly used for microsecond PL measurement, such as direct PMT decay acquisition. Nevertheless, as we showed in the previous section, the RATS method allows a simple and low-cost implementation of FLIM based on the use of a single-pixel camera.

##### 4.1. Single-pixel camera PL map reconstruction

Our method is based on compressive imaging and requires iterative image reconstruction, which was described in Eq. (6). The crucial parameters (together with their set value) were:  $\mu$  ( $2^9$ ),

$\beta$  ( $2^6$ ). The reconstruction parameters were set according to the reconstruction of the testing experiments and simulations, and the same parameters are used for all the presented images.

#### 4.2. Mask preprocessing

We captured the speckle mask on a CMOS chip and, prior to its use, we carried out a set of operations to convert the speckle image into a form suitable for our calculation.

The first part of preprocessing was cropping of the mask. Since the mask did not occupy the entire camera chip, the image was cropped so that the information value remains and at the same time we reduce the number of reconstructed pixels  $N$ .

The second part was the mask rescaling. A laser speckle pattern is a natural random pattern, where the dimensions of each speckle vary around a certain mean value. For this reason, it is unclear how the high-resolution camera image of laser speckles  $a_M$  should be rescaled into the image  $a_M'$  used in the measurement matrix  $A$  while retaining the useful information. An example of such rescaling is presented in Fig. 6.

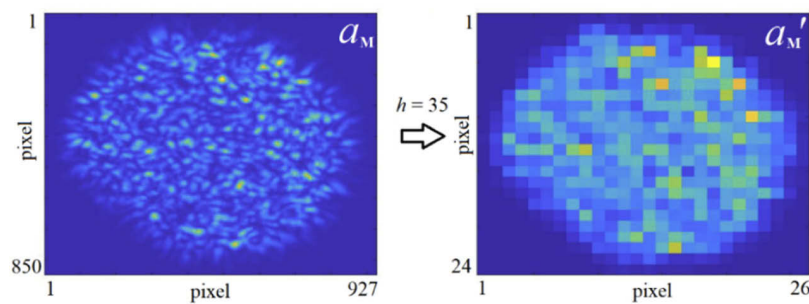


**Fig. 6.** Cropped original camera image of speckle patterns ( $a_M$ , left-hand side) compared to the processed mask pattern ( $a_M'$ , right-hand side) with a scaling factor  $h = 35$  pixels, which corresponds with the mean speckle size of the  $a_M$  pattern.

##### 4.2.1. Mask rescaling effect

By using a set of simulations, we examined how the image reconstruction quality is affected by a varying mask scaling factor. The set of masks employed in the simulations, i.e., camera images of speckles, was acquired in the real measurements. The mean speckle size  $h$  for the examined set of masks is  $h = 35$  pixels, which was calculated as the full width half maximum (FWHM) of the speckle pattern autocorrelation function [21]. The compression ratio  $k$  was set for the purpose of the simulations to 0.4, and the noise level of the PL intensity was set to the  $\sigma = 0.5\%$ .

The reconstruction error of the PL maps was calculated as an  $l_2$  norm of the vectorized reconstructed image  $m$  and the original image  $U$ . To normalize the error for the image intensity, we calculate the relative error  $r$ :

$$r = \frac{\|m - U\|_2}{\|U\|_2}. \quad (7)$$

Since the scaling factor changes the number of pixels of a mask, the number of reconstructed image pixels  $N$  changed accordingly. The straightforward evaluation of the reconstruction quality by using residues was not meaningful because a smaller number of pixels leads to a lower level of residues despite worse image quality since we are solving a highly underdetermined system.

The simulations based on two different PL maps in Figs. 7(A)–7(B) show that the relative error  $r$  does not have a strong systematic dependence on the scaling factor [see Fig. 7(C)]. It is only possible to observe a slightly decreasing trend of the error towards smaller scaling values.

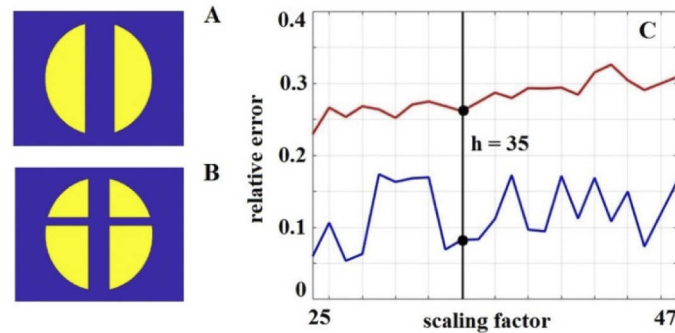


**Fig. 7.** Effect of scaling factor  $h$  on relative error in image reconstruction of two different PL maps depicted in panel A (red line in C) and panel B (blue line in C). The black line in panel C denotes the scaling factor according to the mean speckle size.

However, maintaining a given compression ratio for a higher resolution implies increasing the number of scanned masks, thus increasing the total acquisition time. Therefore, as a reasonable compromise, we used the scaling factor  $h = 35$  that corresponded to the average speckle size of the used patterns. The effect of this scaling is illustrated in Fig. 6, which was processed based on this value.

#### 4.3. Proof-of-principle measurements

The first analyzed sample was an OG565 orange absorbing cut-off filter, which was divided with an opaque line into two regions with the same PL decay dynamics  $I_D$ . Such a situation corresponds, for instance, to a mapping of a single PL marker in a sample. The illuminated spot was the size of  $\sim 18 \text{ mm}^2$ , the number of masks  $M = 400$ . The mask resolution was rescaled according to the speckle size ( $h = 35$  pixels), leading to the image resolution of  $28 \times 36$  ( $N = 1008$ ).

We tested image reconstruction for three different compression ratios  $k$ , where the number of pixels  $N$  remained the same and the number of used masks  $M$  was decreased accordingly. Namely, we employed the compression ratio  $k = 0.4$  [see Fig. 8(A)],  $k = 0.2$  [see Fig. 8(B)], and  $k = 0.05$  [see Fig. 8(C)]. The corresponding data acquisition times were 47 min, 24 min, and 6 min, respectively. The results are summarized in Fig. 8 and divided into areas A, B, and C, correspondingly.

The left part shows the reconstruction of the PL map for two different times. The middle part includes graphs “a” and “b”, which show the  $I_D$  of a randomly selected pixel, which corresponds to the reconstructed area “a” or “b”. The graphs include two time points (blue and violet), which correspond with time points of the PL maps from the left part of the figure. The reconstructed  $I_D$  data (lines) were compared to the OD-RATS method (red circles). In all cases, the PL decays obtained by the 2D-RATS method are in perfect agreement with the data from the OD-RATS method. Although the reconstructed PL maps for the compression ratio  $k = 0.05$  are noisy compared to the higher compression ratios, the PL decays from OD and 2D RATS methods are still in perfect agreement.

The FLIM spectrogram is shown on the right side of the image. Individual  $\tau$  values were determined by the fitting algorithm. The reconstructed  $I_D$  curves for each pixel were fitted with a bi-exponential function. Lifetime  $\tau$  was then determined as the time when the intensity of the fitted bi-exponential decay decreased to 10% of the curve maximum. The impulse response function of the measurement was  $0.47 \text{ }\mu\text{s}$ .



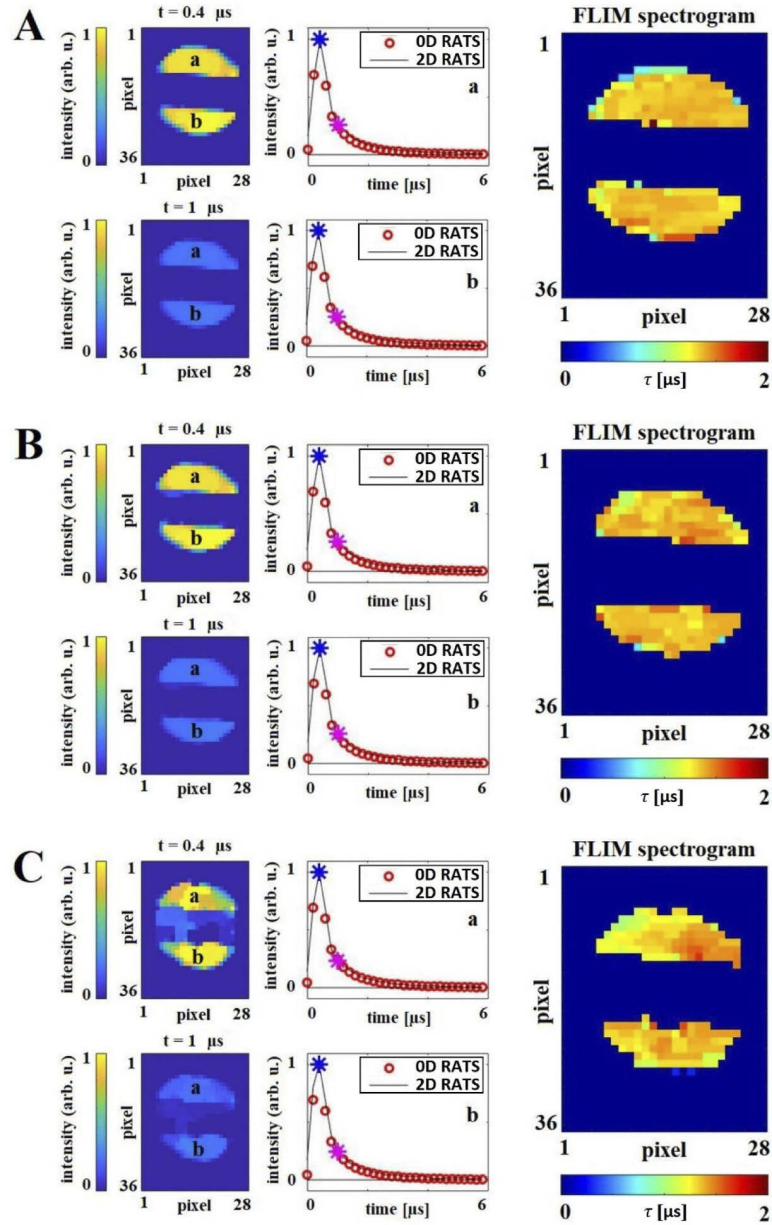


**Fig. 8.** Measurement of a masked OG565 filter: (A) compression ratio 0.4, (B) compression ratio 0.2, (C) compression ratio 0.05. Left panels: reconstruction of the PL map for two different times. Middle section: graphs “a” and “b” show the reconstructed  $I_D$  from 2D-RATS in a randomly selected pixel (“a” pix [14,10], “b” pix [16,25]) and  $I_D$  given via 0D-RATS; blue and violet stars denote the time of the PL maps on the left. Right section: map of the PL lifetimes for the points where the PL amplitude exceeded 10% of the maximum PL intensity.



The mean lifetimes for the sample measured with compression ratios 0.4, 0.2, and 0.05 are 1.31  $\mu\text{s}$ , 1.29  $\mu\text{s}$ , and 1.29  $\mu\text{s}$ . The mentioned average lifetimes vary with standard deviations of 0.09  $\mu\text{s}$ , 0.10  $\mu\text{s}$ , and 0.13  $\mu\text{s}$ . The statistical data do not include points that did not show a luminescence intensity lower than 10% of the sample maximum, as well as data from the sample edge, which were suffering from scattering signal and high noise level.

We observed that the lifetime precision, i.e., acquired standard deviations, are only marginally affected by the used compression ratio. This ratio has more effect on the quality of the lifetime maps.

In the second measurement, we acquired FLIM data of an artificially prepared sample with two different dynamics of PL decays  $I_D$ . The first area was an OG565 colour filter, while the second area consisted of a Si wafer with a nanoporous surface.

Both the OG565 filter and the nanoporous Si had been previously tested with a standard method and the OD-RATS method, and the results from both OD-RATS methods (Fig. 9, red crosses) were compared in randomly chosen pixels of the 2D PL map (see Fig. 9, solid lines). The results are summarized in Fig. 9 which follows the same logic as Fig. 8 but the compression ratios are different.

The measured area was around 18 mm<sup>2</sup>; in total, 600 masks were scanned. Mask resolution was rescaled again according to the mean speckle size (35 pixels), leading to a resolution of the reconstructed PL map of  $26 \times 24$  ( $N = 624$ ). Due to the lower  $I_{PL}$  amplitude of nanoporous Si, the reconstructed data suffer from a lower signal-to-noise ratio. For this reason, we present reconstructed data for compression ratios  $k = 0.9$  [Fig. 7(B)], and  $k = 0.5$  [Fig. 7(C)]. The corresponding data acquisition times were 63 min, 49 min, and 35 min, respectively. The PL maps in Fig. 9 (left-hand side) have been normalized so that each data point has the same amplitude. Therefore, we observe a flat PL image at the early times (0.6  $\mu\text{s}$ ), while for the later time (1.6  $\mu\text{s}$ ), the prominent PL intensity is emitted from the upper part, i.e., nanoporous Si with a long PL decay.

Analogously to the previous measurement, individual  $\tau$  values were determined again by fitting the data with double-exponential decay for both areas (OG565 and nanoporous Si). Lifetime  $\tau$  corresponds, analogously to the previous measurement, to the time where the intensity of fitted  $I_D$  drops to 10% of the curve maximum. The impulse response function of measurement was 0.47  $\mu\text{s}$ . For the nanoporous Si wafer, the mean lifetimes for the compression ratios of 0.9, 0.7, and 0.5 correspond to 21  $\mu\text{s}$ , 21  $\mu\text{s}$ , and 20  $\mu\text{s}$  with a standard deviation of 3  $\mu\text{s}$ , 3  $\mu\text{s}$ , and 4  $\mu\text{s}$ , respectively. For the OG565 filter, the mean lifetimes were 1.19  $\mu\text{s}$ , 1.24  $\mu\text{s}$ , and 1.28  $\mu\text{s}$ , varying with a standard deviation of 0.09  $\mu\text{s}$ , 0.16  $\mu\text{s}$ , and 0.27  $\mu\text{s}$ . The statistics included again only points that did not have a luminescence intensity greater than 10% of the sample maximum, as well as the edge points of the sample with the prevailing scattering signal. In the combined sample, we attained for all measurements a slightly lower lifetime of the OG565 filter area compared to the first sample. This arises due to the highly scattering Si wafer, which leads to a stronger leakage of the excitation signal compared to the first measurement. Subsequently, a larger amount of scattered excitation light reaches the detector and influences the results because it forms a response-function-limited peak, which it is not possible to completely separate from the PL decay.

#### 4.4. Reconstruction error vs. intensity of PL decay

The intensity of PL is crucial for the resulting data reconstruction. This can be documented by the fact that the attained PL decay of the nanoporous Si suffers from a significantly higher noise level compared to the OG565 filter data. Analogously, we observed that the noise level of the PL decay increases with the delay after excitation, as the PL intensity decays and decreases. This effect was studied by using a relative error of reconstruction on the real dataset to capture the realistic behaviour of the experimental system, including the noise characteristics of the detectors.

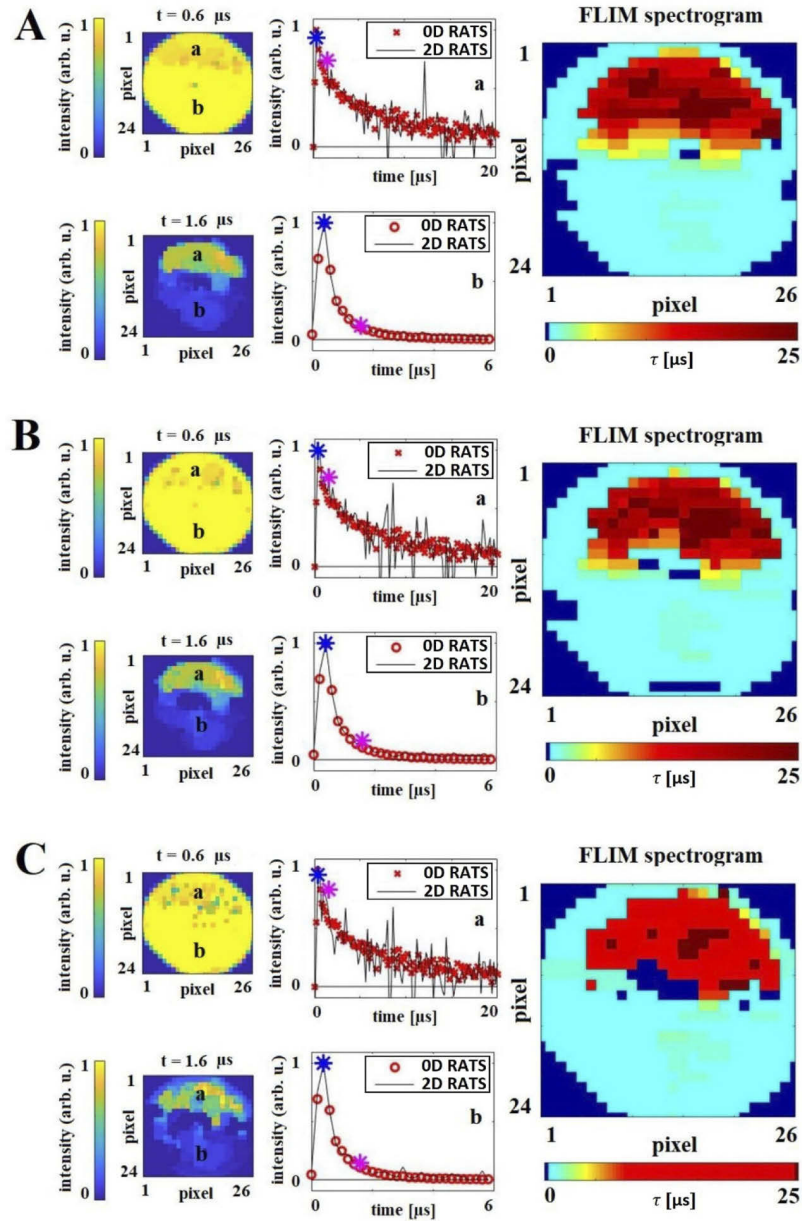


**Fig. 9.** Measurement of nanoporous Si wafer. (A) compression ratio 0.9, (B) compression ratio 0.7, (C) compression ratio 0.5. Left panels: reconstruction of the PL map for two different times. Middle part: graphs “a” and “b” show the reconstructed  $I_D$  from 2D-RATS in a randomly selected pixel (“a” pix [14,10], “b” pix [16,25]) and  $I_D$  given via 0D-RATS; blue and violet stars denote the time of the PL maps on the left. Right part: map of the PL lifetimes for the points where the PL amplitude exceeded 10% of the maximum PL intensity.

The relative error  $\sigma$  was determined as the average absolute deviation of the back reconstructed intensity signal  $d^R = Am$  [see Eq. (6)] and the original signal  $d$  at a given time point relative to the average value  $d$ :

$$\sigma = \frac{1}{M} \sum_{i=1}^M \frac{|d_i^R - d_i|}{d_i}. \quad (8)$$

Figure 10(A) (top panel) shows representative reconstructed decays for the first measurement (two areas with the same PL decay (OG565)). The PL decay of the upper part of the measured sample is indicated by a red line and the lower part with a blue line. In the bottom panel of Fig. 10(A), the relative error of reconstruction is evaluated. The same logic is also applied in Fig. 10(B), which shows representative decays for the combined sample (nanoporous Si + OG565 filter). The red line shows the PL decay of the upper part of the sample (nanoporous Si) and the blue line shows the PL decay of the lower part of the sample (filter OG565). The bottom panel of Fig. 10(B) then shows the relative reconstruction error. The relative error comparison according to Eq. (8) depicted in Fig. 10 (bottom panels) was done for the same compression ratio  $k = 0.6$  and identical image resolution  $26 \times 24$ . This ensures that the length of the vector  $d$  remains constant. For cases where the length of the vector  $d$  changes, it is more appropriate to observe the reconstruction error with Eq. (7) because a lower number of elements of  $d$  can cause the reconstruction algorithm TVAL3 to reach a better agreement between  $d$  and  $d_0$  while the reconstruction of the PL map can feature a lower quality.

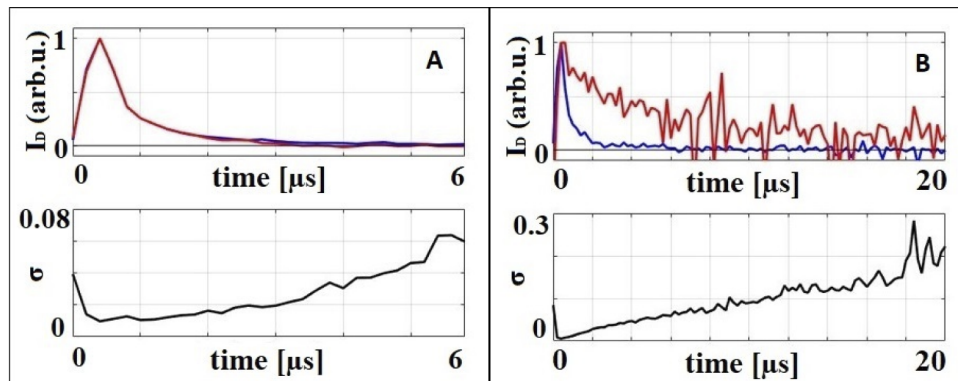


**Fig. 10.** Relative reconstruction error evaluation with respect to the level of  $I_D$  intensity. Upper panels: Two examples of PL decay curves (red and blue lines) extracted from the sample with two identical areas (filter OG565, panel A) and from the sample with two different areas (nanoporous Si + filter OG565, panel B). Bottom panels: reconstruction error  $\sigma$  is evaluated as a relative error via Eq. (8) in each reconstructed time point.

For both cases in Fig. 10, we observe that the relative error level steadily increases with the decreasing PL intensity (see the bottom panels). Thus, we can conclude that for a higher intensity of detected PL it would be possible to reconstruct decays with a lower relative error even for small compression ratios. However, the relative error still increases with the decreasing intensity of PL decay.

## 5. Conclusion

We present a new approach to FLIM, which is based on a combination of the random temporal speckles (RATS) method with the concept of a single-pixel camera. Spatio-temporal random speckle patterns make it possible to track both PL images and dynamics on the microsecond timescale. The speckle generation is based on rotating and movable diffusers, which reduces

system requirements. The result is a low-cost FLIM setup of unrivalled simplicity. The strength of the new concept lies in the imaging of PL decay on the microsecond timescale because the lifetime acquisition time is reduced owing to the use of compressed sensing. At the same time, the method can be performed using a simple single-pixel detector.

When compared to other commonly-used options of FLIM, the sample point-by-point scanning of PL decay rapidly reaches extremely high acquisition times as the resolution of an image increases. For instance, a  $60 \times 60$  pixel image measured at 2 s per decay requires a total acquisition time of two hours. The use of intensified CCD or TCSPC with a 2D array of single-photon avalanche diodes (SPAD) can provide fast FLIM even in the microsecond timescale. Nevertheless, the use of such an array detector dramatically increases the cost of the setup.

The acquisition time of 2D-RATS depends on several factors. The most prominent one is the PL map resolution and the related compression ratio. We have shown that it is reasonable to use scaling according to the mean speckle size. A lower resolution causes a loss in the image quality, while a higher resolution cannot provide more information, as the resolution is limited by the mean speckle size. The FLIM data reconstruction error also highly depends on the intensity of PL. Hence, we can achieve fast acquisition by using a higher PL intensity while decreasing the compression ratio. Under ideal conditions, i.e., highly emitting samples, we were able to reach an acquisition time of 6 minutes. For a standard sample, it was necessary to increase the compression ratio and the resulting acquisition time reached 35 minutes.

We would like to stress that the 2D-RATS method is a general concept, which uses spatio-temporal random patterns to carry out time-resolved imaging. It can be therefore generalized for the imaging of any temporal signal and has many possible ways of implementation. Since this article serves as a demonstration of the new method, further optimization of the optical setup can provide us with more efficient excitation use and PL collection. For instance, the use of a pair of diffusers causes the vast majority of the excitation light energy to be lost in the setup and the resulting low excitation intensity can be limiting. Nevertheless, this can be solved by modifying the approach to mask generation – for instance, by using a digital micro-mirror device (DMD) or a multimode fibre. An increase in the excitation intensity and the signal to noise ratio (SNR) allows a further reduction of the compression ratio, thus decreasing the number of measurements and saving additional data acquisition time.

In summary, the method is a low-cost and straightforward alternative to commonly-used methods, providing the possibility of speedy measurement of fast mapping of PL decays on the microsecond timescale.

**Funding.** Akademie Věd České Republiky (ERC-CZ/AV-B (RUSH, Reg. No. ERC100431901)); Ministerstvo Školství, Mládeže a Tělovýchovy (Reg. No. CZ.02.1.01/0.0/0.0/16\_026/0008390); Technická Univerzita v Liberci (SGS-2020-3057); Grantová Agentura České Republiky (17-26284Y).

**Acknowledgment.** We gratefully acknowledge Lukáš Ondič (Institute of Physics, Czech Academy of Sciences) for providing us with samples of nanoporous Si.

**Disclosures.** The authors declare no conflicts of interest.

## References

1. J. Sytsma, J. M. Vroom, D. Grauw, and H. C. Gerritsen, "Time-gated fluorescence lifetime imaging and microvolume spectroscopy using two-photon excitation," *J. Microsc.* **191**(1), 39–51 (2008).
2. R. V. Krishnan, H. Saitoh, H. Terada, V. E. Centonze, and B. Herman, "Development of a multiphoton fluorescence lifetime imaging microscopy system using a streak camera," *Rev. Sci. Instrum.* **74**(5), 2714–2721 (2003).
3. S. Cheng, R. M. Cuenca, B. Liu, B. H. Malik, J. M. Jabbour, K. C. Maitland, J. Wright, Y.-S. L. Cheng, and J. A. Jo, "Handheld multispectral fluorescence lifetime imaging system for in vivo applications," *Biomed. Opt. Express* **5**(3), 921–931 (2014).
4. A. D. Elder, C. F. Kaminski, and J. H. Frank, " $\phi^2$ FLIM: a technique for alias-free frequency domain fluorescence lifetime imaging," *Opt. Express* **17**(25), 23181–23203 (2009).
5. W. Becker, A. Bergmann, G. Biscotti, K. Koenig, I. Riemann, L. Kelbauskas, and C. Biskup, "High-speed FLIM data acquisition by time-correlated single-photon counting," *Proc. SPIE* **5323**, 27–35 (2004).



6. N. Krstajić, S. Poland, J. Levitt, R. Walker, A. Erdogan, S. Ameer-Beg, and R. K. Henderson, "0.5 billion events per second time correlated single photon counting using CMOS SPAD arrays," *Opt. Lett.* **40**(18), 4305–4308 (2015).
7. X. Liu, D. Lin, W. Becker, J. Niu, B. Yu, L. Liu, and J. Qu, "Fast fluorescence lifetime imaging techniques: A review on challenge and development," *J. Innovative Opt. Health Sci.* **12**(05), 1930003 (2019).
8. V. Studer, J. Bobin, M. Chahid, H. S. Mousavi, E. Candes, and M. Dahan, "Compressive fluorescence microscopy for biological and hyperspectral imaging," *Proc. Natl. Acad. Sci. U. S. A.* **109**(26), E1679–E1687 (2012).
9. Q. Pian, R. Yao, N. Sinsuebphon, and X. Intes, "Compressive hyperspectral time-resolved wide-field fluorescence lifetime imaging," *Nat. Photonics* **11**(7), 411–414 (2017).
10. K. Židek, O. Denk, and J. Hlubuček, "Lensless Photoluminescence Hyperspectral Camera Employing Random Speckle Patterns," *Sci. Rep.* **7**(1), 15309 (2017).
11. J. Junek, L. Ondič, and K. Židek, "Random temporal laser speckles for the robust measurement of sub-microsecond photoluminescence decay," *Opt. Express* **28**(8), 12363–12372 (2020).
12. K. Zheng, K. Židek, M. Abdellah, M. E. Messing, M. J. Al-Marri, and T. Pullerits, "Trap States and Their Dynamics in Organometal Halide Perovskite Nanoparticles and Bulk Crystals," *J. Phys. Chem. C* **120**(5), 3077–3084 (2016).
13. J. M. Griffin, A. J. Miller, A. J. Berry, S. Wimperis, and S. E. Ashbrook, "Dynamics on the microsecond timescale in hydrous silicates studied by solid-state  $^2\text{H}$  NMR spectroscopy," *Phys. Chem. Chem. Phys.* **12**(12), 2989–2998 (2010).
14. K. Dohnalová, L. Ondič, K. Kůsová, I. Pelant, J. L. Rehspringer, and R.-R. Mafouana, "White-emitting oxidized silicon nanocrystals: Discontinuity in spectral development with reducing size," *J. Appl. Phys.* **107**(5), 053102 (2010).
15. A. N. Tikhonov and V. Y. Arsenin, "Solutions of ill-posed problems," *SIAM Rev.* **21**, 266–267 (1977).
16. M. F. Duarte, M. A. Davenport, D. Takhar, J. N. Laska, T. Sun, K. F. Kelly, and R. G. Baraniuk, "Single-pixel imaging via compressive sampling," *IEEE Signal Process. Mag.* **25**(2), 83–91 (2008).
17. C. Li, Wotao Yin, and Yin Zhang, TVAL3 Home, Rice University, 2009, Last updated 11/07/2013, (available from: <https://www.caam.rice.edu/~optimization/L1/TVAL3/>).
18. C. Li, W. Yin, and Y. Zhang, "User's guide for TVAL3: TV minimization by augmented lagrangian and alternating direction algorithms," CAAM Rep. 20, 46–47 (2009).
19. C. Li, "An Efficient Algorithm For Total Variation Regularization with Applications to the Single Pixel Camera and Compressive Sensing," Master Thesis, Rice University (2009).
20. K. Židek, F. Trojánek, P. Malý, L. Ondič, I. Pelant, K. Dohnalová, L. Šiller, R. Little, and B. R. Horrocks, "Femtosecond luminescence spectroscopy of core states in silicon nanocrystals," *Opt. Express* **18**(24), 25241–25249 (2010).
21. I. Hamarová, P. Šmíd, P. Horváth, and M. Hrabovský, "Methods for Determination of Mean Speckle Size in Simulated Speckle Pattern," *Meas. Sci. Rev.* **14**(3), 177–182 (2014).



# SCIENTIFIC REPORTS

OPEN

## Lensless Photoluminescence Hyperspectral Camera Employing Random Speckle Patterns

Karel Židek, Ondřej Denk &amp; Jiří Hlubuček

Received: 13 July 2017

Accepted: 10 October 2017

Published online: 10 November 2017

We propose and demonstrate a spectrally-resolved photoluminescence imaging setup based on the so-called single pixel camera – a technique of compressive sensing, which enables imaging by using a single-pixel photodetector. The method relies on encoding an image by a series of random patterns. In our approach, the image encoding was maintained via laser speckle patterns generated by an excitation laser beam scattered on a diffusor. By using a spectrometer as the single-pixel detector we attained a realization of a spectrally-resolved photoluminescence camera with unmatched simplicity. We present reconstructed hyperspectral images of several model scenes. We also discuss parameters affecting the imaging quality, such as the correlation degree of speckle patterns, pattern fineness, and number of datapoints. Finally, we compare the presented technique to hyperspectral imaging using sample scanning. The presented method enables photoluminescence imaging for a broad range of coherent excitation sources and detection spectral areas.

Photoluminescence (PL) emitted from a material provides an immense amount of information about the emitting matter. It can disclose the degree of molecular aggregation<sup>1</sup>, defects in materials<sup>2</sup>, reveal the size distribution of nanocrystals<sup>3</sup>, etc. For these reasons the PL measurement has become a standard means of spectroscopic sample characterization. PL imaging shifts the abilities of this method even further by the possibility to visualize and map PL characteristics in a sample<sup>4</sup>.

PL imaging in the visible spectral range is nowadays a well mastered task solved by standard hyperspectral imaging approaches<sup>5–7</sup> such as variable spectral filters and push broom or whisk broom scanners. However, the task becomes more complicated in the infrared (IR) region due to the difficulty of adjustment of the IR optics, as well as the need for an expensive two-dimensional sensor and IR imaging elements<sup>8,9</sup>. A solution bypassing the difficulties is to focus the PL excitation to a tight spot and carry out imaging by scanning a sample, i.e. by shifting the excitation spot, and detecting the PL intensity by a single-pixel detector (photodiode, photomultiplier, spectrometer). However, sample scanning can become problematic for samples placed in a bulky device (cryostat, high-power magnets, etc.). Moreover, such an approach is highly time consuming. For instance, for a  $128 \times 128$  pixel image with 1 s PL detection integration time, the total measurement time reaches 4.5 hours.

Here we propose and demonstrate a simple lensless hyperspectral PL camera that allows PL imaging by using a single-pixel detector – a spectrometer providing the camera with spectral resolution<sup>10,11</sup>. Our approach makes it possible to decrease the number of measurements, compared to sample scanning, to about 20% of the image pixel number, while keeping the primary image information. The abovementioned example measurement ( $128 \times 128$  pixel, 1 s acquisition) can therefore be carried out in about one hour. Moreover, we can achieve the imaging using only two optical elements – a transmissive or reflective diffusor and a beam splitting wedge or any equivalent element. Hence the method can be applied to a broad range of coherent excitation sources and PL detection ranges.

The method is based on compressed sensing<sup>12,13</sup>, namely the so-called single-pixel camera<sup>14–16</sup>. Compressed sensing is a novel approach to data acquisition used extensively in imaging. It involves encoding a piece of information, for instance, an image, by a random or a pseudo-random pattern and reconstructing it using computer algorithms. We refer the reader to a number of introductory and review articles for more details<sup>13,17–19</sup>. In our measurements we employ the so-called single-pixel camera concept<sup>14</sup> where an image is encoded by a series of random patterns and the total intensity of light emitted from the sample, is detected and used for the image reconstruction.

Regional Centre for Special Optics and Optoelectronic Systems (TOPTEC), Institute of Plasma Physics, Academy of Sciences of the Czech Republic, Za Slovankou 1782/3, 182 00, Prague 8, Czech Republic. Correspondence and requests for materials should be addressed to K.Ž. (email: [zidek@ipp.cas.cz](mailto:zidek@ipp.cas.cz))





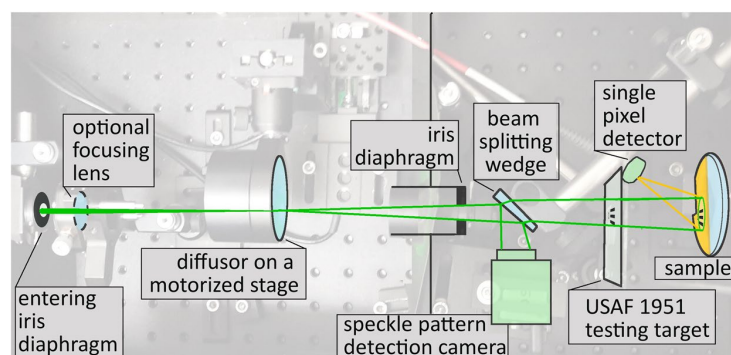


**Figure 1.** Photograph of the experimental setup overlaid with a simple scheme. The laser focusing lens can be used to modify the speckle pattern properties (see text for details). USAF 1951 testing target was used to verify the resolution of the imaging setup. The single pixel detector in the presented results was a fiber-coupled spectrometer.

Unlike in the standard single-pixel camera design, where imaging and relay optics are needed<sup>16,20</sup>, here we encode the detected scene by a random speckle pattern arising via an interference of many wavefronts with random phases. A similar concept was used previously employing sophisticated optical devices (e.g. a digital micromirror device)<sup>21</sup>. To generate the speckle pattern, we, instead, employ a simple approach using a moving diffuser, which can be easily incorporated into any laser-excited PL detection. This leads to a PL imaging setup of unmatched simplicity.

In this article we present a hyperspectral PL camera and demonstrate its performance on a solution of Rhodamine 6G. We address parameters affecting the camera function, such as speckle patterns correlation or fineness. Finally, we discuss the possible range of applicable measurements.

## Imaging System

Our experimental setup (depicted in Fig. 1) was based on a standard PL measurement setup. The entering excitation laser beam was used to generate a speckle pattern. The beam can be optionally focused by a lens to adjust the mean size of speckles, as we discuss later. The lens is, however, not needed for the setup operation. Consequently, a diffuser on a XY-motorized stage (Thorlabs) was placed in the laser beam. The diffuser served as a medium for obtaining a speckle pattern. The speckle pattern was reduced via an iris diaphragm into a narrow cone of patterned light, which was used for the sample excitation. A small fraction of the beam intensity was reflected from a wedge onto a reference CMOS chip (IDS camera). The wedge was used in order to avoid interference of multiple beam reflections on the camera.

The sample PL emission can be collected efficiently by placing the sample into an integrating sphere, by using a parabolic mirror, or it can be collected by a lens. However, we put emphasis on the simplicity of the demonstrated experimental approach. Therefore, the emitted PL was collected by an optical fiber (1 mm core), which was placed in the sample proximity. The detector distance was set so that the light from the entire illuminated area was evenly collected. This was adjusted prior to each experiment by using back-propagating light (Ocean Optics, LS-1 lamp) through the detecting optical fiber. The cone of the back-propagating light illuminating the sample determines the area from which the emission is collected.

We employed Rhodamine 6G (rh6G) in a flat cuvette as a testing sample. A laser source at 532 nm (frequency doubled Nd:YAG laser operating at 1064 nm) at a moderate excitation power of 3 mW was used to generate a speckle pattern. This assured that the PL emission remained in the linear regime. The testing was carried out by using a positive USAF 1951 resolution target or by imaging the edges of the rh6G solution. Due to the diverging speckle pattern, the resulting USAF pattern shadow was scaled up approx. 1.25-times. The illuminated sample area, which at the same time defines the imaging area, was a circle approx. 4 mm in diameter. The light emitted from the sample was analyzed via a spectrometer (Ocean Optics, Flame).

The single-pixel camera concept relies on detecting a series of total intensities for known encoded random-pattern illuminations. We obtained the total intensity value by selecting a spectral range to reconstruct. For each measurement, the PL spectrum in the range was averaged, thus providing the total intensity. The random encoding pattern was obtained as a speckle pattern image on the reference CMOS chip. Since the experimental setup was based on widely available components (laser source, camera, detectors), the signals undergo a minor drift of the ratio between the speckle pattern intensity and the detected intensity. The main source of the drift lies in the reference CMOS chip heating up during the measurement. The drift was corrected by dividing the variation in the total intensity smoothed in a long-term range of datapoints (Savitzky-Golay smoothing, 350-point range).

The reconstruction of an image  $u$  with  $N$  pixels (e.g.  $N = 4096$  for  $64 \times 64$  image) from  $M$  measurements was carried out using TVAL3 algorithm<sup>22</sup> minimizing the expression:

$$\min_{u \in \mathbb{R}^N} \sum_i \|D_i u\|_1 + \frac{\mu}{2} \|Au - b\|_2^2, \text{ s.t. } u \geq 0. \quad (1)$$

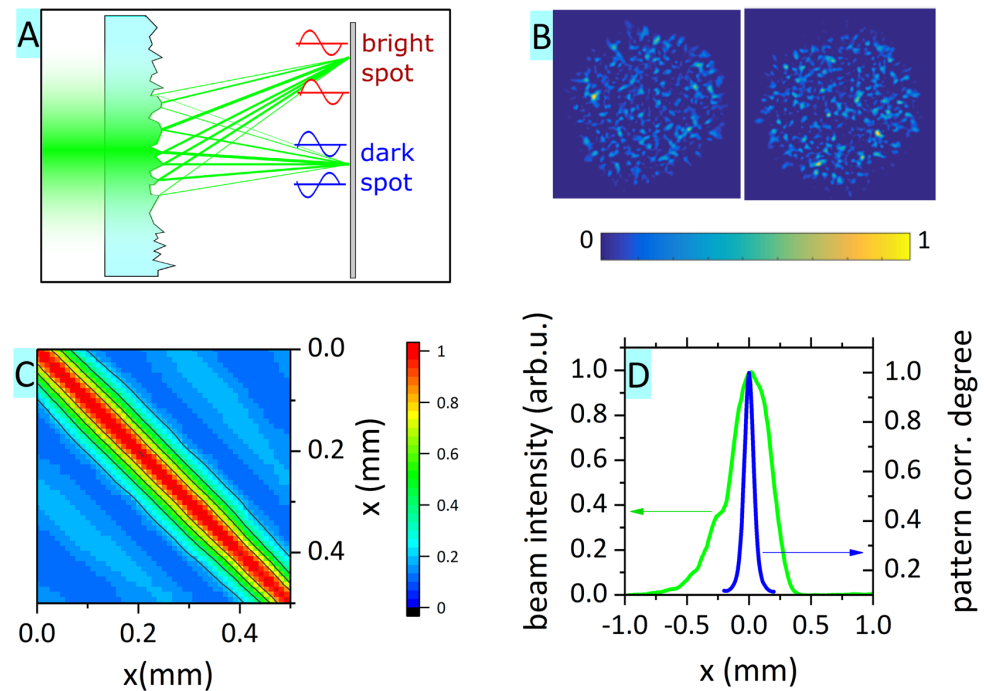


**Figure 2.** (A) Scheme of speckle pattern origin – depending on the random phase, the amplitudes add up (bright spot) or subtract (dark spot); (B) Two examples of fine speckle patterns used in the experiments; (C) Correlation degree (see text for details) between speckle patterns acquired at different diffusor positions; (D) Comparison of beam profile (green line) and averaged correlation degree between neighboring patterns (blue line).

$D$  stands for differentiation along  $x$ - and  $y$ - axis.  $A$  represents the so-called measurement matrix  $N \times M$ , which is composed of  $M$  columns, each representing one speckle pattern with  $N$  pixels. Finally,  $b$  stands for the vector of total intensities ( $M$  elements). A detailed description of the reconstruction procedure and the used parameters can be found in the supplementary information.

## Results and Discussion

**Speckle Patterns Correlation.** A laser speckle pattern is a random intensity pattern resulting from the interference of many wavefronts arising due to multiple scattering of coherent light (see Fig. 2A,B)<sup>23</sup>. First, we focused on ensuring that the acquired random patterns are not correlated with each other. This satisfies the need for incoherence in the measurement matrix  $A$  in the compressed sensing theory<sup>13</sup>.

By shifting the diffusor by a small step and acquiring a speckle pattern for each position, we obtained a set of images. The correlation between two images  $I$  and  $J$  can be evaluated based on the following expression, where  $\sigma_I$  denotes the standard deviation of the image  $I$ :

$$C(I, J) = \frac{\sum_{k,l} \frac{I(k, l) - \langle I \rangle}{\sigma_I} \frac{J(k, l) - \langle J \rangle}{\sigma_J}}{\sqrt{\sum_{k,l} \frac{I(k, l) - \langle I \rangle}{\sigma_I}^2 \sum_{k,l} \frac{J(k, l) - \langle J \rangle}{\sigma_J}^2}} \quad (2)$$

The expression is also similar to the calculation of the so-called mutual coherence of the sensing matrix  $A$ , where each speckle pattern represents one column in the matrix. A lower mutual coherence of a matrix ensures a good information reconstruction under a low number of measurements<sup>17</sup>.

We calculated the degree of correlation for a series of diffusor horizontal shifts (denoted as  $x$ -axis) – see Fig. 2C. The results show that the neighboring patterns were highly correlated due to the so-called memory effect<sup>24</sup> and the correlation degree rapidly decreased on a scale significantly below the beam FWHM (beam FWHM 0.36 mm vs. correlation degree FWHM 0.1 mm, see Fig. 2D). The loss of correlation depends on the typical size of the random features (scattering sites) on the diffusor, as well as on the decrease in the overlap between the beams. The presented measurement therefore provided us with the information that the diffusor shift along the  $x$ -axis of 0.15 mm or greater ensures obtaining a sequence of uncorrelated random patterns. The situation was analogous for the  $y$ -axis, where the beam FWHM and correlation degree FWHM reached 0.4 mm and 0.1 mm, respectively.

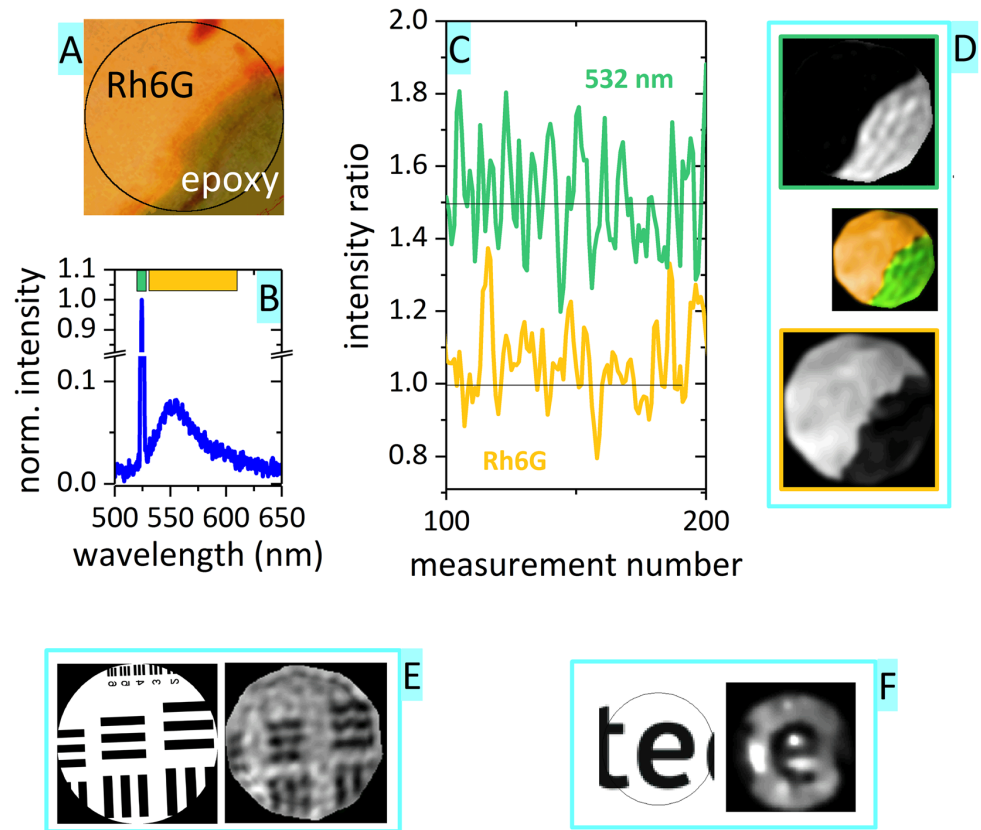


**Figure 3.** Examples of reconstructed images. (A) Scene of an interface between Rhodamine 6 G and scattering epoxy glue (black circle denotes the illuminated area); (B) Example of a spectrum detected during the measurement (normalized), color bars at the top denote the spectral ranges used for reconstruction in panel C; (C) Example of intensity points from the two spectral ranges (the intensity points were divided by the total speckle pattern intensity); (D) Reconstructed images (image:  $128 \times 128$  pixels, 6200 datapoints,  $M/N = 39\%$ ) for the two spectral ranges (grayscale images) and merged image (orange-green image); (E,F) Lensless imaging, left side – original image, right side – reconstructed image; (E) A shadow of a fine USAF pattern on rh6G (image:  $128 \times 128$  pixels, 4000 datapoints,  $M/N = 24\%$ ); (F) Scattered laser light (image:  $64 \times 64$  pixels, 680 datapoints,  $M/N = 17\%$ ).

**Image Reconstruction.** The acquired knowledge was used to generate a series of measurements with the hyperspectral camera. As an example we present a measurement of an interface between PL-emitting rh6G and a scattering layer of epoxy glue (see Fig. 3A). Illumination of the indicated circle (black circle in Fig. 3A) led to a spectrum (see Fig. 3B) with a pronounced laser peak at 532 nm (scattered laser light) and the rh6G PL emission (540–650 nm spectral band). We averaged the detected intensities in the two spectral ranges 528–536 nm and 540–650 nm (see color bars in panel B) and obtained two sets of intensity values for each measurement (see Fig. 3C). The intensity datapoints together with the speckle pattern images were finally used to reconstruct the original image based on eq. (1), leading to a different image (Fig. 3D) for the PL band (bottom panel) and the scattering band (top panel). To provide a better comparison, we also superpose the results into a two-color reconstruction (middle image in panel D), proving that the reconstructed image corresponds very well with the original scene. In addition, we provide two examples of lensless imaging. One is of a fine USAF pattern shadow on rh6G (Fig. 3E) and the other of a scattered laser beam on a text (Fig. 3F).

**Imaging Parameters.** Unlike in the standard implementations of a single pixel camera, speckle patterns can be very easily adjusted for the desired measurement area (by adjusting the pinhole) and pattern fineness (by focusing the laser beam). The mean speckle size for wavelength  $\lambda$  can be approximated in the far-field regime as  $\frac{\lambda z}{d}$ , i.e. the size is determined as a combination of the laser beam width  $d$  and the diffusor-sample distance  $z$ . Both parameters can be used for the speckle pattern fineness adjustment<sup>23</sup>. The fineness of a speckle pattern  $I$  can be quantified by calculating the pattern autocorrelation<sup>25</sup>:

$$c(p, q) = \sum_{m, n} I(m, n) \cdot I(m - p, n - q) \quad (3)$$

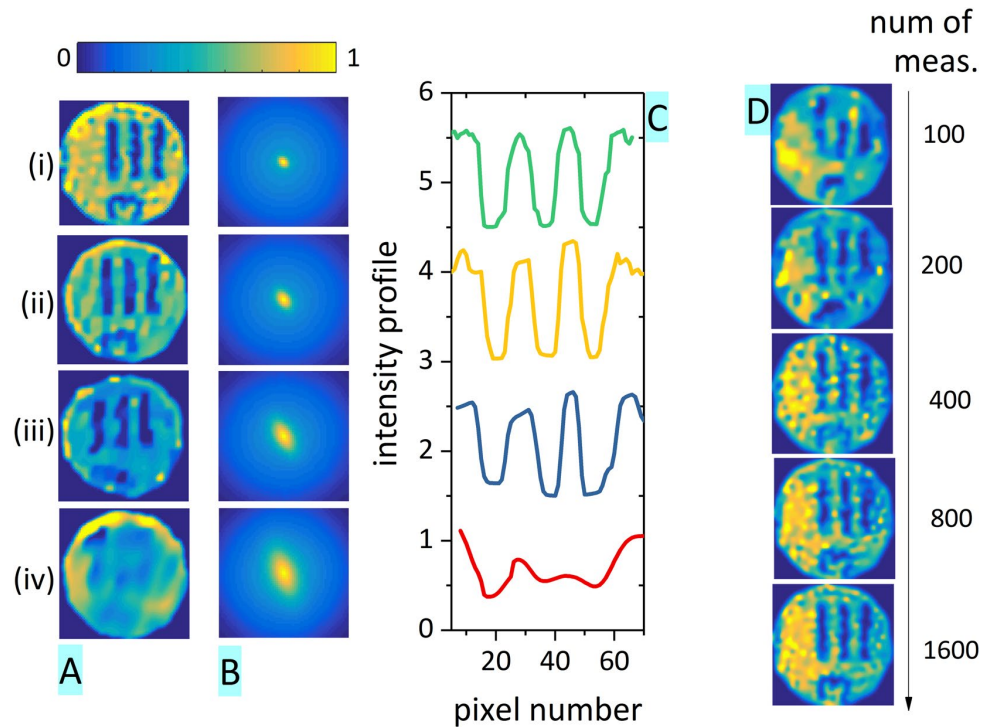


**Figure 4.** Reconstruction of a shadow of a part of USAF 1951 in Rhodamine 6G emission. (A) A reconstructed image for 4 different mean speckle sizes ( $M = 1500$  measurements,  $96 \times 96$  pixel image,  $M/N = 16\%$ ); (B) The mean autocorrelation of all speckle patterns; (C) Cross-section of three vertical target lines (averaged values from lines 50–65) for the 4 reconstructed images; (D) The same scene (USAF target shadow, speckle mean width  $\sigma_x = 3.1$  pixel,  $\sigma_y = 3.2$  pixel) reconstructed from an increasing number of datapoints,  $M/N = 1\%$ ,  $2\%$ ,  $4\%$ ,  $9\%$ , and  $17\%$ , respectively.

meas.	speckle autocorr.		image PSF estimate	
	$\sigma_x$	$\sigma_y$	$\sigma_x$	$\sigma_y$
	[pixel]	[pixel]	[pixel]	[pixel]
i	3.1	3.2	1.7	2.0
ii	4.3	4.7	2.3	3.7
iii	5.4	6.5	3.4	4.7
iv	6.3	7.8	—	—

**Table 1.** Summary of the resulting root-mean-square widths of the speckle autocorrelation peak and image point spread function (PSF) estimate for the four measurements in Fig. 4A,B. For the measurement (iv) the PSF values could not be recovered.

The autocorrelation features a pronounced central peak with width proportional to the mean speckle size.

We investigated the relation between the mean speckle size and the setup resolution. The same testing image – a shadow of USAF resolution etalon on rh6G – was used to acquire a series of measurements with four different laser spot sizes. The variation in the spot size leads to four different degrees of fineness of the patterns, which can be evaluated based on the mean autocorrelation of all patterns (see Fig. 4B). Namely, we determined the root-mean-square width  $\sigma$  by fitting the horizontal and the vertical central peak cut with the Gauss function. The resulting  $\sigma$  values are listed in Table 1.

Imaging of the same testing scene with increasing mean speckle size led to a decrease in the reconstructed image resolution (see Fig. 4A). In order to illustrate this effect, we extracted for each case a horizontal cut through the three vertical lines in the USAF target (Fig. 4C). With the increasing speckle size the line edges become gradually less pronounced.

Furthermore, in order to quantitatively evaluate the resolution of the image reconstruction, we carried out a calculation, where the original image of the USAF target  $u_{orig}$  was convoluted with a Gaussian point spread function (PSF)  $P(\sigma_x, \sigma_y)$  and compared with the reconstructed image  $u_{rec}$ . The PSF root-mean-square widths  $\sigma_x$  and  $\sigma_y$  were optimized with respect to the minimum difference between the original and the reconstructed images. The resulting estimates of the PSF widths are listed in Table 1.



In general, we observe that the image PSF width reached about 50% of the speckle autocorrelation peak width. The results therefore confirm that the resolution is set by the speckle autocorrelation width. Interestingly, even though speckle patterns feature a broad distribution of speckle sizes, the fine details cannot be recovered by a series of coarse speckle patterns, in spite of using a high number of acquisitions reaching 100% of the image pixel count. The mean speckle size therefore represents the native resolution of the system that cannot be easily overcome.

Analogously to other single pixel camera techniques, each measurement here also carries a piece of information about the whole scene. The image can therefore be reconstructed based on a small number of datapoints (Fig. 4D). Nevertheless, a significant improvement is achieved by increasing the datapoint count. In Fig. 4D a reasonable reconstruction can be achieved for  $M = 1600$  datapoints ( $N = 96 \times 96$  pixel image,  $M/N = 18\%$ , detector noise std. dev. of 6%). It is, however, worth noting that in the case of the speckle-based single-pixel camera the resolution is dominantly affected by the mean speckle size and, therefore, the  $M/N$  ratio is, in fact, higher.

**Limitations of the Imaging Parameters.** An important consideration for every imaging system are the limits to achievable spatial and spectral resolution. We will first turn to spectral resolution, which is provided in our case by a spectrometer. In principle the camera resolution is only limited by the resolution of the spectrometer itself. For the wavelengths where the typical detected signal exceeds  $10^4$  counts (maximum 65536 counts) the reconstruction can be carried out from a single spectral datapoint. This is, however, often not the case for a reasonable integration time (1s or below) and a weak PL signal. There the realistic limitation of the system is set by the signal-to-noise ratio. Since the reconstruction discrepancy  $\|u_{rec} - u_{orig}\|_2$  is proportional to the noise level<sup>17</sup>, it is advisable to average a spectral range, thus reducing the noise level by a square root of the number of the averaged spectral datapoints.

The spatial resolution of the imaging setup is determined by the speckle pattern fineness, which can be improved by reducing the sample-diffusor distance  $z$  or by increasing the laser spot diameter on the diffusor. This approach is, however, not valid for short distances  $z$ , where the speckle pattern rapidly changes with the distance from the diffusor (near-field speckle pattern). It is therefore not a straightforward task to assess the best obtainable value and this issue will be addressed in our future work. Nevertheless, the best real resolution obtained so far in the presented setup was about  $20 \mu\text{m}$ . This value is based on an image of a single scattering site on a luminophore.

**Comparison to the sample scanning.** It is worth comparing the setup to the approach where an excitation spot is focused and the sample is scanned in the XY manner to acquire the PL map. Both experiments provide PL hyperspectral imaging by using a single-pixel detector.

Firstly, sample scanning requires motorized stages with well-defined steps and a tightly-focused laser beam – both being determinants of the setup spatial resolution. On the contrary, the presented setup relies on shifting a diffusor, which can be performed randomly – without the necessity to control the exact diffusor position. Measurements with a very short acquisition time can be, for instance, acquired with a continuously-moving motorized stage, without any need to track the actual stage position.

Secondly, the mode of illumination is different for each method. For sample scanning, the sample area is illuminated, point-by-point, with a high-intensity excitation focused on a small fraction of the sample. In contrast, the presented approach continuously illuminates the entire imaging area. Nevertheless, to reach a similar detected PL intensity a low-intensity excitation is sufficient here. The difference has consequences for the samples which suffer from photobleaching. The samples undergoing photobleaching only above a certain light intensity threshold may benefit from using the excitation pattern. On the contrary, photobleaching with a low threshold would lead to a continuously decreasing total intensity. A possible way to abate the issue is to compensate for the long-term drift in the intensity values.

Finally, as we stated in the introduction, by involving compressive imaging, we can carry out the same hyperspectral imaging with a reduced number of measurements and use about 20–40% of datapoints compared to sample scanning.

## Conclusion

We have presented a simple experimental technique able to implement a PL hyperspectral camera by extending a standard PL measurement setup with a shifting diffusor. This approach is very versatile as far as PL detection and imaging parameters, such as imaged area or image resolution, are concerned. The presented experiments were carried out using a spectrometer as a single-pixel detector. However, by replacing the spectrometer with an IR detector, the same setup can serve for PL imaging in the IR region.

Moreover, the excitation pattern is prepared solely based on diffusor and reference imaging. For this reason, the presented setup can be used for excitation of coherent sources in the deep UV region, where a reflecting optical chopper with a luminophore-covered 2D sensor can serve as a pattern reference, or in the IR region, where an up-converting layer can provide the same information.

The presented setup can therefore provide a solution to a broad range of experimentally difficult cases requiring PL imaging.

## References

1. Sherwood, Ga *et al.* Aggregation Effects on the Emission Spectra and Dynamics of Model Oligomers of MEH-PPV. *J. Phys. Chem. C* **113**, 18851–18862 (2009).
2. Liu, D. *et al.* Defect-related photoluminescence and photocatalytic properties of porous ZnO nanosheets. *J. Mater. Chem. A* **2**, 15377 (2014).
3. Alivisatos, A. P. Semiconductor Clusters, Nanocrystals, and Quantum Dots. *Science* **271**, 933–937 (1996).





4. Trupke, T., Bardos, R. A., Schubert, M. C. & Warta, W. Photoluminescence imaging of silicon wafers. *Appl. Phys. Lett.* **89**, 44107 (2006).
5. Olsen, E. & Flø, A. S. Spectral and spatially resolved imaging of photoluminescence in multicrystalline silicon wafers. *Appl. Phys. Lett.* **99**, 11903 (2011).
6. Delamarre, A., Lombez, L. & Guillemoles, J.-F. Contactless mapping of saturation currents of solar cells by photoluminescence. *Appl. Phys. Lett.* **100**, 131108 (2012).
7. Eismann, M. T. *Hyperspectral Remote Sensing*. (SPIE, 2012).
8. Mann, A. & Society of Photo-optical Instrumentation Engineers. *Infrared optics and zoom lenses*. (SPIE, 2009).
9. Driggers, R. G., Friedman, M. H. & Nichols, J. *Introduction to infrared and electro-optical systems*. (Artech House, 2012).
10. Židek, K. & Václavík, J. Imaging in laser spectroscopy by a single-pixel camera based on speckle patterns. *Proc. SPIE 10151, Optics and Measurement International Conference 2016*, 1015105 (SPIE, 2016).
11. Židek, K., Hlubuček, J. & Denk, O. Random Image Encoding via Speckle Pattern: The Effect of Patterns Correlation. In *Imaging and Applied Optics 2017 (3D, AIO, COSI, IS, MATH, pcAOP) JTU5A.1* (OSA, 2017).
12. Donoho, D. L. Compressed sensing. *IEEE Trans. Inf. Theory* **52**, 1289–1306 (2006).
13. Candes, E. J. & Wakin, M. B. An Introduction To Compressive Sampling. *IEEE Signal Process. Mag.* **25**, 21–30 (2008).
14. Duarte, M. F. *et al.* Single-Pixel Imaging via Compressive Sampling. *IEEE Signal Process. Mag.* **25**, 83–91 (2008).
15. Chan, W. L. *et al.* A single-pixel terahertz imaging system based on compressed sensing. *Appl. Phys. Lett.* **93**, 121105 (2008).
16. Starling, D. J., Storer, I. & Howland, G. A. Compressive sensing spectroscopy with a single pixel camera. *Appl. Opt.* **55**, 5198 (2016).
17. Stern, A. *Optical Compressive Imaging*. (CRC Press, 2017).
18. Gamez, G. Compressed sensing in spectroscopy for chemical analysis. *J. Anal. At. Spectrom.* **31**, 2165–2174 (2016).
19. Thapa, D., Raahemifar, K. & Lakshminarayanan, V. Less is more: compressive sensing in optics and image science. *J. Mod. Opt.* **62**, 415–429 (2015).
20. Usala, J. D., Maag, A. & Gamez, G. Compressed sensing spectral imaging for plasma optical emission spectroscopy. *J. Anal. At. Spectrom.* **31**, 2198–2206 (2016).
21. Shin, J., Bosworth, B. T. & Foster, M. A. Compressive fluorescence imaging using a multi-core fiber and spatially dependent scattering. *Opt. Lett.* **42**, 109 (2017).
22. Li, C., Yin, W. & Zhang, Y. User's guide for TVL3: TV minimization by augmented lagrangian and alternating direction algorithms. *CAAM Rep.* **20**, 46–47 (2009).
23. *Laser Speckle and Related Phenomena*. (Springer Berlin Heidelberg, 1975).
24. Freund, I., Rosenbluh, M. & Feng, S. Memory effects in propagation of optical waves through disordered media. *Phys. Rev. Lett.* **61**, 2328–2331 (1988).
25. Hamarová, I., Horváth, P., Šmíd, P. & Hrabovský, M. A new approach for determination of a mean speckle size in simulated speckle pattern. *Meas. J. Int. Meas. Confed.* **88**, 271–277 (2016).

## Acknowledgements

We gratefully acknowledge the financial support of the Grant Agency of the Czech Republic (project 17-26284Y) and the Ministry of Education, Youth and Sports of the Czech Republic (Project NPU LO1206).

## Author Contributions

K.Z. performed a major part of the experimental work and data processing and wrote the manuscript draft. O.D. contributed to the data processing. J.H. contributed to the experimental preparation and data acquisition. All authors reviewed the manuscript.

## Additional Information

**Supplementary information** accompanies this paper at <https://doi.org/10.1038/s41598-017-14443-4>.

**Competing Interests:** The authors declare that they have no competing interests.

**Publisher's note:** Springer Nature remains neutral with regard to jurisdictional claims in published maps and institutional affiliations.



**Open Access** This article is licensed under a Creative Commons Attribution 4.0 International License, which permits use, sharing, adaptation, distribution and reproduction in any medium or format, as long as you give appropriate credit to the original author(s) and the source, provide a link to the Creative Commons license, and indicate if changes were made. The images or other third party material in this article are included in the article's Creative Commons license, unless indicated otherwise in a credit line to the material. If material is not included in the article's Creative Commons license and your intended use is not permitted by statutory regulation or exceeds the permitted use, you will need to obtain permission directly from the copyright holder. To view a copy of this license, visit <http://creativecommons.org/licenses/by/4.0/>.

© The Author(s) 2017







# Influence of the delay line jitter on the SHG FROG reconstruction

PETRA VESELÁ\* AND KAREL ŽÍDEK 

*Institute of Plasma Physics, Czech Academy of Science v.v.i., Czech Republic*

\*vesela@ipp.cas.cz

**Abstract:** Frequency-resolved optical gating (FROG) counts among the most used methods to characterize complex femtosecond pulses. The multishot FROG experiment, studied in this work, relies on varying a delay between two replicas of the measured pulse, where the delay accuracy can suffer from delay line imperfections, setup instability, or minimization of the acquisition time. We present a detailed study on the effect of the delay line jitter on the pulse retrieval. We carried out simulations with the jitter values ranging from high-precision delay lines (100 nm) up to extremely unstable measurements (>1000 nm). For three sets of pulses, we quantified criteria assuring reliable reconstruction, using ptychographic algorithm, of a complex pulse based on the experimentally available FROG trace error. We observe that the effect of the jitter scales together with the spectral bandwidth. However, the pulse reconstruction is relatively robust against the jitter and, even for a severe distortion of the FROG trace (e.g., a jitter of 500 nm for broadband pulses), the main features of all pulses are retrieved with high fidelity. Our results provide guidance for the limitations based on the delay imperfections in the FROG experiment.

© 2021 Optical Society of America under the terms of the [OSA Open Access Publishing Agreement](#)

## 1. Introduction

Femtosecond laser pulses make it possible to access ultrafast processes in a variety of materials and physical phenomena. Although the majority of experiments aim at obtaining simple pulses, which are as short as possible, in many cases, it is, on the contrary, crucial to reliably measure a complex pulse temporal profile. As an example, we can list the characterization of various super continuum generation systems producing complex pulses [1,2], study of speckle patterns formed by the propagation of coherent light through a scattering medium motivated by the fields of medical imaging and communication [3], or the field of coherent control of chemical reactions, where the optimized pulse shape brings the information about the ongoing processes [4].

A number of experimental techniques have been developed to retrieve the pulse shape. One of the most used is the concept of frequency-resolved optical gating (FROG) [5] with various implementations which use second harmonic generation (SHG) or many other non-resonant nonlinear processes to reconstruct the pulse waveform. In the FROG experiment, the nonlinear signal arises due to a mutual interaction of two replicas created from the measured pulse. Spectra of the nonlinear signal acquired for various delays between the replicas form a FROG trace. The trace can be consequently employed to iteratively reconstruct the pulse amplitude and phase in time and spectrum.

Owing to its widespread usage and relative simplicity, FROG is a quite well studied and understood technique, including the imperfections in the experiment, such as excessive amount of noise in the FROG trace [6,7], limited phase-match bandwidth of the nonlinear process [8,9], limited detector spectral resolution [10], or instabilities of the pulse train in multiple shot measurements [11,12]. However, the aspect of error in the delay between the two pulse replicas has so far escaped attention.

Several works have focused on the jitter in the cross-correlation measurements, e.g., in the FROG-CRAB experiment, where the jitter typically arises due to different origin and distinct beam pathways of the two interacting pulses. An example can be the work of Murari et al. [10]

#413765

<https://doi.org/10.1364/OE.413765>

Journal © 2021

Received 29 Oct 2020; revised 18 Jan 2021; accepted 19 Jan 2021; published 27 Jan 2021



who investigated the effect of the relative jitter between the XUV and IR pulse generating a FROG-CRAB spectrogram. An analogous investigation was carried out by He Wang et al. [13]. They were interested in the effect of time jitter of the NIR pulse which resulted from slight variations due to the mechanical vibrations of the different trajectories of the pulses, leading to broadening of the FROG-CRAB trace in the delay axis.

In this article, we investigate the effect of the delay line jitter on the reconstruction of complex pulses in a standard FROG experiment. Unlike previous publications, we study pulse retrieval from a dataset, where the FROG trace is not broadened, yet the measured spectra are acquired for delays suffering from a certain error, i.e., jitter. This work is motivated by the fact that relaxed demands on the delay line precision can provide us with a faster experiment, since the delay line settling time can be shortened. In the case of extremely short acquisition time, it is potentially possible to acquire the FROG trace for short femtosecond pulses even in the sweep mode, where the delay line is continuously moving at a constant speed [14]. At the same time, lower demands on the delay line precision introduce the possibility to reduce the cost of the delay line.

We study the effect of the delay line jitter via an extensive series of simulations of multishot experiments on three sets of pulses, which differ in their spectral bandwidth and pulse waveform complexity. We quantify the variation of error in pulse shape retrieval and error (difference) between the measured and the retrieved FROG trace for the delay line imperfections. We evaluate the dependence of both errors on the delay line jitter, which varied from a nearly ideal delay line (100 nm) up to an extremely inaccurate positioning (>1000 nm). Since the FROG error is always experimentally accessible, our results also provide guidance on judging the pulse reconstruction quality when the delay line jitter is the dominant source of noise.

Based on the error values and their comparison to the effect of noise in the measurement, we can assign a feasible value of the delay line jitter with respect to the bandwidth-limited (BWL) length of the pulse spectrum. Therefore, the presented results can serve as a guideline for limiting the delay jitter in FROG experiments.

## 2. Simulations

### 2.1. Pulse shapes

We studied the effect of delay line jitter on three sets of pulses. All of them were created by applying random variations to the spectral phase dependence of a pulse featuring the Gaussian spectrum. Each set differs in the spectral bandwidth and complexity. This approach corresponds to the case, where a spectrum provided by a laser system is modulated by a pulse shaper or by any other means. The main parameters of the sets are summarized in Table 1.

**Table 1. Characteristics of the three sets of input pulses.**  $\lambda_0$  is the pulse central wavelength,  $\Delta\lambda$  is the FWHM of the spectral intensity,  $\Delta t_{\text{Gauss}}$  is the FWHM of the temporal intensity of the transform limited Gaussian pulse corresponding to the spectral width, if no phase variations were applied,  $N$  is the size of the square FROG trace grid,  $dt_{\text{GRID}}$  is the time interval of the grid (the frequency interval is related by the Fourier transform  $d\nu=1/N \cdot dt$ ), # of pulses denotes number of different pulses in the set.

	$\lambda_0$ [nm]	$\Delta\lambda$ [nm]	$\Delta t_{\text{Gauss}}$ [fs]	$N$	$dt_{\text{GRID}}$ [fs]	# of pulses	note
Set 1	800	151	6.2	128	1.57	50	source: [15]
Set 2	800	37.8	25	200	4	50	Set1 4× prolonged
Set 3	654	32	20	512	4	20	our exp. conditions

Set 1 is taken from the work of Sidorenko et al. [15], which simulates pulses with very broad bandwidth. The pulses correspond to the few-cycle pulses with respect to their spectral bandwidth. However, due to their phase modulation, they are stretched in time. Here, the random spectral chirp has been adjusted so that the temporal support of the pulse is shorter than 200 fs. Set 2 is

formed by pulses with the same shapes as in Set 1; the pulses have, however, been stretched four times in time, i.e., they feature a four times narrower spectral bandwidth. Lastly, Set 3 has been derived from the experimental conditions in our laser laboratory. We applied highly modulated spectral chirps in order to get pulses randomly modulated in time. Hence, the temporal shape of the pulse intensity in Set 3 is more complex compared to Set 2, leading to approximately 2.5-fold increased temporal support. Examples of a pulse for each set are shown in the insets of Fig. 5.

## 2.2. Jitter simulation

In all the presented cases, calculations were run on all three complete sets of laser pulses. For each pulse from a set, we simulated an ideal FROG trace, which was consequently distorted by the simulation of randomly displaced delay line. It is worth stressing that our calculations assume delay line position, thus also the displacement, being constant throughout the single spectrum acquisition.

We take into account two physical models, which we will denote as random jitter and random-walk jitter. The random jitter corresponds to the delay fluctuations, where the jitter for each data point is independent of the previous one, following a normal distribution with standard deviation  $\sigma_{jitter}$ . This case corresponds to the situation, where the delay line is mechanically unstable and its imperfections cause the delay to fluctuate. For instance, the front/rear tilt of 5  $\mu\text{rad}$  of a retroreflector located 50 mm above the delay line will shift the delay by 250 nm.

The random-walk model, on the other hand, simulates the behaviour of a delay line, which is scanning through a set of positions and the error arises due to the sensor and controller limitations. In this case, the displacement from the ideal position depends on the previous data point, because it is calculated by a shift from the previous delay line location, where the shift is burdened by a random error following a normal distribution with standard deviation  $\sigma_{jitter}$ . To simulate realistically the delay line behaviour, it is restricted to (i) move only in the scanning direction, (ii) displacements bigger than a certain value ( $4 \sigma_{jitter}$ ) are not allowed, as such case is expected to be corrected by a controller.

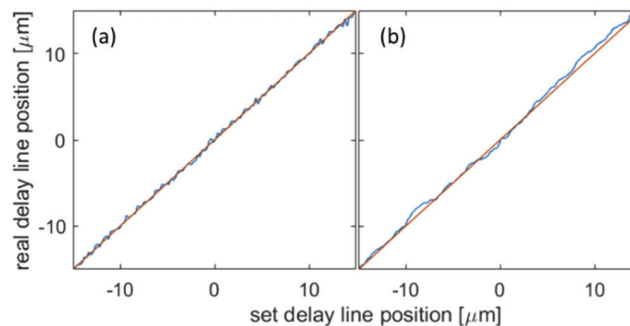


**Fig. 1.** Example of a displacement of a correct delay line position in case of a) random jitter b) random-walk jitter, both with  $\sigma_{jitter} = 500$  nm. The red line is the correct delay line position set in the experiment, the blue lines correspond to the real jitter-influenced delay line position.

The examples of both types of jitter are shown in Fig. 1. For the sake of simplicity, the Figs. 2–5 show only the data for the random jitter, findings from the data experiencing random-walk jitter are presented in Fig. 6. The values of the  $\sigma_{jitter}$  for particular simulations were selected as 0, 100, 250, 500, 1000, and 1500 nm.

### 2.3. SHG FROG reconstruction

The FROG traces were reconstructed using the ptychographic algorithm described in [15], following the version in Ref. [16]. This algorithm is known to be able to reconstruct also incomplete data. However, in our case, the data were reconstructed from a full FROG trace, where no cropping in the temporal and spectral support was introduced. Since the reconstruction algorithm is initiated randomly, we carried out 30 independent runs for each reconstruction in order to eliminate non-converging solutions and to see the statistics of the results.

Figure 2 illustrates a typical reconstruction of a FROG trace of a pulse from the Set 1 corrupted by the delay line random jitter (see top left panel). The jitter value  $\delta_{jitter}$  here is 500 nm, corresponding to 3.3 fs in time, which is significant even with respect to the bandwidth-limited length of the pulse spectrum (6.2 fs). Still, the amplitude of the pulse in the bottom panels (time evolution on the left, spectrum on the right) is reconstructed perfectly and the phase shows reasonable agreement. In both bottom panels, the recovered amplitude (dotted blue line), which corresponds to the actual pulse shape, is overlaid almost perfectly by the solid line of the simulated ansatz across the entire pulse.

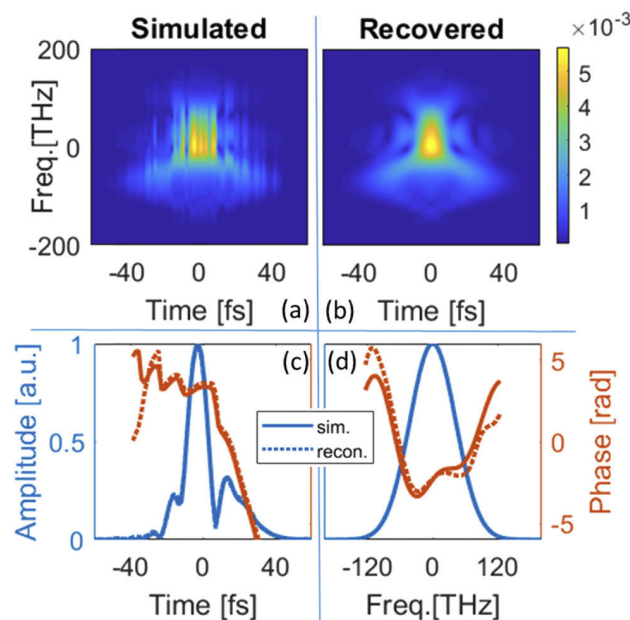


**Fig. 2.** Pulse #4 from Set 1: a) simulated FROG trace taking into account a delay line random jitter with  $\delta_{jitter} = 500$  nm, b) recovered FROG trace, c) and d) reconstructed (dots) and original (line) pulse time and spectrum evolution, respectively. Blue lines denote amplitudes, red phase.

The quality of the FROG reconstruction was significantly enhanced by using the laser spectrum to promote the algorithm convergence. The spectrum is not explicitly required by the FROG reconstruction procedure, the pulse can be reconstructed from the trace even without any prior knowledge. However, since the spectrum is easily experimentally accessible and improves the speed and the result of the reconstruction, all reconstructions here were done by employing the known laser spectrum in the pulse retrieval. Specifically, after the 10-th iteration, the amplitude of the spectrum of the laser pulse was replaced the spectral amplitude of the actual reconstruction of the pulse, while the phase information was retained.

## 2.4. Error evaluation

To quantitatively evaluate the fidelity of the reconstruction, we used two measures: (i) the rms error of the reconstructed FROG trace with respect to the jitter-distorted FROG trace entered into the algorithm; (ii) the rms intensity error of the retrieved pulse with respect to the original pulse as defined in [5, p.197, p.192].

A commonly used measure to evaluate the FROG reconstruction is the  $G$  error [5, p. 160]:

$$G = \left\{ \frac{1}{N^2} \sum_{i,j=1}^N |I_{ij}^{jit} - \hat{\mu} \hat{I}_{ij}|^2 \right\}^{1/2}, \quad (1)$$

where the measured trace  $I^{jit}$  is normalized to the peak value of 1,  $\hat{I}$  is the retrieved trace and  $\mu$  is fitted for the minimum  $G$ . Summation is done through time and frequency axis and  $N$  is the size of the FROG trace grid.

Because the  $G$  error depends on the size of the grid  $N$ , it would not allow a direct comparison of different sets of pulses. Therefore, throughout the text, we mainly employed a normalized rms FROG error, which we will denote as  $\varepsilon_{FROG}$ . The normalized FROG error was calculated as:

$$\varepsilon_{FROG} = \frac{\left\{ \frac{1}{N^2} \sum_{i,j=1}^N (\hat{I}_{ij} - I_{ij}^{jit})^2 \right\}^{1/2}}{\left\{ \frac{1}{N^2} \sum_{i,j=1}^N (I_{ij}^{jit})^2 \right\}^{1/2}}, \quad (2)$$

where the meaning of the symbols is the same as in Eq. (1), only  $I^{jit}$  need not to be normalized. The normalization is provided by dividing by the FROG trace integral, the variable  $N$  cancels out.

The pulse intensity error, denoted as  $\varepsilon_I$ , was determined as:

$$\varepsilon_I = \left\{ \frac{1}{N} \sum_{j=1}^N (I^k(t_j) - I(t_j))^2 \right\}^{1/2}, \quad (3)$$

where  $I^k$  and  $I$  are the intensity of the retrieved and the original pulse respectively; summation is done through the time axis.

In order to illustrate the quality of the pulse reconstruction with respect to the intensity error, we depict in Fig. 3 the pulse waveform of the best and the worst reconstructed case of the reconstruction of 50 pulses from Set 1 for the random jitter  $\sigma_{jitter} = 500$  nm.

The intensity error of the best case is 0.001 and of the worst case it is 0.014, while the normalized FROG error is 0.23 and 0.19, respectively. The fact that the both, the  $G$  error and the normalized FROG error, are fairly large and similar for both cases reveals that it reflects mainly the difference between the corrupted and the correct FROG trace. This is illustrated by the normalized FROG error calculated from the retrieved trace with respect to the ideal trace  $\varepsilon_{FROGideal}$ , which is an order of magnitude lower compared to the normalized FROG error. On the other hand, it is worth stressing that even though the jitter of 500 nm corresponds to the delay of 3.3 fs and the resulting FROG trace is highly distorted [see Fig. 2(a)], the main features of all pulses were captured in good agreement with reality.

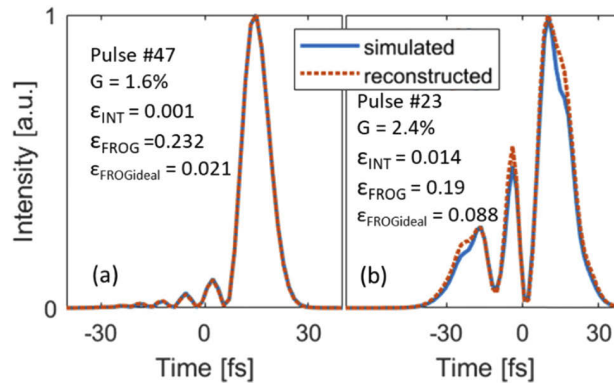


**Fig. 3.** The intensity of the time evolution of the best and the worst retrieved pulses from Set 1 using FROG traces with random jitter  $\delta_{jitter} = 500$  nm; blue full line stands for the original pulse, red dotted line for the reconstructed pulse. The text shows the  $G$  errors, rms intensity and normalized FROG errors as defined in Eqs. (1)–(3), and the rms normalized FROG error of the reconstructed FROG trace in relation to the ideal FROG trace without jitter.

### 3. Results and discussion

The main objective of this work is to determine how large a jitter in the delay in the FROG experiment is still acceptable for a reliable reconstruction of a complex pulse shape. Therefore, the desired information to obtain is the intensity error, which reflects the similarity of the reconstructed pulse waveform to its original shape. Unfortunately, this information cannot be attained from the experiment. On the contrary, the FROG error, i.e., the difference between the reconstructed and the measured FROG trace, is always available. Therefore, the core of our work consists in finding conditions under which the FROG error can also reflect the actual pulse reconstruction quality.

#### 3.1. Normalized FROG vs. intensity error correlation

We carried out an extensive batch of simulations, where measurements of pulses from all three sets were simulated for a broad range of delay line jitters scaling from an ideal case ( $\delta_{jitter} = 0$ ) up to an extremely unreliable delay line behaviour ( $\delta_{jitter} = 5000$  nm).

First, we focus on pulses from Set 1. The upper panels in Fig. 4 provide an example of the resulting intensity and normalized FROG errors for two representative random jitters. We present here results from all the reconstructions. Different colours and symbols denote different pulses; same symbols of the same colour denote several runs of the reconstruction algorithm on one FROG trace (belonging to one pulse).

The two presented random jitter values in Fig. 4 show significantly different behaviour. For the 100 nm jitter, most of the simulation runs ended up with both intensity error and the normalized FROG error close to zero, while some of them did not converge to the original solution and reached a high error level. Nevertheless, the values of both errors are clearly correlated and, consequently, we can select the best pulse reconstructions based on the normalized FROG error level. This correlation gradually vanishes and for data with the  $\delta_{jitter} = 1000$  nm, the data points of the two errors form an uncorrelated cloud. In other words, the knowledge of the normalized FROG error cannot be used to judge the quality of the reconstruction and even a large normalized FROG error does not necessarily mean a large discrepancy between the real and the reconstructed pulse and vice versa.



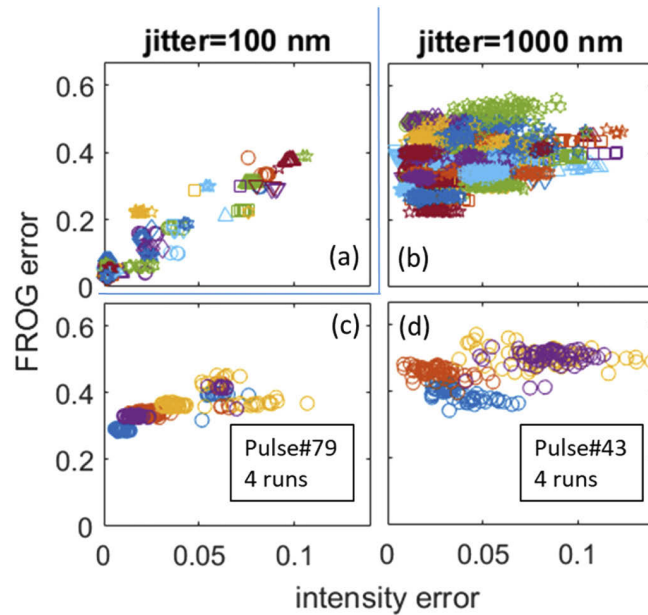


**Fig. 4.** Relation between the intensity and the normalized FROG error for random jitter a)  $\delta_{\text{jitter}} = 100$  nm and b)-c)  $\delta_{\text{jitter}} = 1000$  nm. Top panels show results from all runs of the reconstruction for all retrieved pulses, bottom panels represent results of one pulse reconstructed from 4 different simulated FROG traces (all of them with  $\delta_{\text{jitter}} = 1000$  nm, but different realizations).

A question of interest is the possibility to improve the reconstruction by carrying out several different measurements. The natural choice would be to average a series of measurement (i.e., FROG traces), which would cause the averaged FROG trace to be smeared in its delay axis. The effect of such averaging has been described in several articles [10,13,17]. Another option consists in the possibility to evaluate each of the measurement individually and to choose the best measurement only according to the reconstruction error. In principle, a certain combination of the random delay errors can cause the FROG trace to converge to the right pulse. This is addressed in the lower panels of Fig. 4, where various colours stand for pulse retrieval from different simulated measurements for random jitter  $\delta_{\text{jitter}} = 1000$  nm. The pulse intensity error varies among the data points by more than an order of magnitude. However, the normalized FROG error has no significant dependence and, therefore, it is unfortunately not possible to judge from the experimental results, which FROG trace gives the best results.

### 3.2. Effect of random jitter on the best pulse retrieval

The subsequent task is to determine how the pulse reconstruction quality varies with the delay line jitter. In order to avoid non-converging runs, we will focus in this section on the best reconstructions, which were selected from 30 different runs based on the minimal intensity error. We depict the best reconstructions in Fig. 5 for various  $\delta_{\text{jitter}}$  values (different colours) for three different sets of pulses (panels a, b, c) – note the logarithmic intensity error axis. Each panel also includes an example of a typical pulse from the set. All data in Fig. 5 correspond to the random jitter.

First, we will compare Set 1 (panel a) with Set 2 (panel b). The first set of pulses are short pulses with a relatively simple structure, and the second set are the same pulse waveforms stretched in time so that they meet the spectral bandwidth reachable with our laser system. Therefore, the

only difference between the sets consists in the pulse bandwidth, which is four times lower for Set 2, leading to a four times shorter duration of the BWL pulse for Set 1. In accord with the BWL pulse length, we observe that the intensity error vs. the normalized FROG error for Set 2 follows the results for Set 1, where the same intensity error values are obtained for four times smaller delay line jitters; compare the green cloud in panel b) and the yellow cloud in panel a). Therefore, we can state that the random jitter value has to be accounted relative to the pulse BWL length.

Secondly, we can compare the case of pulses with nearly identical BWL pulse length, Set 2 (25 fs) and Set 3 (20 fs), which differ in their phase modulation and the resulting complexity. Surprisingly, reconstruction of the more complex pulses with reasonable delay line jitters (below 1000 nm) typically features a slightly lower intensity error. Nevertheless, the overall trend and scales remain similar.

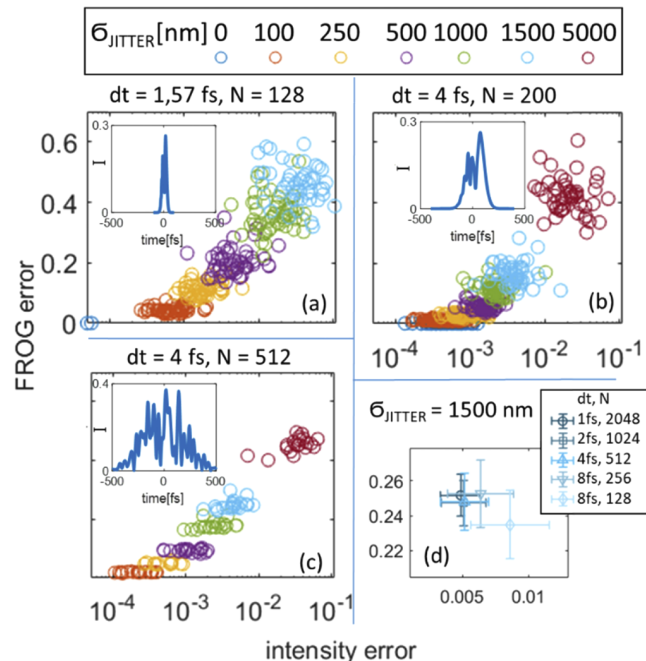


**Fig. 5.** The effect of random jitter on relation between intensity and normalized FROG error. Only the best solutions from 30 reconstructions are shown for every pulse. Colours depict different  $\sigma_{\text{jitter}}$ . a) Set 1, b) Set 2, c) Set 3; insets show an example of a pulse. The time interval and the size of the grid are written above the graphs. d) shows an enlargement of this relation for different (coarser and finer) FROG trace divisions for the pulses from Set 3 with  $\sigma_{\text{jitter}} = 1500$  nm.

It can be argued that the pulses from different sets were simulated by using different time step  $\Delta t$  and number of points  $N$  and, therefore, a direct comparison between the simulations is not meaningful. For this reason, we performed test reconstructions with all 20 pulses from Set 3, where we simulated data with varying parameters  $\Delta t$  and  $N$ . The spectral resolution was set to always satisfy the Fourier transform condition  $\Delta\nu = 1/(\Delta t \cdot N)$ . The calculations were done for random jitter  $\sigma_{\text{jitter}} = 1500$  nm, i.e., the light blue symbols in Fig. 5(c). The data points in Fig. 5(d) represent an average of the five best retrieved pulses, while the error bars scale with their standard deviation. The graph in Fig. 5(d) demonstrates that both errors, the intensity and the normalized FROG, feature very weak dependence on the data sampling. Note that the scale

of the graph is magnified for the sake of comparison, since in the scale of panels a)-c) all the points would overlap.

Based on Fig. 5, we can provide guidance on the required random jitter level, which will make it possible to keep the pulse intensity error below a certain level. The most prominent parameter is the desired intensity error level, which depends on the particular experiment and can be more restricting, for instance, in nonlinear spectroscopy, where a variation of the pulse shape can distort the experimental results [18,19].

### 3.3. Effect of random-walk jitter on the best pulse retrieval

Analogously to the previous sub-section, we carried out a set of simulations, where the delay line imperfections were simulated as a random-walk jitter [see Fig. 1(b)], which caused the delay line position displacement to gradually evolve through the measurement. It is worth noting that depending on the particular random track, the standard deviation of the resulting delay line displacement is 1.2-2× bigger compared to the  $\sigma_{jitter}$  parameter.

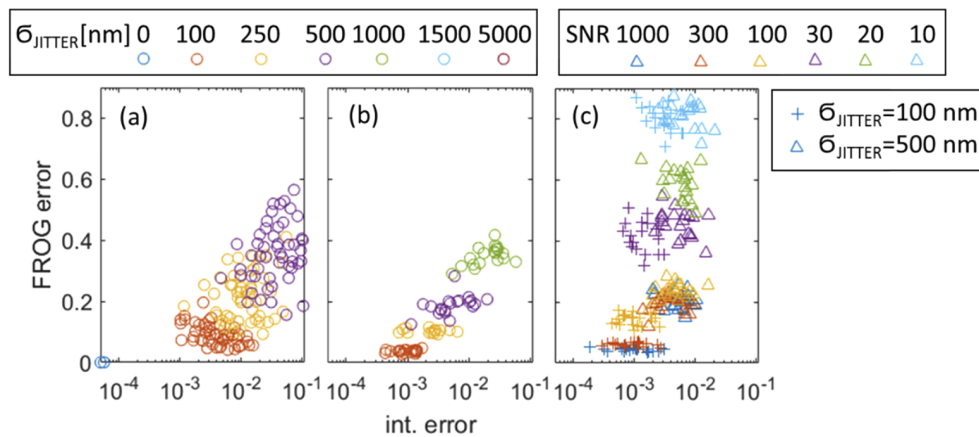


**Fig. 6.** a) and b) Relation between intensity and normalized FROG error for measurements corrupted by a random-walk jitter for Set 1 and Set 3, respectively. Only the best solutions from 30 reconstructions are shown for every pulse. Colours depict different  $\sigma_{jitter}$ . c) random-walk jitter with  $\sigma_{jitter} = 100$  nm (crosses) and 500 nm (triangles) applied together with noise to the pulses of Set 3. Colours depict different signal-to-noise ratio (SNR).

Figures 6(a) and 6(b) illustrates the effect of the random-walk jitter on the pulses from Set 1 and Set 3, respectively. Those can be compared to the corresponding panels Figs. 5(a) and 5(c) for the random jitter. When we focus on the random-walk jitter with  $\sigma_{jitter} = 500$  nm for Set 1 [violet circles, Fig. 6(a)], we can see that the effect of random-walk jitter on the pulse reconstruction is significantly more pronounced compared to the random jitter [violet circles, Fig. 5(a)]. This can be partly ascribed to the fact that the character of the random walk jitter causes the delay line displacement  $\Delta d$  to feature up to 2-times higher standard deviation, i.e.,  $\sigma_{jitter} = 500$  nm leads to standard deviation of the  $\Delta d$  being typically between 600-1000 nm. However, even for the  $\sigma_{jitter} = 250$  nm random-walk jitter [yellow circles, Fig. 6(a)], we can observe that the intensity error is increased compared to that of the random jitter  $\sigma_{jitter} = 500$  nm.

We systematically observed that the gradual drift of the delay line jitter has a significantly worse effect on the pulse reconstruction compared to the randomly fluctuating jitter. This can be ascribed to the fact that the random-walk jitter, unlike the previous case, can displace certain features in the FROG trace along the delay axis and break the symmetry of the SHG FROG with respect to the zero delay.

### 3.4. Jitter vs. noise effect on the pulse retrieval

In this section, we will put the presented simulations in perspective with the effect of noise on the pulse retrieval. The effect of noise itself on the FROG reconstruction was extensively discussed in the published literature [5,6,10,15]. Here we focus on the interplay between the effect of noise and the delay line imperfections.

Namely, we applied a random-walk jitter with the  $\delta_{jitter}$  values of 100 and 500 nm on FROG traces generated for Set 3. The FROG traces were consequently corrupted with an additive noise following a normal distribution, which simulated a dark-count noise for a high level of background. The noise level was adjusted by the signal-to-noise ratio (SNR) so that the noise standard deviation was set to  $1/\text{SNR}$  of the FROG trace electric field amplitude.

The effect of SNR value on the pulse retrieval is illustrated in Fig. 6(c). We observed that with the decreasing SNR, i.e. increasing noise level, the random noise becomes rapidly the dominating source of the normalized FROG error. For the nearly-ideal delay line ( $\delta_{jitter} = 100$  nm), already the SNR of 100 significantly increases the normalized FROG error. Despite this, the pulse intensity error is dominantly affected by the delay line precision and depends very mildly on the SNR. The benefit of the delay line precision is lost only for the highly noisy dataset (SNR=10). For  $\delta_{jitter} = 500$  nm, the normalized FROG error is dominated by the jitter error up to SNR = 100 nm [compare violet circles in Fig. 6(b) and blue, red and yellow triangles in Fig. 6(c)].

To put these results into perspective with other reports on the effect of noise, we will evaluate also the commonly used  $G$  error. A typical  $G$  value in the SHG FROG experiments for a  $128 \times 128$  points grid is  $< 0.5\%$  [20], which arises even for the nearly ideal experimental data due to the inevitable noise in the measurement, such as shot noise or a readout noise. The random walk jitter of 100 nm for the SNR of 1000 (very good standard), leads to the typical  $G$  values of  $0.3\%$ ; for the SNR of 10 (very high noise) the  $G$  value  $8.5\%$ . Our finding is in line with the previous reports [5 p.185], where the FROG reconstruction was demonstrated to be highly robust against the noisy FROG spectra.

### 3.5. Acceptable delay line jitter

As we showed in the previous sub-section, the delay line jitter is one of the important factors, when it comes to the pulse retrieval quality. It is, therefore, natural to address the question of an acceptable delay line jitter. While it is clear that a more precise delay line provides a better pulse reconstruction, Fig. 3(b) demonstrates that even the intensity error of 0.014 corresponds to a dataset, where all major features of the pulse are retrieved.

When we evaluate the acceptable jitter, it is needed to take into account the spectral bandwidth of the studied pulse. Since the spectral and temporal amplitudes of a pulse electric field are connected via Fourier transform, the spectral bandwidth determines the mean width of the pulse features in time. As an example, by increasing the spectral bandwidth two times, we gain a pulse, where all its intensity fluctuations in time are two times narrower. Therefore, a natural time scale to judge on the effect of delay line jitter is the BWL pulse length, which determines the shortest pulse length attainable by a given spectrum.

We will first turn to the random jitter. If we focus on the  $G$  error of the FROG trace, we reach for Set 1 the level of  $G$  around  $0.5\%$  already for the random jitter of 100 nm (0.7 fs). The margin of  $0.5\%$  corresponds, as stated previously, to the nearly-ideal experimental trace [20]. This might indicate that the random jitter could easily become the limiting factor in experiments with short pulses, as its jitter should be  $\sim 7$  times lower than the FWHM of the BWL pulse. However, the  $G$  error calculated between the retrieved trace and the ideal FROG trace reaches the value of  $0.5\%$  only for the random jitter featuring  $\delta_{jitter} = 500$  nm. Hence, the actual demands put on the delay line for the random jitter need not be so strict.

For comparison, see the results for the 500 nm random jitter in Fig. 5(a), where they are clustered around normalized FROG error 0.2 and intensity error  $5 \times 10^{-3}$ . In this case, the jitter

value is comparable to the BWL pulse length itself, yet the pulse retrieval captures all the major features in the pulse shape.

However, the random-walk type of the jitter has significantly more pronounced effect on the pulse reconstruction. In order to assure that the pulse intensity error remains in the majority of cases below 0.02, it is required to keep the random jitter value very low. For our model of the delay line behavior, the acceptable level of  $\delta_{jitter}$  for Set 1 was 100 nm, for the Set 3 it was approx. 500 nm.

Since the actual behaviour of the delay line and the contribution of the random and random-walk jitter can differ from one experimental setup to the other, it is of interest to set a general criterion, which can ensure a reliable pulse reconstruction. Here we suggest using the experimentally available normalized FROG error. Both the data presented in Fig. 5 and Fig. 6 show that setting the normalized FROG error below 0.2 provides us in the vast majority of datasets with pulse reconstruction with intensity error below 0.02 for all types of pulses and jitter examined in our work. Besides, we observed that the value of the FROG error below 0.2 is also a limit which ensures a good pulse reconstruction in our usual SHG FROG experiments. At the same time, it is worth stressing that this criterion can be only applied for the datasets with a low noise level [see Fig. 6(c)]. For the reduced SNR, the normalized FROG error becomes quickly dominated by the FROG signal noise, while the pulse reconstruction quality might not be affected.

#### 4. Conclusions

We presented an extensive set of simulations where we evaluated the effect of the delay line random jitter on FROG reconstruction. Such jitter can result from the necessity to reduce the acquisition time, or it can arise due to imperfections of the delay line, as well as due to instability of the measurement setup. We carried out calculations for jitter values ranging from high-precision delay lines (100 nm, 0.67 fs delay) up to extremely unstable measurements (> 1000 nm, > 6.7 fs). Also, we compared three sets of pulses featuring different bandwidth and waveform complexity.

For all sets of pulses, both the normalized FROG error and the pulse intensity error increase with the increasing delay line jitter. While the normalized FROG error is a good measure of the reconstruction quality for the low delay line jitters, such as 100 nm, this correlation is completely lost for the large jitter values. We observe that the effect of the jitter scales together with the BWL pulse length, which is given by the pulse spectral bandwidth.

We studied two types of jitter behaviour. The randomly displaced delay (random jitter) was acceptable for the reliable pulse retrieval even for the simulations, where the random jitter was comparable to the BWL pulse length. For instance, for the pulses created by the modulation of a spectral phase of a BWL pulse of 6.2 fs, we observe that the FROG trace error introduced by the delay line jitter equals the nearly-ideal noise level from experimental data when the delay line jitter reaches 100 nm. However, a reliable reconstruction can be obtained up to  $\delta_{jitter} = 500$  nm. Nevertheless, the random-walk jitter, where the delay error gradually randomly varies around the ideal value, had significantly more pronounced effect and the reliable pulse retrieval required  $\delta_{jitter}$  more than  $2\times$  lower.

Since each experimental setup can differ in the particular behaviour of the delay line jitter, we propose a general criterion based on the normalized FROG error, which is available for the experimental data. For all our simulations, when the level of normalized FROG error is below 0.2, we observe that the vast majority of the pulse intensity errors does not exceed 0.02 and the reconstructed pulses feature good fidelity. Even for the FROG error well above that value, we might still attain a very well reconstructed pulse. It is, however, difficult to judge the quality from the experimental data, as there can be a number of possible sources of FROG error, such as random noise in the measured data.



A surprising finding was the fact that we obtained better reconstruction of a pulse for the longer and the more complex pulses, which was, beside the error level, also visually apparent by the waveform comparison. This observation is similar to the experiments in [10], where they observed that the presence of multiple sidebands helps the algorithm to reach faster convergence in the case of a temporal jitter between the XUV pulse and a suitably delayed infrared pulse.

We would like to point out that our results were evaluated based on the ptychographical reconstruction, while various other algorithms (e.g., COPRA or PCGPA [21,22]) might differ in their robustness against the FROG trace jitter. This comparison is an interesting question for future work.

The presented results can be used in order to optimize the FROG experiment with respect to the acquisition time and to the experimental setup cost.

**Funding.** Akademie Věd České Republiky (ERC-CZ/AV-B ERC100431901); Ministerstvo Školství, Mládeže a Tělovýchovy (CZ.02.1.01/0.0/0.0/16\_026/0008390).

**Acknowledgement.** We thank for helpful discussion about ptychographic reconstruction to Pavel Sidorenko.

**Disclosures.** The authors declare no conflicts of interest.

## References

1. J. M. Dudley, G. Genty, and S. Coen, "Supercontinuum generation in photonic crystal fiber," *Rev. Mod. Phys.* **78**(4), 1135–1184 (2006).
2. A. M. Heidt, D.-M. Spangenberg, M. Brüggemann, E. G. Rohwer, and T. Feurer, "Improved retrieval of complex supercontinuum pulses from XFROG traces using a ptychographic algorithm," *Opt. Lett.* **41**(21), 4903–4906 (2016).
3. A. Tajalli, D. J. McCabe, D. R. Austin, I. A. Walmsley, and B. Chatel, "Characterization of the femtosecond speckle field of a multiply scattering medium via spatio-spectral interferometry," *J. Opt. Soc. Am. B* **29**(6), 1146 (2012).
4. L. Levin, W. Skomorowski, L. Rybak, R. Kosloff, C. P. Koch, and Z. Amitay, "Coherent Control of Bond Making," *Phys. Rev. Lett.* **114**(23), 233003 (2015).
5. R. Trebino, "Frequency-Resolved Optical Gating: The Measurement of Ultrashort Laser Pulses," Book. Kluwer Academic Publishers (2000).
6. D. N. Fittinghoff, K. W. DeLong, R. Trebino, and C. L. Ladera, "Noise sensitivity in frequency-resolved optical-gating measurements of ultrashort pulses," *J. Opt. Soc. Am. B* **12**(10), 1955–1967 (1995).
7. L. Xu, E. Zeek, and R. Trebino, "Simulations of frequency-resolved optical gating for measuring very complex pulses," *J. Opt. Soc. Am. B* **25**(6), A70 (2008).
8. S. Yermenko, A. Baltuska, M. S. Pshenichnikov, and D. A. Wiersma, "The criterion of pulse reconstruction quality based on Wigner representation," *Appl. Phys. B* **70**(S1), S109–S117 (2000).
9. X. Gu, L. Xu, M. Kimmel, E. Zeek, P. O'Shea, A. P. Shreenath, and R. Trebino, "Frequency-resolved optical gating and single-shot spectral measurements reveal fine structure in microstructure-fiber continuum," *Opt. Lett.* **27**(13), 1174–1176 (2002).
10. M. Murari, G. D. Lucarelli, M. Lucchini, and M. Nisoli, "Robustness of the ePIE algorithm for the complete characterization of femtosecond, extreme ultra-violet pulses," *Opt. Express* **28**(7), 10210–10224 (2020).
11. M. Rhodes, G. Steinmeyer, J. Ratner, and R. Trebino, "Pulseshape instabilities and their measurement," *Laser Photonics Rev.* **7**(4), 557–565 (2013).
12. J. Ratner, G. Steinmeyer, T. C. Wong, R. Bartels, and R. Trebino, "Coherent artifact in modern pulse measurements," *Opt. Lett.* **37**(14), 2874–2876 (2012).
13. H. Wang, M. Chini, S. D. Khan, S. Chen, S. Gilbertson, X. Feng, H. Mashiko, and Z. Chang, "Practical issues of retrieving isolated attosecond pulses," *J. Phys. B: At., Mol. Opt. Phys.* **42**(13), 134007 (2009).
14. J. Garduño-Mejía, E. Ramsay, A. Greenaway, and D. T. Reid, "Real time femtosecond optical pulse measurement using a video-rate frequency resolved optical gating system," *Rev. Sci. Instrum.* **74**(8), 3624–3627 (2003).
15. P. Sidorenko, O. Lahav, Z. Avnat, and O. Cohen, "Ptychographic reconstruction algorithm for frequency-resolved optical gating: super-resolution and supreme robustness," *Optica* **3**(12), 1320 (2016).
16. <https://oren.net.technion.ac.il/homepage/> on 19/8/2019.
17. C. Dorrer, "Effect of jitter on linear pulse-characterization techniques," *Opt. Express* **16**(9), 6567 (2008).
18. V. V. Lozovoy and M. Dantus, "Systematic control of nonlinear optical processes using optimally shaped femtosecond pulses," *ChemPhysChem* **6**(10), 1970–2000 (2005).
19. F. Frei, A. Galler, and T. Feurer, "Space-time coupling in femtosecond pulse shaping and its effects on coherent control," *J. Chem. Phys.* **130**(3), 034302 (2009).
20. R. Trebino, K. W. DeLong, D. N. Fittinghoff, J. N. Sweetser, M. A. Krumbugel, B. A. Richman, and D. J. Kane, "Measuring ultrashort laser pulses in the time-frequency domain using frequency-resolved optical gating," *Rev. Sci. Instrum.* **68**(9), 3277–3295 (1997).
21. N. C. Geib, M. Zilk, T. Pertsch, and F. Eilenberger, "Common pulse retrieval algorithm: a fast and universal method to retrieve ultrashort pulses," *Optica* **6**(4), 495–505 (2019).





22. D. J. Kane, "Real-time measurement of ultrashort laser pulses using principal component generalized projections," *IEEE J. Sel. Top. Quantum Electron.* **4**(2), 278–284 (1998).

# Dispersion Scan Frequency Resolved Optical Gating For Evaluation of Pulse Chirp Variation

M. GUESMI,<sup>1,\*</sup> PETRA VESELÁ,<sup>1</sup> AND KAREL ŽÍDEK<sup>1,\*</sup>

<sup>1</sup> Regional Center for Special Optics and Optoelectronic Systems (TOPTEC), Institute of Plasma Physics, Czech Academy of Science v.v.i., Za Slovankou 1782/3, 182 00 Prague 8, Czech Republic

\*[guesmi@ipp.cas.cz](mailto:guesmi@ipp.cas.cz), [zidek@ipp.cas.cz](mailto:zidek@ipp.cas.cz)

**Abstract:** The commonly used methods to characterize ultrafast laser pulses, such as frequency-resolved optical gating (FROG) and dispersion scan (d-scan), face problems when they are used on pulses with a chirp varying within the laser beam or the acquisition time. The presence of such chirp variation can be identified by a discrepancy between the measured FROG and d-scan traces and their reconstructed counterparts. Nevertheless, quantification of the variation from the experimental data is a more complex task. In this work, we examine the quantification of chirp variation based on three different pulse characterization techniques. Two commonly used techniques FROG and d-scan are compared to a new method dispersion scan FROG (D-FROG) that combines the idea of dispersion scanning with the FROG method. By using the three techniques, we analyze the chirp variation of pulses generated from NOPA together with pulses processed by a 4f-pulse shaper without and with SLM-adjusted phase. We evaluate the performance of the new D-FROG method for the chirp variation estimate and the improved reconstruction of the measured results. Furthermore, we discuss the origin of chirp variation in each of the measurements by using fast-scan autocorrelation traces.

© 2020 Optical Society of America under the terms of the [OSA Open Access Publishing Agreement](#)

## 1. Introduction

Ultrafast laser pulses are used in many different application domains, including the pulsed laser deposition [1], femtochemistry, femtobiology [2], or optical code division multiple access [3]. All the listed domains depend on reliable control and characterization of complex fs pulses, which can be carried out by a variety of methods. The simplest approach based on the autocorrelation technique provides only the minimum information about the shape of the pulse and a general waveform cannot be reliably recovered [4]. However, a range of other techniques makes it possible to recover even the complex pulse shapes. The most commonly used techniques are frequency-resolved optical gating (FROG) [5-7], cross-correlation frequency-resolved optical gating (XFROG) [6,7], spectral phase interferometry for direct electric-field reconstruction (SPIDER) [8], multiphoton intrapulse interference phase scan (MIIPS) [9], and dispersion scan (d-scan) [10].

Many of these methods face a problem when they are applied to characterize a pulse shape varying the laser beam or the acquisition time. We denote this situation as a chirp variation. In other words, the majority of standard pulse retrieval methods, including FROG, SPIDER, and d-scan, assume that the pulse shape is constant throughout the measured beam. However, even a small misalignment of a pulse compressor or a pulse shaper introduces a certain amount of spatial chirp (also denoted as chirp distortion) [11-13]. The spatially distorted pulse chirp also occurs due to the space-time coupling, which inevitably arises in the 4f pulse shapers [14,15]. An analogous situation can occur when the measured pulse is not stable in time and its chirp rapidly varies during the measurement. An example of this can be the effect of thermal fluctuations in spatial light modulators (SLMs) [16]. The chirp variation manifests itself



in the standard FROG setup as a discrepancy between the measured and the retrieved FROG traces. Nevertheless, the quantification of distortion from the FROG experimental data represents a more challenging task that has not been yet addressed.

In this article, we study the use of three different methods to quantify the chirp variation. Two commonly used techniques, FROG and d-scan, are compared to a new method, where we acquire FROG traces while we controllably vary the pulse dispersion by a known value of group delay dispersion (GDD) and third-order dispersion (TOD). We denote this method as dispersion scan FROG, shortly D-FROG. The D-FROG dataset includes both the d-scan and a range of FROG traces. We demonstrate the use of the three different methods on a characterization of pulses (i) generated from a non-collinear optical parametric amplifier (NOPA); (ii) the NOPA pulse passing through a 4f-pulse shaper without any modulation device; (iii), the NOPA pulse passing through a 4f-pulse shaper with SLM-adjusted phase.

We fit the experimental data by a model, where we assume that the GDD values are not a single value, which would correspond to an ideal pulse, but rather a distribution of the GDD values. The width of the distribution reflects the pulse variation. To reveal the origin of this chirp variation, we used a rapid autocorrelation scan, which allowed us to assign the variation to the chirp distortion across the laser beam.

By scrutinizing the attained results, we show that the D-FROG method provides a means of careful evaluation of the laser pulse, which can reveal and quantify the variation of the pulse chirp on the order of tens of  $\text{fs}^2$ . We also demonstrate that even in the cases, where a single measured FROG trace can be well reproduced with an ideal pulse, the D-FROG data provide a consistency checkable to identify the chirp variation.

## 2. Experimental procedure

The used experimental setup is depicted in Fig. 1. We employed a fs laser system Pharos (Light Conversion) operated at 1028 nm, which generated pulses 290 fs long at 10 kHz repetition rate, 100  $\mu\text{J}/\text{pulse}$ . A part of the output power (50  $\mu\text{J}/\text{pulse}$ ) was converted by a non-collinear optical parametric amplifier (NOPA) N-3H Orpheus (Light Conversion) into a visible laser pulse at 640 nm, spectral width FWHM 757  $\text{cm}^{-1}$ . We used a prism pulse compressor integrated into the NOPA to adjust pulse length and to vary the dispersion. The prism consisted of fused silica prisms separated by 775 mm, where the prism P2 insertion was adjusted by a motorized stage to alter the pulse dispersion. It is worth noting that the measured pulse did not represent the best attainable pulse compression of the NOPA pulses. The presence of distinct features in the FROG traces was beneficial for the demonstration of the instability effect and dispersion scanning.

The pulse from NOPA was either directly characterized in a FROG setup, which is described later, or it was modified by a pulse shaper. We used a standard 4f pulse shaper – see Fig. 1b -- employing grating 600 gr/mm, which spectrally disperse the beam in the horizontal direction. The dispersed beam was collimated and focused in the vertical direction by a spherical mirror ( $f = 500$  mm) onto a spatial light modulator SLM-S640 (Jenoptik) placed in the Fourier plane. SLM was calibrated by using a procedure described in [17]. Consequently, symmetrically aligned mirrors were used to refocus the beam on the grating.

Finally, the temporal and spectral shape of the output pulse was measured by using the FROG setup. In this setup, the pulse was split with a pair of 50:50 beam splitters into two pulse replicas with an identical chirp. The delay between the pulses was varied by a motorized delay line (PIMag Linear Stage) and the pulses were focused on a 0.05 mm thick beta barium borate (BBO) crystal (Eksma Optics), where they generated a sum-frequency signal. Due to the non-collinearity of the incident pulses, the sum-frequency signal can be spatially separated by a pinhole and coupled with a lens into a fiber and analyzed by a spectrometer (AvaSpec-ULS4096CL-EVO). The laser spectrum was measured from a scattered beam on the pinholes (Ocean Optics Flame T).

The second harmonic generation autocorrelation (SHG-AC) was acquired for the rapid scanning as a sum of the measured spectra. The acquisition time of a single SHG-AC trace was 60 ms. The traces were measured in the sweep mode, ie. continuously moving delay line with velocity 1 mm/s, spectrometer integration time 1 ms. To attain a sufficiently high signal, we increased in this experiment the repetition rate of the laser to 100 kHz.

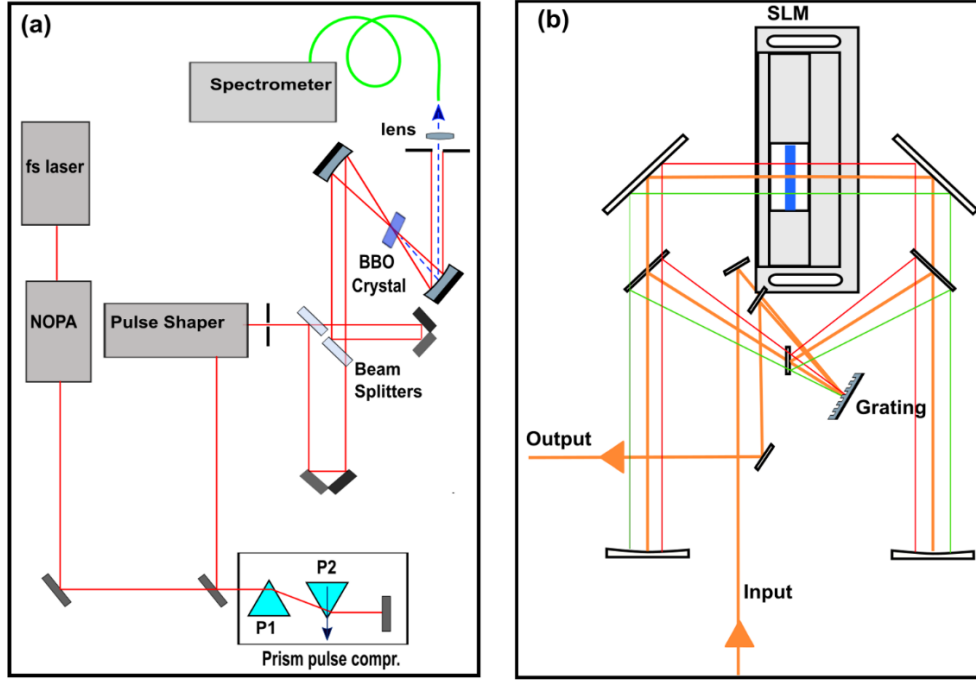


Fig. 1: (a) Experimental setup for the D-FROG. (b) Pulse shaper in 4f geometry.

### 3. Methods

#### 3.1 FROG

Our setup is based on the second harmonic FROG, where the intensity of the measured trace is given by:

$$I_{FROG}(\omega, \tau) = |\int E(t)E(t - \tau)\exp(-i\omega t)dt|^2, \quad (1)$$

where  $\tau$  and  $\omega$  are the pulse delay and the light frequency, respectively.  $E(t) = \sqrt{I(t)} \exp(-i\Phi(t))$  is a complex amplitude of the pulse, where  $I(t)$  is proportional to the light intensity and  $\Phi(t)$  denotes the phase as a function of time. The spectrum for  $\tau = 0$  corresponds to the SHG from a single pulse used in the d-scan measurements:

$$I_{SHG}(\omega) = |\int E(t)^2 \exp(-i\omega t)dt|^2. \quad (2)$$

A wide variety of algorithms can be used to retrieve the original pulse field  $E(t)$  from the from trace  $I_{FROG}(\omega, \tau)$ . We employed a ptychographic reconstruction procedure by Sidorenko et al. [18], which is illustrated in Fig. 2. Before the reconstruction, the experimental SHG FROG trace (upper left panel) was interpolated from the measured data to form  $N \times N$  matrix to reconstruct  $N$  elements of intensity and phase vector. The depicted experimental trace represents the electric field amplitude, i.e.  $\sqrt{|I_{FROG}(\omega, \tau)|}$ . This was very well reproduced by

the theoretical trace (upper right panel). The pulse reconstruction provided us with the temporal and spectral intensities and phases of the pulse depicted in the lower panels.

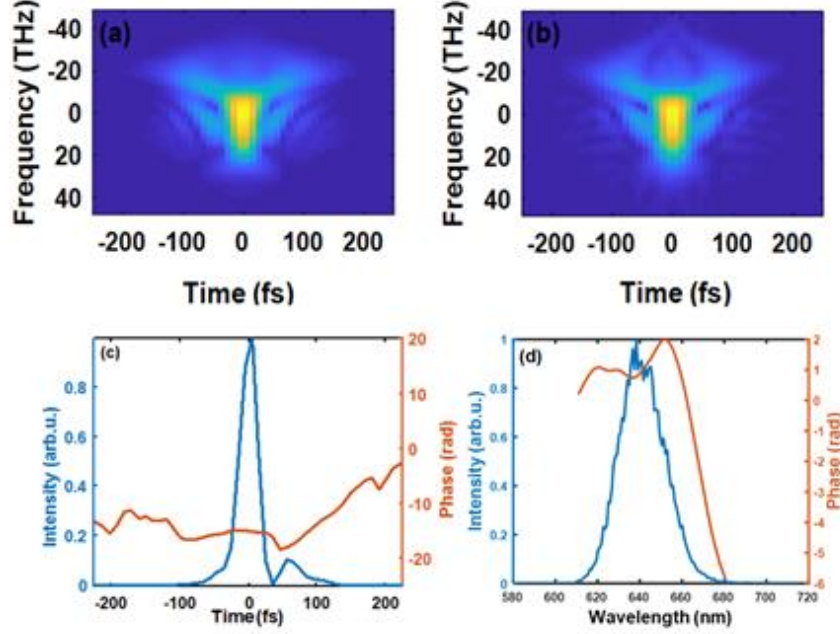


Fig. 2: Measured (a) and Retrieved (b) FROG traces from a compressed NOPA pulse. (c) Retrieved temporal intensity profiles and phases. (d) Retrieved spectral intensity profiles and phases.  $N=156$ ,  $T=800$ ,  $dt=10.32$  fs.

In all the presented reconstructions, we corrected the FROG trace for marginals, which nevertheless lead only to subtle changes in the FROG trace owing to the use of the very thin SHG-generating crystal (0.05 mm). We also applied the measured laser spectrum in the reconstruction. Starting from the 11<sup>th</sup> iteration, we replaced the retrieved spectrum of the pulse amplitude with the measured one. The FROG trace reconstruction was used as an initial step in all the presented measurements to estimate the spectral phase of the pulse  $\varphi_C$  for the reference prism insertion  $\Delta p = 0$ .

The FROG reconstruction, where we extract  $2N$  values from  $N^2$  is an overdetermined system, which can be used to check the consistency of the results. Inconsistency leads to a difference between the experimentally measured  $I_{FROG}^{exp}$  and the theoretically retrieved  $I_{FROG}^{th}$  FROG traces, which is commonly evaluated by the G-error:

$$G_{FROG} = \sqrt{\frac{1}{N^2} \sum_{\omega, \tau} |I_{FROG}^{exp}(\omega, \tau) - \mu \cdot I_{FROG}^{th}(\omega_i, \tau)|^2}, \quad (3)$$

where both experimental and theoretical traces are normalized to their maximum value and the parameter  $\mu$  is optimized to obtain the minimum  $G$  value. A high value of the error  $G$  indicates an issue in the measurement. However, it is problematic to judge the actual origin of the issue only from the experimental FROG trace, because the increased  $G$  error is affected by many factors, including the noise level of the FROG spectra [19], delay line imprecision [20], or chirp variation.

### 3.2 Dispersion-scan FROG

To overcome this problem, we employed an additional consistency check, where we controllably scan dispersion over a selected range to observe the phase change of the reconstructed pulse and the corresponding FROG trace. We scan the dispersion by varying position  $p$  of a prism in the prism compressor (see experimental section). In the spectral domain, the electrical field is given by:  $\tilde{E}(\omega) = \sqrt{S(\omega)} \exp(i\varphi(\omega)) = \mathcal{F}\{E(t)\}$ , where  $\sqrt{S(\omega)}$  and  $\varphi(\omega)$  are the spectral amplitude and phase, respectively. The phase  $\varphi(\omega, \Delta p)$  for a certain change in prism insertion  $\Delta p$  is given by a Taylor series as:

$$\varphi(\omega, \Delta p) = \varphi_c + \varphi_1(\omega - \omega_0) + \frac{1}{2}GDD(\Delta p) \cdot (\omega - \omega_0)^2 + \frac{1}{3}TOD(\Delta p) \cdot (\omega - \omega_0)^3, \quad (4)$$

where  $\omega_0$  is the central frequency,  $GDD$  represents the group delay dispersion and  $TOD$  is the 3rd-order dispersion.  $\varphi_c$  stands for the phase of the pulse for  $\Delta p = 0$ . The second term  $\varphi_1$  causes the pulse translation in time and it can be ignored in the FROG calculation. At the same time, the higher dispersion terms can be neglected.

### 3.3 Chirp variation

Under certain *conditions*, for instance, due to the space-time coupling induced in a 4fpulse shaper, it has been observed that pulse varies across the laser beam [14,15]. In this case, FROG trace becomes a sum of FROG traces with a distribution of spectral chirp  $\varphi(\omega, \Delta p)$ .

We can simulate the chirp variation by assuming that the resulting FROG trace arises as a sum of FROG traces from a set of pulses, where the quadratic chirp  $GDD$  is not a single value  $GDD(\Delta p)$ , but rather a distribution  $D(g)$ . We will use in the article a Gaussian distribution centered around the mean value  $GDD(\Delta p)$  with the standard deviation  $\sigma_{GDD}$ :

$$D(g) = \frac{1}{\sqrt{2\pi}\sigma_{GDD}} \exp\left[-\frac{(g-GDD(\Delta p))^2}{2\sigma_{GDD}^2}\right]. \quad (5)$$

Nevertheless, a various set of models can be applied, depending on the expected chirp behavior. The field corresponding to the  $GDD$  value  $g$  can be expressed as:

$$E(t, g, \Delta p) = \mathcal{F}^{-1}\left\{\sqrt{S(\omega)} \cdot \exp\left[\varphi_c + \frac{1}{2}g \cdot (\omega - \omega_0)^2 + \frac{1}{3}TOD(\Delta p) \cdot (\omega - \omega_0)^3\right]\right\}, \quad (6)$$

which allows us to calculate the D-FROG signal  $I_{DF}$  from a distorted pulse as a function of prism insertion:

$$I_{DF}(\omega, \tau, \Delta p) = \frac{1}{\sqrt{2\pi}\sigma_{GDD}^2} \int \exp\left[-\frac{(g-GDD(\Delta p))^2}{2\sigma_{GDD}^2}\right] |\int E(t, g, \Delta p) E(t - \tau, g, \Delta p) \exp(-i\omega t) dt|^2 dg. \quad (7)$$

By using Eq. (6), we can extract the d-scan signal  $I_{DS}$  by setting  $\tau = 0$ , ie

$$I_{DS}(\omega, \Delta p) = \frac{1}{\sqrt{2\pi}\sigma_{GDD}^2} \int \exp\left[-\frac{(g-GDD(\Delta p))^2}{2\sigma_{GDD}^2}\right] |\int E(t, g, \Delta p)^2 \exp(-i\omega t) dt|^2 dg. \quad (8)$$

To theoretically calculate the D-FROG, FROG and d-scan signal, we need to determine the  $GDD$  and  $TOD$  change with prism insertion  $GDD(\Delta p)$  and  $TOD(\Delta p)$ . These can be attained by using the approach introduced as a self-calibrating d-scan [22,23]. The spectral intensity shape  $S(\omega)$  was determined based on the laser spectrum. Finally, the spectral phase  $\varphi_c$  for the reference prism insertion  $\Delta p = 0$  was estimated by a standard FROG trace reconstruction (described in detail later). Therefore, we could use Eqs. (7) and (8) to fit a single unknown parameter  $\sigma_{GDD}$  from FROG, D-FROG and d-scan datasets. The quality of the fit for the FROG trace can be evaluated based on the  $G$ -error in Eq. (3). For the D-FROG and d-scan data, we



introduced an analogous  $G$ -error definition, where we sum the data also over the set of prism insertions  $\Delta p_i$  i:

$$G_{DF} = \sqrt{\frac{1}{N_i N^2} \sum_{\omega, \tau, i} | (I_{DF}^{exp}(\omega, \tau, \Delta p_i) - \mu \cdot I_{DF}^{th}(\omega, \tau, \Delta p_i)) |^2}, \quad (9)$$

$$G_{DS} = \sqrt{\frac{1}{N_i N^2} \sum_{\omega, \tau, i} | (I_{DS}^{exp}(\omega, \Delta p_i) - \mu \cdot I_{DS}^{th}(\omega, \Delta p_i)) |^2}. \quad (10)$$

In this case, we use an additional factor  $N_i$ , which indicates the number of scanned prism insertion positions.

#### 4. Results and discussion

We used three different methods: FROG, D-FROG, and d-scan to study and quantify the chirp variation. We will first introduce our methods on a simple case, where we directly measured a pulse generated from NOPA, which bypassed the pulse shaper.

The D-FROG and d-scan datasets were attained by scanning the prism insertion and FROG trace acquisition for each of the positions – see upper panels in Fig. 3 (a) – and d-scan trace depicted in Fig.3 (b) – upper panel. To retrieve the corresponding theoretical traces, we needed to find the dispersion change with the prism insertion, which we assumed to change linearly:  $G(\Delta p) \propto \Delta p$  and  $T(\Delta p) \propto \Delta p$ . The values were extracted by using the self-calibration d-scan approach, where we fitted the d-scan experimental trace by using Eq. (2). We set the FROG-reconstructed pulse as an initial guess, while the  $GDD(\Delta p)$  and  $TOD(\Delta p)$  scaling was left as a free fitting parameter. We extracted the values of  $GDD(\Delta p)/\Delta p = 500 \text{ fs}^2/\text{mm}$  and  $TOD(\Delta p)/\Delta p = 10 \text{ fs}^3/\text{mm}$ .

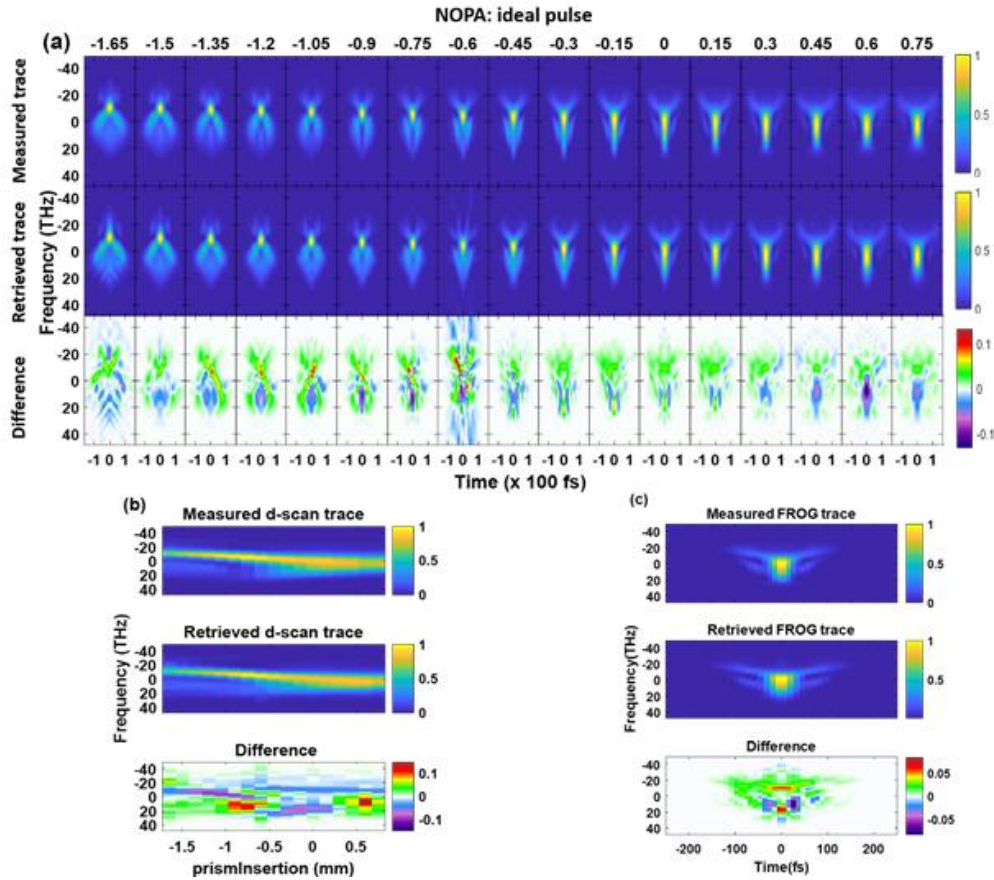


Fig. 3: Measured and retrieved traces of an ideal pulse, generated from NOPA, and their differences. (a) D-FROG traces (the traces are acquired for different prism insertion positions from -1.65 to 0.75 mm, as stated above the panels) (b) d-scan trace (c) FROG trace of a compressed pulse. The traces are retrieved using Eqs. (1) and (2), respectively, where  $N=156$ ,  $T=800$ ,  $dt=10.32$  fs.

This allowed us to calculate the FROG, D-FROG and d-scan traces, which we first evaluated from Eqs. (1) and (2) for an ideal pulse. Even by assuming the ideal chirp stability, we attained for the FROG traces the  $G$  error of about 0.5%, which is a value commonly-obtained for the SHG FROG experiments and the remaining minor difference can arise, for instance, by an error in the delay line position, imperfections in the spectral calibration of the spectrometers, or other factors [19,20]. It is worth stressing that the agreement in 17 FROG traces in Fig. 3a with very different shapes is achieved by using a single reconstructed spectral phase  $\varphi_C$  and two values of  $GDD(\Delta p)$  and  $TOD(\Delta p)$ .

The small  $G$  errors between the measured and recovered traces for the NOPA pulse (listed in Table 1 for all experiments) are a sign of the low chirp variation. This is also confirmed by the d-scan trace in Fig. 3b, which is not smeared along the prism insertion axis, as it would be expected for the distorted chirp. We can therefore expect a subtle chirp variation in this dataset.

To study and quantify the chirp variation, we fitted the FROG, D-FROG and d-scan traces from Eqs. (7) and (8) by leaving the chirp distribution width  $\sigma_{GDD}$  as a free fitting parameter. The retrieved D-FROG and FROG traces are shown in Fig. 4 (a) and Fig. 4 (c), where their fitted standard deviations  $\sigma_G$  are equal to 30 and 0 fs<sup>2</sup>, respectively. The difference between each measured and calculated trace is depicted in the panel below with a different color scheme.

Naturally, by using an additional fitting parameter, we were able to improve the retrieved traces and lowers the  $G$  error values (see Table 1). This improvement is visually apparent for the lowest prism insertion  $\Delta p = -1.65$  mm, where the fine structure present in the ideal reconstruction (see positive frequencies) is smeared by the chirp variation, and for the prism insertion  $\Delta p = -0.6$  mm, where the same takes place for the fine structure at the negative frequencies. Nevertheless, in agreement with the qualitative analysis, the chirp variation is close to zero. Such small variation can arise due to a slight misalignment of the prism compressor or by the pulse generation in NOPA, where both can cause a minor spatial chirp variation across the beam.

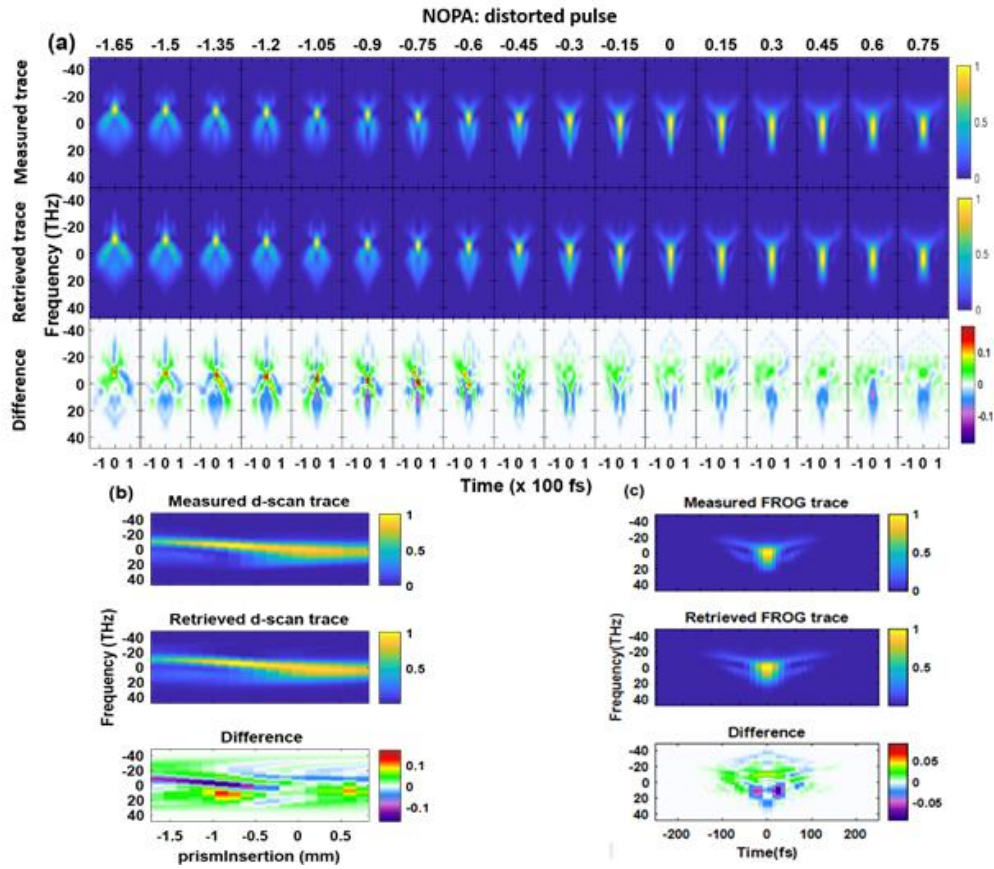


Fig. 4: Measured and retrieved traces of a distorted pulse, generated from NOPA, and their differences. (a) D-FROG traces (the traces are acquired for different prism insertion positions from -1.65 to 0.75 mm, as stated above the panels) (b) d-scan trace (c) FROG trace of a compressed pulse. The traces are retrieved using Eqs. (7) and (8), respectively, where  $N=156$ ,  $T=800$ ,  $dt=10.32$  fs.

Since the pulses generated from NOPA are expected to feature very low chirp variation, we extended our methods on the characterization of pulses processed with a 4f-pulse shaper. Firstly, we evaluated the configuration, where the 4f-pulse shaper is used without the SLM device. The measured D-FROG, d-scan, and FROG trace are depicted in Fig. 5 and they are compared to the theoretical traces computed by using Eqs. (7) and (8). The spectral phase was extracted from the FROG experiment at  $\Delta p = 0$ , analogously to the previous dataset. In this case, the use of an ideal pulse without chirp variation leads to a significant difference between the measured and calculated traces—see Fig. S1 in the Supplementary material. This is also reflected by an increased G error of 0.79%, which becomes higher, while all experimental parameters, including the noise level, remained the same. A likely explanation is the presence of chirp variation.

To quantify the level of chirp variation, we fitted the D-FROG traces and observed that the fitted value of chirp variation, which reproduced best the experimental D-FROG data, reached  $120 \text{ fs}^2$ . In contrast to the NOPA pulses, here the inclusion of the chirp variation highly improved the G error to the level of the original NOPA pulses (0.79% before, 0.52% after). When we applied the minimization of the G error with respect to the chirp variation on the d-scan trace in Fig. 5 (b), we also reached the same value of  $120 \text{ fs}^2$ . By fitting the chirp variation by using a single FROG trace (at  $\Delta p = 0$ ) in Fig. 5 (c), we derive the chirp variation of  $80 \text{ fs}^2$ .

While the D-FROG and d-scan data provided us with consistent values, the optimization of a single FROG trace provided a significantly lower value. This result can be explained by the fact that since the FROG trace is used for the phase reconstruction and the retrieved phase can partly compensate for the chirp variation. Therefore, we tested the optimization of  $\sigma_{GDD}$  value on three different spectral phases  $\varphi_C$ , where two were extracted from the FROG data (ptychographic reconstruction) and one derived from d-scan pulse retrieval, which followed the procedure of Ref. [23]. All three phases are compared in Fig. 6(a). Phase 1 (black line in Fig. 6(a)) corresponds to the spectral phase employed in the previous reconstruction. Note that the phases differ substantially only in the parts, where the laser spectrum is below 5% of the peak intensity, otherwise, the differences are rather minor.

We studied the  $G$  error as a function of the chirp variation  $\sigma_{GDD}$  for each of the characterization methods (FROG, d-scan and D-FROG) and spectral phase – see Fig. 6(b). Each panel in Fig. 6 (b) corresponds to one curve in Fig. 6(a). For the sake of better comparison, the  $G$  error data were normalized on their lowest value.

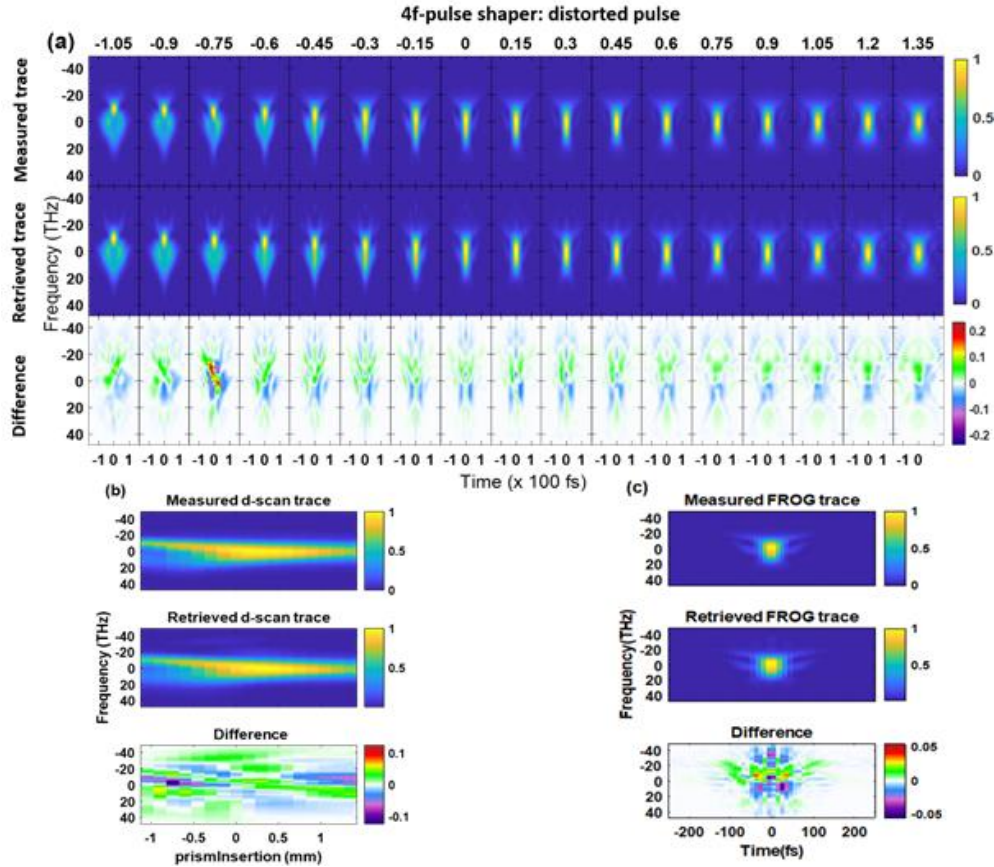


Fig. 5: Measured and retrieved traces of a distorted pulse, generated from NOPA and measured with a 4f-pulse shaper, and their differences. (a) D-FROG traces (the traces are acquired for different prism insertion positions from -1.05 to 1.35 mm, as stated above the panels) (b) d-scan trace (c) FROG trace of a compressed pulse. The traces are retrieved using Eqs. (7) and (8), respectively, where  $N=156$ ,  $T=800$ ,  $dt=10.32$  fs.



Table 1. the  $G$  error and chirp variation  $\sigma_{GDD}$  values estimated using the FROG, D-FROG and d-scan methods of the pulses generated from a NOPA then measured through a 4f-pulse shaper (PS) without and with SLM-adjusted phase (PS+SLM). The ideal case corresponds to the value  $\sigma_{GDD}=0$ .

Methods	FROG			D-FROG			d-scan		
Pulses	ideal	distorted		ideal	distorted		ideal	distorted	
Values	$G$ (%)	$\sigma_{GDD}$ (fs <sup>2</sup> )	$G$ (%)	$G$ (%)	$\sigma_{GDD}$ (fs <sup>2</sup> )	$G$ (%)	$G$ (%)	$\sigma_{GDD}$ (fs <sup>2</sup> )	$G$ (%)
NOPA	0.49	0	0.49	0.66	30	0.64	0.31	30	0.34
PS	0.60	80	0.37	0.79	120	0.52	0.32	120	0.20
PS+SLM	0.72	120	0.57	0.81	180	0.57	0.36	180	0.25

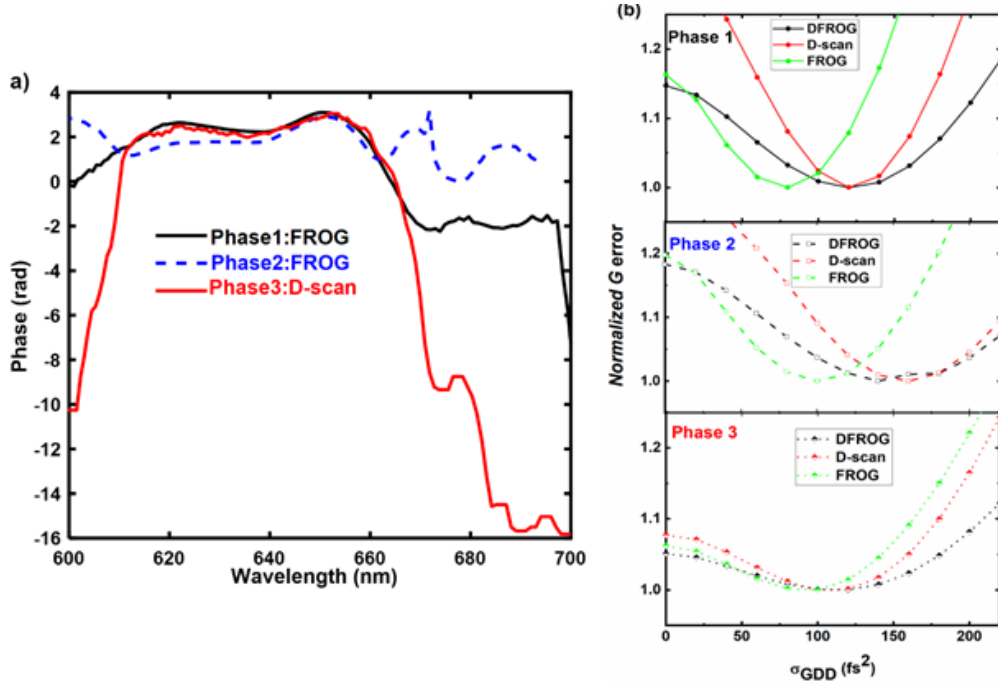


Fig. 6: (a) Spectral phases, retrieved using FROG and d-scan methods, of a pulse generated from a NOPA and measured through a 4f-pulse shaper without any modulation device. (b) Normalized  $G$  error versus the chirp variation  $\sigma_{GDD}$ , using three different phases. We observe that depending on the initial spectral phase  $\varphi_C$ , the values can differ in the order of tens of fs<sup>2</sup>.

To elucidate more the sensitivity of  $\sigma_{GDD}$  value extraction with respect to the use of different phases, we carried out a set of calculations, where we extracted the pulse spectral phase from the FROG reconstruction initiated by randomly varied phases. For each reconstruction, we scanned the  $\sigma_{GDD}$  value between 0 to 200 fs<sup>2</sup> and calculated the corresponding  $G$  error for all three methods. This allowed us to extract the optimized  $\sigma_{GDD}$  value, which varied for all the methods with the standard deviation of 10 fs<sup>2</sup>. While the FROG method (green lines in Fig. 6(b)) can reveal the chirp variation and provide a consistent value, it tends to underestimate the chirp variation. The d-scan method (red lines) is more reliable to detect the chirp variation than FROG. However, when we used the d-scan for

the phase retrieval, the method also partly compensated for the chirp variation in the pulse shape (see Fig. 6(b), lowest panel). In other words, the pulse characterization by the d-scan or FROG only leads to an underestimated value of  $\sigma_{GDD}$ . Finally, the D-FROG method was the most robust one to extract and quantify chirp variation, where we observe differences of tens of  $\text{fs}^2$  based on different approaches to reconstructions of the experimental data.

As the final step, we characterized pulses generated from a NOPA and processed by a 4f-pulse shaper with an SLM-adjusted phase. The SLM phase was adjusted to provide a constant phase, i.e. not to alter the pulse shape. Based on the measured DFROG, d-scan, and FROG traces compared with calculated ideal traces by using Eqs. (1) and (2), see Fig. S2 in the Supplementary material, we expect the presence of chirp variation and therefore we present the fit of the experimental data with Eqs. (7) and (8) – see Fig. 7. By comparing this dataset to the D-FROG traces measured without the SLM (Fig. 5), we observed both D-FROG and d-scan experimental traces to be smeared along their horizontal axis, confirming the presence of the chirp variation.

The extracted chirp variation  $\sigma_{GDD}$  increased by the SLM involvement from 120 to 180  $\text{fs}^2$ , which was consistently obtained from the D-FROG and d-scan datasets. Analogously to the previous case, the inclusion of chirp variation decreased the  $G$ -error to the level induced by the experimental imperfections themselves, which was observed for the NOPA pulses.

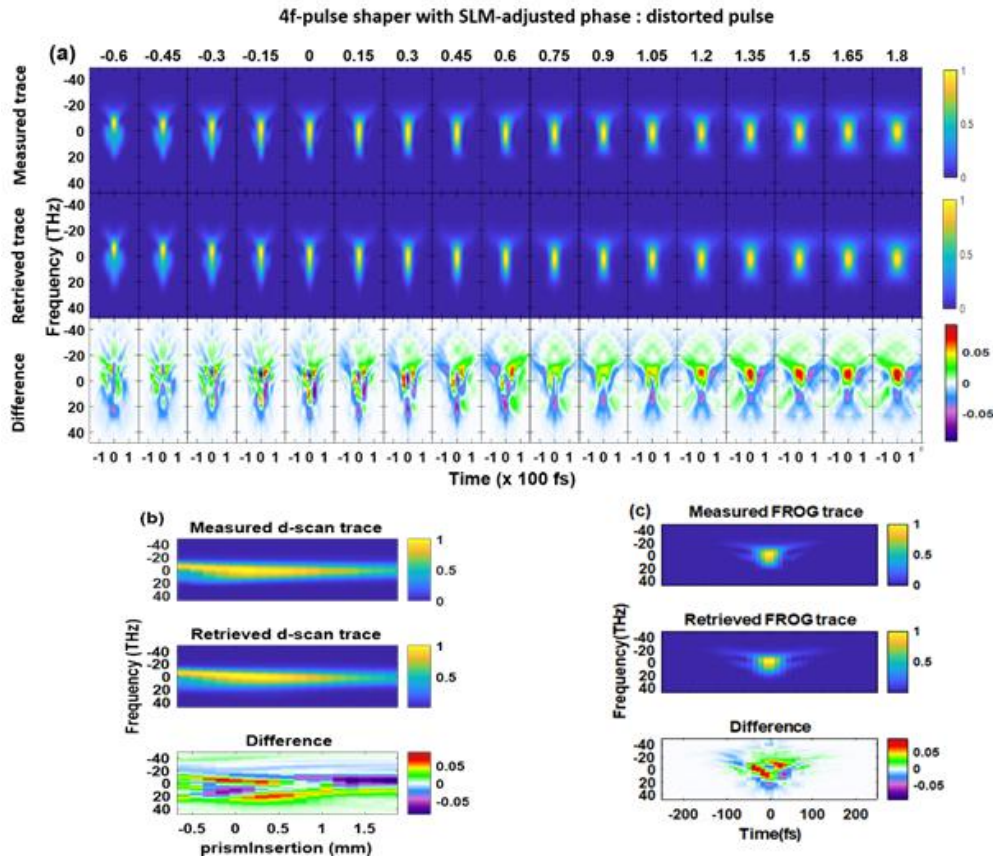


Fig. 7: Measured and retrieved traces of a distorted pulse, generated from NOPA and measured with a 4f-pulse shaper with SLM-adjusted phase, and their differences. (a) D-FROG traces (the traces are acquired for different prism insertion positions from -0.6 to 1.8 mm, as stated above the panels) (b) d-scan trace (c) FROG trace of a compressed pulse. The traces are retrieved using Eqs. (7) and (8), respectively, where  $N=156$ ,  $T=800$ ,  $dt=10.32 \text{ fs}$ .



An important question of interest was the actual source of the chirp variation. The increased value of  $\sigma_{GDD}$  can be both the signature of chirp instability in time, as well as chirp variation across the measured laser beam, often denoted as a spatial chirp or chirp distortion. To discriminate between the two cases, we measured a series of FROG traces by using a rapid delay line sweeping. We converted the traces by spectral integration into the second harmonic generation autocorrelation (SHG-AC) traces. Even for the acquisition time of 60 ms per scan (see Supplementary material for the data), all the measured cases show ideally stable autocorrelation traces. This means, that the observed chirp variations for the pulses processed by the pulse shaper originate very likely from the spatial chirp distortion. The occurrence of chirp temporal instability would need to take place on the timescale significantly below 60 ms, which is very unlikely in light of the previous results from the group of M. Motzkus, where the vast majority of noise level on a similar experimental configuration was present on frequencies  $< 20$  Hz (timescale  $> 50$  ms) [16]. Hence, we can conclude that the dominating origin of the chirp variation is the spatial chirp distortion across the laser beam. Such distortion can arise due to the misalignment of the PS [21], which is even more pronounced for the SLM by the pixelation in the SLM and its position outside of the Fourier plane [14,15].

## 5. Conclusion

In conclusion, we present a method of dispersion-scan frequency-resolved optical gating (D-FROG), which measures FROG traces as a function of dispersion and combines the idea of the FROG technique and the d-scan. We used this method to quantify the chirp variation of the ultrafast pulse.

By employing a model that assumes that the quadratic chirp GDD is not a single value but rather a Gaussian distribution, we studied the ability of the FROG, D-FROG and d-scan methods to quantify the chirp variation. We applied the methods on the characterization of pulses generated from a NOPA and the same pulses processed by a 4f-pulse shaper, which was used with and without SLM. By extracting the chirp variation for different pulse retrieval approaches, we observed that the D-FROG method provided the most consistent values of chirp variation. This can be understood in terms of the large dataset, which provides a broad consistency check.

Our measurement showed that while the NOPA-generated pulses are ideal throughout the measurement, the chirp variation appears for the pulses processed by the pulse shaper (approx.  $120 \text{ fs}^2$ ) and it becomes larger with the use of SLM ( $180 \text{ fs}^2$ ). Nevertheless, the rapid-scan measurements, where a single FROG trace was acquired within 60 ms, did not show any variation in the pulse shape. Therefore, we ascribe this effect to the space-time coupling induced by a misalignment of the pulse shaper.

Our results demonstrate that the pulse chirp variation reaching  $100\text{--}200 \text{ fs}^2$  can be present even in the cases, where a single FROG trace of a  $20 \text{ fs}$  pulse can be reliably reproduced with a realistic pulse shape. In such cases, the D-FROG method provides a way to identify and quantify the variation level and, for instance, to identify misalignment of the pulse shaper.

## Funding

The authors gratefully acknowledge the financial support from The Czech Academy of Sciences (ERC-CZ/AV-B, Project Random-phase Ultrafast Spectroscopy; ERC100431901), and the Ministry of Education, Youth and Sports ("Partnership for Excellence in Superprecise Optics," Reg. No. CZ.02.1.01/0.0/0.0/16\_026/0008390).

## Disclosures

The authors declare no conflicts of interest.

## References

1. P. Balling and J. Schou, "Femtosecond-laser ablation dynamics of dielectrics: basics and applications for thin films," *Rep. Prog. Phys.* **76**, 036502 (2013).
2. W. ShuFeng, G. QiHuang, "Progress in femtochemistry and femtobiology," *Science China Physics, Mechanics and Astronomy* **54**, 2103–2108 (2011).
3. X. Wang and N. Wada, "Spectral phase encoding of ultra-short optical pulse in time domain for OCDMA application," *Opt. Express* **12**, 7320 (2007).
4. J. Paye, M. Ramaswamy, J. G. Fujimoto, and E. P. Ippen, "Measurement of the amplitude and phase of ultrashort light pulses from spectrally resolved autocorrelation," *Opt. Lett.* **18**, 22 (1993).
5. Bern Kohler, Vladislav V. Yakovlev, and Kent R. Wilson, "Phase and intensity characterization of femtosecond pulses from a chirped-pulse amplifier by frequency-resolved optical gating," *Opt. Lett.* **20**, 5 (1995).
6. Rana Jafari and Rick Trebino, Member, IEEE, "Highly Reliable Frequency-Resolved Optical Gating Pulse-Retrieval Algorithmic Approach," *IEEE Journal of quantum electronics* **55**, 4 (2019).
7. Y. Kida, Y. Nakano, K. Motoyoshi, and T. Imasaka, "Frequency-resolved optical gating with two nonlinear optical processes," *Opt. Lett.* **39**, 10 (2014).
8. C. Iaconis and I. A. Walmsley, "Spectral phase interferometry for direct electric-field reconstruction of ultrashort optical pulses," *Opt. Lett.* **23**, 792–794 (1998).
9. V. V. Lozovoy, I. Pastirk, and M. Dantus, "Multiphoton intrapulse interference IV Ultrashort laser pulse spectral phase characterization and compensation," *Opt. Lett.* **29**, 775–777 (2004).
10. F. Silva, M. Miranda, B. Alonso, J. Rauschenberger, V. Pervak, H. Crespo, "Simultaneous compression, characterization and phase stabilization of GW-level 1.4 cycle VIS-NIR femtosecond pulses using a single dispersion-scan setup," *Opt. Express* **22**, 10181–10190 (2014).
11. X. Gu, S. Akturk, R. Trebino, "Spatial chirp in ultrafast optics," *Optics Communications* **242**, 599–604 (2004).
12. S. Akturk, M. Kimmel, P. O'Shea, R. Trebino, "Measuring spatial chirp in ultrashort pulses using single-shot Frequency-Resolved Optical Gating," *Optics Express* **11**, 68–78 (2003).
13. S. Akturk, M. Kimmel, P. O'Shea, R. Trebino, "Measuring pulse-front tilt in ultrashort pulses using GRENOUILLE," *Optics Express* **11**, 491–501 (2003).
14. F. Frei, A. Galler, and T. Feurer, "Space-time coupling in femtosecond pulse shaping and its effects on coherent control," *The Journal of chemical physics* **130**, 034302 (2009).
15. B. J. Sussman, R. Lausten, and A. Stolow, "Focusing of light following a 4-f pulse shaper: Considerations for quantum control," *Physical review A* **77**, 043416 (2008).
16. E. Brühl, T. Buckup, and M. Motzkus, "Minimization of 1/fn phase noise in liquid crystal masks for reliable femtosecond pulse shaping," *Opt. Express* **25**, 23376–23386 (2017).
17. B. Döpke, J. C. Balzer and M. R. Hofmann, "Phase and amplitude calibration of dual mask spatial light modulator for high resolution femtosecond pulse shaping," *Electronics Letters* **51**, 642–644 (2015).
18. P. Sidorenko, O. Lahav, Z. Avnat, and O. Cohen, "Ptychographic reconstruction algorithm for frequency-resolved optical gating: super-resolution and supreme robustness," *Optica* **3** (12) 1320–1330 (2016).
19. R. Trebino, "Frequency-Resolved Optical Gating: The Measurement of Ultrashort Laser Pulses," Book. Kluwer Academic Publishers (2000).
20. P. Vesela and K. Židek, "Influence of the delay line jitter on the SHG FROG reconstruction," *Opt. Express* **29**, 4392–4404 (2021).
21. T. Tanabe, H. Tanabe, Y. Teramura, and F. Kannari, "Spatiotemporal measurements based on spatial spectral interferometry for ultrashort optical pulses shaped by a Fourier pulse shaper," *Journal of the Optical Society of America B* **19**, 2795–2802 (2002).
22. B. Alonso, S. Torres-Peiró, R. Romero, P. T. Guerreiro, A. Almagro-Ruiz, H. Muñoz-Marco, P. Pérez-Millán & H. Crespo, "Detection and elimination of pulse train instabilities in broadband fibre lasers using dispersion scan," *Scientific Reports* **10**, 7242 (2020).
23. B. Alonso, Í. J. Sola & H. Crespo, "Self-calibrating d-scan: measuring ultrashort laser pulses on-target using an arbitrary pulse compressor," *Scientific Reports* **8**, 3264 (2018).



# Precision of silicon oxynitride refractive-index profile retrieval using optical characterization

Vít Kanclír\*, Jan Václavík and Karel Žídek\*\*

Regional Centre for Special Optics and Optoelectronic Systems (TOPTEC), Institute of Plasma Physics, Academy of Sciences of the Czech Republic, Za Slovankou 1782/3, 182 00 Prague 8, Czech Republic

## ARTICLE INFO

### Keywords:

gradient refractive-index layers  
optical thin films  
silicon oxynitride  $\text{SiO}_x\text{N}_y$   
dual ion beam sputtering  
precision of optical characterization

## ABSTRACT

Layers with gradient refractive-index profile are an attractive alternative to conventional homogeneous stack coatings. However, the optical characterization and monitoring of the graded refractive-index profile is a complex issue, which has been typically solved by using a simplified model of mixed materials. Although this approach provides a solution to the problem, the precision, which can be expected from optical characterization of the refractive index gradient, remains unclear. In this work, we study optical characterization of  $\text{SiO}_x\text{N}_y$  layers deposited via reactive dual ion beam sputtering. To characterize the deposited layers, we use several methods including reflectance, and transmittance spectra at a broad range of incident angles, together with spectral ellipsometry. All the data were simultaneously fitted with a general profile of refractive index. The expected profile used in our fit was based on characterization of  $\text{SiO}_x\text{N}_y$  layers with a varying stoichiometry. By altering of the profile, we discussed sensitivity of such alternation on fit quality and we studied ambiguity of merit-function minimization. We demonstrate that while the scanning of particular parameters of the profile can be seemingly very precise, we obtain a very good agreement between the experimental data and model for a broad range of gradient shapes, where the refractive-index value on major part of the profile can differ as much as 0.02 from the mean value.

## 1. Introduction

Optical coatings consisting of a stack of thin dielectric layers are extensively employed to improve characteristics of optical elements, most commonly by adjusting their reflectance and transmittance. The desired optical response is typically attained by a deposition of alternating materials with a low and a high refractive index. Thicknesses of the layers of each of the materials determine the resulting properties of the stack. For several decades, there has also been employed an alternative approach, where the refractive index within the coating is changing gradually. This approach features several advantages, such as the absence of interfaces between the high and the low refractive-index films which can improve the laser-induced damage threshold [1, 2]. In case of rugate filters, which have graded refractive-index profile, their stop bands are not surrounded by sidelobes and produce no harmonic stop bands, in contrast to quarter-wave stack of homogeneous layers [3].

A material which is commonly used in deposition of gradient layers is silicon oxynitride ( $\text{SiO}_x\text{N}_y$ ). Its advantages are transparency in VIS and NIR spectra, together with wide range of refractive index varying between 2.063 for  $\text{Si}_3\text{N}_4$  [4] and 1.468 for  $\text{SiO}_2$  [5] at the wavelength 500 nm. A variety of techniques can be used for  $\text{SiO}_x\text{N}_y$  deposition, including plasma enhanced chemical vapour deposition [6], ion assisted deposition [7], magnetron sputtering [8], or dual ion beam sputtering (DIBS) [9–12].

In order to attain a desired optical response, it is necessary to control and measure the refractive-index gradient. This is commonly characterized by two non-destructive methods: spectral ellipsometry (SE) and spectrophotometry, i.e. reflectance (R) and transmittance (T) measurements. Both methods are indirect, thus a proper model is needed to retrieve the refractive and extinction index. Typical problem of this method is the ambiguity of solutions, which arises even for the standard layers. The problem can be partly resolved by using measurements of SE, T and R taken at several angles [13, 14].

\*Corresponding author

\*\*Principal corresponding author

✉ kanclir@ipp.cas.cz (V. Kanclír); zidek@ipp.cas.cz (K. Žídek)

ORCID(s): 0000-0001-5422-231X (V. Kanclír); 0000-0002-3275-2579 (K. Žídek)



The characterization of the graded-index films is even more complex problem as it is necessary to characterize the gradually varying profile. This is typically solved by dividing the layer to several homogeneous sublayers, where their number should be high enough to ensure that the thickness of the sublayers is thinner than quarter of the smallest wavelength in the calculations [15]. A number of groups have already applied this approach using either SE data [6, 7, 15–17], or both SE and spectrophotometric data [12, 13]. Most of the groups used effective medium approximation (EMA) developed by Bruggeman [18] to model the refractive-index profile, where the profile is obtained from the knowledge of relative volume fraction between  $\text{SiO}_2$  and  $\text{Si}_3\text{N}_4$ . Nevertheless, this method strongly depends on accuracy of outer indices and on the accuracy of the volume ratio. At the same time, EMA is a model for composite materials, and thus it is not physical for  $\text{SiO}_x\text{N}_y$  although it is functioning as a reasonable approximation [19]. As a different approach, Tonova et al. [17] implemented a method to reconstruct a general refractive-index profile. She simulated application of the Newton–Kantorovitch algorithm on ellipsometric data measured at multiple angles of incidence.

An important issue connected with the measurements of gradient refractive-index profile consists in the fact that there is no reliable method able to set the true profile. For this reason, it is very problematic to discuss the reconstruction precision, beside the use of synthetic data [17]. In all the listed EMA-based articles, the precision of the attained gradient refractive-index model was not discussed. Hence, it remains unclear what is the actual precision attainable by using commonly used optical characterization of a gradient thin film.

In this paper, we provide a detailed experimental study of optical characterization of an arbitrary gradient refractive index, where we focus on precision of the gradient shape reconstruction. Namely we employed DIBS-deposited  $\text{SiO}_x\text{N}_y$  layers, which were characterized by using a broad set of commonly used methods: SE measurements and spectrophotometry measured at multiple incident angles. We attained an initial estimate of a refractive-index profile from the characterization of individual homogeneous thin films with a distinct oxygen and nitrogen stoichiometry. Then we used the same parameters with a varying stoichiometry to deposit a gradient thin layer and we measured its optical response.

The goal of our work was to alter the expected gradient profile to attain the best agreement between the experimental and the calculated optical response. We focused on the sensitivity of the agreement towards variation in the profile offset, addition or subtraction of a quadratic function, or a random subtle modification of the initial model. While the controlled modification of the gradient refractive-index profile might suggest that the profile can be determined with a very high precision, we demonstrate that the experimental data can be reproduced by a broad set of profiles with the refractive index varying as much as 0.02 around the central value. Therefore, our work provides an insight into the precision which can be expected from refractive-index profile retrieval based on an optical characterization of a general gradient refractive-index thin film.

## 2. Experimental details

We deposited  $\text{SiO}_x\text{N}_y$  thin layers by DIBS apparatus described in [20]. DIBS is employed in this paper for enhanced control of stoichiometry and for qualities of deposited layers i.e. density, adhesion, nucleation etc. [21] The primary ion source sputtered silicon from a target, and the assistant ion source generated reactions of oxygen and nitrogen with the sputtered silicon atoms to form  $\text{SiO}_x\text{N}_y$ . The beam voltage and beam current of the primary ion source was set to 600 V and 108 mA, respectively.

The assistant ion source parameters were set to 120 V for discharge voltage and 0.6 A for discharge current. Other parameters of the assistant ion source are representing gas flow. Flow of nitrogen was set to 49 sccm, and flow of oxygen varied within 0 and 3 sccm (see below).

We used plane-parallel N-BK7 as a substrate for all the depositions, except the deposition of homogeneous layers with flow of oxygen 2.5 and 3 sccm. For those, plane-parallel N-SF10 was used because deposited refractive index of the layers was too similar to the one of N-BK7, and lack of contrast would not allow reliable refractive index retrieval.

Both transmittance  $T$  and reflectance  $R$  spectra were measured within wavelengths 380 and 980 nm by EssenOptics Photon RT spectrometer. The measurements were carried out for the incident angles  $4^\circ$ ,  $8^\circ$ ,  $20^\circ$ ,  $30^\circ$ ,  $40^\circ$ ,  $50^\circ$ ,  $60^\circ$ , and  $70^\circ$ , where the angle of  $4^\circ$  was used only for the measurement of transmittance. All the spectra were measured for both p- and s-polarization.

The ellipsometry measurements were carried out via Sentech SE850 with micro-spots. We measured visible range of wavelengths between 280 nm and 850 nm under the incident angle of  $70^\circ$ .



**Table 1**

Retrieved refractive indices of the deposited homogeneous  $\text{SiO}_x\text{N}_y$  layers at 500 nm for a range of oxygen flows  $Q$ . Degree of the experiment-theory agreement is represented by merit function  $f_{\text{mer}}$  – see text for details.

$Q(\text{O}_2)$ [sccm]	Substrate	$d$ [nm]	$n$ [-]	$f_{\text{mer}}$ [-]
0.00	N-BK7	295	2.026	1.53
0.25	N-BK7	291	1.994	1.14
0.50	N-BK7	299	1.857	1.90
0.75	N-BK7	303	1.880	1.37
1.00	N-BK7	327	1.746	1.63
1.50	N-BK7	329	1.682	0.87
2.00	N-BK7	346	1.610	1.44
2.50	N-SF10	352	1.565	1.25
3.00	N-SF10	357	1.543	1.48

### 3. Results and discussion

#### 3.1. Homogeneous layers

The initial goal was to create a reliable model where the deposition parameters of  $\text{SiO}_x\text{N}_y$  are linked to a certain refractive-index dispersion curve. Therefore, we first deposited a set of samples of layers with homogeneous refractive index where each sample had different stoichiometry of  $\text{SiO}_x\text{N}_y$ . In other words, we deposited a standard thin film for each sample featuring step-like refractive-index changes over interfaces.

In order to describe optical response of the optical coating, we applied a commonly used transfer-matrix approach described in detail in literature [22]. The transfer-matrix method allows us to calculate the optical response (T,R and SE spectra at several incident angles), provided that we know the complex refractive index of a layer  $n_L$ , substrate and incident medium, together with the layer thickness. It is worth noting that the listed measurements represent the complete linear optical response of the sample. In order to reproduce the experimental data, we correct the transmittance and reflectance curve for a reflection from the uncoated (backside) substrate surface. The multiple reflections from the substrate backside were neglected.

In order to describe spectral shape of the optical characteristics for incident angle  $\theta$  and wavelengths  $\lambda$ , we used the Tauc-Lorentz model of refractive index [23]. This model is commonly used for wide-band gap dielectric materials. We used two oscillators, where in all the studied cases, one oscillator dominated and the second one accounted for a minor correction (1 % of the amplitude). Parameters of the model were fitted by using a complete dataset acquired for a homogeneous layer of  $\text{SiO}_x\text{N}_y$ . The fitting included all the  $T$ ,  $R$ ,  $\Psi$  and  $\Delta$  curves, and all of them optimized the model parameters with respect to the merit function:

$$f_{\text{mer}} = \eta_T \sqrt{\sum_{\theta,\lambda} (\tilde{T}_{\theta\lambda} - T_{\theta\lambda})^2} + \eta_R \sqrt{\sum_{\theta,\lambda} (\tilde{R}_{\theta\lambda} - R_{\theta\lambda})^2} + \eta_\Delta \sqrt{\sum_{\theta,\lambda} (\tilde{\Delta}_{\theta\lambda} - \Delta_{\theta\lambda})^2} + \eta_\Psi \sqrt{\sum_{\theta,\lambda} (\tilde{\Psi}_{\theta\lambda} - \Psi_{\theta\lambda})^2}, \quad (1)$$

where tilde marks theoretical spectra made of Tauc-Lorentz model, whereas letters without tilde represent measured spectra. Weight coefficients of transmittance ( $\eta_T$ ), reflectance ( $\eta_R$ ), function  $\Psi$  ( $\eta_\Psi$ ) and function  $\Delta$  ( $\eta_\Delta$ ) were set to 0.474, 0.474, 0.037 and 0.0046, respectively, to account for the different range and noise level of the T, R and ellipsometric functions. For the given weights, all the types of data contributed comparably to the resulting merit function values.

Fig. 1, upper panels, provides a comparison between the experimentally measured data (blue lines) and the model-based calculated curves (red lines) for selected incident angles and polarization. The applied Tauc-Lorentz model allowed us to achieve a refractive-index profile (Fig. 1, lower panel) with a nearly ideal agreement. The fit was carried out for the whole set of deposited homogeneous layers, where the oxygen flow into the assistant ion source controlled the  $\text{SiO}_x\text{N}_y$  composition – see Table 1 for details. In close agreement with the previously reported values, we observe the refractive index to decrease with the increasing oxygen flow rate, ranging from 2.02 (0 sccm, wavelength 500 nm) up to 1.54 (3 sccm, wavelength 500 nm), where the value approaches the refractive index of silica [7, 8, 19].

By taking into account that the refractive index is expected to gradually and smoothly change with the oxygen ratio, we can fit the attained refractive-index dependence on the oxygen flow with a 4th order polynomial function –

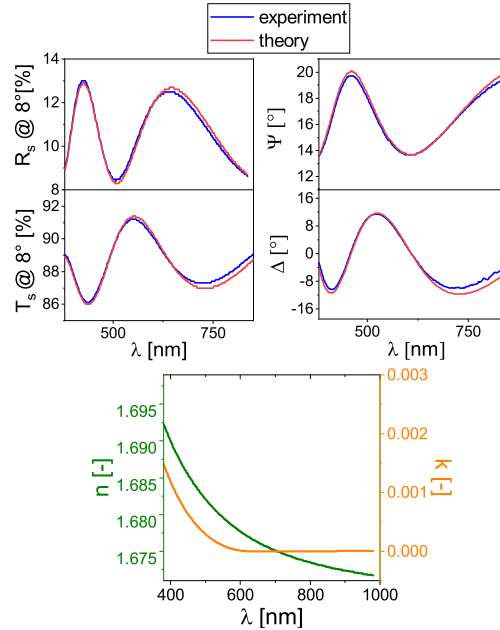


**Figure 1:** Illustration of the homogeneous film characterization (oxygen flow 1.5 sccm). Upper panels: Comparison of experimental (blue lines) and fitted theoretical spectra (red lines) of reflectance  $R$ , transmittance  $T$  (both s-pol., incident angle 8 deg), and ellipsometric functions  $\Delta$  and  $\Psi$ . (incident angle 70 deg). Lower panel: attained refractive index (green line) and extinction coefficient (orange line) of the  $\text{SiO}_x\text{N}_y$  layer.

see Fig. 2, upper panel. From the deviation of the data points from the fit in Fig. 2, we can estimate that our model leads to an error in the refractive index within approx. 0.03. We reached the same precision when we employed this procedure on  $\text{Si}_3\text{N}_4$  layers with various thicknesses ranging from 250 nm to 1500 nm. We ascribe this inaccuracy to the limitations posed by the double-oscillator Tauc-Lorenz model, where the model is an approximation of a more complex refractive-index dispersion curve of  $\text{SiO}_x\text{N}_y$ .

### 3.2. Gradient layers

The previous step allowed us to reliably trace changes of the refractive index for a varying oxygen flow in the assistant ion source. As a result, it was possible to attain a layer with a gradient refractive index by a slow variation in the oxygen supply. We deposited the gradient layer with a linear increase of oxygen flow rate in time which leads to the refractive index decreasing with the increasing  $z$  – see Fig. 2 upper panel. Note that  $z = 0$  corresponds to the substrate surface.

The gradient layers were simulated as a set of 100 thin sublayers with a constant thickness by using the same approach as described in the previous subsection. Owing to the fact that the composition for a depth  $z$  can be derived from the deposition procedure, we can assign a refractive index  $n(z_i)$  for the sublayers  $i$  with a known refractive-index model. The resulting refractive-index gradient  $n(z)$  for each wavelength was determined based on spline interpolation of the  $n(z_i)$  datapoints – see Fig. 2 upper panel, black line.

Optical response of the gradient layer was fitted by using the same merit function described in Eq. (1). However, the only fitting parameter was the layer thickness and the refractive index was fixed according to the estimated profile depicted in Fig. 2. The resulting merit function of 1.17 was comparable to the ones attained for homogeneous layers. We attained a very good agreement between the experimental data and the theoretical curves – see Fig. 2 lower panel – which we ascribe to the fact that the interpolation of the refractive index partly compensates for the errors in the models of the homogeneous layers.



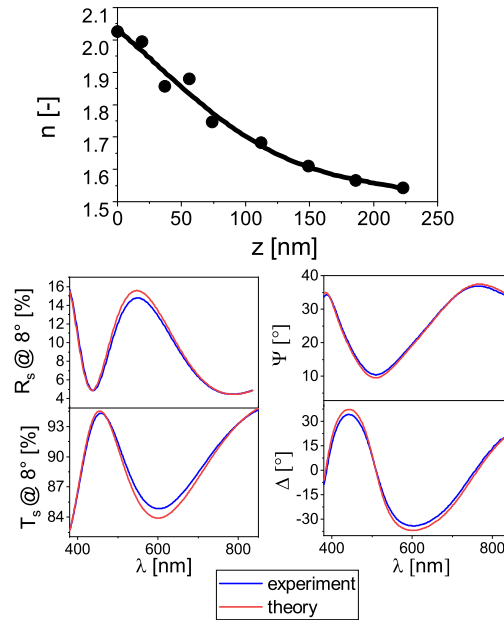


**Figure 2:** Upper panel: Gradient profile of the refractive index at  $\lambda = 500$  nm attained by 4th order polynomial fit (line) of the refractive index attained for homogeneous films (circles). Lower panel: Comparison of measured (blue lines) and simulated (red lines) optical response – reflectance, transmittance (both s-pol., incident angle 8 deg), and ellipsometric functions  $\Psi$  and  $\Delta$  (incident angle 70 deg).

As a result, we were able to form a reliable initial model of the gradient layer together with its thickness determination. Nevertheless, the ultimate question of interest was to evaluate precision of the estimated profile.

### 3.3. Systematical model variation

Using a free fit of all Tauc-Lorentz parameters for each of the nine concentrations (in total 81 parameters), is prohibitively computationally costly and the substantial number of parameters is likely not to converge to the best result. Therefore, we firstly studied the effect of two main expected imperfections: (i) offset in the gradient refractive index, (ii) change in the overall shape of the gradient.

The offset in a refractive index is one of the problematic issues in material models, since the optical parameters can be often reproduced by using a higher or lower refractive index, which is compensated with a lower or higher layer thickness, respectively. We used the same refractive index as it was used in Fig. 2, and we added an offset of ranging from -5 to 5 percent of the origin refractive-index profile – see Fig. 3 a). For each offset, we fitted the layer thickness and compared the merit functions of the samples – see Fig. 3 c). We observe that the optimum offset was placed around 2 % within the expected value. The effect of the offset on  $\Psi$  function around  $\lambda = 500$  nm is illustrated in Fig. 3 b).

Secondly, we evaluated the effect of the change in the gradient shape. We altered the original gradient presented in Fig. 2 by adding a quadratic term – see Fig. 3 d). Analogously to the previous case, we fitted the layer thickness in order to achieve the best merit function – see Fig. 3 f).

We observed that the merit function values, i.e., the agreement between the experimental value and our gradient refractive-index model, are highly dependent on both offset and gradient profile bending. This suggests that we can, in principle, determine the gradient refractive-index profile with a very high precision. Optimum offset can be located within 0.25 % precision, implying the refractive-index precision reaching 0.005. We verified that we can optimize the profile curve in arbitrary order of the parameters and we attained closely-lying curves, where the one with the lowest

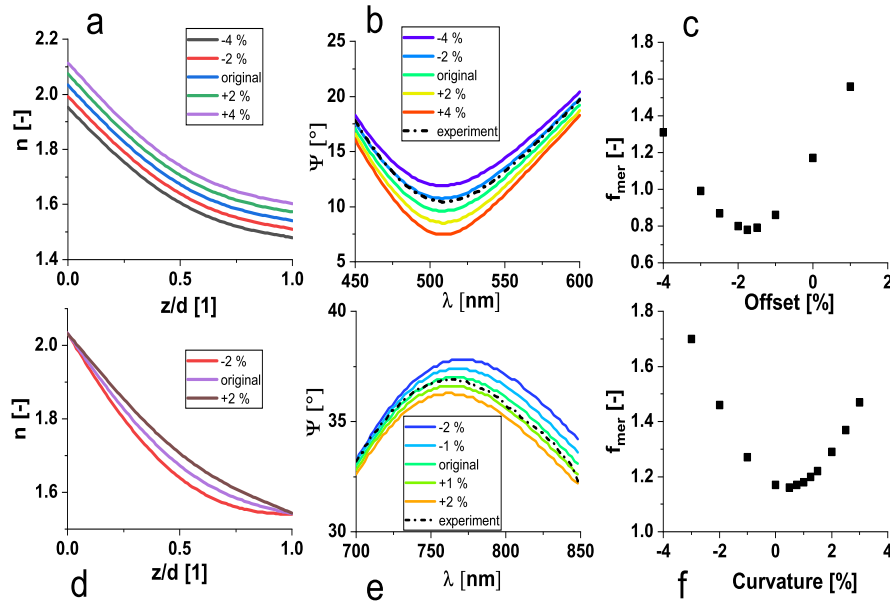


**Figure 3:** Fit evaluation for systematic refractive-index variations by variation of offset (upper panels) and quadratic term addition (lower panels). a,d) Examples of evaluated profiles with a different parameters. b,e) The sensitivity of  $\Psi$  function to the shape variation. c,f) A change of the merit-function value with to the shape variation.

merit function is depicted in Fig. 4 (dashed black line). Therefore, the systematic fitting suggests that we can determine the refractive-index profile with a very high precision. However, as we will show in the next section, the systematical variation of the refractive-index model highly underestimates the actual profile determination inaccuracy.

### 3.4. Random model variation

To test the actual precision of the optical characterization, we created a simulation, where the refractive indices presented in the upper panel of Fig. 2 (symbols) were altered by a set of random offsets with uniform distribution in the range of  $\pm 0.06$ . For each case, we fitted the refractive-index profile with the 4th order polynomial and carried out the fitting of the layer thickness. By doing 5000 simulations, we attained an extensive set of gradient profiles with minute variations in their shape, which closely followed the original curve, and which featured in some cases the merit function value below the systematically optimized curve.

We selected the randomly modified profiles with merit function below 0.8063, which corresponds to 10 % higher value compared to the best value attained via the systematical gradient variation (0.733) – see colored lines in Fig. 4. The curves with the lowest merit function differ from the systematically attained curve, and we evaluated their spread at several  $z$  points. The smallest spread is at  $z = 200$  nm and  $z = 225$  nm, where the value ranges are 1.559 – 1.577, and 1.537 and 1.555, respectively. More generally, at most points the values differ by 0.02 from the mean value. The spread is the biggest at the edges of the layer – for instance, at  $z = 0$ , the refractive-index values vary from 1.969 to 2.043. However, this can be ascribed to the polynomial fitting of the data points, which is affected by the random change in the position of the last data point.

The comparison between the curve retrieved by the systematical variation (black dashed line in Fig. 4) with the randomly tested curves (colored lines in Fig. 4) raises a question why the systematical optimization did not converge to a curve located in the center of the best matching profiles of the random simulations. This is caused by the fact that even a minor change in the refractive-index profile highly alters the optimum offset and curvature. As an illustration, only by increasing the refractive index expected at 1 sccm flow of oxygen by +0.02, we attain, by the systematic optimization,

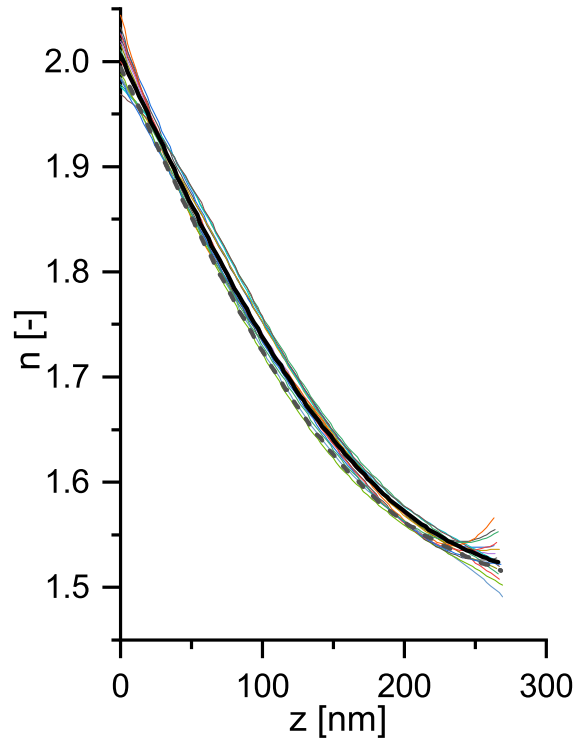


**Figure 4:** Comparison of the refractive-index profiles attained by the random modification of refractive-index datapoints (colored lines) with the systematically optimized ones (black lines – see text for details). Randomly modified curves were selected so that their fitting merit function was lower compared to the systematic optimization (12 curves out of 5000 modifications).

a profile (solid black curve in Fig. 4), which lies in the center of the randomly optimized profile. In such case, we also reached a significantly lower merit function value of 0.681. Therefore, the systematically varied parameters, in spite of featuring a sharp optimum value, do not reveal the actual profile precision.

#### 4. Conclusions

We carried out a detailed study of optical characterization of  $\text{SiO}_x\text{N}_y$  graded thin films, where we aimed at extracting the refractive-index gradient shape based on the measurements of transmittance, reflectance and ellipsometry. We first attained an estimate of the refractive-index profile based on characterization of  $\text{SiO}_x\text{N}_y$  homogeneous thin films with varying stoichiometry. The estimated profile was varied in order to get the best agreement between the measured and simulated gradient thin film optical response.

We observed that the results might be seemingly very accurate when we scan one particular parameter – for instance, an offset of the gradient. Nevertheless, we can reproduce our experimental data with high precision by using a relatively broad range of gradients with the refractive index varying at most points of the profile by 0.02 from the mean value. We observe that the particular agreement highly varies with subtle modification of the fixed points.

We propose that the precision of the measurement can be improved partly by forming a complex model, where we take into account multiple reflections on the thin layers and substrate. However, the solution of this problem highly depends on a particular experimental device, such as the dimension of the spectrometer's detector and light collection.

Another prominent pathway is to propose a complex specific gradient shape, where the optical response will be more sensitive to the gradient actual shape.

## 5. Acknowledgement


We gratefully acknowledge the financial support of Ministry of Education, Youth and Sports ("Partnership for Excellence in Superprecise Optics," Reg. No. CZ.02.1.01/0.0/0.0/16\_026/0008390), and The Czech Academy of Sciences (Strategy AV21, programme 17).

## References

- [1] O. Arnon and P. Baumeister. Electric field distribution and the reduction of laser damage in multilayers. *Applied Optics*, 19(11):1853, jun 1980. doi: 10.1364/ao.19.001853.
- [2] E. Welsch and D. Ristau. Photothermal measurements on optical thin films. *Applied Optics*, 34(31):7239, nov 1995. doi: 10.1364/ao.34.007239.
- [3] William H. Southwell. Extended-bandwidth reflector designs by using wavelets. *Applied Optics*, 36(1):314, jan 1997. doi: 10.1364/ao.36.000314.
- [4] Kevin Luke, Yoshitomo Okawachi, Michael R. E. Lamont, Alexander L. Gaeta, and Michal Lipson. Broadband mid-infrared frequency comb generation in a  $\text{Si}_3\text{N}_4$  microresonator. *Optics Letters*, 40(21):4823, oct 2015. doi: 10.1364/ol.40.004823.
- [5] L. Gao, F. Lemarchand, and M. Lequime. Refractive index determination of  $\text{SiO}_2$  layer in the UV/vis/NIR range: spectrophotometric reverse engineering on single and bi-layer designs. *Journal of the European Optical Society: Rapid Publications*, 8, jan 2013. doi: 10.2971/jeos.2013.13010.
- [6] S. Callard, A. Gagnaire, and J. Joseph. Fabrication and characterization of graded refractive index silicon oxynitride thin films. *Journal of Vacuum Science & Technology A: Vacuum, Surfaces, and Films*, 15(4):2088–2094, jul 1997. doi: 10.1116/1.580614.
- [7] Paul G. Snyder, Yi-Ming Xiong, John A. Woollam, Ghanim A. Al-Jumaily, and F. J. Gagliardi. Graded refractive index silicon oxynitride thin film characterized by spectroscopic ellipsometry. *Journal of Vacuum Science & Technology A: Vacuum, Surfaces, and Films*, 10(4):1462–1466, jul 1992. doi: 10.1116/1.578266.
- [8] O. D. Volpian, A. I. Kuzmichev, and Yu. A. Obod. Magnetron technology of production of gradient optical coatings. *Inorganic Materials: Applied Research*, 6(3):234–239, may 2015. doi: 10.1134/s2075113315030132.
- [9] M. F. Lambrinos, R. Valizadeh, and J. S. Colligon. Effects of bombardment on optical properties during the deposition of silicon nitride by reactive ion-beam sputtering. *Applied Optics*, 35(19):3620, jul 1996. doi: 10.1364/ao.35.003620.
- [10] Huang-Lu Chen and Jin-Cherng Hsu. Deposition of silicon oxynitride films by ion beam sputtering at room temperature. *Optical Review*, 16(2):226–228, mar 2009. doi: 10.1007/s10043-009-0042-3.
- [11] H.-J. Erler, G. Reisse, and C. Weissmantel. Nitride film deposition by reactive ion beam sputtering. *Thin Solid Films*, 65(2):233–245, jan 1980. doi: 10.1016/0040-6090(80)90257-6.
- [12] J. Rivory. Characterization of inhomogeneous dielectric films by spectroscopic ellipsometry. *Thin Solid Films*, 313-314:333–340, feb 1998. doi: 10.1016/s0040-6090(97)00842-0.
- [13] Vesna Janicki, Jordi Sancho-Parramon, Olaf Stenzel, Marc Lappschies, Bjorn Gartz, Christoph Rickers, Christina Polenzky, and Uwe Richter. Optical characterization of hybrid antireflective coatings using spectrophotometric and ellipsometric measurements. *Applied Optics*, 46(24):6084, aug 2007. doi: 10.1364/AO.46.006084.
- [14] Alexander V. Tikhonravov, Tatiana V. Amotchkina, Michael K. Trubetskov, Robert J. Francis, Vesna Janicki, Jordi Sancho-Parramon, Hrvoje Zorc, and Vladimir Pervak. Optical characterization and reverse engineering based on multiangle spectroscopy. *Applied Optics*, 51(2):245, jan 2012. doi: 10.1364/ao.51.000245.
- [15] C. K. Carniglia. Ellipsometric calculations for nonabsorbing thin films with linear refractive-index gradients. *Journal of the Optical Society of America A*, 7(5):848, may 1990. doi: 10.1364/josaa.7.000848.
- [16] G. Parjadis de Larivière, J. M. Frigerio, J. Rivory, and F. Abelès. Estimate of the degree of inhomogeneity of the refractive index of dielectric films from spectroscopic ellipsometry. *Applied Optics*, 31(28):6056, oct 1992. doi: 10.1364/ao.31.006056.
- [17] Diana A. Tordova and Anka A. Konova. Characterization of inhomogeneous dielectric coatings with arbitrary refractive index profiles by multiple angle of incidence ellipsometry. *Thin Solid Films*, 397(1-2):17–23, oct 2001. doi: 10.1016/s0040-6090(01)01400-6.
- [18] D. A. G. Bruggeman. Berechnung verschiedener physikalischer konstanten von heterogenen substanzen. i. dielektrizitätskonstanten und leitfähigkeiten der mischkörper aus isotropen substanzen. *Annalen der Physik*, 416(7):636–664, 1935. doi: 10.1002/andp.19354160705.
- [19] Yi-Ming Xiong, Paul G. Snyder, John A. Woollam, G.A. Al-Jumaily, F.J. Gagliardi, and Eric R. Krosche. Controlled index of refraction silicon oxynitride films characterized by variable angle spectroscopic ellipsometry. *Thin Solid Films*, 206(1-2):248–253, dec 1991. doi: 10.1016/0040-6090(91)90430-6.
- [20] K. Židek, J. Hlubuček, P. Horodyská, J. Budasz, and J. Václavík. Analysis of sub-bandgap losses in  $\text{TiO}_2$  coating deposited via single and dual ion beam deposition. *Thin Solid Films*, 626:60–65, mar 2017. doi: 10.1016/j.tsf.2017.02.036.
- [21] James K. Hirvonen. Ion beam assisted thin film deposition. *Materials Science Reports*, 6(6):215–274, jul 1991. doi: 10.1016/0920-2307(91)90008-B.
- [22] H. Angusmaeleod. Recent developments in deposition techniques for optical thin films and coatings. pages 3–25, 2013. doi: 10.1533/9780857097316.1.3.
- [23] G. E. Jellison and F. A. Modine. Parameterization of the optical functions of amorphous materials in the interband region. *Applied Physics Letters*, 69(3):371–373, jul 1996. doi: 10.1063/1.118064.



# Bulk and interface second harmonic generation in the $\text{Si}_3\text{N}_4$ thin films deposited via ion beam sputtering

Nirmal Kumar Das<sup>1,\*</sup>, Vít Kanclíř<sup>1,2</sup>, Pavel Mokřý<sup>1,2</sup> and Karel Židek<sup>1,\*</sup> 

<sup>1</sup> Regional Center for Special Optics and Optoelectronic Systems (TOPTEC), Institute of Plasma Physics, Czech Academy of Science v.v.i., Za Slovankou 1782/3, 182 00 Prague 8, Czech Republic

<sup>2</sup> Faculty of Mechatronics, Informatics and Interdisciplinary Studies, Technical University of Liberec, Studentská 2, CZ-461 17 Liberec, Czech Republic

E-mail: [das@ipp.cas.cz](mailto:das@ipp.cas.cz) and [zidek@ipp.cas.cz](mailto:zidek@ipp.cas.cz)

Received 14 December 2020, revised 18 January 2021

Accepted for publication 8 February 2021

Published 15 March 2021



## Abstract

The nonlinear optical second harmonic generation (SHG) in  $\text{Si}_3\text{N}_4$  has attracted considerable attention due to a variety of promising applications in optoelectronics. However, reports on SHG in  $\text{Si}_3\text{N}_4$  thin films and microstructures lead to diverse conclusions about the SHG origin, pointing towards the  $\text{Si}_3\text{N}_4$  bulk, as well as to the  $\text{Si}_3\text{N}_4$ -Si interface. Here we report on the measurement of polarization-resolved angle-dependent SHG in  $\text{Si}_3\text{N}_4$  thin films in the reflective mode. This mode allowed us to measure the nonlinear response of  $\text{Si}_3\text{N}_4$  thin films on the Si single crystal substrate. By measuring three samples deposited via ion beam sputtering, we were able to analyze the bulk and interface contributions. We have demonstrated that apart from the bulk SHG, the  $\text{Si}_3\text{N}_4$ -Si interface contributes with a significant amount of SHG for the thin sample (600 nm). Our result provides a link between the previous measurements in the  $\text{Si}_3\text{N}_4$  thin films and on the microstructures.

Supplementary material for this article is available [online](#)

Keywords: silicon nitride, thin films, ellipsometry, second harmonic generation (SHG), bulk, interface

(Some figures may appear in colour only in the online journal)

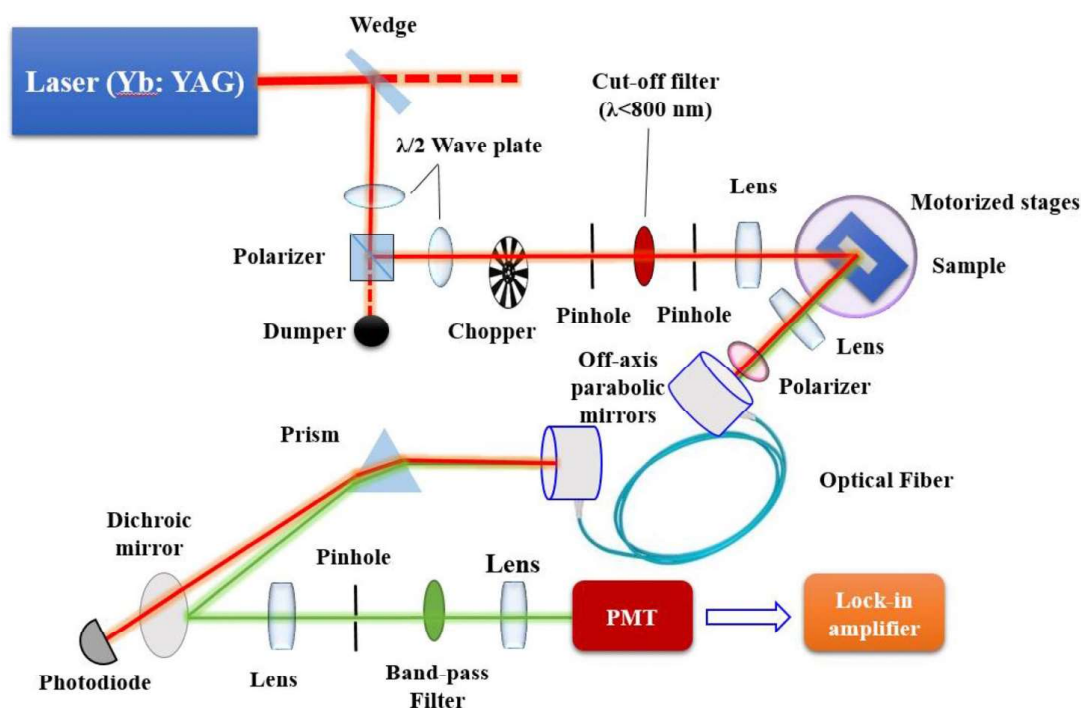
The integration of multiple photonic devices together on a substrate according to the concept of integrated photonics has attracted a considerable attention during the last years [1, 2]. The Si-based photonic materials, including  $\text{Si}_3\text{N}_4$ , stand out due to their promising applications in photonics and optoelectronics [1, 3, 4]. Besides its use in the nano- and microelectronics industry [5, 6],  $\text{Si}_3\text{N}_4$  has a wide range of applications, like light-emitting materials, waveguide structures, photonic crystal nanocavities, plasmonic structures, and optical modulators [4–6]. Therefore, exploring its complete optical properties,

linear and nonlinear optical features, is of utmost importance [1–4].

A number of works have reported on exploring the nonlinear optical properties of  $\text{Si}_3\text{N}_4$ , where the origin of an efficient second harmonic generation (SHG) was one of the major topics [5, 6]. SHG is a nonlinear optical process, where the photons of frequency ( $\omega$ ) interact with a nonlinear material and generate new photons with a doubled frequency ( $2\omega$ ) [2, 4, 7–10]. The second-order nonlinear process via the electric dipole contribution is allowed only in materials with the broken inversion symmetry. For bulk centrosymmetric materials, the SHG occurs only at the material surface or interface or due to the multipole interaction [2, 4, 11–18]. Since amorphous  $\text{Si}_3\text{N}_4$  poses the inversion symmetry, the efficient SHG has

\* Authors to whom any correspondence should be addressed.





**Scheme 1.** Optical setup used for the angle-dependent SHG measurement.

been highly debated in the literature. Several reports have documented the second-order optical properties of the  $\text{Si}_3\text{N}_4$  thin films prepared by plasma-enhanced chemical vapor deposition method [7, 8, 19, 20], as well as by the low-pressure chemical vapor deposited and sputtered microresonators and waveguides [21, 22]. The reports brought controversial conclusions ascribing the SHG generation to the  $\text{Si}_3\text{N}_4$  volume [7, 23], as well as the silicon nitride–crystalline silicon (c-Si) interface [21].

In this article, we report on the SHG in  $\text{Si}_3\text{N}_4$  films deposited by using dual ion beam sputtering (IBS). Unlike in the previous reports, where the SHG in the thin films of  $\text{Si}_3\text{N}_4$  was measured in the transmission regime, here we use a setup capable to record the angle-dependent SHG signal in the reflective mode. This allowed us to carry out SHG characterization of  $\text{Si}_3\text{N}_4$  thin films deposited on a c-Si wafer. In such a case, the SHG signal is expected to contain both bulk and interface contributions. By using the polarization-resolved angle-dependent SHG signal for three different thicknesses of the  $\text{Si}_3\text{N}_4$  films, we discuss the relative contribution of the surface, interface, and bulk dipole SHG responses of thin-film systems. The SHG in the thick sample (3890 nm) can be well reproduced by the bulk SHG model with the second-order nonlinear tensor values, which are in agreement with the previously reported ones. Nevertheless, we observe the significant contribution of the Si– $\text{Si}_3\text{N}_4$  interface SHG for the 600 nm thick film, pointing out its importance for the thin  $\text{Si}_3\text{N}_4$  structures. Our results provide a connecting link between the reports on the bulk-like SHG in the  $\text{Si}_3\text{N}_4$  thin films and interface-like SHG commonly observed in the microstructures.

We deposited  $\text{Si}_3\text{N}_4$  thin films by the dual IBS apparatus described elsewhere [25, 26]. The primary  $\text{Ar}^+$  ion source sputtered Si atoms on a substrate (c-Si with <100> orientation and BK-7) from a Si target, while the assistant ion source aimed nitrogen ions on the sample to form  $\text{Si}_3\text{N}_4$ . The beam voltage and beam current of the primary ion source was set to 600 V and 108 mA, respectively. The assistant ion source parameters were set to 120 V for discharge voltage and 0.6 A for discharge current. Other parameters of the assistant ion source are representing gas flow. The flow of nitrogen was set to 49 sccm.

Both transmittance (T) and reflectance (R) spectra were measured within wavelengths 380 and 980 nm by EssenOptics Photon RT spectrometer. The measurements were carried out for the incident angles  $4^\circ$ ,  $8^\circ$ ,  $20^\circ$ ,  $30^\circ$ ,  $40^\circ$ ,  $50^\circ$ ,  $60^\circ$ , and  $70^\circ$ , where the angle of  $4^\circ$  was used only for the measurement of transmittance. The spectra were measured for both p- and s-polarizations. The ellipsometric measurements were carried out via Sentech SE850 with microspots. We measured the visible range of wavelengths between 280 nm and 850 nm under the incident angle of  $70^\circ$ .

We employed an amplified Yb:YAG femtosecond laser system Pharos (Light Conversion) at 1028 nm with a pulse length of 225 fs, which was operated at the repetition rate of 10 kHz. From the output pulse energy of 100  $\mu\text{J}$ , we targeted 2  $\mu\text{J}$  into the SHG experiment. In our SHG set-up (scheme 1), the laser beam intensity was set by a  $\lambda/2$  waveplate combined with a polarizing cube. The desired polarization of the fundamental radiation was controlled by the second  $\lambda/2$  waveplate. The laser beam passed through a color filter that suppressed any



radiation at the SHG wavelength generated by the laser or optical components in the beam. Then the laser beam with a diameter of 3.7 mm was focused by a lens ( $f = 500$  mm) on the sample mounted on the motorized rotation stage. The SHG photons were collimated by a lens with a selected polarization and coupled by an off-axis parabolic mirror into a multiple-mode fiber. The used thin-film polarizer selectively transmits the SHG photons, while the IR (fundamental) beam stays unaffected. Owing to the fiber, the collected radiation is highly depolarized and outcoupled in a fixed detection set-up. It is worth noting that the present set-up can serve both for the measurement of SHG in both reflectance and transmittance mode. By using a fused silica prism and dichroic mirror, we split the IR beam and the SHG beam, and we detect them by using a large-area photodiode (Thorlabs, DET100A/M) and a photomultiplier module (Hamamatsu H9306-03) with a built-in amplifier, respectively. The SHG detection is shielded from the IR (fundamental) beam detection by using a pin-hole and a set of filters, which efficiently block both the fundamental and the third harmonic radiation. The SHG signal was pre-filtered by a low-pass frequency filter, and the SHG intensity was extracted by using lock-in Anfatec 250 combined with an optical chopper. The simultaneously detected reflected IR signal was used to verify the quality of the light collection for the used range of incident angles by its comparison to the expected sample reflectance (figure S1 (available online at [stacks.iop.org/JOPT/23/024003/mmedia](https://stacks.iop.org/JOPT/23/024003/mmedia)), supporting materials).

We deposited three samples of  $\text{Si}_3\text{N}_4$  thin films on c-Si and BK-7 substrates with highly different layer thickness. Firstly, we characterized the  $\text{Si}_3\text{N}_4$  layers with respect to their linear optical response, i.e. refractive index, and subsequently used this information to evaluate the SHG properties. We characterized the refractive index of the  $\text{Si}_3\text{N}_4$  layer and the layer thicknesses by globally fitting their linear optical response (transmittance, reflectance, and ellipsometry). We applied the commonly used transfer-matrix approach, where the refractive index dispersion was approximated by using the Tauc–Lorentz model [25, 26]. This model is commonly used for wide-bandgap dielectric materials. We fitted the layer thickness and parameters of two oscillators, where one oscillator dominated and the second one accounted for a minor correction (1% of the amplitude). The fitting procedure is described in detail in our previous work [25, 26].

Figure 1 (left panels) provides a comparison between the experimentally measured transmittance and reflectance data (blue curves) and calculated curves (red lines) for s- and p-polarizations for the incident angle of 60 degrees. This angle is close to the Brewster angle, and therefore the optical response highly depends on the refractive index. A good agreement is also present for the ellipsometric data (top right graphs). The used Tauc–Lorentz model allowed us to achieve a very good agreement over the broad range of wavelengths 380–980 nm. The fit was carried out for all three deposited homogeneous layers, where the fitted refractive index (figure 1, bottom right graph) agreed with the precision of  $\pm 0.015$  and the resulting thicknesses were 600 nm, 1510 nm, and 3890 nm, respectively. Owing to the smooth refractive index wavelength dependence,

the values at the wavelength of 1028 nm were extrapolated from the fitted model. This data was further used to fit the experimentally observed SHG signal.

Even though a centrosymmetric material does not generate SH in its bulk by the electric dipole contribution, the thin film is a special case. The symmetry is broken in the direction perpendicular to the surface, which is commonly denoted as the  $z$ -axis, and the resulting  $C_{\infty v}$  symmetry yields three non-zero  $\chi^{(2)}$  components, which are denoted as  $\chi_{xxz}$ ,  $\chi_{zxx}$ , and  $\chi_{zzz}$ , respectively [2, 7, 23]. Moreover, the deposition process of the thin film can cause local inhomogeneities and strains, which can effectively break the local symmetry of the material.

Two approaches have been reported in the literature: the first approach focuses on the signal generated at the interfaces between the thin layer and adjacent materials, i.e. substrate and superstrate [2]. This approach considers the SHG in two thin polarization sheets located at the thin film interfaces and we will denote it as an ‘interface SHG’. The second approach is based on the use of a Green’s function to extract the SHG signal by the integration of the infinitely thin sheets along the direction of the thin film thickness [7, 23]. This contribution still has the dipole origin, and we will call it ‘bulk SHG’. Finally, there is a contribution due to the electrical multipole interaction, which will be discussed as well.

To characterize the thin films, we acquired SHG signals for a range of incident angles (35–65 degrees) and varying orientations of light polarization. We verified the second-order nonlinear origin by measuring the SHG signal intensity as a function of the fundamental laser intensity, which followed the quadratic dependence (figure S2, supporting materials).

Bulk SHG, which was reported as a dominating source of SHG in  $\text{Si}_3\text{N}_4$  thin films, is known to be prominent for the thick samples measured under a high incident angle [24]. Therefore, we extracted the second-order susceptibility tensor components of the  $\text{Si}_3\text{N}_4$  bulk SHG from the measurement of the sample with 3890 nm layer thickness at 55 degree incidence angle. In the case of polarization measurements, the SHG field for p- and s-polarized light outside the thin film can be expressed as [23]:

$$E_{\text{SHG}}^p = f^p (e^p)^2 + g^p (e^s)^2, \quad (1a)$$

$$E_{\text{SHG}}^s = h^s e^p e^s, \quad (1b)$$

where  $e^p$  ( $e^s$ ) is the amplitude of the polarization component of the fundamental field parallel (perpendicular) to the plane of incidence, and  $f^p$ ,  $g^p$ , and  $h^s$  are the auxiliary expansion coefficients indicating the polarization signatures of the SHG response [23, 24]. To describe the nonlinear response correctly, we had to take into account multiple reflections since the beam spot is greater than the thickness of the thin films [15, 23]. Hence, the expansion coefficients can be expressed as functions of the SHG tensor components as:

$$\begin{bmatrix} f^p \\ g^p \\ h^s \end{bmatrix} = \mathbf{M} \begin{bmatrix} \chi_{xxz} \\ \chi_{zxx} \\ \chi_{zzz} \end{bmatrix}, \quad (2)$$

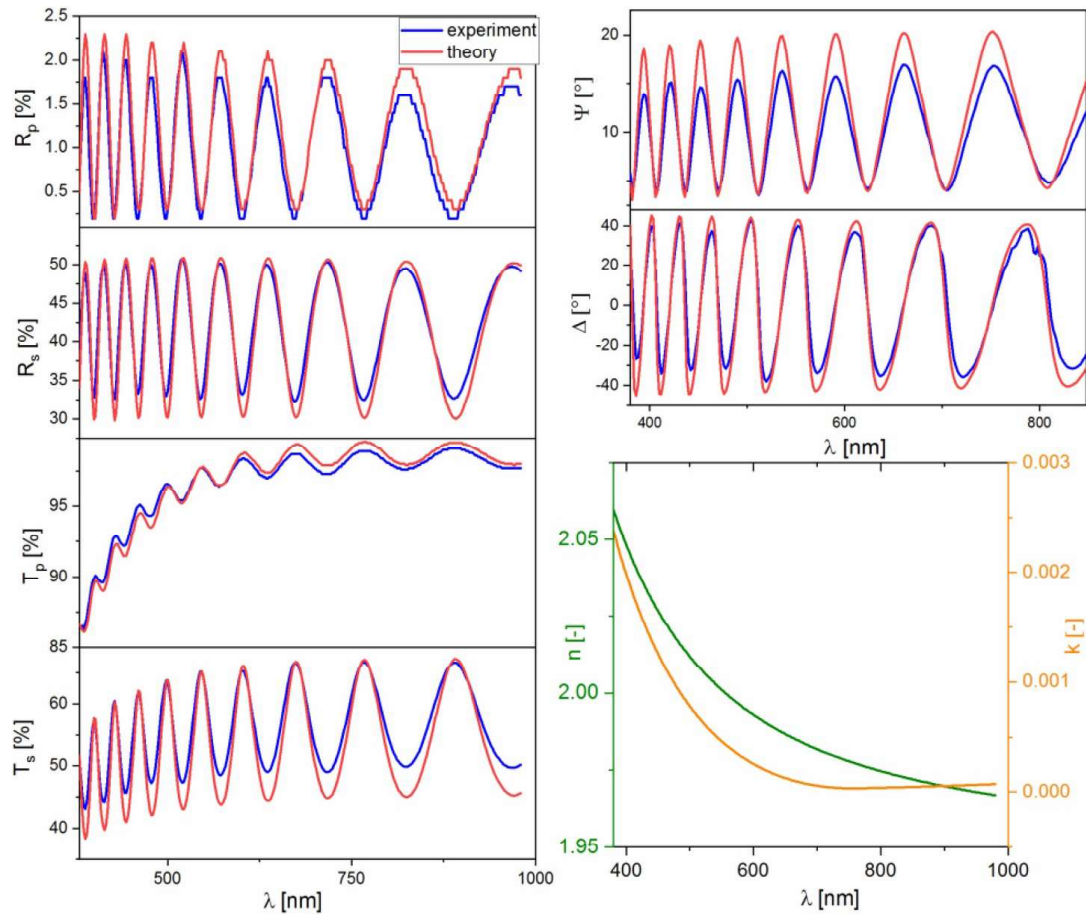


**Figure 1.** Illustration of the optical response fitting for the layer thickness 3980 nm; left graphs: reflectance  $R$  and transmittance  $T$  at 60 degree incidence angle for s and p polarization, comparison of experimental data (blue) with theoretical calculation (red). Top right graph: experimental ellipsometric data (blue lines)  $\psi$  and  $\Delta$  fitted (red lines) for incident angle 70 degree. Bottom right graph: refractive index  $n$  (green line) and its imaginary coefficient  $k$  (orange line) wavelength dependence.

where the matrix  $M$  depends on the experimental geometry of polarization and the linear optical material parameters of the nonlinear film and the substrate, which were determined in the previous section. We adopted the approach used by Koskinen *et al* [15, 23]. The polarization-dependent SHG signal for a range of  $\lambda/2$ -waveplate angles is depicted in figure 2 for two SHG polarizations with corresponding fitted curves. Note that the  $\lambda/2$ -waveplate rotation by an angle  $\alpha$  corresponds to the polarization angle rotated by  $2\alpha$ .

Analogously to the previous reports, the s-polarized SHG intensity is low as compared to p-polarized one. The results from all four measurements were simultaneously fitted for  $f^p$ ,  $g^p$ , and  $h^s$  values, which were recalculated into relative bulk tensor components  $\chi_{zzz}$ ,  $\chi_{xxz}$ ,  $\chi_{zxx}$ , and listed in (table S1, supporting materials) leading to their relative values 0.03, 0.03, and 1.0, respectively. It is evident from the tensor components that the most prominent contribution is coming from the  $\chi_{zzz}$ , which is well corroborated with the previous reports [7, 23].

In order to estimate the absolute values of the tensor components of  $\text{Si}_3\text{N}_4$ , we have performed a calibration against

the Y-cut quartz crystal, which has the dominant tensor component of  $\chi_{xxx} = 0.80 \text{ pm V}^{-1}$  [7, 13, 23]. We have followed Ning *et al* to calibrate the  $\text{Si}_3\text{N}_4$  tensor components using the transmission mode SHG photon collection of the Y-cut quartz crystal [7]. The sample thickness was precisely measured (precision  $<300 \text{ nm}$ ) by using Mitutoyo LEGEX 774 and consequently confirmed by angle-dependent SHG signal from the reference sample. The estimated absolute values for the independent tensor components ( $\chi_{zzz}$ ,  $\chi_{xxz}$ , and  $\chi_{zxx}$ ) of the bulk were found to be 2.6, 0.08, and 0.08, respectively (table S1, supporting materials). It is worthwhile to mention here that the estimated absolute value of the  $\chi_{zzz}$  tensor component is very similar to the previously reported literature values for the  $\text{Si}_3\text{N}_4$  thin films, where Koskinen *et al* reported the calibrated value of  $\chi_{zzz}$  tensor components ranging from 0.8 to  $5.1 \text{ pm V}^{-1}$  for  $\text{Si}_x\text{N}_y$  thin films with a varying content of Si [23]. In another work, Kauranen and co-workers also reported the calibrated of  $\chi_{zzz}$  tensor components of  $2.47 \text{ pm V}^{-1}$  for the  $\text{Si}_3\text{N}_4$  thin film [7, 23].

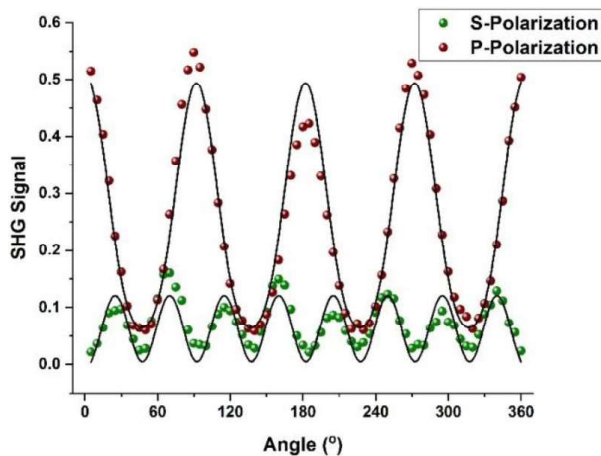


**Figure 2.** Dependence of the SHG signal on the  $\lambda/2$  waveplate angle  $\alpha$ , which rotates the fundamental beam polarization by  $2\alpha$ . Data show for s-polarized (green symbols) and p-polarized (brown symbols) SHG signal for the 3890 nm thick  $\text{Si}_3\text{N}_4$  layer at 55-degree incident angle with associated fitted data (black lines) following equation (1).

To gain insight into the origin of the second-order optical response of thin-film systems, we have carried out angle-dependent SHG studies. Owing to the fact that we use the unusual reflectance mode of the SHG optical set-up, we can track the SHG in the thin film on the opaque c-Si substrate and we can avoid the SHG signal from the substrate. We verified that the substrate itself did not generate any signal (data not shown). The experimental values of SHG intensities in  $\text{Si}_3\text{N}_4$  thin films of three different thicknesses in the reflective geometry are shown in figure 3 (symbols; green = 600 nm, brown = 1610 nm, and blue = 3890 nm, respectively). These values were compared to the bulk-SHG contribution calculated via equations (1) and (2), where we employed the  $\chi^{(2)}$  values for the bulk extracted in the previous section (see dashed black lines). We observed a reasonable agreement between the theory and experiment, including the scaling factor between the curves. However, we observed clear discrepancies in the curve shapes in the case of thin-film samples.

Therefore, we also included into our analysis the interface-SHG model described by Gielis *et al*, where we took into account both the superstrate-layer (surface) and substrate-layer (interface) contributions [2]. We fitted the experimental data by a combination of bulk and interface SHG, where the bulk  $\chi^{(2)}$  values were fixed, while the interface and surface contribution to SHG were left as a fitting parameter. By carrying out a set of optimization with random starting parameters, we attained a set of fitting parameters, where the statistics between the best matching fit served to determine the precision of the values. The fitted values of the SHG susceptibility tensor components of the  $\text{Si}_3\text{N}_4$  are presented in table 1. The resulting curves (solid lines in figure 3) significantly decreased a deviation from the measured SHG signal, especially for the thinner layers, where the contribution

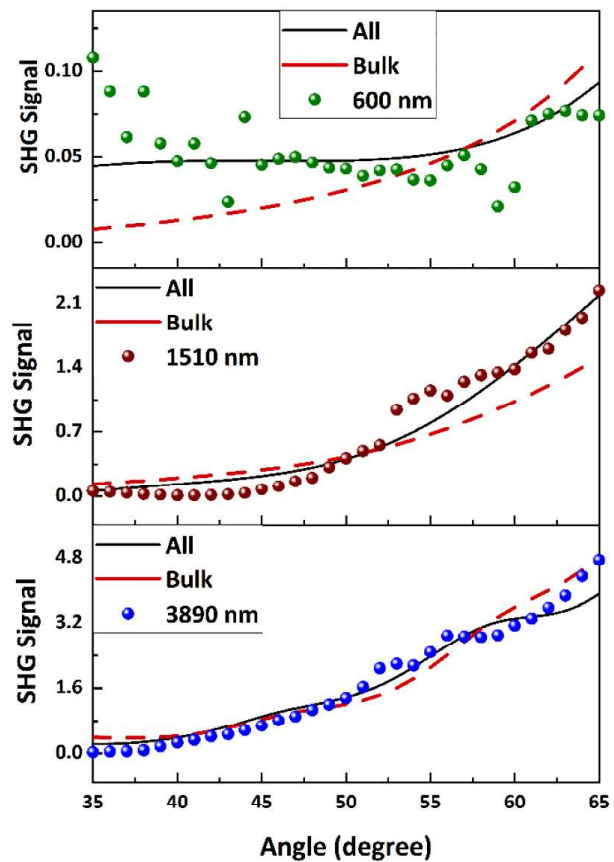


**Figure 3.** Angle dependent SHG responses from  $\text{Si}_3\text{N}_4$  thin films on Si substrate. Film thickness was (a) 600 nm, (b) 1510 nm, and (c) 3890 nm, respectively. The black and full lines correspond to the fitted data by taking accounts of all contributions, whereas the dashed line represents corresponding fitting with bulk contribution only.

**Table 1.** Relative values of second-order susceptibility tensor components of the studied  $\text{Si}_3\text{N}_4$  thin films systems.

	Interface	Surface	Bulk
$\chi_{zzz}$	$0.1 \pm 0.1$	$0 \pm 0.1$	$1.0 \pm 0.2$
$\chi_{zxx}$	$0.8 \pm 0.3$	$0 \pm 0.1$	$0.03 \pm 0.02$
$\chi_{xzz}$	$0.7 \pm 0.3$	$0.1 \pm 0.04$	$0.03 \pm 0.02$

from the surface SHG is expected to be more pronounced. In accordance with the expectations, the fit revealed a significant contribution of the  $\text{Si}_3\text{N}_4$ -Si interface, while the  $\text{Si}_3\text{N}_4$ -air contribution was subtle. It is worth noting that the signal for the 600 nm sample is relatively low due to the necessity to adjust the incident power well below the damage threshold of the material. Nevertheless, the angular dependence of SHG intensity of 600 nm sample could not be reproduced for low incident angles by any form of the bulk SHG contribution and the interface SHG contribution was dominating the signal.

The observed significant  $\text{Si}_3\text{N}_4$ -Si interface contribution is in the agreement with the results of the M. Kauranen group



[23], who studied the Si<sub>3</sub>N<sub>4</sub>-silica thin film samples and were able to describe the SHG layer response based on the bulk model only, since the Si<sub>3</sub>N<sub>4</sub>-Si interface is not present.

We observed that the consideration of the surface and interface SHG contributions enhanced the agreement between measured data and the predictions of the theoretical model. However, a combination of the number of fitting parameters with the remaining discrepancies between the model and data lead to high relative errors of the  $\chi^{(2)}$  tensor components. The remaining difference between the theoretical values and experimental data can be partly subscribed to the minor inhomogeneity in the SHG signal depending on the beam position on the sample, which inevitably slightly drifted during the measurement. By measuring on multiple spots of each sample, we verified that the variation of curves does not exceed the noise level and the shape of the curve is consistent. Nevertheless, this variation was pronounced the most on the 600 nm sample. We ascribe it to the fact that while the bulk of the thin film produced by IBS was highly uniform, the uniformity of the layer-substrate interface was more prone to vary and caused the fluctuation.

It is also worth noting that we did not take into account the complete SHG signal originating from the multipole interactions and dipole magnetic interaction, denoted in the literature by the coefficients,  $\gamma$ , and,  $\delta$  [15]. Even though the  $\beta$  coefficient vanishes for the isotropic materials and  $\gamma$  is indistinguishable from the interface SHG, and it is therefore included, the  $\delta$  coefficient was not taken into account.

In summary, we report on linear and nonlinear optical properties of Si<sub>3</sub>N<sub>4</sub> thin films deposited via the dual IBS method. The reflective indices, transmittance, and thickness of the films have been evaluated by global analysis of ellipsometric, transmittance, and reflectance data. The deposited Si<sub>3</sub>N<sub>4</sub> thin films exhibit significant second-order nonlinear optical behavior, which we studied by means of the unconventional reflectance mode of the SHG optical set-up. This allowed us to study the response of samples deposited on a c-Si substrate. We observe that the dominating origin of the SHG for the thick layer (3980 nm) consists in the dipole bulk contribution, where the absolute value is similar to the previously reported values. However, for the thin layer (600 nm) the Si<sub>3</sub>N<sub>4</sub>-Si interface contribution was comparable to the bulk origin. Our work provides the first quantification of SHG on IBS-deposited thin films. Moreover, we provide a link between the contradictory results proposing the SHG in Si<sub>3</sub>N<sub>4</sub> to occur either in the material volume or its interface.

### Data availability

The data that support the findings of this study are available from the corresponding author upon reasonable request.

### Acknowledgments

The authors gratefully acknowledge the financial support from The Czech Academy of Sciences (ERC-CZ/AV-B, Project Random-phase Ultrafast Spectroscopy; reg. no. ERC100431901), the Ministry of Education, Youth and Sports ('Partnership for Excellence in Superprecise Optics,' Reg. No. CZ.02.1.01/0.0/0.0/16\_026/0008390), and the Czech Science Foundation (GACR 19-22000S).

### ORCID iD

Karel Židek  <https://orcid.org/0000-0002-3275-2579>

### References

- [1] Alduino A and Paniccia M 2007 *Nat. Photon.* **1** 153
- [2] Gielis J J H, Gevers P M, Aarts I M P, Van De Sanden M C M and Kessel W M M 2008 *J. Vac. Sci. Technol. A* **26** 1519
- [3] Butet J, Russier-Antoine I, Jonin C, Lascoux N, Benichou E and Brevet P F 2012 *Nano Lett.* **12** 1697
- [4] Leuthold J, Koos C and Feude W 2010 *Nat. Photon.* **4** 535
- [5] Espinola R L, Dadap J I, Osgood R M, McNab S J and Vlasov Y A 2004 *Opt. Express* **12** 3713
- [6] Vlasov Y, Green W M J and Xia F 2008 *Nat. Photon.* **2** 242
- [7] Ning T, Pietarinen H, Hyvarinen O, Simonen J, Genty G and Kauranen M 2012 *Appl. Phys. Lett.* **100** 161902
- [8] Lettieri S, Merola F, Maddalena P, Ricciardi C and Giorgis F 2007 *Appl. Phys. Lett.* **90** 021919
- [9] Davidson R B, Yanchenko A, Ziegler J I, Avanesyan S M, Lawrie B J and Haglund R F 2016 *ACS Photonics* **3** 1477
- [10] Larciprete M C and Centini M 2015 *Appl. Phys. Rev.* **2** 031302
- [11] Makarov S V et al 2017 *Nano Lett.* **17** 3047
- [12] Watts K E, Blackburn T J and Pemberton J E 2019 *Anal. Chem.* **91** 4235
- [13] Boyd R W 2003 *Nonlinear Optics* (New York: Academic)
- [14] Rulliere C 1998 *Femtosecond Laser Pulses* (Berlin: Springer)
- [15] Koskinen K, Czaplicki R, Kaplas T and Kauranen M 2016 *Opt. Express* **24** 4972
- [16] Zhou X, Cheng J, Zhou Y, Cao T, Hong H H, Liao Z, Wu S, Peng H, Liu K and Yu D 2015 *J. Am. Chem. Soc.* **137** 7994
- [17] Aktsipetrov O A, Fedyanin A A, Mishina E D, Rubtsov A N, Hasselt C W V and Devillers M A C 1996 *Phys. Rev. B* **54** 1825
- [18] Accanto N, Piatkowski L, Hancu I M, Renger J and Van Hulst N F 2016 *Appl. Phys. Lett.* **108** 083115
- [19] Kitao A, Imakita K, Kawamura I and Fujii M 2014 *J. Phys. D: Appl. Phys.* **47** 215101
- [20] Pecora E F, Capretti A, Miano G and Negro L D 2013 *Appl. Phys. Lett.* **102** 141114
- [21] Cazzanelli M et al 2012 *Nat. Mat.* **11** 148
- [22] Levy J S, Foster M A, Gaeta A L and Lipson M 2011 *Opt. Express* **19** 11415
- [23] Koskinen K et al 2017 *Opt. Lett.* **42** 5030
- [24] Sipe J 1987 *J. Opt. Soc. Am. B* **4** 481
- [25] Židek K, Hlubucek J, Horodyská P, Budasz J and Václavík J 2017 *Thin Solid Films* **626** 60
- [26] Kanclř V and Židek K (physics.optics) (arXiv:2012.04260)

